

# tRNA thiolation defects disrupt cellular proteostasis and tissue homeostasis in mammals

Doctoral thesis at the Medical University of Vienna  
for obtaining the academic degree

**Doctor of Philosophy**

Submitted by

**Lukas Englmaier, MSc**

Supervisor:

Univ.-Prof. Dr. rer. nat. Andreas Villunger

CeMM Research Center for Molecular Medicine of the Austrian  
Academy of Sciences

Vienna, 12/2025

“The more you know who you are,  
and what you want,  
the less you let things upset you.”

*Lost in Translation, 2003*

*To Lucy, Ida and the boy.*

## Declaration

The research presented in this thesis was conducted at the **CeMM Research Center for Molecular Medicine of the Austrian Academy of Sciences** in Vienna, Austria, from September 2020 to December 2025 under the supervision of **Prof. Dr. Andreas Villunger**.

This thesis is based on a manuscript that was first submitted for peer review in October 2025. Findings were made accessible to the broader research community via the preprint server bioRxiv. While most of the experimental work was carried out by the author, this thesis benefited significantly from fruitful collaborations with partner laboratories. A detailed description of individual contributions, affiliations, and expert support can be found within the "Author contributions" and "Acknowledgments" sections of the included preprint.

To fulfill the requirement for a first-author publication, a shared co-first author manuscript published in *Nature Communications* (2023) is included in this thesis. This project was initiated in the laboratory of Prof. Igor Adameyko, PhD, at the Center for Brain Research of the Medical University of Vienna. It was completed during the author's doctoral studies at CeMM. As this work represents a distinct line of research outside the primary focus of this dissertation, it is provided as a stand-alone appendix.

Permission to include the bioRxiv preprint and article published in *Nature Communications* has been granted under the Creative Commons Attribution 4.0 International License (CC-BY 4.0).

## Statement on the use of generative AI tools

The author utilized generative artificial intelligence (AI) tools to enhance specific elements of this thesis. OpenAI's GPT-5 was employed exclusively to improve the conciseness, grammar, and readability of the preprint included in Chapter two. Google's Gemini 3 was utilized for data visualization of a figure in "Extended Results", and to assist in refining chapter titles and sub-headings throughout the thesis, as well as in translating the abstract to German. No AI tools were used to generate intellectual content, scientific conclusions, or the primary text of any scientific section. The author has reviewed all AI-assisted output and takes full responsibility for the final content of this thesis.

ChatGPT.....34-51

*These statements were enhanced by AI.*

# Table of contents

## Contents

Declaration.....	ii
Table of contents.....	iii
List of figures.....	vi
List of tables.....	vi
List of algorithms.....	vi
List of abbreviations.....	vii
Abstract.....	x
Zusammenfassung (German).....	xi
Publications arising from this thesis.....	xii
Additional publications.....	xii
Acknowledgments.....	xiii
1. General introduction.....	1
1.1. A brief history of translation.....	1
1.1.1. From DNA to protein.....	1
1.1.2. Solving the genetic code.....	2
1.1.3. The emergence of tRNA as the genetic adaptor.....	2
1.2. Key RNA components of protein synthesis.....	4
1.2.1. The ribosomal catalytic core.....	4
1.2.2. Biogenesis of transfer RNA.....	4
1.2.3. Structural features of the tRNA molecule.....	5
1.3. The mRNA translation cycle.....	6
1.3.1. Initiation.....	6
1.3.2. Elongation.....	7
1.3.3. Termination.....	7
1.3.4. Recycling.....	8
1.4. tRNA modifications.....	8
1.4.1. Structural modifications of the tRNA body.....	8
1.4.2. The anticodon loop as modification hotspot.....	9
1.5. Wobble translation.....	9
1.5.1. Crick's wobble hypothesis.....	9
1.5.2. Diversity in wobble base pairing.....	10
1.6. tRNA thiolation – Assembly of mcm <sup>5</sup> s <sup>2</sup> U <sub>34</sub> .....	11
1.6.1. Biosynthesis of 5-methoxycarbonylmethyl (mcm <sup>5</sup> ) – the prerequisite.....	11

1.6.2. Sulfur mobilization via the URM1 pathway (s <sup>2</sup> U <sub>34</sub> ).....	12
1.7. Structural mechanics of 5-methoxycarbonylmethyl-2-thiouridine .....	13
1.7.1. Stabilizing the anticodon loop .....	13
1.7.2. Facilitating U:G wobble interactions .....	15
1.8. Consequences of modification defects.....	16
1.8.1. Growth impairment .....	16
1.8.2. Reduced ribosomal A-site binding .....	17
1.8.3. Frameshifting .....	17
1.8.4. Ribosome pausing .....	17
1.8.5. Proteostasis defects .....	18
1.9. Linking tRNA modification defects to organismal physiology .....	20
1.9.1. Selective translation impairment: the codon-bias model .....	20
1.9.2. The global stress response hypothesis.....	21
1.9.3. tRNA thiolation as a metabolic and environmental sensor.....	22
1.10. Human pathology .....	23
1.10.1. Complexity as a driver of pathogenicity .....	23
1.10.2. Mitochondrial versus cytosolic manifestations .....	25
1.10.3. A link to tumorigenesis? .....	25
1.10.4. Tissue-specific vulnerability .....	26
1.11. CTU2 deficiency: DREAM-PL syndrome .....	27
1.11.1. Identification of recurrent pathogenic variants .....	27
1.11.2. Global incidence and carrier frequency.....	27
1.11.3. Clinical presentation and phenotypic spectrum.....	28
1.11.4. Clinical outcomes and therapeutic approaches .....	28
1.12. Aims of the thesis .....	30
1.12.1. Aim 1: Define the molecular and cellular consequences of impaired tRNA wobble thiolation in human <i>in vitro</i> models .....	30
1.12.2. Aim 2: Investigate a possible impact on translation and proteome remodeling in CTU2 deficiency .....	30
1.12.3. Aim 3: Identify putative disease-causing pathway dysfunction in DREAM-PL syndrome .....	30
1.12.4. Aim 4: Establish a mouse model to study organismal and tissue-specific vulnerability of DREAM-PL syndrome <i>in vivo</i> .....	30
2. “tRNA thiolation defects disrupt cellular proteostasis and tissue homeostasis in mammals” (Preprint).....	32
2.1. Prologue .....	32
2.2. Extended Results (Zebrafish).....	75
2.3. Methods (Zebrafish) .....	75
2.4. Results (Zebrafish).....	76

2.5. Discussion (Zebrafish).....	78
2.6. Acknowledgements (Zebrafish).....	78
3. Discussion.....	80
3.1. DREAM-PL pathogenesis and ciliopathies: similarities and differences .....	80
3.2. Species-specific divergence in the essentiality of tRNA thiolation .....	80
3.2.1. Zebrafish.....	80
3.2.2. Mice .....	81
3.3. Genomic architecture and physiological regulation of thiolated tRNAs .....	83
3.3.1. Genomic redundancy and tRNA overexpression .....	83
3.3.2. Tissue-specific tRNA expression .....	84
3.3.3. The mammalian thiolation landscape .....	85
3.3.4. Expression and activity of the tRNA thiolation machinery.....	86
3.4. Prospective research directions .....	86
3.4.1. Resolving tissue-specific thiolation dependence .....	86
3.4.2. Quantitative profiling of the tRNA modification landscape .....	87
3.4.3. Possible link between tRNA modifications and tumorigenesis .....	88
3.4.4. Non-canonical functions of CTU2 .....	89
3.5. Theoretical intervention concepts.....	89
3.6. Conclusion.....	91
4. Materials and methods.....	93
References.....	94
Appendix .....	105
Prologue II .....	105
Curriculum vitae .....	170

## List of figures

<b>Figure 1.</b> Major scientific milestones of translation and tRNA biology.....	4
<b>Figure 2.</b> Schematic of tRNA and eukaryotic ribosome during elongation .....	5
<b>Figure 3.</b> tRNA modifications and wobble translation.....	11
<b>Figure 4.</b> Modification of uracil to mcm <sup>5</sup> s <sup>2</sup> U and the sulfur mobilization route.....	14
<b>Figure 5.</b> Molecular impact on translation upon tRNA thiolation loss .....	19
<b>Figure 6.</b> Size of thiolation-incompetent zebrafish mutants .....	76
<b>Figure 7.</b> Confirmation of the loss of tRNA thiolation in mutants .....	77
<b>Figure 8.</b> RNAseq of <i>ctu1</i> knockout zebrafish .....	77
<b>Figure 9.</b> Effects of tRNA thiolation loss on zebrafish cilia .....	78

## List of tables

<b>Table 1.</b> Disease causing genes related to tRNA thiolation .....	23
<b>Table 2.</b> tRNA modification enzymes found mutated in human disease .....	25
<b>Table 3.</b> Single guide RNA sequences for thiolation-null zebrafish .....	75
<b>Table 4.</b> Predicted genomic tRNA genes across different species .....	84
<b>Table 5.</b> List of <i>Saccharomyces cerevisiae</i> tRNA species .....	85
<b>Table 6.</b> List of RNA modifications detected by NAIL-MS.....	88

## List of algorithms

GPT-5 (October 2025 version), developed by OpenAI, was accessed via <https://chat.openai.com>. Google Gemini 3 (November 2025 version), developed by Google DeepMind, was accessed via <https://gemini.google.com>.

## List of abbreviations

Abbreviation	Definition
AA	amino acid
aaRS	aminoacyl-tRNA-synthetase
ALS	amyotrophic lateral sclerosis
APM	[(N-acryloylamino)phenyl]mercuric chloride
ATP	adenosine triphosphate
bp(s)	base pair(s)
Cas9	CRISPR-associated protein 9
cm <sup>5</sup> U	5-carboxymethyluridine
CRISPR	clustered regularly interspaced short palindromic repeats
CTU1	cytosolic thiouridylase 1
CTU2	cytosolic thiouridylase 2
DNA	deoxyribonucleic acid
DREAM-PL	dysmorphic facies, renal agenesis, ambiguous genitalia, microcephaly, polydactyly, lissencephaly
eEF	eukaryotic elongation factor
eIF	eukaryotic initiation factor
ELP	elongator complex protein
eRF	eukaryotic release factor
ER	endoplasmic reticulum
gnomAD	Genome Aggregation database
GO	Gene Ontology
GTP	guanosine triphosphate
IMPC	International Mouse Phenotyping Consortium
ISR	integrated stress response
KD	knockdown
KO	knockout
LC-MS	liquid chromatography-mass spectrometry
m <sup>1</sup> G	1-methylguanosine
m <sup>5</sup> C	5-methylcytidine
mcm <sup>5</sup>	5-methoxycarbonylmethyl

mcm <sup>5</sup> s <sup>2</sup> U	5-methoxycarbonylmethyl-2-thiouridine
mESC	mouse embryonic stem cell
MOCS3	molybdenum cofactor synthesis 3
MPST	mercaptopyruvate sulfurtransferase
mRNA	messenger RNA
mt-tRNA	mitochondrial tRNA
NAIL-MS	nucleic acid isotope labeling mass spectrometry
NFS1	cysteine desulfurase
nTPM	normalized transcripts per million
PIC	pre-initiation complex
Pol III	RNA polymerase III
PTC	peptidyl transfer center
RNA	ribonucleic acid
RNAseq	RNA sequencing
RPE1	Retinal Pigment Epithelium cells
RQC	ribosome-associated quality control
rRNA	ribosomal RNA
s <sup>2</sup> U	2-thiouridine
sgRNA	single guide RNA
t <sup>6</sup> A	N6-threonylcarbamoyladenosine
tRNA	transfer RNA
tRNAi	initiator tRNA
UPR	unfolded protein response
URM1	ubiquitin related modifier 1
yW	wybutosine
Ψ	pseudouridine

## Abstract

Sulfur modification, or thiolation, of transfer RNA (tRNA) wobble uridine is an evolutionarily conserved mechanism ensuring efficient and accurate protein synthesis. In humans, the loss of this anticodon modification causes DREAM-PL syndrome, a severe congenital disorder characterized by multi-systemic developmental defects and early lethality. Genetically, it is caused by loss-of-function mutations in the *cytosolic thiouridylase 2 (CTU2)* gene. However, the molecular mechanisms linking these mutations to disease pathology remain poorly understood.

Research presented in this thesis sought to describe the consequences of the loss of tRNA thiolation in human cells and determine its essentiality across higher organisms. We characterized primary cells from DREAM-PL patients alongside isogenic cell lines engineered for acute *CTU2* depletion. These human models revealed that loss of tRNA thiolation triggers significant proteostasis defects. Mechanistically, structural and biochemical analyses demonstrated that the recurring pathogenic *CTU2*<sup>L63P</sup> mutation destabilizes the CTU1/CTU2 complex, abolishing its ability to bind and modify tRNA. Ribosome profiling uncovered that CTU2 deficiency led to codon-specific ribosome pausing at AAA, CAA, GAA, and AGA, which are decoded by thiolated tRNAs. Furthermore, ribosome occupancy of transcripts enriched in these codons decreased in a dosage-dependent manner, resulting in codon-biased proteome remodeling. Bioinformatic analyses predicted that codon-biased mRNAs transcribed from genes critical for ciliogenesis are disproportionately affected, linking their reduced translation to the etiology of DREAM-PL in humans.

To investigate organismal vulnerability *in vivo*, we established a comprehensive toolkit of animal models. We generated a *Ctu2*<sup>L63P</sup> knock-in mouse model and constitutive knockouts of *urm1*, *ctu1*, and *ctu2* in zebrafish. Strikingly, findings from these models revealed a profound biological divergence. While *Ctu2*<sup>L63P</sup> mice displayed severe thiolation defects across tissues, they developed normally and remained viable and fertile. Similarly, zebrafish lacking the core thiolation machinery remained viable.

Collectively, this work demonstrates that while tRNA thiolation is critical for proteostasis and human health, it is not strictly essential for development and survival in other vertebrates. This implies that the requirement for tRNA thiolation during embryogenesis is species-specific, possibly due to the existence of compensatory mechanisms. The models and mechanistic insights established in this thesis provide a foundation for resolving these evolutionary differences and developing future therapeutic strategies for DREAM-PL syndrome.

## Zusammenfassung (German)

Die Modifikation des „wobble Uridins“ in tRNA mit Schwefel (tRNA Thiolierung) ist ein evolutionär konservierter Mechanismus, der eine effiziente und genaue Proteinsynthese gewährleistet. Beim Menschen verursacht der Verlust dieser Anticodon-Modifikation das DREAM-PL-Syndrom, eine schwere angeborene Erkrankung, die durch multisystemische Entwicklungsstörungen und frühe Sterblichkeit gekennzeichnet ist. Genetisch wird sie durch Mutationen im *CTU2* (*cytosolic thiouridylase 2*) Gen verursacht. Die molekularen Mechanismen, die diese Mutationen mit der Krankheitspathologie verbinden, sind jedoch weitgehend unbekannt.

Die Forschung, die dieser Dissertation zugrunde liegt, zielte darauf ab, die Folgen des Verlusts der tRNA Thiolierung in menschlichen Zellen zu beschreiben und ihre Lebensnotwendigkeit in höheren Organismen zu bestimmen. In humanen Zellmodellen zeigen wir, dass der Verlust der tRNA Thiolierung signifikante Defekte in der Proteostase auslöst. Die pathogene *CTU2*<sup>L63P</sup> Mutation destabilisiert den CTU1/CTU2-Komplex und beeinträchtigt dessen Fähigkeit zur Bindung und Modifikation von tRNA. Durch „Ribosome Profiling“ fanden wir heraus, dass ein *CTU2* Mangel zu einem codon-spezifischen Pausieren der Ribosomen an AAA, CAA, GAA und AGA führt. Diese Codone werden von thiolierten tRNAs decodiert. Zudem verringerte sich die Anzahl an Ribosomen auf diesen mRNAs, wodurch es zu einer codon-abhängigen Umgestaltung des Proteoms kommt. Bioinformatische Analysen legten nahe, dass hier codon-abhängige mRNAs kritisch für die Ziliogenese überproportional betroffen sind, was das Krankheitsbild von DREAM-PL erklären könnte.

Um den Zusammenhang im ganzen Organismus zu untersuchen, etablierten wir ein umfassendes Set an Tiermodellen: ein *Ctu2*<sup>L63P</sup> Knock-in-Mausmodell, sowie konstitutive Knockouts von *urm1*, *ctu1* und *ctu2* im Zebrafisch. Diese Modelle offenbarten eine tiefgreifende biologische Divergenz. Während *Ctu2*<sup>L63P</sup> Mäuse Thiolierungsdefekte in allen Geweben aufwiesen, entwickelten sie sich normal. Analog dazu erwiesen sich auch Zebrafische, denen die Kernmaschinerie der Thiolierung fehlte, als lebensfähig.

Zusammenfassend zeigt diese Arbeit, dass die tRNA-Thiolierung zwar kritisch für die Proteostase und die menschliche Gesundheit ist, jedoch für die Entwicklung und das Überleben anderer Wirbeltiere nicht strikt essenziell ist. Dies impliziert, dass die Notwendigkeit der tRNA-Thiolierung während der Embryogenese speziesspezifisch ist. Die in dieser Arbeit etablierten Modelle und mechanistischen Erkenntnisse bilden eine Grundlage, um diese evolutionären Unterschiede aufzuklären und zukünftige Therapiestrategien für das DREAM-PL-Syndrom zu entwickeln.

## Publications arising from this thesis

**Englmaier L**, Walczak M, Malzl D, Eggers C, Eichin F, Sladky VC, Gallob FM, Tyshchenko Y, Zarif Z, Kolbe T, Al-Abdi L, Menche J, Spassky N, Geley S, Rossmanith W, Alkuraya FS, Leidel SA, Glatt S, Villunger A (2025) tRNA thiolation defects disrupt cellular proteostasis and tissue homeostasis in mammals. *bioRxiv* 24.10.25

Petersen J\*, **Englmaier L\***, Artemov AV, Poverennaya I, Mahmoud R, Boudier T, Tesarova M, Deviatiiarov R, Szilvásy-Szabó A, Akkuratov EE, *et al* (2023) A previously uncharacterized Factor Associated with Metabolism and Energy (FAME/C14orf105/CCDC198/1700011H14Rik) is related to evolutionary adaptation, energy balance, and kidney physiology. *Nat Commun* 14: 3092

(See appendix)

## Additional publications

Zhang S, Owyong TC, Sanislav O, **Englmaier L**, Sui X, Wang G, Greening DW, Williamson NA, Villunger A, White JM, *et al* (2025) Global analysis of endogenous protein disorder in cells. *Nat Methods* 22: 124–134

Zupančič M, Keimpema E, Tretiakov EO, Eder SJ, Lev I, **Englmaier L**, Bhandari P, Fietz SA, Härtig W, Renaux E, *et al* (2024) Concerted transcriptional regulation of the morphogenesis of hypothalamic neurons by ONECUT3. *Nat Commun* 15: 8631

Rizzotto D, **Englmaier L** & Villunger A (2021) At a Crossroads to Cancer: How p53-Induced Cell Fate Decisions Secure Genome Integrity. *Int J Mol Sci* 22: 10883 (Review)

## Acknowledgments

Nothing in science is possible without the right people. And people may just be the best part of it.

I am endlessly grateful to everyone that kept me company during the last 10 years of my scientific journey. Julian and Igor, my early mentors. Marilena for friendship and advice. Zdenek and Taras for trusting me and help shaping me into an independent scientist.

To Andy Villunger for hiring me. We both took a chance and ended up with something impactful. Thank you for the academic freedom, the support, the grants, and the quick email responses.

To the Vienna Villunger lab members, Filip, Dario, Zhenya, my students Efi and Zarghun. Thank you for the memories, coffee break discussions, support and motivation. I learned a lot about science and myself. To the Innsbruck Villunger lab members, especially Felix. Thanks for all the questions, the experimental help and the couch.

To CeMM. A truly unique place. And the Pandemic Cohort. The best of them all.

To Marcus and Vassilis. For sharing my mindset. Hope to see us all being PIs one day.

To my family. My parents, my sister. For being there for me. For letting me be who I am.

To Lucy. Scientist, best friend, lover of depressed musicians, wife, soon to be mother. You are the best thing that science has brought, and ever will bring, me.

# Chapter one

# 1. General introduction

Every living cell relies on error-free protein translation for survival. This ensures that the hereditary information stored in a cell's genome can be transformed into functional units that support cellular physiology. Proteins, representing one entity of such units, serve diverse functions, including their prominent roles in acting as enzymes, but they also contribute to cellular signaling, building and safeguarding of cellular structures, and coordinating transport of molecules within and between cells in tissues or bloodstream.

Translation – the process of generating proteins – is an intricate process that is regulated at different levels within the cell. To complete the flow of information during gene expression, DNA needs to be first transcribed into an intermediate messenger, messenger RNA (mRNA), which is later used as a template for transfer RNAs (tRNAs) to produce a corresponding polypeptide chain within a ribosome, which then folds into a functional protein.

## 1.1. A brief history of translation

2025 marks the 70<sup>th</sup> anniversary of the discovery of the ribosome by George E. Palade (Palade, 1955). Shortly after, in 1957 transfer RNA was discovered in the laboratory of Paul Zamecnik (Hoagland *et al*, 1958). Together with the discoveries of the structure of DNA (Watson & Crick, 1953), and mRNA as information carrier (Brenner *et al*, 1961), breakthrough laboratory findings of this period enabled molecular biologists to devise ways to wholistically understand protein translation. **(Figure 1)**

### 1.1.1. From DNA to protein

Genes are encoded by four nucleotide bases in DNA, adenine (A), cytosine (C), guanine (G) and thymine (T). It is the series of specific base triplets that will later define the amino acid order in a nascent polypeptide chain. DNA is a double-stranded helix containing a template and a coding strand. It is a very stable structure, through its base pairing between G:C and A:T with three and two hydrogen bonds, respectively. As suggested by the name, RNA polymerase II uses the template strand to transcribe information from DNA into mRNA. RNA differs from DNA chemically. It contains ribose instead of deoxyribose, is present as a single-stranded less stable molecule, and uses uracil (U) instead of thymine. Transcribed mRNA undergoes a series of maturation steps in the nucleus, most importantly splicing and capping, before being exported to the cytosol, where it associates with translation initiation factors and ribosomal subunits. Canonical translation starts at a defined base triplet or codon, termed start codon (*i.e.* ATG in most organisms). For each successive codon, one amino acid is recruited and linked into a polypeptide chain, catalyzed by ribosomal RNA (rRNA) and proteins. tRNAs

carry out the bridging function of decoding mRNA codons and delivering the respective amino acid to the ribosome.

### 1.1.2. Solving the genetic code

There are 21 proteinogenic amino acids in eukaryotes, including 20 “standard amino acids” and selenocysteine, a rare amino acid incorporated instead of a canonical stop codon. Scientists had experimentally detected 20 amino acids and four DNA bases by chromatography for decades, but never more. After having identified the nature and structure of DNA as genetic information storage in the 1950s, scientists hypothesized that a specific code of the DNA bases must provide information about a protein’s sequence. Studies on bacteriophage mutants experimentally validated this hypothesis, proving that genes are stored in “reading frames” assembled from non-overlapping base triplets with a defined starting point (Crick *et al*, 1961). These experiments convincingly showed that base insertions (+1, +2) or deletions (-1, -2) in an essential gene rendered the bacteriophage T4 growth-incompetent in *Escherichia coli* K12. This phenotype was reversed by suppressor mutations that restored the reading frame (-3, 0, +3). Another major contribution to solving the genetic code was made by using simple synthetic RNA molecules in *in vitro* translation experiments to systematically decipher which nucleotide triplet corresponded to which amino acid (Nirenberg, 2004; Nirenberg & Leder, 1964; Nirenberg & Matthaei, 1961; Söll *et al*, 1965).

The genetic code is degenerate, since there are 64 possible codons ( $4^{\text{bases}^3\text{positions}} = 64$ ) but only 20 different amino acids. More than one codon can encode a specific amino acid. Interestingly, the number of codons each amino acid is defined by is not evenly spread (*i.e.* 3 per AA). Some amino acids like arginine are encoded by as many as 6 different codons (AGA, AGG, CGU, CGC, CGA, CGG) whereas others like phenylalanine, the amino acid first decoded by using a poly-U RNA template (Nirenberg & Matthaei, 1961), is only defined by two codons (UUU, UUC). By 1965 the genetic code was fully solved and found to be universally true, meaning that it is shared amongst different species (Nirenberg *et al*, 1966).

Marshall Nirenberg, Har Gobind Khorana and Robert Holley went on to receive the Nobel Prize in Physiology or Medicine in 1968 “for their interpretation of the genetic code and its function in protein synthesis” (Singer, 1968). While Nirenberg’s and Gobind Khorana’s contribution was the deciphering of codon-amino acid relations, Robert Holley determined the first complete nucleotide sequence of a tRNA molecule.

### 1.1.3. The emergence of tRNA as the genetic adaptor

Using a methodology not dissimilar to Frederick Sanger’s with Insulin (Sanger & Tuppy, 1951), Robert Holley and colleagues first purified alanine tRNA (then termed sRNA, for soluble RNA)

extracted from yeast, digested it enzymatically and identified overlapping polypeptides using chromatography (Holley *et al*, 1965). The resulting 77 base long RNA was the first nucleic acid to be sequenced. The molecular function of this highly specialized RNA molecule is to serve as adapter molecule between genetic information (mRNA) and the molecular machinery of protein production (ribosome). Many of its functional requirements were correctly predicted by Francis Crick's "adaptor hypothesis" in his seminal theoretical article from 1958 (Crick, 1958). Indeed, as predicted, amino acids are delivered to the mRNA template confined within a ribosome as independent units bound to tRNA. The process of loading tRNAs with amino acids through an ester bond, also known as tRNA charging, is carried out by a group of specialized enzymes termed aminoacyl-tRNA-synthetases (aaRS). Each amino acid – tRNA combination is recognized exclusively by one of 20 aaRS providing the required specificity (reviewed in Ibba & Soll, 2000).

By the early 1950s electron microscopy had matured to allow scientists to visualize more and more organelles of eukaryotic cells (Sabatini, 1999). By magnifying rat and chicken cells up to 91,000 times, George Palade noted that the endoplasmic reticulum (ER) of almost all investigated cell types was lined with small spherical granular components, that would later be referred to as ribosomes (Palade, 1955). Fascinatingly, he observed some ribosomes forming short chains, what was likely the first observation of translation in action via polysomes, a series of ribosomes producing proteins from one mRNA. Equally interestingly, it was noted that these structures were predominantly found in cellular locations of known high RNA content. A few years later Palade's group provided evidence for the ribosome as primary site of protein synthesis, by injecting radioactively labelled amino acids into Guinea pigs and following their incorporation in pancreatic cell fractions (Siekevitz & Palade, 1958). Palade later shared the Nobel Prize in Physiology or Medicine in 1974 with Christian de Duve and their mentor and collaborator Albert Claude.

Cell fractionation, pioneered by Claude in the 1940s (Claude, 1946), had been (and remains to date) a common means of studying isolated ribosomes. Using this, Mahlon Hoagland conducted an elegant study in Paul Zamecnik's lab that studied protein synthesis using cell-free systems (*i.e.* isolated ribosomes, nucleic acids and enzymes). The major finding that an intermediate RNA molecule – tRNA – was first activated by aminoacylation and then delivered to the ribosome, where the amino acid was incorporated into a nascent polypeptide (Hoagland *et al*, 1958), ultimately validated Crick's "adaptor hypothesis".

## Milestones in Early Translation Biology

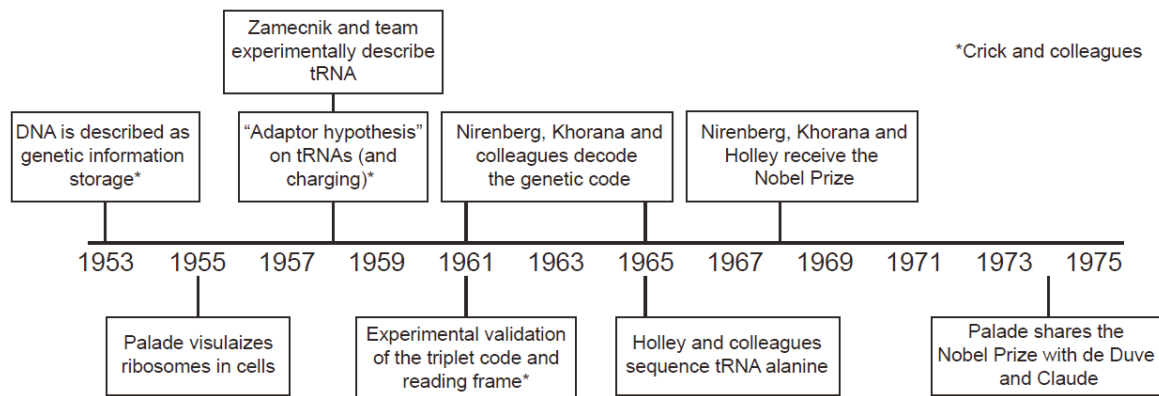


**Figure 1.** Selection of major scientific milestones of translation and tRNA biology of the 1950s and 1960s illustrating how discoveries in DNA structure and protein synthesis led to solving of the genetic code and understanding the role of tRNA as adapter molecule.

## 1.2. Key RNA components of protein synthesis

### 1.2.1. The ribosomal catalytic core

Ribosomes – the sites of protein synthesis – are ribozymes, a term coined by the group around Thomas Cech, referring to certain RNAs themselves being catalytic entities (Kruger *et al*, 1982). The conglomerate of human ribosomes consists of four distinct rRNA species (28S, 5.8S, 5S and 18S) and about 80 different proteins (Armache *et al*, 2010). Of these, 28S rRNA, an approximately 5,000-nucleotide long RNA molecule of the large subunit, is the core catalyst of peptide bond formation. It transiently stabilizes ribosome and tRNA interactions without direct protein contribution (Nissen *et al*, 2000).

### 1.2.2. Biogenesis of transfer RNA

tRNAs, the adapter molecules bridging genetic information to structural output, are equally specialized RNA molecules. Their biogenesis and maturation processes encompass many highly coordinated steps, including tRNA transcription, trimming, splicing, modifying and aminoacylation. Approximately 500 tRNA genes are found within the human genome that are transcribed into precursor transcripts by RNA polymerase III (Pol III). Pol III is recruited to respective tRNA loci by transcription factors that bind conserved tRNA loop sequences and terminates at poly-U stretches. In the nucleolus, these precursors are processed by the endonuclease RNase P that cleaves off a leader sequence at their 5' end. Furthermore, different enzymes will decorate tRNAs with the first series of chemical modifications that are important for folding and function (more information on modifications below). Upon relocation to the nucleus, also the 3' end will be processed, first by RNase Z/ELAC2, followed by the

addition of the three nucleotides -C-C-A. This is an essential requirement for later tRNA charging. Following a second round of modifications, tRNAs are exported to the cytosol, where the subset of intron-containing species undergoes splicing, before all tRNAs will be charged by their respective aaRS. Finally, cytosolic tRNA modification enzymes will further modify the tRNA molecule. The anticodon loop, the specific tRNA component which is in contact with mRNA within the ribosome during translation is a particular modification hotspot. (Phizicky & Hopper, 2023)

### 1.2.3. Structural features of the tRNA molecule

All tRNAs share a highly conserved structure. The secondary structure (Holley *et al*, 1965), commonly depicted as a “cloverleaf”, is defined by complementary RNA regions, where base pairing takes place. These stretches are interspersed with unpaired regions or loops that subdivide tRNA into five distinct parts: the acceptor stem (aminoacylation, CCA end), the D-arm (dihydrouridine), the TΨC-arm (ribothymidine T, pseudouridine Ψ, cytidine C), the variable loop and the anticodon loop (required for pairing with respective mRNA codons) (**Figure 2a**). In 3D, tRNA folds into an L-shaped conformation that has been extensively characterized by X-ray crystallography (Shi & Moore, 2000) and more recently cryo-EM (Biela *et al*, 2023; Hammermeister *et al*, 2025). Intriguingly, tRNAs show a high degree of sequence variations (Lin *et al*, 2019). At the anticodon level this diversity is essential for interpreting encoded genetic information. Yet, the tRNA bodies of all species need to form consistent structural elements for recognition and translational functions within the ribosome. These must allow aminoacylation, elongation factor binding and A-site accommodation with correct AA placement in the PTC.

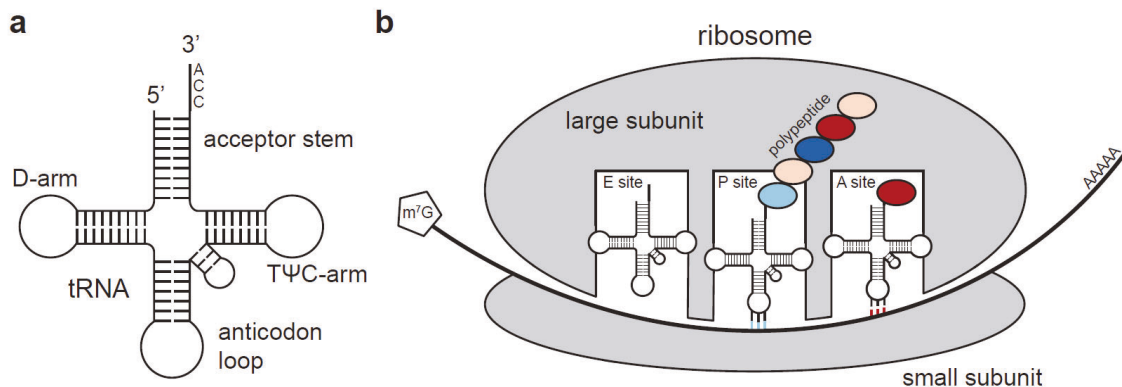


**Figure 2.** Schematic of tRNA and simplified representation of a eukaryotic ribosome during elongation **(a)** 2D representation of the key structural features of a tRNA molecule, omitting AA and modifications. In 3D, tRNAs fold into an identical L-shaped conformation via D- and T-arm proximity. **(b)**. The ribosome moves along the mRNA as charged tRNAs enter the aminoacyl site (A site) and probe codon:anticodon compatibility. A match is indicated (red AA, red codon) and the elongation cycle is triggered.

### 1.3. The mRNA translation cycle

Eukaryotic translation encompasses four general phases: initiation, elongation, termination and recycling (Brito Querido *et al*, 2024; Dever *et al*, 2018). Requirements are a template to decode (*i.e.* a polyadenylated and m<sup>7</sup>G-capped mRNA), recycled ribosomal 40S (containing the 18S rRNA) and 60S (28S, 5.8S and 5S rRNAs) subunits, charged tRNAs, and a plethora of ancillary proteins (eukaryotic initiation, elongation, termination, and recycling factors), as well as guanosine and adenosine triphosphate (GTP, ATP), as energy sources.

Together with DNA replication, translation is one of the most energy intense cellular processes. Preceding ribosomal translation, tRNA charging itself requires the hydrolysis of two high energy bonds (Rubio Gomez & Ibba, 2020). The aminoacylation reaction catalyzed by an aaRS, which predominantly takes place in the cytoplasm, happens in two successive steps: first amino acid activation (Cavarelli *et al*, 1994), followed by tRNA binding (Giege *et al*, 1998). At first an AA-AMP intermediate is created through ATP hydrolysis followed by AA-tRNA conjugation. Intriguingly, the second step does not necessarily depend on the sequence information of a tRNA anticodon, but other structural determinants within the tRNA body can suffice for specificity and thereby implementation of the genetic code (Schimmel & De Poupiana, 1995). In case errors arise, some aaRSs also have proofreading and deacetylation capabilities (Martinis & Boniecki, 2010). The energy expended during charging represents 50% of the cell's energy cost of translation per AA. The other 50% are consumed in form of GTP during the elongation phase, where the ribosome advances by one codon and catalyzes one peptide bond formation. Additional GTP is spent during initiation and termination and ATP during recycling.

#### 1.3.1. Initiation

Initiation marks the starting point of translation, with a recycled 40S small ribosomal subunit binding to eukaryotic initiation factors (eIF1, EIF1A and eIF3). Next, a translation pre-initiation complex (43S PIC) is assembled with the additional binding of eIF5 and a ternary complex, consisting of eIF2-GTP and the initiator tRNA (tRNA<sub>i</sub>). Translation in virtually all organisms starts with a methionine-tRNA<sub>i</sub>, or a chemically modified form thereof. In eukaryotic mRNA, the AUG codon predominantly marks the start of an open reading frame, although non-AUG translation initiation with near-cognate codons such as CUG has been reported (Kearse & Wilusz, 2017). While a cognate codon represents a base triplet that perfectly base pairs with a tRNA anticodon (e.g. glycine: mRNA<sup>GGC</sup> with lysine tRNA<sup>GCC</sup>), near-cognate codons differ by one base and may be misread by tRNAs that only partially base-pair. Before an mRNA is scanned for its start codon, it needs to pass an additional quality control checkpoint exerted by the eIF4F cap-binding complex and the poly(A)-binding protein. Ensuring the recruitment

of a mature capped and tailed mRNA, it will then bind the 43S PIC and form an open 48S scanning complex. During scanning for the start codon GTP is hydrolyzed and upon encountering an AUG, eIF2-GDP and most other initiation factors are released. This closed 48S complex then binds eIF5B-GTP, which provides energy to recruit the 60S large ribosomal subunit, yielding an 80S ribosome. Methionine is placed into the peptidyl transfer center (PTC) of the ribosome and elongation commences. Interestingly, met-tRNA<sub>i</sub> has unique structural features that enable eIF2a binding and its direct placement into the P site, allowing subsequent AA incorporations to occur (Drabkin *et al*, 1998). (Brito Querido *et al*, 2024)

### 1.3.2. Elongation

Elongation is the repetitive recruitment of an AA-tRNA to its cognate mRNA codon and incorporation of the respective AA into the nascent polypeptide chain (**Figure 2b**). Upon delivery, AAs are linked together via peptide bonds as the 80S ribosome moves along the mRNA. The catalytic center for peptide bond formation is located within the large ribosomal subunit, whereas mRNA binding is confined to the small subunit (Hansen *et al*, 2002; Lomakin & Steitz, 2013). Together, both subunits form three distinct sites that successively accommodate tRNA: the A site (aminoacylation), P site (peptidyl) and E site (exit). Upon binding of eukaryotic elongation factor 1 (eEF1A) loaded with GTP, AA-tRNAs enter the ribosomal A site and probe their compatibility for the respective mRNA codon aligned with the A site. When there is a match, GTP is hydrolyzed, eEF1a-GDP is released and the tRNA firmly placed into the A-site. The proximity of P- and A-site tRNAs, together with the E-site binding of eukaryotic initiation factor 5a (eIF5A), induces the formation of the peptide bond. The nascent polypeptide is handed over to the A-site tRNA, and both tRNAs shift forward into hybrid states. eEF2-GTP binds in the freeing A-site and upon hydrolysis ensures correct translocation of the ribosome. The deacylated tRNA finding itself in the E-site is released and the elongation cycle repeats. (Dever *et al*, 2018)

### 1.3.3. Termination

Termination is the coordinated release of a nascent polypeptide upon reaching a stop codon in an open reading frame. Once one of the three eukaryotic stop codons UAA, UAG, or UGA is reached, the eukaryotic translation termination factor 1 (eRF1) binds to the empty A-site. A second associated factor and member of the pre-termination complex, eRF3-GTP assists by conformational rearrangement through GTP hydrolysis (Shao *et al*, 2016). Parts of eRF1 can then extend into the PTC within the large subunit and release the forming protein. (Hellen, 2018)

### 1.3.4. Recycling

Recycling enables ribosomal subunits and, importantly, released mRNA to be reused for further cycles of translation. Splitting of the 80S ribosome into its 60S and 40S subunits is performed by ABCE1 using ATP as energy source (Pisarev *et al*, 2010). tRNA and mRNA release are coordinated by initiation factors, completing the translation cycle. (Hellen, 2018)

## 1.4. tRNA modifications

To normalize their function irrespective of sequence variations, tRNAs have co-evolved with enzymes that can modify their bases and ribose moieties to adapt electrochemical, physical and functional properties. In fact, all major classes of RNA have been found to carry post-transcriptional modifications (Delaunay *et al*, 2024). The emerging field of research, which focuses on chemical modification of RNA molecules to regulate gene expression, has been termed epitranscriptomics.

Although being a small, non-coding RNA with an average length of 70-80 nucleotides, tRNA is a complex and stable molecule. Mature tRNAs carry the most post-transcriptional modifications of all RNA species, with up to 20% of nucleotides modified in some species (Pan, 2018). Simple modifications such as the addition of a methyl group (-CH<sub>3</sub>), for example m<sup>1</sup>A58 (methylation of nitrogen 1 of adenosine at positions 58 of tRNA), are nearly universal in both cytosolic and mitochondrial tRNAs and have been shown to be important for structure (Oerum *et al*, 2017). This is true for less common modifications, such as 4-thiouridine (s<sup>4</sup>U) that decorates position 8 of half of the *E. coli* tRNA repertoire. When hypomodified, these species were found to be rapidly degraded (Kimura & Waldor, 2019).

### 1.4.1. Structural modifications of the tRNA body

Pseudouridine ( $\Psi$ ) is the most common modification, found in all types of RNA.  $\Psi$  synthases are the enzymes catalyzing isomerization reactions of uridine. Often, tRNA modifications depend on complex enzymatic cascades and functional complexes. Found most frequently at tRNA positions 13 and 55 in the D- and T $\Psi$ C-arm, respectively,  $\Psi$  contributes to stability, as recently shown by single particle cryo-electron microscopy and biophysical measurements (Biela *et al*, 2025). The bacterial homologue of human Pus4 was further shown to be a tRNA chaperone, assisting in folding irrespective of its enzymatic activity (Keffer-Wilkes *et al*, 2016). Of note, the properties of  $\Psi$  extend beyond stabilizing tRNA. When introduced into mRNA instead of uridine,  $\Psi$  suppresses endogenous immune responses to foreign RNA (Karikó *et al*, 2005) and increases their translational capacity (Karikó *et al*, 2008). These findings, originating from tRNA research, proved to be key in the establishment of mRNA vaccines against COVID19 in the early 2020s.

Other frequent tRNA body modifications include dihydrouridine (Yu *et al*, 2011), mainly in the D-loop, and 5-methylcytidine (m<sup>5</sup>C) (Shinoda *et al*, 2019) (**Figure 3a**). Some serve functions beyond ensuring structural integrity (Yared *et al*, 2024).

#### **1.4.2. The anticodon loop as modification hotspot**

Positions 34, 35 and 36 form the anticodon of a tRNA molecule. It is these three bases within the anticodon loop that will recognize mRNA codons in the ribosomal A site. Together with the adjacent position 37, these nucleotides are the most frequently and most diversely modified within tRNA. The nucleotide at position 37 is nearly always a purine (A or G) and modified (m<sup>1</sup>G, N6-isopentenyladenosine i<sup>6</sup>A, N6-threonylcarbamoyladenine t<sup>6</sup>A, Wybutosine yW). These modifications are key in structuring the anticodon-loop and thereby prevent frameshifting during translation (Jäger *et al*, 2013). Given their direct interactions with both mRNA and rRNA, the anticodon and respective anticodon modifications are safeguarding translation fidelity. The chemical makeup of a codon-anticodon pair defines the modification need for accurate decoding. A- and U-containing codon:anticodon pairs bind weakly compared with C- and G-rich ones that form an additional, third hydrogen bond per pair. To streamline translation, all pairings must adopt favorable, stable conformations. To ensure this, A and U are often enhanced with sophisticated anticodon modifications (Agris, 2008).

### **1.5. Wobble translation**

Position 34 is also referred to as “wobble position”. It marks the location of the most flexible tRNA nucleotide that aligns itself with the third base of an mRNA codon. mRNA is translated from its 5' to 3' end, with incorporating tRNA binding respective codons in an anti-parallel 3' to 5' manner. The first two bases follow strict Watson-Crick pairing, i.e. G-C and A-U. Structural analyses of bacterial ribosomes revealed that the small subunit conformationally restricts mRNA to only allow conventional pairing of the first two bases. Near-cognate – partially binding – tRNAs that would form non-conventional base pairings there are rejected from the A-site (Demeshkina *et al*, 2012).

#### **1.5.1. Crick's wobble hypothesis**

The third base of an mRNA codon can be read more ambiguously by certain tRNA species. This non-canonical base pairing was first postulated by Francis Crick in his 1966 Wobble hypothesis (Crick, 1966). The three commonly encountered wobble bases in human cells are inosine (deaminated and converted adenine), (modified) guanine and modified uridine. As predicted by Crick, inosine at the wobble position has the highest decoding capacity, being able to form two hydrogen bonds with C, U or A (Crick, 1966).

### 1.5.2. Diversity in wobble base pairing

In humans, inosine wobble translation is essential with up to 8 tRNA species being I<sub>34</sub> modified. Certain groups of proteins have co-evolved with wobble modifications, correlating in inosine-dependent codon composition and expression of inosine-modified tRNA species (Torres *et al*, 2021). Guanine at the wobble position is frequently replaced by queuine, a hypermodified base salvaged from food or the gut microbiome. The resulting queuosine base Q<sub>34</sub> still canonically pairs with cytosine but has the additional capacity to “wobble” with uracil, allowing these modified tRNAs to decode U-ending codons. Human cells and germ-free mice devoid of queuine show proteostasis defects. Therefore, the modification status of Q-modified tRNAs, and in extension, global translation depend on nutritional availability of the metabolite (Tuorto *et al*, 2018). In contrast to guanine, a uridine at position 34 is almost invariably modified (Johansson *et al*, 2008). This can be explained by a phenomenon termed “superwobbling”, where a single tRNA with an unmodified U<sub>34</sub> can universally pair and decode all four synonymous codons within a 4-fold degenerate codon box (i.e. NNA/U/G/C) (Rogalski *et al*, 2008). This is important in bacteria and eukaryotic organelles, such as mitochondria, in which translation is carried out with reduced tRNA sets. When a full tRNA repertoire is available, unmodified wobble uridine may prove to be too promiscuous and cause mRNA misreading and AA misincorporation. U<sub>34</sub> modifications are catalyzed by exceptionally sophisticated co-dependent enzymatic cascades. Certain tRNA wobble uridines are even modified twice, altering their properties to both diversify decoding (U:A/G), while restricting misincorporations that are prone especially in split codon boxes (N<sub>x</sub>N<sub>x</sub>A/G and N<sub>x</sub>N<sub>x</sub>C/U encoding different AA) (Smith *et al*, 2024).

Wobble decoding is an ingenious invention, allowing the 61 sense codons to be decoded by a theoretical minimal set of 32 tRNA species (Berg & Brandl, 2021). Factually, most organisms have more. *E. coli*, for example, have 43 tRNA transcriptional units, not all of which are essential (Tiefenbacher *et al*, 2024). Organisms and organelles with small genomes depend on this translational fine-tuning for survival.

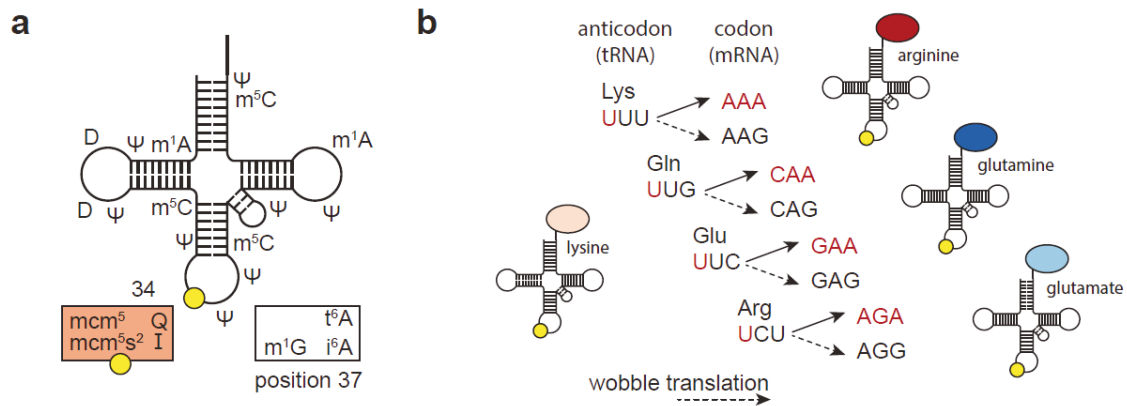


**Figure 3. (a)** A selection of tRNA modifications at common locations is indicated. Wobble position (34) and anticodon loop modifications (37) are highlighted in boxes. tRNA thiolation (sulfur) is depicted with a yellow circle. Note that not all tRNA species carry the same modifications.  $\Psi$  pseudouridine, D dihydrouridine (D-arm). **(b)** U:G wobble translation is indicated with the example of  $mcm^5s^2$ -modified uridine. Canonically, U will pair with A. Thiolated human tRNA species with respective anticodons are shown. Recognized mRNA codons are indicated, either canonical (solid arrow) or via wobble base pairing (dashed arrows).

## 1.6. tRNA thiolation – Assembly of $mcm^5s^2U_{34}$

The thiolation of tRNA wobble uridines is a highly conserved modification found in all domains of life. It ensures efficient and accurate translation at the codon:anticodon interface by correctly arranging the wobble base pair (Smith *et al*, 2024). A subset of tRNA species carry this additional sulfur, which requires the presence of a second uracil modification,  $mcm^5$ . Functionally, fully assembled 5-methoxycarbonylmethyl-2-thiouridine ( $mcm^5s^2U_{34}$ ) is responsible for correctly reading codons from mixed codon boxes, where the mistranslation of near-cognate codons may result in the incorporation of a different amino acid. For example, while AA\_A and AA\_G both encode lysine, incorrect base pairing with their near-cognate AA\_U and AA\_C might result in incorporation of asparagine. In humans, four cytosolic tRNAs have been found to be thiolated: Lys<sup>UUU</sup>, Glu<sup>UUC</sup>, Gln<sup>UUG</sup>, and Arg<sup>UCU</sup> (Shigi, 2014; Yoshida *et al*, 2015) (**Figure 3b**).

### 1.6.1. Biosynthesis of 5-methoxycarbonylmethyl ( $mcm^5$ ) – the prerequisite

Under physiological conditions, wobble uridines undergo thiolation only when the uracil 5-carbon is modified with a 5-methoxycarbonylmethyl group ( $mcm^5U$ ). Its precursor, 5-carboxymethyluridine ( $cm^5U$ ), is first introduced by the Elongator complex using acetyl-CoA as co-factor (Abbassi *et al*, 2024; Selvadurai *et al*, 2014) (**Figure 4a**). Elongator was first identified when it was co-purified with elongating RNA polymerase II (Otero *et al*, 1999), hence it was named accordingly. However, as research on its function(s) intensified, it was mostly found to be important for tRNA wobble uridine modifications, rather than transcriptional

elongation (Huang *et al*, 2005). The highly conserved elongator complex is large and multimeric, comprised of ELP1-ELP6, and regulated by a plethora of ancillary factors (Jaciuk *et al*, 2023).

Depending on their respective substrate tRNAs, diverse enzymes can hyper modify  $\text{cm}^5$  to  $\text{mcm}^5$ ,  $\text{mcm}^5\text{Um}$ ,  $\text{mchm}^5\text{U}$ ,  $\text{ncm}^5$ , and  $\text{ncm}^5\text{Um}$ . The methyltransferase converting  $\text{cm}^5$  into  $\text{mcm}^5$  in humans is ALKBH8, which requires TRMT112 as associated factor (Fu *et al*, 2010; Songe-Møller *et al*, 2010).  $\text{mcm}^5$  is a requirement for subsequent tRNA thiolation. However, not all tRNA species carrying  $\text{mcm}^5$  will be further modified to  $\text{mcm}^5\text{s}^2\text{U}$ . In yeast, for example, 13 of 42 active tRNAs have a wobble uridine, of which two are  $\text{mcm}^5$  and three  $\text{mcm}^5\text{s}^2$  modified, respectively (Johansson *et al*, 2018). Only a single tRNA species has an unmodified  $\text{U}_{34}$ . In yeast, Elongator/ALKBH8 and thiolation are not fully co-dependent, as *elp4* knockout mutants still showed remaining, albeit reduced, tRNA thiolation levels (Noma *et al*, 2009). In humans, 2-thiouridine ( $\text{s}^2\text{U}$ ) does not exist by itself.

#### 1.6.2. Sulfur mobilization via the URM1 pathway ( $\text{s}^2\text{U}_{34}$ )

Put simply, tRNA thiolation is the substitution of the oxygen atom with sulfur at the 2-position of the uracil ring, generating  $\text{s}^2\text{U}$  (**Figure 4b**). Thiolation requires the coordinated relay of sulfur from L-cysteine, as source, to the tRNA molecule. In humans, this pathway is initiated when the cysteine desulfurase NFS1 and its cofactor pyridoxal phosphate – the active form of vitamin B6 – catalyze the conversion of L-cysteine to L-alanine by removing sulfur to create a persulfide intermediate (R-S-S-H). The activated sulfur now linked to cysteine of NFS1 can then be transferred to other proteins in a coordinated and oxidation-protected manner. The sulfur relay takes part in the cytosol in three stages, from NFS1 via Mercaptopyruvate Sulfurtransferase (MPST) to Molybdenum Cofactor Synthesis 3 (MOCS3), from MOCS3 to the activated C-terminus of Ubiquitin Related Modifier 1 (URM1), and finally via the Cytosolic Thiouridylase complex (CTU1 and CTU2) to tRNA. (Leimkühler *et al*, 2017; Pabis *et al*, 2020; Shigi, 2014)

Interestingly, while the first two sulfur shuttles depend on persulfide chemistry mediated by rhodanese-like-domains in MPST and MOCS3, the transfer to URM1 depends on a system resembling protein ubiquitination. Here, the C-terminus of URM1 is first activated by MOCS3 using ATP, forming an URM1-COAMP intermediate, which then receives sulfur (URM1-COSH). Depending on incompletely understood factors, such as upstream sulfur availability and its localization within target complexes, URM1-COSH either participates in tRNA thiolation or “urmylation”, where URM1 itself is conjugated to target proteins, often under reactive oxygen stress conditions (Cairo *et al*, 2024; Ravichandran *et al*, 2022).

As final step, sulfur is substituted at the wobble uridine of specific tRNA species. This is orchestrated by the CTU1/CTU2 complex, which positions the target tRNAs and extracts sulfur from URM1-COSH to complete the thiolation reaction (Dewez *et al*, 2008; Schlieker *et al*, 2008). CTU1 is the enzymatically active component of the complex, coordinating the iron-sulfur cluster (Liu *et al*, 2016) that is required for thiolation (Nakai *et al*, 2007). Mechanistically, CTU1 first uses ATP to adenylate the C2 carbonyl oxygen (U<sub>34</sub>-O-AMP), trapping the tRNA as activated intermediate, and then coordinates a sulfur exchange from URM1-COSH (s<sup>2</sup>U<sub>34</sub>) (Numata *et al*, 2006). CTU2 is less well understood, but has been suggested to serve as non-enzymatic tRNA scaffold that contributes to complex stability (Leidel *et al*, 2009). In line with this, a recently identified NCS2\*/CTU2 mutant from a clinical isolate of baker's yeast showed increased stability and enhanced thiolation capabilities at high temperatures (Alings *et al*, 2023).

It is noteworthy that prokaryotes employ a less complex system for tRNA thiolation based on a simple linear sulfur relay, using persulfide chemistry, and a single terminal thiouridylase (Leimkühler, 2025). What selective pressure led eukaryotes to switch to thiocarboxylation through URM1 and thiouridylation with CTU2 as additional requirement remain open questions.

## **1.7. Structural mechanics of 5-methoxycarbonylmethyl-2-thiouridine**

Translation depends on ordered base pairing between tRNAs and mRNA within the ribosome. Given its partial complementary and ample modifications, tRNA is an intrinsically structured molecule. Nevertheless, bases within unpaired regions such as the anticodon loop exhibit high degrees of rotational flexibility that negatively affect codon recognition and thereby translation accuracy.

### **1.7.1. Stabilizing the anticodon loop**

This is counteracted by “base stacking”, noncovalent interactions between the  $\pi$ -electron clouds of their aromatic rings. Purines (A and G) are larger than pyrimidines (C and U, in RNA), have more  $\pi$  electrons, and hence engage in stronger stacking interactions. Uracil base stacking is the weakest, due to its size and additional lack of an amino group compared to cytosine. Uridine-rich anticodon loops therefore are extensively modified to improve base stacking, both within their anticodon (34-36) and proximal to it, at position 37 (mostly t<sup>6</sup>A) (Konevega *et al*, 2004).

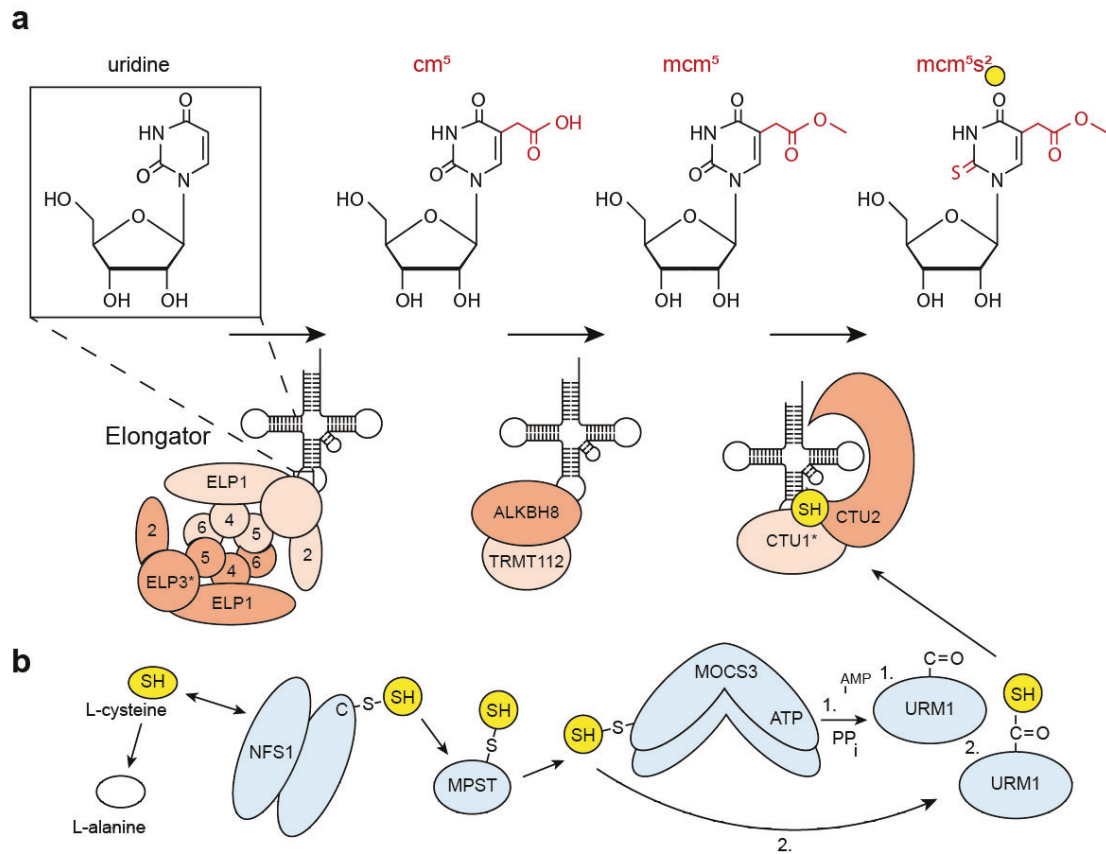


**Figure 4. (a)** Progressive modification of uracil base to  $mcm^5s^2U$ . The Elongator complex initiates the modification by adding a carboxymethyl group at the 5-carbon. The methyltransferase ALKBH8, with its co-factor TRMT112, catalyzes the methyl-ester formation to  $mcm^5U$ . Finally, the CTU1/CTU2 complex replaces the oxygen at the 2-carbon with sulfur. The enzymatic subunits ELP3 and CTU1 are highlighted by an \*. **(b)** Schematic representation of the sulfur mobilization route via the URM1 pathway. NFS1 uses L-cysteine as sulfur source, converting it to L-alanine and a persulfide (-S-SH) intermediate. The persulfide is relayed via the catalytic cysteine of MPST to the rhodanese domain of MOCS3. MOCS3 is an E1-like activating enzyme of URM1 that functions in a two-step reaction. First, MOCS3 adenylates the C-terminus of URM1 using ATP, which then enables the sulfur transfer onto URM1. The resulting thiocarboxylated URM1 then serves as sulfur donor for tRNA thiolation to the cytosolic thiouridylases 1 and 2 (CTU1 and CTU2). Figure (b) adapted from (Leimkühler et al, 2017).

Although present on the same base,  $mcm^5$  and  $s^2$  must be separated in terms of function.  $s^2$  improves the base stacking of their respective anticodon bases  $U_{34}$  and  $U_{35}$ . Mechanistically, when it replaces oxygen, the larger sulfur atom introduces steric and electrostatic changes within the base that shifts the adjacent ribose sugar into a mostly C3'-*endo* conformation, restricting movement (Durant *et al*, 2005). This pre-structuring of the anticodon stem loop stabilizes canonical U:A binding. Therefore, tRNA thiolation is important for decoding A-ending codons for Lysine (AAA), Glutamic acid (GAA), Glutamine (CAA), and the split Arginine box (AGA) (Schaffrath & Leidel, 2017).

### 1.7.2. Facilitating U:G wobble interactions

While  $s^2U_{34}$  restricts decoding errors by rigidifying uracil's inherently weak anticodon:codon interactions,  $mcm^5$  serves a contrasting role by stabilizing U:G wobble interactions. Within his famous "wobble hypothesis", Francis Crick theorized that U can pair with G, requiring the bases to minimally shift their orientation by 2.5Å (Crick, 1966). After initial experimental conformation, U:G or G:U pairs were found to be present in various RNA structures with slightly altered orientations and electronic properties (Westhof *et al*, 2019). Zooming into the ribosome, uridine modifications were found to alter base pairing and decoding capacity (Weixlbaumer *et al*, 2007). Strikingly, in a crystallography study of human Lys<sup>UUU</sup> tRNA anticodons within a translating bacterial ribosome, U:G pairs adopted perfect classical Watson-Crick geometry, but only when the wobble uridine was fully modified with  $mcm^5s^2$  (Vendeix *et al*, 2012). The effect strength  $mcm^5$  alone exerts on uracil is small (Durant *et al*, 2005). Nevertheless, increased polarity through the added methoxy and carbonyl groups are contributing to base pairing. It has been suggested, that  $mcm^5$  modification pushes the keto-enol tautomerism towards enol, allowing the formation of a third hydrogen bond and mimicking conventional pairing with G (Vendeix *et al*, 2012).

In summary, ribosomes depend on streamlined codon:anticodon pairing of mRNA and tRNA. The space and structure the RNAs can occupy is predefined, as is the speed at which codon recognition needs to occur. Proteins start to fold already as they are still being translated. Changes in synonymous codons – different codons encoding the same amino acid – have been found to affect translation speed and thereby folding dynamics (Thommen *et al*, 2017). While U:G base pairing does not strictly depend on neither  $mcm^5$  nor  $s^2$ , these chemical modifications act as translational modulators by pre-structuring flexible uridine-rich anticodon loops and optimizing redundancy mechanisms such as wobble translation through electrostatic interactions. This underscores their importance in the universally essential process that is translation and explains why modification pathways are so highly conserved.

## 1.8. Consequences of modification defects

### 1.8.1. Growth impairment

Certain organisms can be genetically manipulated to study the functional consequences of lacking wobble uridine modifications (**Figure 5**). Such *in vivo* studies in eukaryotes have been overwhelmingly conducted in *Saccharomyces cerevisiae*, otherwise known as Baker's yeast (Huang *et al*, 2005, 2008; Johansson *et al*, 2008). This is due to its ease of cultivation and tolerance of the loss of  $s^2$  or  $mcm^5U_{34}$ . Interestingly, some strains of *S. cerevisiae* are viable under laboratory conditions even when lacking both modifications simultaneously, linking genetic background to susceptibility to altered translation dynamics (Klassen *et al*, 2015). However, losing  $mcm^5$ ,  $s^2$ , or both, comes at fitness cost that compounds under stress conditions. Yeast strains lacking parts of the modification machinery, including *uba4/MOCS3*, *urm1/URM1*, *elp3/ELP3*, *ncs6/CTU1*, or *NCS2/CTU2*, show growth phenotypes at elevated growth temperatures, under nutrient starvation (Rapamycin treatment), oxidative stress (diamide) and general stress (caffeine) (Karlsborn *et al*, 2014).

The underlying mechanism behind delayed growth can be manifold but using growth as a phenotypic readout provides the benefit of being able to conduct rescue experiments. In a landmark paper to address Elongator's physiological role in yeast, the overexpression of Lys<sup>UUU</sup> and Gln<sup>UUG</sup> tRNAs was found to suppress (temperature-sensitive) growth defects in *elp* deleted mutants (Esberg *et al*, 2006). The same was true in *NCS2/CTU2* mutants, which strongly suggested that the observed pleiotropic growth defects were not caused by Elongator's hypothesized transcriptional function, but by a lack of wobble uridine modifications. Overexpressing tRNAs in an  $mcm^5(s^2)$ -deficient background resulted in an increased number of unmodified tRNA transcripts that were nonetheless sufficient to restore growth. These findings proved that the lack of wobble modifications affected translation *in vivo*. Further, they indicated that in yeast  $mcm^5s^2U_{34}$  enhanced translation of cognate A/G codons, rather than misreading non-cognate codons. The argument is that if a lack of modifications made tRNA recognition more error prone, the overexpression of the same unmodified tRNAs would result in even more mistranslation (e.g. in mixed codon boxes). Yet, as growth delays were rescued rather than worsened, the observed 2-fold increased tRNA levels likely counteracted codon:anticodon binding deficiencies by their increased frequency in the ribosomal A-site leading to eventual pairing.

### 1.8.2. Reduced ribosomal A-site binding

A later study sought to further validate the contribution of  $mcm^{5s^2}$  to ribosomal A-site binding by extracting Lys<sup>UUU</sup> tRNA from *urm1* and *elp3*-null *S. cerevisiae* mutants and measuring binding of the cognate AAA codon (Rezgui *et al*, 2013). Using an *in vitro* bacterial translation system, hypomodified tRNAs carrying either  $mcm^5$  or  $s^2$  showed a more than 50% reduction in ribosomal A-site binding compared to the fully modified wildtype tRNA.

### 1.8.3. Frameshifting

Another phenomenon associated with weak A-site interactions is frameshifting. Commonly found are +1 displacements from the open reading frame, leading to mistranslation of mRNA. If frameshifting occurs early in the coding region of an mRNA, or if it results in a premature stop codon, the protein may misfold or be degraded. Frameshifting is often found after “slippery codons”, for example homopolymeric stretches (i.e. AAA, GGG, CCC, UUU), which include cognate codons of  $mcm^{5s^2}$  modified tRNAs. Using bicistronic reporters transformed into wildtype and modification-mutant yeast, the contribution of hypomodified tRNAs to frameshifting was investigated. In this context, frameshifting between two coding regions on the same mRNA allows the translation of a secondary reporter that can be quantified (e.g. Firefly/Renilla luciferase or LacZ/ $\beta$ -galactosidase). The loss of  $mcm^5$  and  $s^2$  independently increased +1 frameshifting (Tükenmez *et al*, 2015). This effect seems to be strongest in a fully hypomodified setting as an *urm1/elp3* double mutant displayed higher frameshifting rates than individual knockouts (Klassen *et al*, 2017). In both studies the overexpression of tRNA Lys<sup>UUU</sup> ameliorated frameshifting.

### 1.8.4. Ribosome pausing

Frameshifting occurs in windows of opportunity when ribosomes slow down. Translation speed is influenced, amongst others, by the sequence and secondary structure of mRNAs and by limiting tRNA availability or modification status. Ribosome pausing influences protein output through altered folding. It may be a requirement for correct folding, but may also lead to the degradation of both mRNA and nascent protein in a worst-case ribosome stalling event (Collart & Weiss, 2020). Ribosome pausing can be quantified using Ribosome profiling or Ribo-seq (Ingolia *et al*, 2009). This adapted next-generation sequencing technique provides information on the location of ribosomes on mRNAs during active translation. In more technical detail, translating ribosomes are “arrested” by cycloheximide treatment, which blocks the translocation step of elongation. Cells are lysed and treated with ribonucleases to degrade all RNA except for the approximately 30 nucleotide long footprints that are protected by the surrounding ribosomes. These footprints are sequenced and mapped back to the transcripts

to defining the translome. Accumulated reads define sites where translation has slowed or stalled. Even information about E, P and A-site codons can be inferred.

Ribosome profiling is a powerful technique within the field of epitranscriptomics, especially when studying wobble uridine modifications that are found only at a subset of tRNA species, responsible for a defined number of cognate codons. Lacking machinery for  $mcm^{5s^2}$  had been shown to affect growth in yeast mutants, which was attributed to translational inefficiency largely due to its rescue by tRNA overexpression. Nevertheless, endogenous translation within these mutants had not been assessed. Resolving this question on a codon-level, ribosome profiling was performed both in *S. cerevisiae* and *Caenorhabditis elegans* that were lacking *elp6*, *NCS2/CTU2* or *elp6/NCS2* and *tuc-1/CTU1* respectively (Nedialkova & Leidel, 2015). Ribosome pausing was observed exclusively at A-ending synonymous codons of Lys<sup>UUU</sup>, Glu<sup>UUC</sup>, Gln<sup>UUG</sup> – AAA, GAA and CAA. It is important to mention here that in yeast and worms Arg<sup>UCU</sup> is not thiolated as in humans. The pausing phenotype was strongest for AAA and GAA, which is in line with studies that showed that the overexpression of Lys<sup>UUU</sup> or Gln<sup>UUG</sup> individually was sufficient to restore growth (Björk *et al*, 2007; Leidel *et al*, 2009). G-ending cognate codons AAG, GAG and CAG were not affected. Even considering distinct tRNA species with C<sub>34</sub> decoding these codons, these findings provide strong evidence that  $mcm^{5s^2}$  is not required for wobble translation, at least in yeast and worms.

#### 1.8.5. Proteostasis defects

The worst outcome of impaired tRNA thiolation – from a ribosomal standpoint – is the loss of the polypeptide before, or just after completion. This can occur because of mistranslation or changes in translation speed that would affect protein function and folding. During phases of active translation, the formation of polysomes, where several ribosomes assemble on one mRNA molecule, is desired, as this increases protein output. However, in severe cases of ribosome stalling, ribosomes can collide, leading to the activation of Ribosome-Associated Quality Control (RQC), and ultimately to the degradation of both truncated polypeptides and mRNA (Brandman *et al*, 2012). This activation of the RQC was observed in yeast mutants lacking both *NCS2/CTU2* and *elp6*. Stalling was triggered upon encountering specific codon pairs that appear particularly suboptimal for translation when wobble uridine modifications are absent (Wu *et al.*, 2024, bioRxiv). While the RQC helps safeguard the proteome by resolving stalled translation, the resultant downregulation of ‘hard-to-translate’ mRNAs may result in deficiencies and stress signaling.

$mcm^{5s^2}U_{34}$  is important for maintaining proteostasis. Proteostasis includes all processes from protein synthesis, folding and function, as well as degradation that together maintain a balanced proteome. Cells that lack tRNA modifications accumulate toxic protein aggregates

(Klassen *et al*, 2020). This aggregation is likely triggered by impaired co-translational folding in response to slowed ribosomal translation. In line with this, *S. cerevisiae* mutants lacking ribosome-associated chaperones show similar protein aggregation patterns to  $mcm^{5s^2}$  mutants (Nedialkova & Leidel, 2015). Furthermore, this aggregate formation – most pronounced in double mutants – could be partially rescued by restoring  $mcm^{5s^2}$  modification-dependent ribosome pausing via tRNA overexpression, as had been shown to alleviate growth phenotypes. Similar aggregation phenomena have been observed in *C. elegans*, motor neuron-mimicking murine cells and human cancer cell lines (Bento-Abreu *et al*, 2018; Nedialkova & Leidel, 2015; Rapino *et al*, 2018, 2021).

Translation is clearly affected when tRNA thiolation is impaired. The capacity of overexpressed tRNAs (mainly Lys<sup>UUU</sup>) to rescue both growth and aggregation phenotypes supports this. The individual contribution of reduced ribosomal A-site binding, frameshifting, ribosome pausing and protein aggregation in causing growth delays is unknown. They may well be compounding. The strongest phenotypes are seen when both  $mcm^5$  and  $s^2$  are lacking. While investigated systematically mostly in yeast, with Elongator mutants, studies on the specific contributions of tRNA thiolation in higher eukaryotes – especially human cells – are currently lacking.

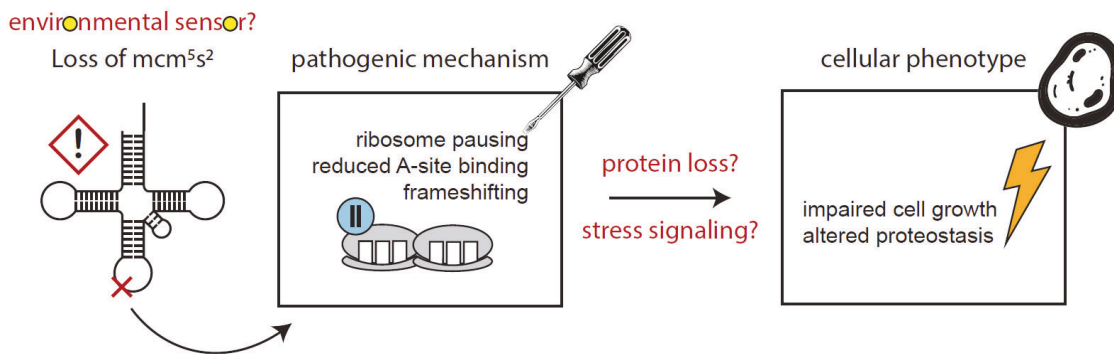


**Figure 5.** Schematic illustration of the molecular impact on translation when tRNA thiolation has been lost and how this may manifest in a cellular phenotype.  $mcm^{5s^2}$  levels may be regulated by changing environmental conditions. Hypothiolation affects protein output by altering translation dynamics or frameshifting. This could lead to either loss of protein or stress signaling that cause cellular dysfunction and initiate cellular compensatory responses.

## 1.9. Linking tRNA modification defects to organismal physiology

The loss of tRNA wobble modifications results in pleiotropic phenotypes that amongst others include growth delay, stress sensitivity and impaired proteostasis. Different models have been proposed to consolidate these (Schaffrath & Leidel, 2017).

### 1.9.1. Selective translation impairment: the codon-bias model

As the identity of the four tRNA species decorated with mcm<sup>5</sup>s<sup>2</sup>U in mammals is known – Lys<sup>UUU</sup>, Glu<sup>UUC</sup>, Gln<sup>UUG</sup>, and Arg<sup>UCU</sup> – their contribution to translation is equally well defined in terms of recognized codons: AAA/AAG (wobble), GAA/GAG, CAA/CAG and AGA/AGG. Several studies have addressed the question whether mcm<sup>5</sup>s<sup>2</sup>U affects wobble translation (G-ending codon) or cognate codon recognition (A-ending). Most evidence supports the latter, confining the “vulnerable codon content” to A-ending codons (Nedialkova & Leidel, 2015; Rezgui *et al*, 2013; Zinshteyn & Gilbert, 2013). Studies were conducted in different species, including *S. cerevisiae* and *C. elegans* mutants (Nedialkova & Leidel, 2015; Zinshteyn & Gilbert, 2013). Whereas AAA codons were consistently found to be strongly affected, reproducible ribosome pausing on CAA and GAA codons varied in severity amongst species. In higher organisms this “codon-bias” was confirmed in a murine pancreatic cancer cell line through the conditional knockout of *Ctu1*. Importantly, this study also validated ribosome stalling at AGA codons, as tRNA<sup>ARG</sup><sup>UCU</sup> is additionally thiolated in mammals (Hermann *et al*, 2025).

These findings led to the proposal of the “codon-bias model” that seeks to explain phenotypes downstream of defective tRNA wobble modifications through the selective loss of proteins that are encoded by mRNAs with a high AAA, CAA, GAA (and AGA) codon content.

In support of this hypothesis, several candidate proteins have been identified that are insufficiently expressed in a state of tRNA hypomodification (Bauer *et al*, 2012; Chen *et al*, 2022; Delaunay *et al*, 2016; Rapino *et al*, 2018, 2021; Wathieu *et al*, 2024; Xu *et al*, 2019). These proteins are not essential for survival but rather modulate cellular signaling and oncogenic capacity. For example, the oncogene(s) DEK and HIF1 $\alpha$ , two codon-biased factors, depend on wobble uridine modifications to sustain proliferation and metastasis in breast cancer and melanoma cell lines, respectively (Delaunay *et al*, 2016; Rapino *et al*, 2018). Accordingly, these cancer types show increased expression of ELP3 and CTU1/2. Their expression also defines responses to changes in the cellular environment given by the expression of codon-biased RIC8B or NLRP2 that modulate mTOR responses and hnRNP Q that activates p53 (Chen *et al*, 2022; Wathieu *et al*, 2024; Xu *et al*, 2019). To mechanistically validate that codon-content is the defining factor of expression, mutated mRNA variants in

which the A-ending thiolation-dependent codons were replaced by their respective G-ending wobble codons (i.e. AAA > AAG, GAA > GAG, CAA > CAG). This was indeed sufficient in all studies to rescue protein expression. On a side note, even though most of the mentioned studies were performed in mammalian cell lines, AGA was not considered. Like the rescue of growth phenotypes in yeast mentioned above, some codons – especially AAA – may affect protein stability more than others. In line with this, the first experimental codon exchange to rescue protein expression was successfully conducted in yeast by solely exchanging AAA with AAG codons (Bauer *et al*, 2012). Since this first report on codon-bias, additional factors have been identified that influence protein expression when *mcm*<sup>5</sup>*s*<sup>2</sup> synthesis is impaired. These include the repetitive sequence context of charged hydrophilic amino acids (Lysine, Arginine, Glutamic acid) and aforementioned suboptimal codon-pairs that show increased ribosome pausing (Rapino *et al.*, 2021; Wu *et al.*, 2024, bioRxiv).

### 1.9.2. The global stress response hypothesis

Altered translational output, including the loss of proteins through the RQC and the toxic gain of protein aggregates, can result in cellular stress signaling and adaptation that aim to restore proteostasis. This is at the core of the second model that links cellular phenotypes to global stress responses – rather than to the loss-of-function of individual proteins. Both models are not mutually exclusive, and codon-biased translation defects may well cause the induction of stress responses when reaching a certain threshold.

An additional consideration for stress induction is tissue context. The activation of the unfolded protein response (UPR), a branch of the integrated stress response (ISR), has been predominantly observed *in vivo*, in mice, with tissue-specific conditional ablation of Elongator subunits. *Elp3* knockout in neuronal progenitors (*FoxG1:Cre*) resulted in induction of endoplasmic reticulum (ER) stress signaling via the PERK-eIF2 $\alpha$ -ATF4 axis of the UPR (Lagousse *et al*, 2015). In brief, misfolded proteins in the ER are indirectly sensed by the ISR kinase PERK which then phosphorylates the eukaryotic initiation factor eIF2 $\alpha$ , decreasing global protein translation while selectively stabilizing the key transcription factors ATF4 that in turn drives expression of chaperones and other UPR mediators to resolve ER stress (Hetz *et al*, 2020). While naturally playing a role in stem cell fate, the prolonged UPR activation caused by the loss of tRNA wobble modifications impaired the generation of intermediate neuron progenitors, which led to decreased indirect neurogenesis and resulted in microcephaly (Lagousse *et al*, 2015).

Conditional *Elp3* deletion in hematopoietic stem cells (*Vav1:Cre*) led to p53-dependent bone marrow failure (Rosu *et al*, 2021). Yet, while an ATF4 response was mounted in progenitor cells, this was not a consequence of the UPR/ISR but resembled a response to amino acid

deprivation. In line with perceived starvation responses, evidence exists in yeast that tRNA thiolation serves as a sensor of sulfur amino acid availability (Laxman *et al*, 2013). Accordingly, when yeast was grown in minimal medium, tRNAs were found to be hypo-thiolated and amino acid biosynthesis was broadly induced. Even when nutrients were abundantly available, thiolation-null *S. cerevisiae* mutants showed a starvation signature (Gupta *et al*, 2019), which mirrors the observed phenotypes in *Elp3*-deficient murine bone marrow.

### **1.9.3. tRNA thiolation as a metabolic and environmental sensor**

tRNA thiolation as a dynamic cellular sensor of stress is an intriguing concept. Culturing yeast at an elevated temperature of 37°C, causes an overall decrease in tRNA thiolation, as Urm1 pathway components including Ncs2 are destabilized (Damon *et al*, 2015). Furthermore, thiolation-incompetent mutants transcriptionally upregulate the heat shock response, which includes chaperones for protein re-folding. Upon proteotoxic stress elicited by the treatment with tunicamycin, a model drug causing protein accumulation in the ER, these same mutants are better protected than wildtype *S. cerevisiae* (Damon *et al*, 2015). Therefore, a state of hypothiolation may be advantageous upon short, low-dose exposure to ER stress. tRNA thiolation levels regulate overall protein load, as recently shown in an elegant study using CRISPR editing and an inducible Cas9 endonuclease in a murine pancreas cell line (Hermann *et al*, 2025). The acute knock-out of *Ctu1* led to decreased protein levels of 90% of the quantified newly synthesized cellular proteome compared to wildtype cells, with a stronger impact on cells enriched in AAA, CAA, and GAA codons. The impact of AGA was not determined, although ribosome profiling clearly highlighted increased A-site occupancy of all four thiolation-dependent codons (Hermann *et al*, 2025).

While a high tRNA thiolation-dependent codon content clearly increases the inaccuracy of ribosomal translation of a given mRNA, tRNA thiolation defects seem to have profound implications on the total proteome – especially when studied in acute depletion contexts. Interestingly, however protein synthesis was mildly increased in murine hematopoietic cells with reduced *mcm5s2* in constitutive knock-out cells (Rosu *et al*, 2021), indicating that with sufficient time, cells can compensate for the loss of the tRNA modification. Whether thiolation can serve as dynamic sensor – of amino acid availability, oxidative stress, temperature, or other stress triggers – remains an attractive model but needs to be fully elucidated.

## 1.10. Human pathology

tRNA modifications are essential for human embryonic development and healthy adult life. This is apparent from reports of more than 50 mutated human modification genes that cause or contribute to human diseases (Chujo & Tomizawa, 2021). Collectively, these pathologies are grouped as “tRNA modopathies”.

### 1.10.1. Complexity as a driver of pathogenicity

Amongst these, complex modifications like  $\text{mcm}^5\text{s}^2\text{U}$  are overrepresented as they require a series of enzymes for synthesis (**Table 1, Fig. 4a**). In vertebrates, the addition of  $\text{s}^2$  can only occur once the  $\text{mcm}^5$  sidechain has been completed (Songe-Møller *et al*, 2010). Hence, all mutations in Elongator subunits (*ELP1-6*) and *ALKBH8* will also result in tRNA hypothiolation in humans. The same is true if sulfur relay is interrupted (*NFS1*, *MPST* and *MOCS3*) (**Fig. 4b**), or iron-sulfur cluster assembly interfered with (*CIAO1*, *NUBP1*). Dysfunction of any of these key cellular processes would globally impact cellular respiration, metabolism and proteostasis, explaining the spectrum of reported disease conditions.

Modification	Gene	Disease
$\text{s}^2\text{U}/\text{mcm}^5\text{s}^2\text{U}$	<i>CTU1</i>	Cancer-associated
$\text{s}^2\text{U}/\text{mcm}^5\text{s}^2\text{U}$	<i>CTU2</i>	<u>DREAM-PL syndrome</u> , cancer-associated
$\text{mcm}^5\text{U}/\text{mcm}^5\text{s}^2\text{U}$	<i>ALKBH8</i>	Developmental delay, epilepsy, intellectual disability (Monies <i>et al</i> , 2019)
$\text{cm}^5\text{U}/\text{ncm}^5\text{U}/\text{mcm}^5\text{U}/\text{mcm}^5\text{s}^2\text{U}$	<i>ELP1</i>	Familial dysautonomia, cancer-associated
$\text{cm}^5\text{U}/\text{ncm}^5\text{U}/\text{mcm}^5\text{U}/\text{mcm}^5\text{s}^2\text{U}$	<i>ELP2</i>	Autism spectrum disorder, intellectual disability (Kojic <i>et al</i> , 2021)
$\text{cm}^5\text{U}/\text{ncm}^5\text{U}/\text{mcm}^5\text{U}/\text{mcm}^5\text{s}^2\text{U}$	<i>ELP3</i>	Familial dysautonomia, Charcot–Marie–Tooth disease, cancer-associated, amyotrophic lateral sclerosis (ALS)
$\text{cm}^5\text{U}/\text{ncm}^5\text{U}/\text{mcm}^5\text{U}/\text{mcm}^5\text{s}^2\text{U}$	<i>ELP4</i>	Autism spectrum disorder, intellectual disability
$\text{cm}^5\text{U}/\text{ncm}^5\text{U}/\text{mcm}^5\text{U}/\text{mcm}^5\text{s}^2\text{U}$	<i>ELP5</i>	Cancer-associated, diabetes
$\text{cm}^5\text{U}/\text{ncm}^5\text{U}/\text{mcm}^5\text{U}/\text{mcm}^5\text{s}^2\text{U}$	<i>ELP6</i>	Developmental delay, epilepsy, intellectual disability (Gaik <i>et al</i> , 2022)
$\text{s}^2\text{U}/\text{mcm}^5\text{s}^2\text{U}$	<i>CIAO1</i> *	Hereditary paraganglioma–pheochromocytoma syndromes, retinitis pigmentosa
$\text{s}^2\text{U}/\text{mcm}^5\text{s}^2\text{U}$	<i>MOCS3</i> *	Molybdenum cofactor deficiency
$\text{s}^2\text{U}/\text{mcm}^5\text{s}^2\text{U}$	<i>MPST</i> *	Mercaptolactate-cysteine disulfiduria (MCDU), intellectual disability
$\text{s}^2\text{U}/\text{mcm}^5\text{s}^2\text{U}$	<i>NFS1</i> *	Friedreich ataxia
$\text{s}^2\text{U}/\text{mcm}^5\text{s}^2\text{U}$	<i>NUBP1</i> *	Cancer-associated

**Table 1.** Mutated genes related to tRNA wobble uridine thiolation that have been reported to cause disease in humans. Adapted from de Crécy-Lagard *et al.*, 2019 and expanded. The \* denotes genes that serve roles upstream of thiolation and hence may be pathogenic irrespective of modification loss.

<b>Modification</b>	<b>Gene</b>	<b>Disease association</b>
ac <sup>4</sup> C	<i>NAT10</i> , <i>THUMPD1</i>	Cancer-associated
C <sub>m</sub> /G <sub>m</sub> /f <sup>5</sup> C <sub>m</sub> /h <sub>m</sub> <sup>5</sup> C <sub>m</sub>	<i>WDR6</i>	Cancer-associated
C <sub>m</sub> /U <sub>m</sub> /G <sub>m</sub> /f <sup>5</sup> C <sub>m</sub> / h <sub>m</sub> <sup>5</sup> C <sub>m</sub> /m <sub>cm</sub> <sup>5</sup> U <sub>m</sub>	<i>FTSJ1</i>	Intellectual disability
D	<i>DUS2</i>	Cancer-associated
f <sup>5</sup> C (mito)	<i>NSUN3</i>	Cancer-associated
G <sub>m</sub>	<i>TARBP1</i>	Cancer-associated
I	<i>ADAT1</i>	Coronary artery disease
I	<i>ADAT3</i>	Intellectual disability, microcephaly
i <sup>6</sup> A	<i>TRIT1</i>	Microcephaly, developmental delay, epilepsy, cancer-associated
m <sup>1</sup> A	<i>TRMT6</i>	Cancer-associated
m <sup>1</sup> G/m <sup>1</sup> A (mito)	<i>HSD17B10</i>	Neurodegeneration, cardiomyopathy
m <sup>1</sup> G/m <sup>1</sup> A (mito)	<i>TRMT10C</i>	Lactic acidosis, hypotonia, feeding difficulties, deafness
m <sup>1</sup> A	<i>TRMT61A</i>	Cancer-associated
m <sup>1</sup> A (mito)	<i>TRMT61B</i>	Cancer-associated, Alzheimer's disease
m <sup>1</sup> G	<i>TRMT5</i>	Failure to thrive, hypertrophic cardiomyopathy, exercise intolerance
m <sup>1</sup> G	<i>TRMT10A</i>	Diabetes, intellectual disability, microcephaly, developmental defects
m <sup>2,2</sup> G	<i>TRMT1</i>	Intellectual disability, microcephaly
m <sup>3</sup> C	<i>METTL6</i>	Cancer-associated
m <sup>5</sup> C	<i>NSUN2</i>	Intellectual disability, developmental delay, reduced fertility, cancer-associated
m <sup>5</sup> C	<i>TRDMT1</i>	Metabolism, cancer-associated
m <sup>5</sup> U	<i>TRMT2A</i>	Cancer-associated
m <sup>7</sup> G	<i>METTL1</i>	Multiple sclerosis, cancer-associated
m <sup>7</sup> G	<i>WDR4</i>	Microcephaly, cancer-associated, nephrotic defects, developmental defects
ms <sup>2</sup> i <sup>6</sup> A (mito)	<i>CDK5RAP1</i>	Cancer-associated, type II diabetes, vitiligo
ms <sup>2</sup> t <sup>6</sup> A	<i>CDKAL1</i>	Diabetes, microcephaly, cancer-associated
o <sub>2</sub> yW/yW	<i>TYW2</i> , <i>TYW4</i>	Cancer-associated
t <sup>6</sup> A	<i>YRDC</i>	Cancer-associated
t <sup>6</sup> A	<i>LAGE3</i> , <i>TPRKB</i> , <i>OSGEP</i>	Galloway–Mowat syndrome, microcephaly, nephrotic defects
t <sup>6</sup> A (mito)	<i>OSGEPL1</i>	Cancer-associated, MERRF
t <sup>6</sup> A	<i>TP53RK</i>	Galloway–Mowat syndrome, microcephaly, nephrotic defects, cancer-associated
τ <sub>m</sub> <sup>5</sup> U (mito)	<i>GTPBP3</i>	MELAS, non-syndromic hearing loss
τ <sub>m</sub> <sup>5</sup> U (mito)	<i>MTO1</i>	Lactic acidosis, cardiomyopathy, encephalopathy, MERRF, cancer-associated, epilepsy
τ <sub>m</sub> <sup>5</sup> s <sup>2</sup> U (mito)	<i>TRMU</i>	Leigh syndrome, hyperlactatemia, non-syndromic hearing loss
U <sub>m</sub>	<i>TRMT44</i>	Partial epilepsy with pericentral spikes (PEPS)
Ψ	<i>PUS1</i>	Mitochondrial myopathy and sideroblastic anemia (MLASA)
Ψ	<i>PUS3</i>	Intellectual disability
Ψ	<i>PUS10</i>	Autoimmune diseases, intellectual disability
Q	<i>QTRT1</i>	Cancer-associated
xG	<i>THG1L</i>	Microcephaly, developmental delay, nephrotic defect

**Table 2.** Expanded list of tRNA modification enzymes found mutated in human disease. (mito) denotes enzymes that exclusively modify mitochondrial tRNA species. Some others have dual specificity. Adapted from de Crécy-Lagard *et al.*, 2019.

### 1.10.2. Mitochondrial versus cytosolic manifestations

Many pathologies caused by impaired tRNA modification are syndromic in nature, where several different organ systems are affected. This can be explained by a common dysfunction of cellular organelles, such as mitochondria (mt). This is the case, for example, in the mitochondrial tRNA modopathies MELAS and MERRF where the absence of taurine modifications on mt-tRNA anticodons causes a collapse of oxidative phosphorylation – with a dramatic negative impact across organs. In general, mitochondria are particularly sensitive to changes in their tRNA epitranscriptome, as mitochondrial DNA encodes a minimal set of 22 mt-tRNA species that are required to sustain respiration (Suzuki *et al*, 2011).

In contrast, disease phenotypes and severity of aberrantly modified cytoplasmic tRNAs will depend on tissue-specific gene expression as well as the size of the tRNA substrate pool. One example for a modification present in a large subset of all tRNAs is t<sup>6</sup>A<sub>37</sub>. Catalyzed by the KEOPS complex (OSGEP, TP53RK, TPRKB, LAGE3), it is important for decoding all 16 ANN codons (Beenstock & Sicheri, 2021). The absence of this modification causes the often lethal Galloway-Mowat syndrome (Braun *et al*, 2017). On the other side of the spectrum, the loss of less frequent modifications often results in non-life-threatening disease. tRNA<sup>Phe</sup>, for example, carries 2'-O-methylations via FTSJ1. FTSJ1 mutations have been found to cause intellectual disability, which severely affects patients but is not a lethal condition (Guy *et al*, 2015).

### 1.10.3. A link to tumorigenesis?

Apart from impaired neurodevelopment, an association with cancer appears most prevalent, when considering all disease-relevant tRNA modifiers (**Tables 1 and 2**). This, however, does not mean that patients suffering from tRNA modopathies generally have a higher risk of developing cancer. Rather, tRNA modifying enzymes are commonly linked to cancer through their overexpression in certain cancer types or by identifying them as biomarkers during cancer progression. One notable exception in which the silencing of a tRNA modifier was associated with tumorigenesis is TYW2 (Rosselló-Tortella *et al*, 2020). In human colorectal cancer cells, the TYW2 promotor was found to be hypermethylated, which resulted in the hypomodification of G37 of tRNA<sup>Phe</sup> that is normally decorated with wybutosine (yW) modifications. *In vitro*, this modification loss promoted cell migration and epithelial-to-mesenchymal transition (Rosselló-Tortella *et al*, 2020).

#### **1.10.4. Tissue-specific vulnerability**

tRNA modopathies show a clear pattern of organ dysfunction, including the brain and kidneys, and to a lesser extent the inner ear and pancreas. While a unifying disease mechanism is still being investigated, certain connecting factors are noteworthy. One example is that brain, kidney and inner ear are organs highly dependent on primary cilia, either during development or function (Waters & Beales, 2011), warranting the investigation of potential ciliogenesis defects upon tRNA hypomodification. Another commonality is the limited regenerative potential of these organs, as major cell types carrying out organ function, such as neurons and podocytes, are terminally differentiated. Furthermore, they have high translational demand, as neurotransmitters and pancreatic insulin production need to be sustained, which also depends on correct protein folding and secretion. Neurons further require localized translation at their synapses, which sensitizes them to translation impairment caused by altered tRNA-ribosome interaction dynamics. Consequently, several tRNA modifiers and aminoacyl-tRNA-synthetases have been recently described to contribute to intellectual disability (Franz *et al*, 2020).

## 1.11. CTU2 deficiency: DREAM-PL syndrome

tRNA thiolation is essential for human health. This is clear, as the loss-of-function of the cytosolic thiouridylases 2 enzyme (CTU2) causes a severe disorder termed DREAM-PL syndrome. It was first identified and investigated by Fowzan Alkuraya and colleagues, who described the first patients in 2016 (Shaheen *et al*, 2016a, 2016b). Inherited in an autosomal recessive manner, the syndromic congenital condition manifests when both *CTU2* alleles are mutated. Given the lack of reported heterozygosity, a single functional *CTU2* copy can likely maintain the thiolated tRNA pool that is required for homeostasis. While a compound heterozygous patient (Helsmoortel *et al*, 2015) – carrying two different *CTU2* mutations – has been reported, a majority of the cases described in literature represent children with bi-allelic homozygous *CTU2* variants. In many cases this is explained by the consanguinity of the parents, who are often first- and second-degree cousins. Currently, 14 cases of DREAM-PL have been reported (Barrak *et al.*, 2024; Helsmoortel *et al.*, 2015; Mahoney *et al.*, 2023; Shaheen, Al-Salam, *et al.*, 2016; Shaheen *et al.*, 2019; Shaheen, Patel, *et al.*, 2016, personal communication).

### 1.11.1. Identification of recurrent pathogenic variants

Amongst the disease-causing mutations two are recurrent: NM\_001012759.3(CTU2): c.873G>A (p.Thr291=) and NM\_001012759.3(CTU2): c.188T>C (p.Leu63Pro). The former affects the last nucleotide of exon 8 and results in splicing defects by disrupting the consensus donor recognition motif of the 5' splice site (Shaheen *et al*, 2016b). As a result exon 8 is not retained and the fusion of exons 7 to 9 shifts the reading frame and a premature termination codon. Whether a truncated protein is produced or the mRNA directly degraded by nonsense mediated decay has not been established. The other common mutation in DREAM-PL patients is a pathogenic leucine to proline point mutation at position 63 that is situated in an N-terminal helical region of the CTU2 protein. A proline substitution at this position likely acts as a “helix-breaker” and might interfere with protein stability (Nilsson *et al*, 1998).

### 1.11.2. Global incidence and carrier frequency

Using publicly available data from the Genome Aggregation Database (gnomAD) (Karczewski *et al*, 2020), one can estimate the carrier probabilities based on the allelic frequencies of these variants under Hardy-Weinberg equilibrium, at 1 in 55.556 (c.873G>A) and 1 in 885 (c.188T>C), respectively. The remaining reported pathogenic *CTU2* variants are so rare that they are not observed in this dataset. Combined this would result in a carrier frequency of 1 in 871, corresponding to an approximate global incidence of 1 in 3.035.000 and an order of 2.500-3.000 affected individuals. However, these values are likely an underestimation, as

gnomAD is not globally representative, but dominated by European ancestry and lacking sufficient genomic information representing the Middle East and other founder populations where DREAM-PL is more commonly observed. Using sequencing data from a Saudi Arabian cohort, representing one of the countries with the highest prevalence of consanguinity (Oniya *et al*, 2019), *CTU2* c.873G>A is present on one allele in about 1 in 769 individuals (Abouelhoda *et al*, 2016), a 70-fold increase compared to the global average.

### **1.11.3. Clinical presentation and phenotypic spectrum**

Fetal development is severely impacted upon the loss of *CTU2* function. While the original characterization of DREAM-PL patient-derived cell lines did not include analyses of *CTU2* protein levels, Epstein-Barr virus transformed B-lymphoblastoid cell lines showed a drastic decrease of wobble thiolation on the tRNA level, suggesting *CTU2* dysfunction (Shaheen *et al*, 2019). The disease name DREAM-PL is an acronym originally established based on the clinical presentation of the first patients: dysmorphic facies (D), renal agenesis (RE), ambiguous genitalia (A), microcephaly (M), polydactyly (P) and lissencephaly (L). As more patients have been diagnosed, the phenotypic spectrum has expanded to include congenital heart defects and brain abnormalities beyond microcephaly, such as seizures. All patients show dysmorphic facial features and brain anomalies. Heart and kidney defects are observed in most patients, while other disease features vary between patients.

### **1.11.4. Clinical outcomes and therapeutic approaches**

DREAM-PL is a devastating disease, with high infant mortality and an average life expectancy of one year, according to one report (Barrak *et al*, 2024). At the time of reporting, four patients, with *CTU2* mutations confirmed by next-generation sequencing, had passed away before the age of one, and one infant remained on respiratory support with a do-not-resuscitate status (Barrak *et al*, 2024; Shaheen, Al-Salam, *et al*, 2016, personal communication). Five older siblings of confirmed patients, whose genomes were not sequenced, had also died in early childhood before reaching the age of two, often with similar phenotypic presentation (Barrak *et al*, 2024; Shaheen *et al*, 2016b). In two cases, infants homozygous carrying *CTU2* c.873G>A were alive at the time of reporting but remained dependent on intensive medical intervention, including respiratory and feeding support (Shaheen *et al*, 2016a). Four cases of DREAM-PL show a less severe disease presentation, with patients surviving well into childhood (two, four and six years old) or even early adulthood (19 years old) (Mahoney *et al*, 2023; Shaheen *et al*, 2019). What defines disease severity is unknown. Additional genetic factors may be involved, as most survivors were born to non-consanguineous parents. Furthermore, some of these patients display less severe renal impairment (Shaheen *et al*, 2019).

Currently, there is no curative treatment for DREAM-PL syndrome. The clinical management centers around the treatment of symptoms such as respiratory distress, hypotonia and consequences of congestive heart failure, and often requires prolonged stays in neonatal intensive care units and long-term treatment facilities. Heart failure (digoxin, furosemide), seizures (phenobarbitone) and infections can be managed pharmacologically (Shaheen *et al*, 2016a). Patient care for children and adolescents focuses on the management of global developmental delay and seizure control.

## 1.12. Aims of the thesis

### 1.12.1. Aim 1: Define the molecular and cellular consequences of impaired tRNA wobble thiolation in human *in vitro* models

tRNA modifications have been extensively studied in lower organisms – mostly *Saccharomyces cerevisiae* – because they can be easily genetically altered. The identification of DREAM-PL syndrome necessitates a systematic investigation in a human context.

**Goal:** Establish DREAM-PL patient-derived and isogenic cellular models, for example *CTU2* knock-down cell lines using short-hairpin RNA, for characterization of tRNA hypothiolation.

### 1.12.2. Aim 2: Investigate a possible impact on translation and proteome remodeling in *CTU2* deficiency

Current consensus links the loss of tRNA anticodon modifications to translation defects, but the resulting impact on the proteome and cellular stress signaling remains debated.

**Goal:** Leverage state-of-the-art tools to identify the unfolded proteome (TME) and altered translation dynamics (ribosome profiling).

### 1.12.3. Aim 3: Identify putative disease-causing pathway dysfunction in DREAM-PL syndrome

Although *CTU2* mutations are the genetic origin of DREAM-PL syndrome, the underlying pathomechanism or disease etiology remains undefined.

**Goal:** Integrate data from Aims 1 & 2 to select and validate the specific pathway candidates responsible for the (organ-specific) disease presentation.

### 1.12.4. Aim 4: Establish a mouse model to study organismal and tissue-specific vulnerability of DREAM-PL syndrome *in vivo*

The field lacks an established mammalian model to investigate the developmental and tissue-specific consequences of mutations.

**Goal:** Utilize CRISPR-Cas9 to generate homozygous *Ctu2*<sup>L63P</sup> knock-in mice, assess viability, analyze tRNA thiolation status, and screen for phenotypes on the organ level.

# Chapter two

## **2. “tRNA thiolation defects disrupt cellular proteostasis and tissue homeostasis in mammals” (Preprint)**

### **2.1. Prologue**

This chapter encompasses the primary experimental body of this doctoral thesis, addressing the aims laid out above. The results have been compiled into a manuscript entitled “tRNA thiolation defects disrupt cellular proteostasis and tissue homeostasis in mammals.” This work was submitted for peer review in October 2025 and is available on the preprint server bioRxiv.

## **tRNA thiolation defects disrupt cellular proteostasis and tissue homeostasis in mammals**

Lukas Englmaier<sup>1</sup>, Marta Walczak<sup>2,3</sup>, Daniel Malzl<sup>1,4,5</sup>, Cristian Eggers<sup>6</sup>, Felix Eichin<sup>7</sup>, Valentina C. Sladky<sup>7</sup>, Filip M. Gallob<sup>1</sup>, Yevheniia Tyshchenko<sup>1</sup>, Zarghun Zarif<sup>1</sup>, Thomas Kolbe<sup>8,9</sup>, Lama Al-Abdi<sup>10</sup>, Jörg Menche<sup>1,4,5,11,12</sup>, Nathalie Spassky<sup>13</sup>, Stephan Geley<sup>14</sup>, Walter Rossmann<sup>15</sup>, Fowzan S. Alkuraya<sup>8</sup>, Sebastian A. Leidel<sup>6</sup>, Sebastian Glatt<sup>2,16</sup> and Andreas Villunger<sup>1,7\*</sup>

1. CeMM Research Center for Molecular Medicine of the Austrian Academy of Sciences, Vienna, Austria
2. Malopolska Centre of Biotechnology (MCB), Jagiellonian University, Krakow, Poland
3. Doctoral School of Exact and Natural Sciences, Jagiellonian University, Krakow, Poland
4. Max Perutz Labs, Department of Structural and Computational Biology, University of Vienna, Vienna, Austria
5. Center for Molecular Biology, Department of Structural and Computational Biology, University of Vienna, Vienna, Austria
6. Department of Chemistry, Biochemistry and Pharmaceutical Sciences, University of Bern, Bern, Switzerland
7. Institute for Developmental Immunology, Biocenter, Medical University of Innsbruck, Innsbruck, Austria
8. Institute of in vivo und in vitro Models, University of Veterinary Medicine Vienna, Vienna, Austria
9. Department for Agricultural Sciences, University of Natural Resources and Life Sciences, Vienna, Austria
10. Department of Translational Genomics, Center for Genomic Medicine, King Faisal Specialist Hospital and Research Center, Riyadh, Saudi Arabia
11. Faculty of Mathematics, University of Vienna, Vienna, Austria
12. Ludwig Boltzmann Institute for Network Medicine at the University of Vienna, Vienna, Austria
13. Institut de Biologie de l'Ecole Normale Supérieure, Ecole Normale Supérieure, CNRS, INSERM, Université PSL, Paris, France
14. Institute of Pathophysiology, Biocenter, Medical University of Innsbruck, Innsbruck, Austria
15. Center for Anatomy and Cell Biology, Medical University of Vienna, Vienna, Austria
16. University of Veterinary Medicine Vienna, Vienna, Austria

\* Corresponding author: [avillunger@cemm.oeaw.ac.at](mailto:avillunger@cemm.oeaw.ac.at)

## ABSTRACT

Sulfur modification of tRNA wobble uridines is an evolutionarily conserved mechanism that ensures efficient protein synthesis. In humans, loss of this anticodon modification due to mutations in *CTU2* (cytosolic thiouridylase 2) causes DREAM-PL syndrome, a severe congenital disorder often leading to early postnatal death. However, the mechanisms by which loss of tRNA thiolation drives pathology remain unclear. Here, we show that loss of *CTU2* triggers significant cellular proteostasis defects in patient cells and model cell lines. Structural and biochemical analyses reveal that the pathogenic *CTU2*<sup>L63P</sup> mutation destabilizes the CTU1/CTU2 complex and abolishes tRNA binding and thiolation. Acute loss of *CTU2* caused codon-specific ribosome pausing at A-ending codons decoded by thiolated tRNAs, and decreased ribosome occupancy of A-rich transcripts in a dosage-dependent manner. Codon-biased mRNAs transcribed from genes critical for ciliogenesis are predicted to be most affected, linking their reduced translation to DREAM-PL etiology in humans. Surprisingly, *Ctu2*<sup>L63P</sup> mice display severe thiolation defects, but develop normally, are viable and fertile. Our findings highlight the importance of functional tRNA thiolation for organismal health in humans and identify species-specific vulnerabilities during embryonic development in mammals.

## INTRODUCTION

Transfer RNAs (tRNAs) ensure accurate translation of messenger RNA (mRNA) into protein. Although approximately 430 human tRNA genes are predicted in the human genome (Chan & Lowe, 2016), only a subset is actually expressed. Because the expressed tRNA anticodon repertoire does not cover all 61 sense codons used in mRNA (Gao et al., 2024), decoding relies on flexible base pairing at the third, or “wobble,” position of the codon (Crick, 1966). tRNA modifications at the corresponding anticodon position 34, particularly of uridine, expand pairing capacity while maintaining translational accuracy (Agris et al., 2018).

Among these “wobble modifications”, tRNA thiolation is a key regulator of translation conserved across all domains of life. In vertebrates, a complex enzymatic cascade replaces oxygen at the 2-carbon of uracil ( $U_{34}$ ) with sulfur ( $s^2$ ) in tRNA $_{UUU}^{Lys}$ , tRNA $_{UUC}^{Glu}$ , tRNA $_{UUG}^{Gln}$ , and tRNA $_{UCU}^{Arg}$  (Björk et al., 2007; Yoshida et al., 2015). This modification is catalyzed by the cytosolic thiouridylase CTU1:CTU2 complex (Dewez et al., 2008) as the final step of the URM1 sulfur relay pathway (Huang et al., 2008; Leidel et al., 2009; Noma et al., 2009; Schlieker et al., 2008). In eukaryotes, thiolation is strongly enhanced when  $U_{34}$  is first modified with a methoxycarbonylmethyl group ( $mcm^5$ ) that is initiated by the Elongator complex (ELP1-6) and completed by the methyltransferase ALKBH8 (Abbassi et al., 2024; Huang et al., 2005; Songe-Møller et al., 2010). The  $s^2$  group stabilizes the anticodon loop for cognate U:A pairing, while  $mcm^5$  facilitates U:G wobbling, allowing  $mcm^5s^2$ -modified tRNAs to decode both A- and G-ending codons efficiently (Durant et al., 2005; Vendeix et al., 2012). Together with other anticodon modifications, tRNA thiolation helps maintain the reading frame and prevents mistranslation within mixed codon boxes (Tükenmez et al., 2015).

At the molecular level, tRNA $_{UUU}^{Lys}$  lacking  $s^2$  at  $U_{34}$  binds to AAA codons with lower affinity and is frequently rejected by the ribosome (Ranjan & Rodnina, 2017). Accordingly, the speed of translation is decreased, which is in line with observed ribosome pausing at cognate AAA and CAA codons upon the loss of either  $mcm^5$  or  $s^2$  in yeast (Nedialkova & Leidel, 2015; Zinshteyn & Gilbert, 2013). This codon-specific slowdown triggers stress signaling and perturbs proteostasis, which in its most severe form can cause protein loss through aggregation (Nedialkova & Leidel, 2015; Rapino et al., 2021). In yeast, these phenotypes can be alleviated by overexpressing tRNA $_{UUU}^{Lys}$  and tRNA $_{UUG}^{Gln}$  that are normally subject to modification, thereby restoring translation (Björk et al., 2007; Leidel et al., 2009; Nedialkova & Leidel, 2015).

Dependence on tRNA wobble modifications varies across biological systems. Yeast and plants are generally viable without fully modified tRNAs, but mutants show growth defects under stress (Björk et al., 2007; Esberg et al., 2006; Leiber et al., 2010; Leidel et al., 2009; Xu et al.,

2020). Likewise, HEK293T cells can tolerate loss of *ELP3* or *CTU2* (Linder et al., 2025). However, the combined loss of mcm<sup>5</sup> and s<sup>2</sup> modifications has additive detrimental effects, exemplified by developmental defects in double-mutant worms (C. Chen et al., 2009). In contrast, deletion of the elongator subunit *Elp3* is lethal in fruit flies and mice (Bento-Abreu et al., 2018; Walker et al., 2011). Mutations in human Elongator subunits and other tRNA wobble modifiers lead to severe neurological and developmental disorders, including Familial Dysautonomia (*ELP1*) (Slaugenhaupt et al., 2001), amyotrophic lateral sclerosis (*ELP3*-associated) (Simpson et al., 2009), and neurodevelopmental disorders (*ELP1*, *ELP2*, *ELP3*, *ELP4*, *ELP6*, *ADAT3* and *ALKBH8*) (Alazami et al., 2013; Gaik et al., 2022; Kojic et al., 2021, 2023; Monies et al., 2019; Strug et al., 2009).

Similarly, defects in the tRNA thiolation machinery have been linked to a complex pathology that is often severe and may lead to early postnatal death of affected patients (Shaheen, Al-Salam, et al., 2016; Shaheen, Patel, et al., 2016). Consistent with the essential role of this pathway, multiple URM1 pathway components across many human cell lines are predicted to be indispensable (NFS1, MOCS3, URM1, CTU2) (DepMap, 2024; Tsherniak et al., 2017) and their deletion in mice causes embryonic lethality (*Urm1*, *Ctu1*, *Ctu2* – International Mouse Phenotyping Consortium IMPC (Groza et al., 2023)). In affected patients, biallelic *CTU2* loss-of-function mutations manifest in impaired tRNA thiolation at the cellular level (Shaheen, Al-Salam, et al., 2016; Shaheen, Patel, et al., 2016). Most mutations disrupt splice sites of the *CTU2* transcript, leading to frameshifts, premature stop codons and protein degradation (Mahoney et al., 2023; Shaaban et al., 2024; Shaheen et al., 2019). Other pathogenic alterations include C-terminal protein truncations and a leucine-to-proline point mutation (*CTU2*<sup>L63P</sup>) (Helsmoortel et al., 2015; Shaheen et al., 2019). The resulting syndrome was termed DREAM-PL syndrome, as severe cases exhibit congenital anomalies including dysmorphic facies, renal agenesis, ambiguous genitalia, microcephaly, polydactyly and lissencephaly (Shaheen, Al-Salam, et al., 2016). The clinical presentation shares features of ciliopathies, with multi-system involvement of the kidneys, brain, and reproductive organs, and typically associated features like polydactyly and lissencephaly (Waters & Beales, 2011). The underlying cellular and molecular defects explaining the complex pathology remain unknown. Here, we present complementary *in vitro* systems and a patient mutation knock-in mouse model to study DREAM-PL syndrome.

## RESULTS

### CTU2 deficiency in DREAM-PL syndrome disrupts tRNA thiolation, cell growth and proteostasis

To investigate the disease mechanisms, we characterized primary dermal fibroblasts and EBV-transformed B-lymphoblastoid cell lines (LCLs) from DREAM-PL patients carrying mostly bi-allelic splice-site mutations in *CTU2*. We also included LCLs carrying either the *CTU2*<sup>L63P</sup> point mutation or a 4-nucleotide deletion resulting in a C-terminal frameshift (**Table 1**). All DREAM-PL patient cells showed a drastic reduction in CTU2 protein levels (**Fig. 1a**). CTU1 and CTU2 form a conserved complex, with CTU1 serving as the catalytic tRNA-modifying subunit (Dewez et al., 2008; Liu et al., 2016). Hence, we tested to which degree the absence of CTU2 functionally impacted tRNA thiolation. To this end, we used ([N-acryloylamino]phenyl)mercuric chloride (APM)-containing polyacrylamide gels followed by northern blotting (Igloi, 1988). APM slows the migration of modified tRNAs, causing a detectable shift when probed with radiolabeled tRNA-specific probes. Our analysis confirmed a severe reduction of 2-thiolation of tRNA<sub>UUU</sub><sup>Lys</sup>, tRNA<sub>UUC</sub><sup>Glu</sup>, and tRNA<sub>UUG</sub><sup>Gln</sup> in patient cells, and extends previous findings (Shaheen et al., 2019) by revealing markedly reduced modification of tRNA<sub>UCU</sub><sup>Arg</sup> (**Fig. 1b, Suppl. Fig. S1a**). Importantly, we were able to fully restore tRNA thiolation upon transduction with wildtype *CTU2* (**Fig. 1b**), confirming that CTU2 is essential for this process in human cells. Interestingly, tRNA thiolation defects varied between fibroblasts and LCLs, as well as among different patient LCLs (**Suppl. Fig. S1b**).

Several patient LCLs displayed markedly reduced growth compared to controls. To test whether this defect resulted from the loss of CTU2 protein function, we transduced LCLs with retroviral particles encoding CTU2-eGFP. Wildtype CTU2 expression increased growth rates, with transduced cells outcompeting non-transduced ones in mixed cultures (**Fig. 1c, Suppl. Fig. S1c**). This effect was pronounced in LCLs carrying splice site mutations but absent in the line with a compound heterozygous *CTU2*<sup>L63P</sup> mutation (**Suppl. Fig. S1c**).

Loss of tRNA wobble thiolation causes codon-dependent ribosome pausing – particularly at CAA and AAA codons – and protein aggregation in yeast (Nedialkova & Leidel, 2015). Similar aggregation effects have been observed in human breast cancer cell lines (Rapino et al., 2021). To assess proteostasis in DREAM-PL patient cells, we analyzed protein folding, which is impacted by changes in ribosomal translation speed (Buhr et al., 2016; Nedialkova & Leidel, 2015). We used the sensor tetraphenylethene maleimide (TPE-MI), which fluoresces upon binding exposed cysteines that are normally buried in properly folded proteins and thus indicative of proteostasis defects (M. Z. Chen et al., 2017). Indeed, DREAM-PL fibroblasts exhibited significantly elevated cysteine reactivity, suggesting increased protein misfolding (**Fig. 1d**). The same was observed in two patient LCLs harboring *CTU2* splice site mutations

(Fig. 1e). Interestingly, all patient LCLs showed a drastic reduction in the central endoplasmic reticulum chaperone BiP (HSPA5/GRP78) (Fig. 1f), indicating disrupted ER homeostasis, as BiP levels would normally adjust to increased ER protein load (Bakunts et al., 2017). Consistent with altered translational control, eIF2 $\alpha$  phosphorylation was also increased (Fig. 1f), which indicates activation of the unfolded protein response. Notably, *CTU2*<sup>L63P</sup> LCLs showed intermediate levels of these markers, consistent with their hypomorphic growth behavior (Suppl. Fig. S1c).

Collectively, DREAM-PL patient cells display altered growth and proteostasis due to impaired tRNA thiolation. Although the severity varies with cell type and the mechanism of *CTU2* inactivation, the consistent reduction of thiolation across patient samples indicates a conserved negative impact at the cellular level.

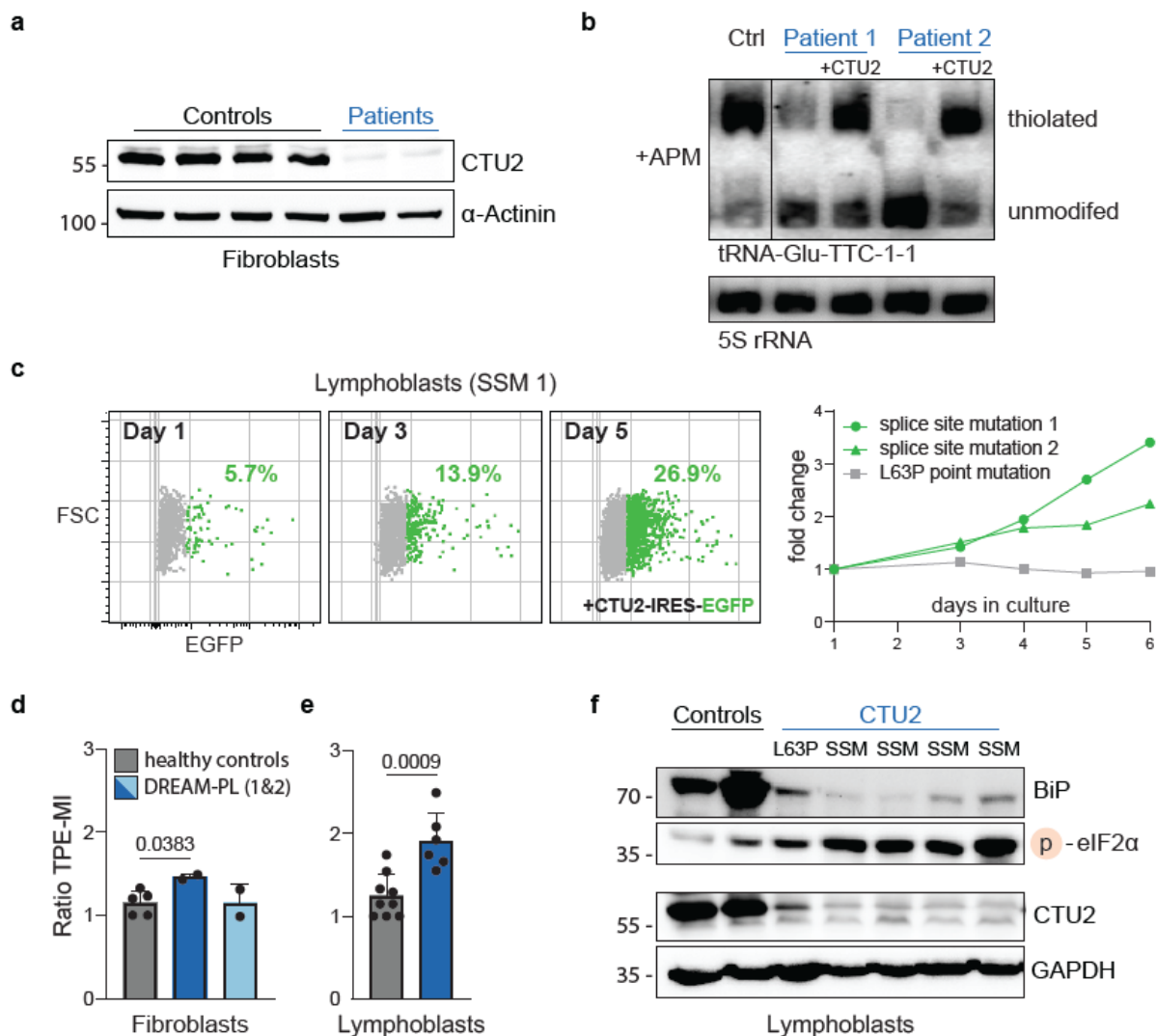


**Figure 1. CTU2 deficiency in DREAM-PL disrupts tRNA thiolation, cell growth and proteostasis**

(a) Western blot analysis of fibroblasts from DREAM-PL patients and controls.

(b) APM-northern blot in patient fibroblasts. Thiolation is restored upon *CTU2* overexpression. 5S rRNA serves as a loading control.

(c) Growth rescue of patient lymphoblastoid cell lines (LCLs) by CTU2 complementation. Left: CTU2-eGFP-expressing cells (green) outcompete non-transduced cells (grey). Right: comparison of three patient LCLs with the indicated CTU2 mutations (technical replicates).

(d, e) Quantification of protein unfolding by TPE-MI staining in patient fibroblasts (technical duplicates) and (e) lymphoblasts ( $n = 3$ , technical triplicates) analyzed by flow cytometry. Controls from healthy donors are shown in grey. Normalized mean fluorescence intensity reflects TPE-MI binding to exposed cysteines. Data represent mean  $\pm$  SD; two-tailed unpaired t-tests, p-values are indicated.

(f) Western blot analysis of proteostasis-related markers in patient LCLs. SSM, splice-site mutation.

### **CTU2<sup>L63P</sup> fails to support the formation of a functional CTU1/CTU2 complex**

To obtain a mechanistic understanding of how CTU2<sup>L63P</sup> leads to DREAM-PL in humans and how it compares to complete protein loss due to CTU2 splice site mutations (**Fig. 1a**), we assessed the functional and structural impact of this pathogenic point mutation. Leucine 63 is located at the distal end of an N-terminal  $\alpha$ -helix, predicted by AlphaFold3 to be in contact with its substrate tRNAs (**Fig. 2a-b and Suppl. Fig. S2a, S2b**). Substituting leucine with proline at this position is expected to act as a “helix breaker” by disrupting hydrogen bonding in the cyclic side chain (Nilsson et al., 1998). Consistent with this, the CTU2<sup>L63P</sup> mutation destabilized the protein. Using insect cells for expression, wildtype CTU2 readily co-purified with CTU1, but the mutant failed to do so (**Fig. 2c**). Even when using a codon-optimized construct, CTU2<sup>L63P</sup> did not form a complex with CTU1 despite being expressed, indicating that the mutation renders the protein insoluble.

Interestingly, sequence analysis revealed several positively charged residues in proximity of leucine 63 – histidine 57, arginine 60, lysine 65 and arginine 76 (**Fig. 2b**). As these may mediate interactions with negatively charged tRNA, we generated and expressed double mutants for functional investigation. Unlike CTU2<sup>L63P</sup>, both mutants were soluble, and each stoichiometric complex could be purified in amounts comparable to the wildtype complex (**Suppl. Fig. S2c**). Next, we performed *in vitro* tRNA binding assays confirming that both CTU2<sup>H57A/R60A</sup> and CTU2<sup>K65A/R67A</sup> had markedly reduced affinity for tRNA (**Fig. 2d**). Together, these findings suggest that CTU2 supports tRNA binding, and that the pathogenic CTU2<sup>L63P</sup> mutation disrupts substrate, and possibly also CTU1 interactions, leading to impaired tRNA thiolation.

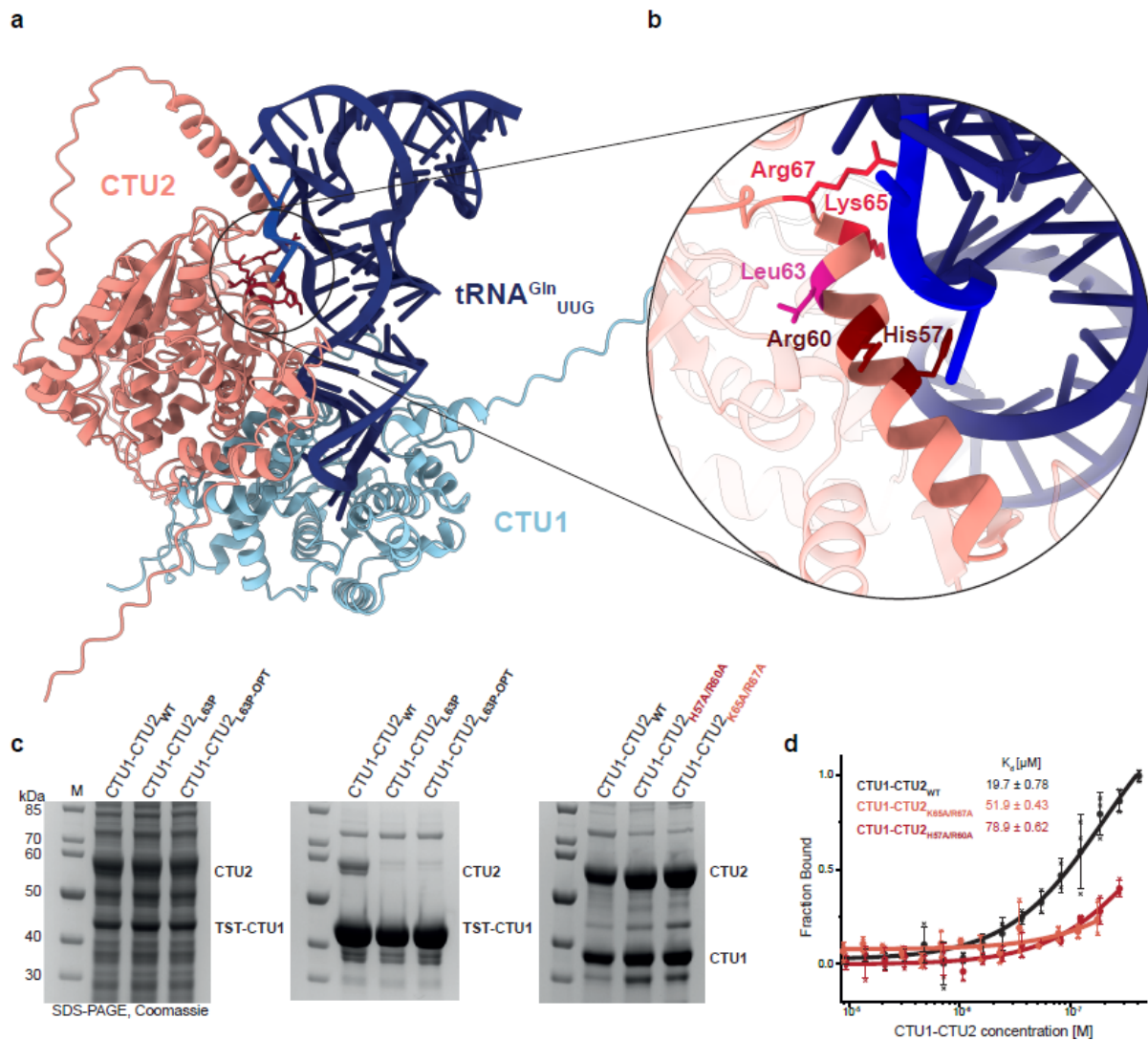


**Figure 2. CTU2<sup>L63P</sup> fails to support the formation of a functional CTU1/CTU2 complex**

**(a)** Representative AlphaFold 3 model of the human CTU1:CTU2 complex bound to tRNA<sup>Gln</sup><sub>UUG</sub>. CTU1 is shown in light blue, CTU2 in red, and tRNA in navy blue.

**(b)** Close-up view of the CTU2  $\alpha$ -helix containing Leu63, which is mutated to proline in DREAM-PL syndrome (pink). Positively charged residues selected for mutational analysis are highlighted in shades of red.

**(c)** Pull-down analysis of CTU1:CTU2 complex formation and solubility. Left: whole cell extract confirming expression of CTU2<sup>WT</sup>, CTU2<sup>L63P</sup>, CTU2<sup>L63P-OPT</sup> (codon-optimized for insect cell expression). Center: eluates from TST-CTU1 pull-downs assessing soluble complex formation. Right: purified human wildtype and mutant CTU1:CTU2 complexes.

**(d)** tRNA-binding assay using Cy5-labeled *in-vitro* transcribed human tRNA<sup>Gln</sup><sub>UUG</sub> incubated with increasing concentrations of purified CTU1:CTU2 complexes. Dissociation constants  $K_d$  are indicated.

### Multi-omics analysis reveals transcriptome and proteome rewiring in DREAM-PL cells

To assess how cells respond to defective tRNA thiolation, we examined possible ways to adapt. Therefore, we performed transcriptome analyses in primary patient fibroblasts comparing them to healthy donor controls and found a significant upregulation of genes required for mitochondrial ATP production via oxidative phosphorylation and ribonucleotide metabolism (**Fig. 3a**). In contrast, downregulated genes were associated with cell migration

(e.g., SRC, ROCK1/2), kidney and vascular development (WNT4, SOX18), PKB/AKT survival signaling (PDGFRB, PIK3R1) and tube morphogenesis (VASP, EDNRB), in line with the developmental defects seen in DREAM-PL patients (**Fig. 3a**).

Since CTU2-deficient cells accumulate misfolded proteins, we hypothesized that cells might transcriptionally compensate for these non-functional proteins. To test this, we profiled the unfolded proteome using TME, a second-generation TPE-MI probe (**Fig. 1e**) that selectively enriches unfolded proteins via its alkyne handle (Zhang et al., 2025). Mass spectrometry revealed an enrichment of mitochondrial proteins, oxidoreductases, and proteins involved in amino acid biosynthesis (**Fig. 3b, Suppl. Fig. S3a**). In line with results of this STRING analysis (Szklarczyk et al., 2023), we detected significant differences in reactive oxygen species levels in patient fibroblasts compared to the healthy controls (**Suppl. Fig. S3b**). Among the most enriched proteins were ETHE1 and SQOR, involved in mitochondrial sulfur detoxification, the m<sup>6</sup>A readers and mRNA-binding proteins IGF2BP1 and IGF2BP3, and factors linked to cell cycle and death regulation, including CDKN2A and PHLDA1. We confirmed expression changes of several of these candidates by immunoblotting, with IGF2BP3 and PHLDA1 showing the most pronounced increase in patient fibroblasts (**Fig. 3c**).

Next, we performed a multi-omics analysis comparing transcriptomic and proteomic datasets and found a substantial overlap between upregulated mRNAs and TME-enriched unfolded proteins, including IGF2BP3, PHLDA1, and ETHE1 (**Fig. 3d**). This overlap indicates that signaling networks are re-wired by a cellular stress response to impaired thiolation, as many unfolded proteins are also transcriptionally upregulated in patient cells, indicative of compensatory measures that secure cell growth and survival.

Since inefficient translation of A-ending thiolation-dependent codons has been linked to protein aggregation in yeast (Nedialkova & Leidel, 2015), we assessed whether these codons are differentially represented in the coding sequences of the unfolded proteome of DREAM-PL patients. Intriguingly, proteins enriched in the TME pull-down had a lower average frequency of AAA, CAA, GAA, and AGA codons in their mRNAs compared to unchanged or underrepresented proteins, while the frequency of corresponding G-ending codons (e.g. AAG) remained unchanged (**Fig. 3e**).

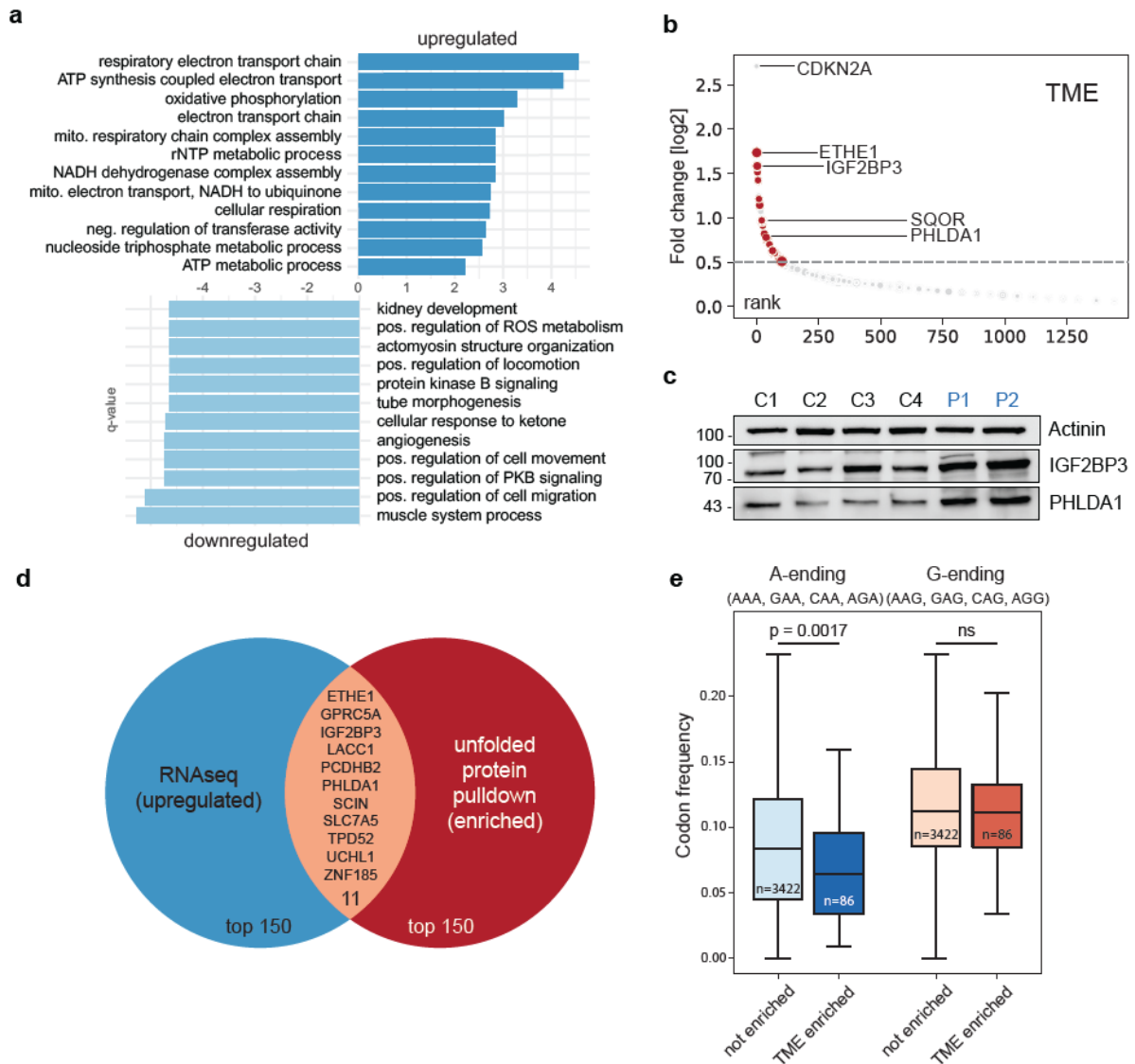


**Figure 3. Multi-omics analysis reveals altered mitochondrial activity in DREAM-PL cells**

**(a)** Gene Ontology (GO) enrichment analysis of differentially expressed genes in DREAM-PL patient fibroblasts. Bar plots show significantly upregulated (top), and downregulated (bottom) biological processes compared with healthy donor controls (n = 2 DREAM-PL fibroblast lines, n = 10 healthy donor controls; FDR < 0.05, Benjamini-Hochberg adjusted).

**(b)** Unfolded proteome profiling using TME-based pulldown in patient fibroblasts. Significantly enriched proteins (adjusted p < 0.05, log<sub>2</sub> fold change > 0.5) are shown in red. Dot size indicates statistical significance (−log<sub>10</sub> p-value). n = 2 DREAM-PL fibroblasts profiled as technical quadruplicates; n = 4 controls profiled as technical duplicates.

**(c)** Validation of selected proteins by Western blotting in patient fibroblasts. Actinin serves as loading control.

**(d)** Venn diagram illustrating the overlap between upregulated transcripts and TME-enriched unfolded proteins.

**(e)** Cumulative codon frequency analysis (AAA/G, CAA/G, GAA/G, AGA/G) of coding sequences of proteins identified in the unfolded proteome pulldown. n numbers are indicated. Two-tailed unpaired t-test for G-ending codons: p = 0.68.

### Acute CTU2 depletion induces codon-biased proteome remodeling

Because the patient cell data indicated altered proteostasis and a potential codon-specific translation defect, we generated an RNAi-based conditional *CTU2*-depletion system to directly test the consequences of timed *CTU2* loss and thiolation defects in isogenic cells. Using two independent doxycycline-inducible short hairpin RNAs (shRNAs), we were able to significantly reduce *CTU2* protein expression in HeLa cervical carcinoma and hTERT-immortalized retinal pigmented epithelial cells (RPE1) over time (**Fig. 4a**, **Suppl. Fig. S4a**), coinciding with a significant reduction of tRNA thiolation (**Fig. 4b**). Interestingly, *CTU2* depletion markedly reduced viability in HeLa cells, while RPE1 cells showed no signs of cell death (**Fig. 4c**). This phenotype in HeLa cells was rescued by the overexpression of an shRNA-resistant variant of *CTU2*, confirming the on-target design of our construct (**Fig. 4c**). These model cell lines recapitulated the molecular hallmarks of impaired thiolation observed in patient cells, including BiP loss and increased eIF2 $\alpha$  phosphorylation (**Fig. 4d**). We then asked whether proteins identified in the unfolded proteome were similarly affected upon acute *CTU2* knockdown. Indeed, ETHE1 and IGF2BP3 expression increased from day 4 onward, mirroring stress responses seen in patient cells (**Fig. 4e**).

Next, to test whether thiolation loss elicits similar translational defects in human cells as reported in invertebrates (Nedialkova & Leidel, 2015; Zinshteyn & Gilbert, 2013), we performed ribosome profiling in acutely depleted RPE1 cells, a non-transformed, near-primary cell model. *CTU2* knockdown for 96 h led to a striking increase in ribosome occupancy at AGA and CAA codons (**Fig. 4f**). Across all 61 sense codons, AGA exhibited the most pronounced increase in ribosome occupancy (**Suppl. Fig. S4b**). As expected, loss of thiolation did not affect the translation of synonymous AAG, CAG, GAG or AGG codons, which showed decreased ribosome dwell times compared to their respective A-ending codons and were comparable to fully thiolation-competent controls (**Fig. 4f**). Given this codon-specific ribosome pausing, we next asked whether the frequency of A-ending codons of a given mRNA influences its translation under hypothiolation. Therefore, we grouped all mRNAs quantified by ribosome profiling (**Fig. 4f**) into ten bins from lowest to highest AAA, CAA, GAA, AGA content, and measured total ribosome occupancy. Strikingly, mRNAs in the highest A-ending codon bin had the fewest translating ribosomes, with a gradual and significant increase in ribosome occupancy toward bins with lower A-ending codon content (**Fig. 4g**). These findings suggest that the loss of thiolation affects translation of A-ending codon in a dosage-dependent manner. To validate this at the protein level, we performed quantitative proteomics of *CTU2*-depleted RPE1 cells after 96 h. Consistent with the ribosome occupancy results, proteins that decreased in abundance were significantly enriched for coding sequences containing AAA,

CAA, GAA, and AGA codons, whereas proteins encoded by mRNAs with few A-ending codons increased in abundance (**Fig. 4h**).

This prompted us to perform a codon enrichment analysis to systematically identify pathways potentially disrupted in DREAM-PL syndrome. We reasoned that DREAM-PL, as a syndromic disorder, likely arises from disruption of multiple, potentially tissue-specific signaling pathways. To this end, we ranked all human coding sequences (CDS) by A-ending codon content and performed gene set enrichment analysis on the top 5% (GSEA) (**Fig. 4i**). Strikingly, among the top 10 gene sets, three were linked to cilia biology (cilium assembly, cilium organization, and plasma membrane–bounded cell projection assembly). Additional potentially affected pathways included chromosome segregation and mitotic spindle organization, both also dependent on centrosome formation and function (**Fig. 4i**).

Intriguingly, DREAM-PL syndrome presents with ciliopathy-like features, suggesting that the loss of tRNA thiolation may affect cilia formation or function, along with mitotic spindle performance. Given this unexpected link to ciliogenesis, we examined whether the absence of tRNA thiolation impaired primary cilia formation. Using RPE1 cells, which form primary cilia upon serum withdrawal, we compared ciliogenesis between wildtype and *CTU2*-depleted cells. Upon starvation, *CTU2* knockdown markedly reduced the fraction of cells that could form primary cilia (**Fig. 4j**). We also observed instances of abnormal centriole counts and occasional multipolar spindles in *CTU2*-deficient HeLa cells, consistent with our GO-term analysis indicating defects in chromosome segregation (**Suppl. Fig. S5a-b**).

In summary, acute loss of tRNA thiolation in human cells broadly alters the proteome, with a predominant impact on pathways regulating ciliogenesis and cell division.

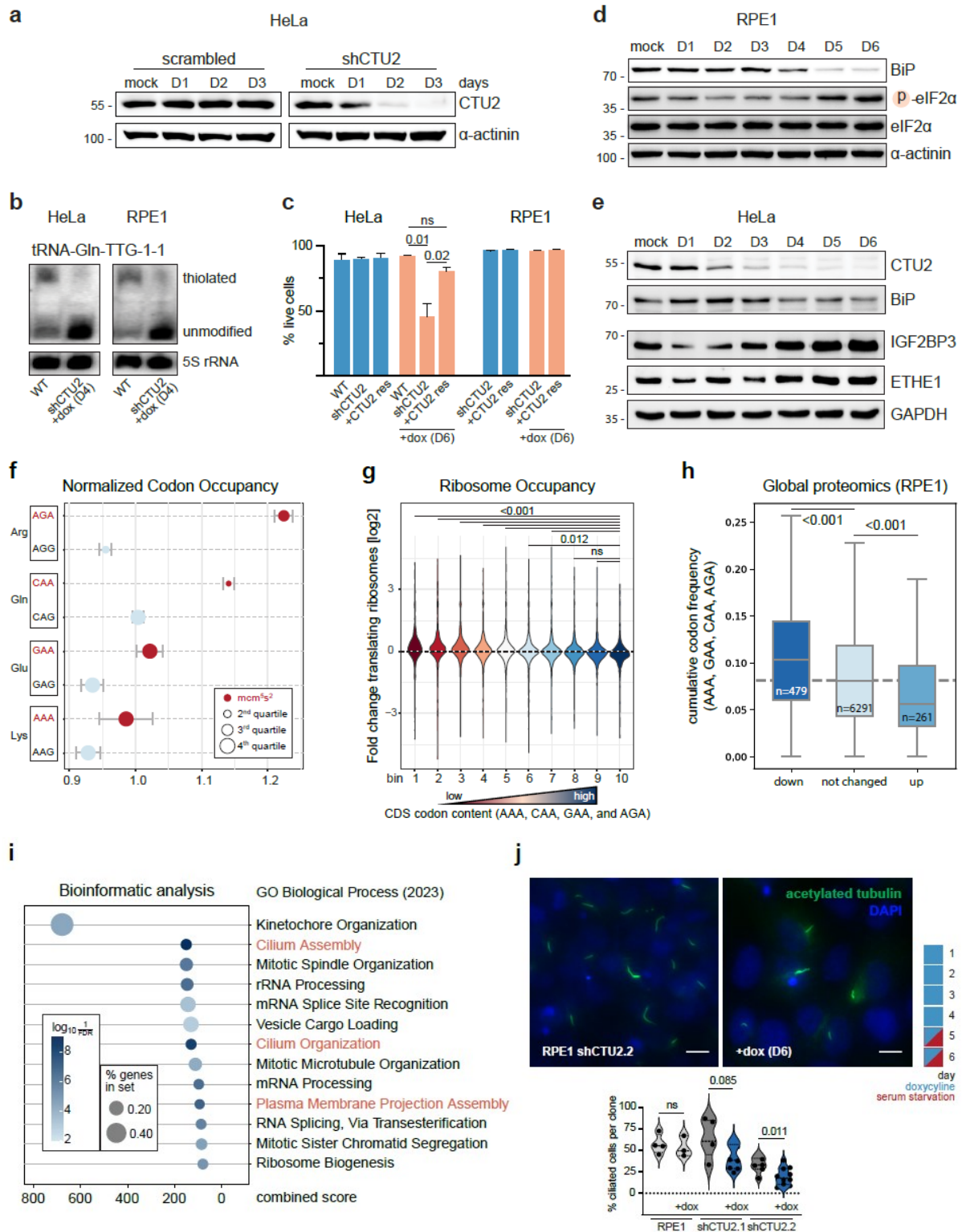


**Figure 4. Acute CTU2 depletion induces codon-biased proteome remodeling**

(a) Western blot analysis of doxycycline (dox)-inducible *CTU2* knockdown in HeLa cells over time. Duration of dox treatment is indicated in days. scrambled, non-targeting shRNA control.

(b) APM-northern blot validation of tRNA thiolation loss in HeLa and RPE1 cells after 4 days of dox treatment. tRNA<sup>Gln</sup><sub>UUG</sub> is shown representatively.

(c) Viability analysis of *CTU2* knockdown cell lines by Annexin V staining. +CTU2 res indicates shRNA-resistant *CTU2* overexpression. One-way ANOVA, WT vs. *CTU2* res  $p = 0.264$ .  $n = 3$  technical replicates.

- (d) Western blot analysis of unfolded protein response (UPR) checkpoints during progressive tRNA thiolation in RPE1 cells. Time points indicate days of *CTU2* depletion.
- (e) Western blot validation of selected proteins identified in DREAM-PL patient fibroblasts, analyzed under acute *CTU2* knockdown conditions.
- (f) Ribosome profiling in 96 h *CTU2*-depleted RPE1 cells compared with untreated controls. Normalized codon occupancy is shown for A- and G-ending codons of the indicated amino acids. Codons are divided into quartiles according to relative library abundance. n = 2 technical replicates.
- (g) Cumulative A-ending codon frequency (AAA, CAA, GAA, and AGA) in coding sequences (CDSs) of proteins quantified in *CTU2*-depleted RPE1 cells after 96 hours. The dashed line indicates the average A-ending codon content (7.6%) across 19,085 analyzed human CDSs. Two-tailed unpaired t-test, p > 0.001 (down and up).
- (h) Gene Ontology (GO) enrichment analysis on the top 5% of human coding sequences ranked by A-ending codon content (AAA, CAA, GAA, AGA). Enriched pathways were clustered by GO Biological Process (2023). Cilium-associated terms are highlighted in orange.
- (i) Ribosome occupancy analysis of all mRNAs measured by ribosome profiling (f). Transcripts were ranked by A-ending codon frequency (AAA, CAA, GAA and AGA) and divided into ten equal bins (bin 1 = lowest, bin 10 = highest). A negative correlation was observed between A-ending codon frequency and ribosome abundance. ANOVA with post hoc test. Adjusted p-values are indicated.
- (j) Ciliogenesis assay in *CTU2*-knockdown and wildtype RPE1 cells upon serum starvation. Representative immunofluorescence images show primary cilia (green) and nuclei (blue). The treatment scheme is shown above. Quantification of fractions of cilia-forming RPE1 cells under tRNA thiolation is provided. Two-tailed unpaired t-test, p-values are indicated. n = 3 technical replicates. Scale bars 10µm.

### ***Ctu2*<sup>L63P/L63P</sup> knock-in mice escape DREAM-PL pathology despite reduced tRNA thiolation**

*CTU2* is highly conserved between mice and humans. Consistent with this, we found that the murine protein can thiolate human tRNAs, when overexpressed in *CTU2*-knockdown cell lines (**Suppl. Fig. S6a**). Hence, we anticipated that *Ctu2*<sup>L63P</sup> would be equally pathogenic in mice and humans and cause comparable downstream effects.

To validate this, we used CRISPR–Cas9 to introduce the leucine-to-proline substitution into KH2 mouse embryonic stem cells for blastocyst injection, generating transgenic heterozygous animals. Surprisingly, intercrosses of *Ctu2*<sup>WT/L63P</sup> mice yielded homozygous *Ctu2*<sup>L63P/L63P</sup> offspring at only mildly reduced Mendelian ratios and a slightly skewed sex distribution (**Fig. 5a**). Viable offspring were also born after backcrossing to the C57Bl/6N genetic background (**Suppl. Fig. S6b**), contrasting previous reports of embryonic lethality following whole-body deletion of *Ctu1*, *Ctu2*, or *Urm1* (Birling et al., 2021; Elrick et al., 2024; Groza et al., 2023; The International Mouse Phenotyping Consortium et al., 2016). Both female and male *Ctu2*<sup>L63P/L63P</sup> animals were fertile and showed no developmental defects resembling those seen in DREAM-PL patients carrying the same point mutation (**Suppl. Fig. S6c**).

To confirm tRNA thiolation deficiency, we conducted APM-northern blot analyses and found a striking reduction of tRNA thiolation in mouse embryonic fibroblasts (MEFs) isolated from homozygous *Ctu2*<sup>L63P/L63P</sup> E14.5 embryos, highlighting the functional importance of leucine 63

both in humans and mice (**Fig. 5b**). Furthermore, CTU2 protein levels were markedly reduced (**Suppl. Fig. S6d**), consistent with observations in patient cells (**Fig. 1a**) and heterologous expression studies in insect cells (**Fig. 2c**). Wildtype and heterozygous MEFs showed comparable thiolation levels, indicating that a single functional *Ctu2* allele is sufficient to maintain the thiolated tRNA pool, at least in fibroblasts. We monitored multiple tissues for tRNA thiolation and found that mutant animals showed markedly reduced thiolation across all major organs analyzed (**Fig. 5c**). However, the ratio of thiolated to unmodified tRNAs seemed to differ among organs, with a pronounced shift best notable in the spleen (**Fig. 5c**). Intriguingly, several aged *Ctu2*<sup>L63P/L63P</sup> animals analyzed presented with splenomegaly when compared to wildtype controls (**Fig. 5d**), warranting more detailed analyses of ageing phenotypes in future analyses.

Finally, we explored whether the codon biases associated with loss of tRNA thiolation are conserved among vertebrates. An analysis of coding sequences from different species with annotated human homologs showed that thiolation-dependent codon usage is most conserved in mammals and decreases progressively with evolutionary distance (**Suppl. Fig. S6e**). Hence, we decided to make use of our mouse model and performed ribosome profiling of wildtype and homozygous *Ctu2*<sup>L63P</sup> MEFs and were able to confirm the pausing of ribosomes at A-ending, rather than synonymous G-ending, codons. Notably, in mice, CAA emerged as the most affected thiolation-dependent codon, in contrast to AGA in CTU2-depleted RPE1 cells (**Suppl. Fig. S6f, Fig. 4h**). At the pathway level, nearly half of the top AAA-, CAA-, GAA-, and AGA-enriched GO terms are shared between mice and humans, including those linked to cilia and chromosome segregation (**Fig. 5e**). Accordingly, we repeated the ciliogenesis assay upon serum withdrawal in MEFs and found a comparable reduction of ciliation-competent cells in a state of hypo-thiolation (**Fig. 5f-g, Fig. 4j**).

In summary, despite conserved molecular signatures of impaired tRNA thiolation, mice remain largely unaffected at the organismal level, suggesting the presence of compensatory mechanisms that allow them to escape the development of DREAM-PL-like pathology.

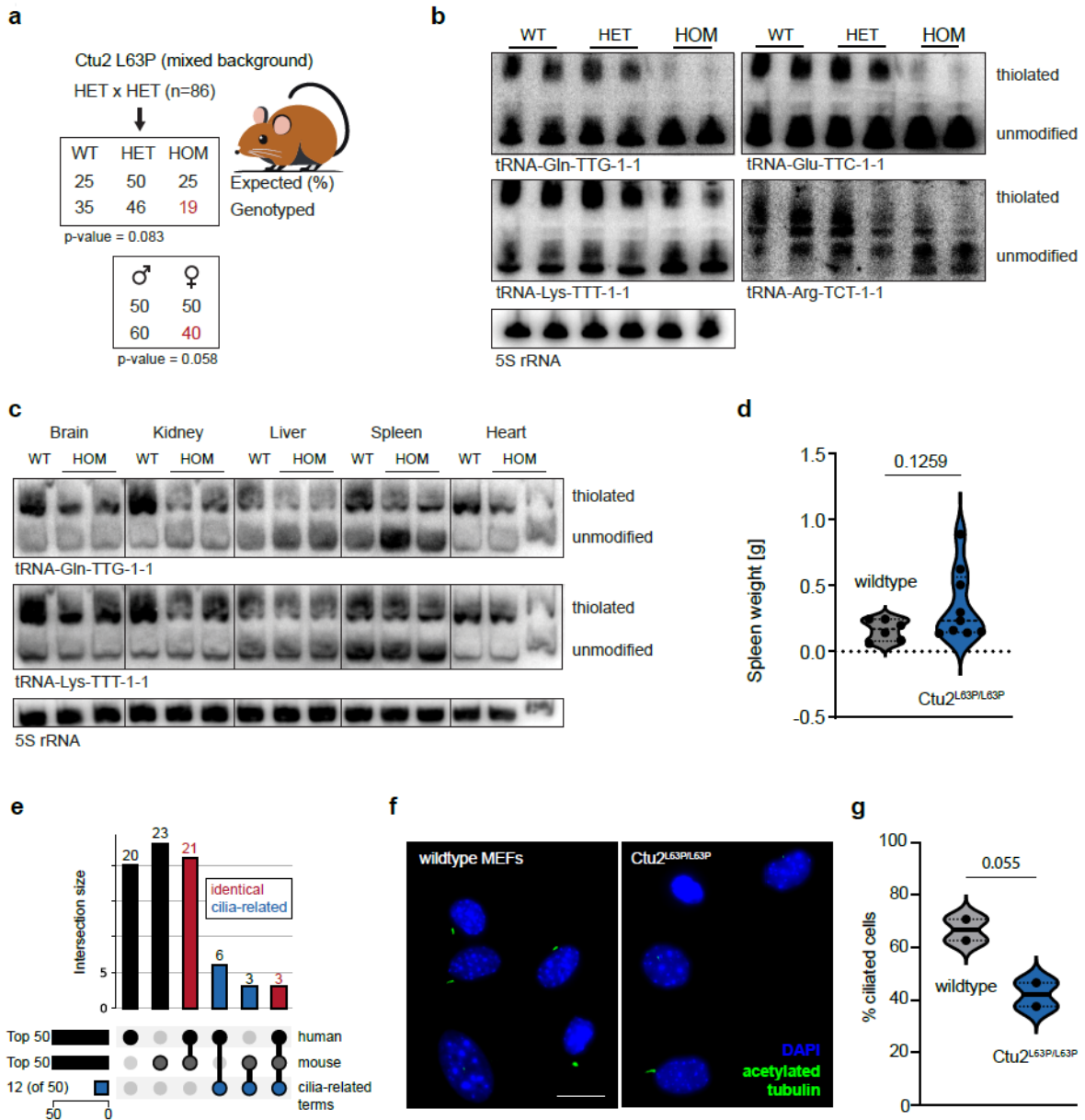


**Figure 5: *Ctu2*<sup>L63P/L63P</sup> knock-in mice escape DREAM-PL pathology despite reduced tRNA thiolation**

(a) Breeding results of heterozygous *Ctu2*<sup>WT/L63P</sup> knock-in mice born at Mendelian ratios, showing a trend toward underrepresentation of homozygous and female offspring. Chi-square goodness-of-fit test. p-values are indicated.

(b) APM-northern blots detecting all thiolated tRNA species in mouse embryonic fibroblasts (MEFs). 5S rRNA serves as a loading control.

(c) APM-northern blots for the indicated tRNA species extracted from different organs of *Ctu2*<sup>L63P/L63P</sup> mice. 5S rRNA serves as a loading control.

(d) Spleen weights of aged *Ctu2*<sup>L63P/L63P</sup> mice ( $\geq 1.5$  years, n = 9) compared with age-matched wildtype controls (n = 6). Two-tailed unpaired t-test. p-value is indicated.

(e) UpSet plot showing conserved tRNA thiolation-dependent pathways between humans and mice. 24 Gene Ontology (GO) terms are conserved (red). Cilium-associated terms account for 9 (human) and 6 (mouse) GO terms, of which 3 are shared (red, right bar). Unique GO terms are shown in black.

(f, g) Ciliogenesis assay in wildtype and *Ctu2*<sup>L63P/L63P</sup> MEFs. (f) Representative immunofluorescence images of primary cilia (green) and nuclei (blue). (g) Quantification of fraction of ciliated MEFs under serum starvation. Two-tailed unpaired t-test. p-value is indicated.

## DISCUSSION

Here, we investigated the cellular and organismal consequences of impaired 2-thiolation of tRNA wobble uridines in mammals, using patient-derived cells, acute cellular depletion models, and a *CTU2*<sup>L63P</sup> knock-in mouse. This work expands the study of tRNA thiolation from yeast to mammalian systems and provides insight into its role in the pathogenesis of DREAM-PL syndrome.

We identify *CTU2* as an integral, non-catalytic component of the thiouridylase complex, likely positioning tRNA for modification by *CTU1* (Fig. 2d). Interestingly, a recently characterized *S. cerevisiae* strain isolated from a patient carried an *NCS2/CTU2* gain-of-function variant (H71L) that stabilized the *CTU1/2* complex to sustain tRNA thiolation and remain virulent even at elevated temperatures (Alings et al., 2023). This residue lies close to the pathogenic human L63P mutation, which we show destabilizes the *CTU1/2* complex (Fig. 2c). Together, these findings illustrate that *CTU2* mutations can modulate the strength and functionality of the thiouridylase complex in both directions. Notably, some bacteria and archaea perform thiolation using a single homodimeric enzyme (Shigi, 2014). Why eukaryotes evolved to use a two-subunit system remains an open question.

Once tRNA thiolation is impaired, all human cell models we profiled showed signs of impaired proteostasis, including increased protein unfolding and stress signaling, yet only some were affected in their viability (Fig. 1d-f, Fig. 4c-e). Patient and RPE1 cells tolerated hypothiolation, while HeLa cells progressively died. Transcriptomic and proteomic rewiring likely underlies this variability, enabling some cell types to adapt despite persistent proteostasis stress. A systematic follow-up on these changes (Fig. 3), especially hydrogen sulfide (H<sub>2</sub>S) metabolism is warranted (ETHE1, SQOR), as the loss of tRNA as the final sulfur acceptor could trap sulfur at thiocarboxylated URM1, diverting it to alternative biological use (Pabis et al., 2020; Ravichandran et al., 2022; Sokołowski et al., 2024). Sensitivity to hypothiolation may also reflect changes in metabolic or translational demands, as U<sub>34</sub>-modifying enzymes are known to become critical under nutrient-limiting conditions or during cancer metastasis (Hermann et al., 2025; Rapino et al., 2018). Differences in RNA modification patterns could also contribute, as loss of mcm<sup>5</sup>s<sup>2</sup> was shown to alter mRNA turnover through crosstalk with m<sup>6</sup>A (Linder et al., 2025).

On the translation level, impaired tRNA thiolation perturbs decoding fidelity in a codon-dependent manner. Our ribosome profiling data show markedly slowed decoding of thiolation-dependent CAA and AGA codons in mcm<sup>5</sup>s<sup>2</sup>-deficient human and murine cells (Fig. 4f, Fig. S6f), which is consistent with previously described U<sub>34</sub> modification mutants (Linder et al., 2025; Nedialkova & Leidel, 2015; Zinshteyn & Gilbert, 2013). This in turn alters translational

output, suggested by the underrepresentation of proteins encoded by “biased” mRNAs in the unfolded protein pulldown (Fig. 3e) and the frequency-dependent decrease of overall ribosome occupancy on these transcripts (Fig. 4i). Mechanistically, such difficult-to-translate mRNAs, together with their nascent protein products, may be degraded by cellular ribosome-associated quality control mechanisms, as shown in yeast (Wu et al., bioRxiv, 2024). However, codon content alone does not fully define translational efficiency. Only a subset of proteins is likely affected, as shown in yeast thiolation mutants (Rezgui et al., 2013), and additional determinants such as di-codon context, amino acid patterns and mRNA stability further modulate protein output (Linder et al., 2025; Rapino et al., 2021; Wu et al., bioRxiv, 2024).

Therefore, to capture a spectrum of “biased” transcripts, we performed gene ontology analysis, which revealed an enrichment for pathways related to ciliogenesis and centrosome organization (Fig. 4h). Dysfunction of cilia, cilia-anchoring centrosomes, and their coordination with the cell cycle align well with the ciliopathy-like presentation of DREAM-PL syndrome. Notably, ciliopathies are the most common cause of multisystem and renal anomalies in abnormal fetuses studied in a highly consanguineous parent cohort (Al-Hamed et al., 2022). Consistent with these observations, we confirmed reduced ciliogenesis capacity in *CTU2*-deficient human and mouse cells (Fig. 4j, Suppl. Fig. 5f, g).

The finding that *Ctu2*<sup>L63P/L63P</sup> knock-in mice exhibited strongly reduced tRNA thiolation yet completed development was unexpected (Fig. 5a–b). Together with organ-specific differences in thiolation levels (Fig. 5c), this suggest that either a low but functional threshold of tRNA thiolation is sufficient for sustaining cellular homeostasis in mice, or that individual organs differ in their dependence on thiolation for proper function. The latter is consistent with the striking tissue selectivity of DREAM-PL. Nevertheless, we observed codon-specific ribosome pausing (Fig. S6f) and reduced ciliogenesis capacity in MEFs, which may reflect a stress-dependent vulnerability, as the assay is performed under serum starvation (Fig. 5f, g). Future studies employing conditional *Ctu2* ablation – like *Elp3* deletion in neural progenitors that causes microcephaly (Laguesse et al., 2015) – will be critical to define the cell type–specific requirements for tRNA thiolation and how its loss translates into organ-level pathology.

Taken together, our data support a model in which disrupted tRNA thiolation compromises translation in a context- and codon-dependent manner, specifically affecting vulnerable pathways such as ciliogenesis. Our newly established tools and models will be valuable for further mechanistic studies of DREAM-PL syndrome and may ultimately guide the development of therapies targeting epitranscriptomic dysfunction.

## **Acknowledgements**

We are grateful to Patrick Connolly, Tamas Szabo, and Michael J. Kraakman for insightful discussions. We thank Kaan Boztug, Georg Stary, and colleagues for providing healthy donor B-LCLs and fibroblasts, and Yuning Hong for the kind gift of TPE-MI and TME. We further thank Andrzej Chramiec-Głębik for producing the labelled tRNA, and Julia Heppke and Mathias Drach for their contributions to histological analyses. pMSCV-IRES-GFP was a gift from William Hahn (Addgene plasmid #9044).

We thank the Molecular Discovery Platform at CeMM for assistance with proteomics analyses and the Next Generation Sequencing Platform of the University of Bern for sequencing ribosome profiling libraries.

This work was supported by the European Research Council (ERC) under the European Union's Horizon 2020 research and innovation program (grant agreement No 101001394 to S. G.). A.V. acknowledges support by the European Research Council, ERC AdG POLICE (787171). S.A.L. was supported by Swiss National Science Foundation grants 310030\_219536, and 320030\_236130. This research was funded in part by the Austrian Science Fund (FWF) [10.55776/PIN1183123]. For open access purposes, the author has applied a CC BY public copyright license to any author accepted manuscript version arising from this submission.

## **Author Contributions**

L.E. and A.V. designed the study. L.E., M.W., C.E., F.E., V.C.S, F.M.G., Y.T., Z.Z., and N.S. performed experiments. D.M., C.E. analyzed the data. L.A. and F.S.A. provided patient samples. F.E. and T.K. established the mouse model. J.M., S.A.L., L.E, S.G. and A.V. secured funding. W.R. provided critical reagents. S.A.L., S.G. and A.V. supervised parts of the study. L.E. and A.V. wrote the manuscript with input from all coauthors.

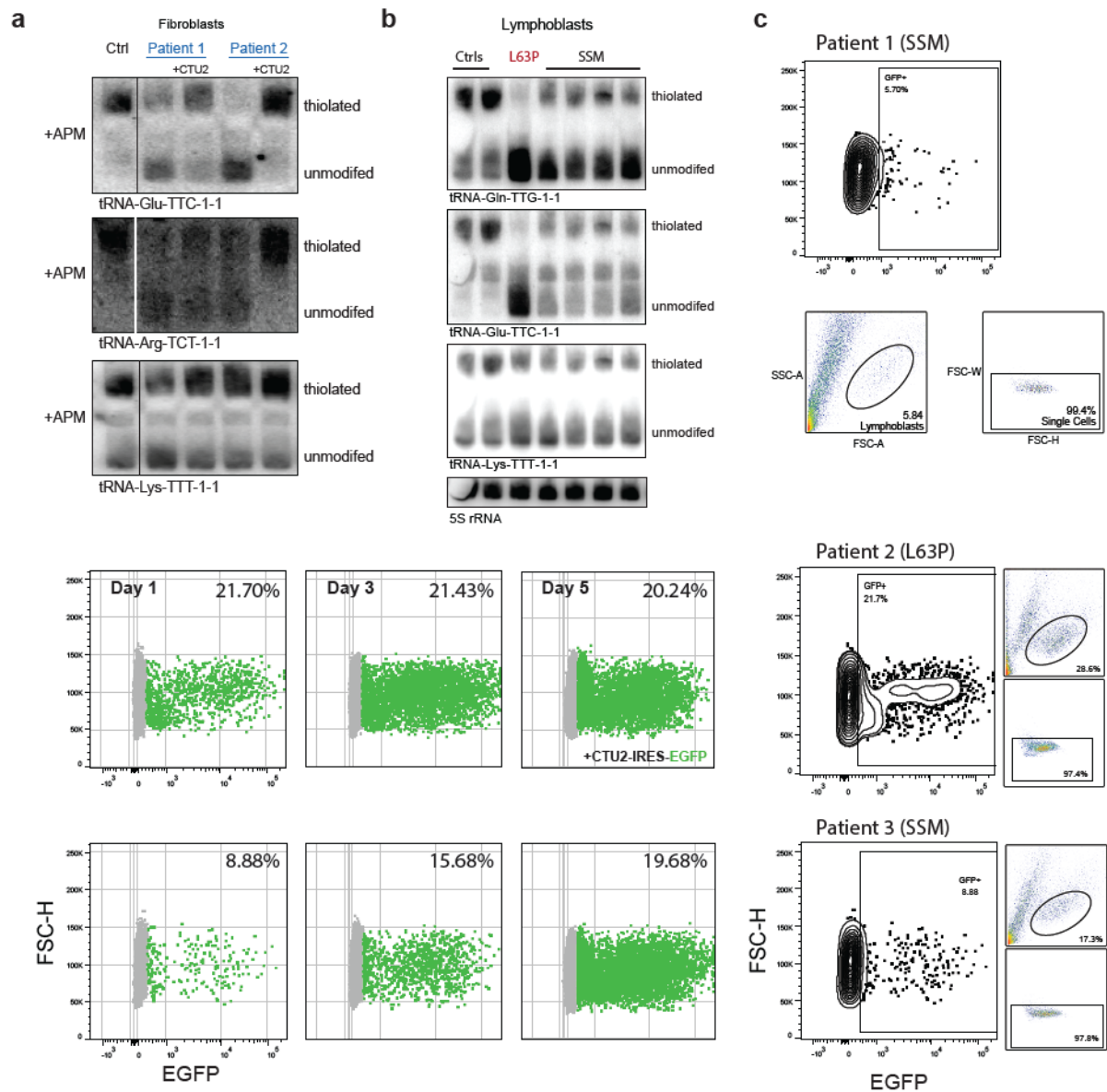
## **Competing Interests**

The authors declare no competing interests.

**Table 1. DREAM-PL patient derived cells**

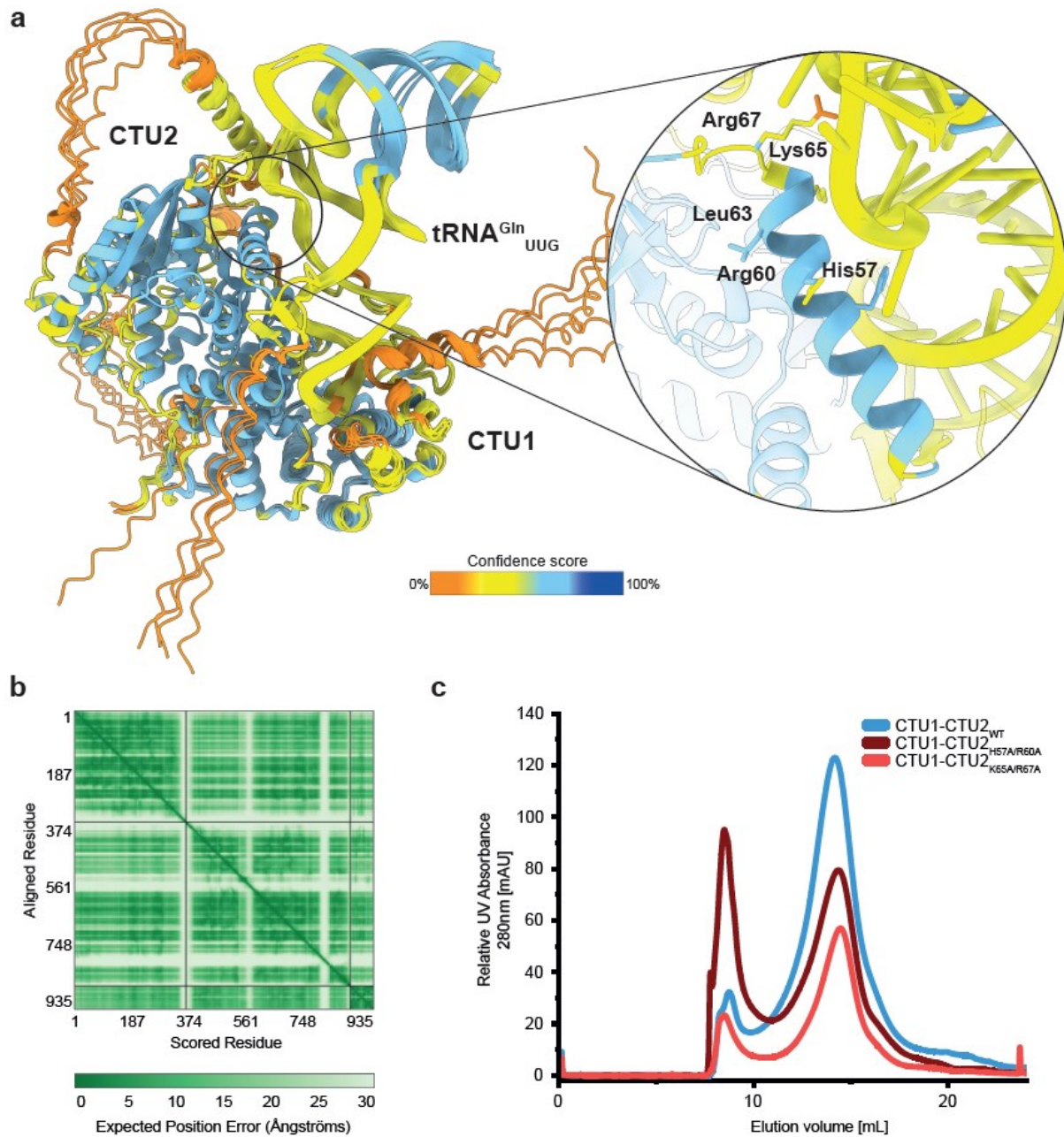
<b>ID</b>	<b>DNA sequence</b>	<b>Protein sequence</b>	<b>Cell type</b>	<b>Description</b>	<b>Reference</b>
Patient 1	c.282+5G>A (CTU2)	p.(Asp49Alafs*2) (CTU2)	Fibroblast	Splice site mutation (SSM)	(Shaheen et al., 2019)
Patient 2	c.873G>A	p.(Thr247Alafs*21)	Fibroblast	Splice site mutation	(Shaheen, Patel, et al., 2016)
LCLs L63P (0900)	c.188T>C	p.(Leu63Pro)	B-LCL	Point mutation	(Shaheen et al., 2019)
LCLs SSM 1 (0881)	c.282+5G>A	p.(Asp49Alafs*2)	B-LCL	Splice site mutation	(Shaheen et al., 2019)
LCLs SSM 2 (0352)	c.282+5G>A	p.(Asp49Alafs*2)	B-LCL	Splice site mutation	Alkuraya lab
LCLs SSM 3 (0993)	c.873G>A	p.(Thr247Alafs*21)	B-LCL	Splice site mutation	(Shaheen, Patel, et al., 2016)
LCLs SSM 4 (0001)	c.873G>A	p.(Thr247Alafs*21)	B-LCL	Splice site mutation	Alkuraya lab, unpubl.
LCLs DEL (0260)	c.1511_1514del	p.(Leu504fs*)	B-LCL	Deletion	Alkuraya lab, unpubl.

## Supplementary Fig. 1



**(a)** APM-northern blot of patient fibroblasts and healthy control. The membrane was stripped and re-probed from Fig. 1b. 5S rRNA serves as a loading control.  
**(b)** APM-northern blot of patient lymphoblastoid cell lines (LCLs). 5S rRNA is used as loading control.  
**(c)** Top: flow-cytometric gating strategy for competition assays. Left: rescue of growth defects in additional patient LCLs shown in Fig. 1c. No growth advantage is observed upon CTU2 overexpression in L63P mutant LCLs. Data for patient 1 are shown in Fig. 1c. SSM, splice-site mutation; L63P, leucine-to-proline substitution at residue 63.

## Supplementary Fig. 2

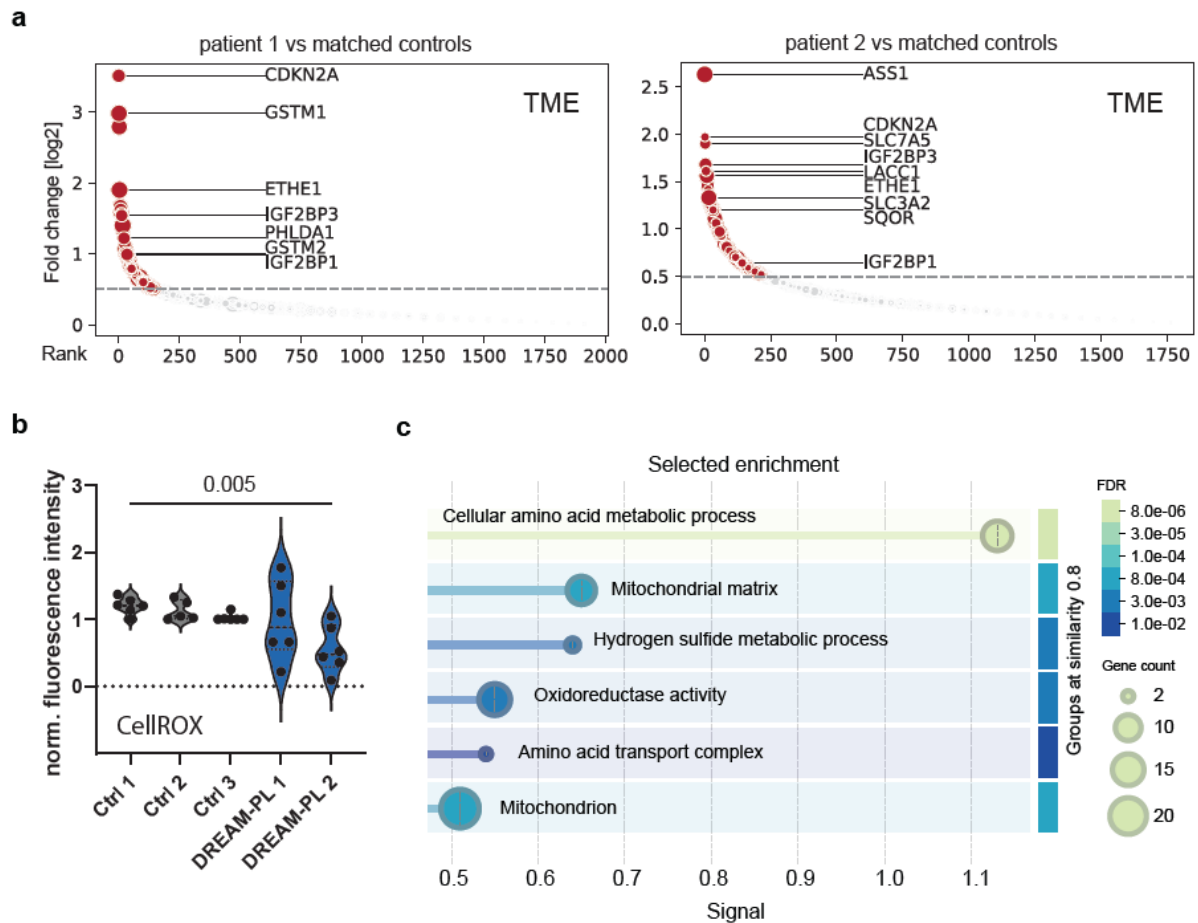


**(a)** Superimposed AlphaFold 3 predictions of the human CTU1-CTU2<sup>WT</sup> complex bound to tRNA<sup>Gln</sup><sub>UUG</sub>, colored by per-residue confidence. Right: close-up view of the  $\alpha$ -helix containing tRNA-binding mutants and leucine 63.

**(b)** Predicted Aligned Error (PAE) plot highlighting regions of higher (dark green) and lower (pale green) inter-domain prediction confidence.

**(c)** Size-exclusion chromatography profiles of purified human wildtype and mutant CTU1/CTU2 complexes from insect cells.

### Supplementary Fig. 3

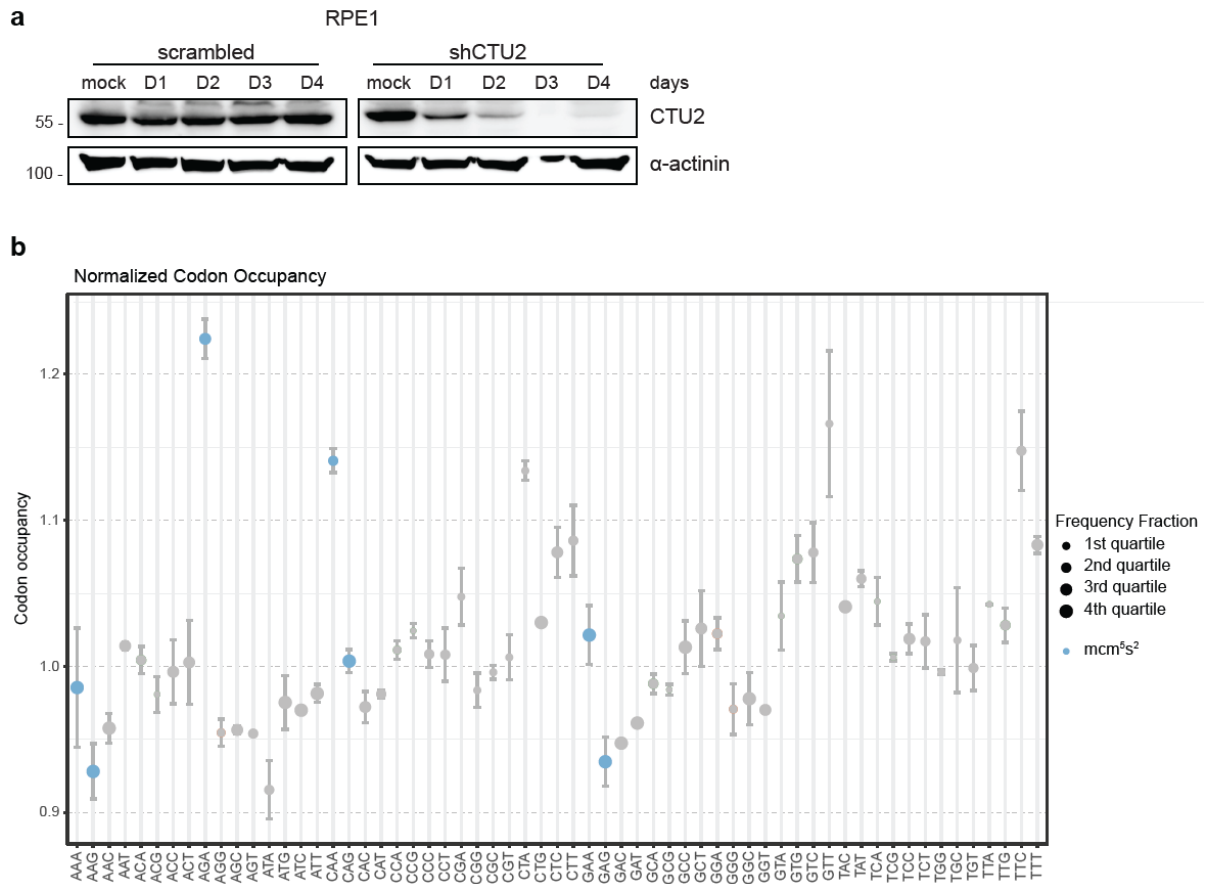


**(a)** Unfolded proteome pulldown data stratified by individual patients compared with two matched healthy controls selected by proteome similarity. Proteins detected at an adjusted  $p$ -value  $< 0.05$  are marked in red.

**(b)** Detection of reactive oxygen species in patient fibroblasts using CellROX. Welch's  $t$ -test (Control 1 vs DREAM-PL 2)  $p = 0.0049$ .  $n = 3$  technical replicates (measured in duplicate).

**(c)** 86 proteins showing a  $\log_2$  fold change  $> 0.5$  in the TME-based unfolded proteome pulldown were analyzed using STRING (v12.0) without additional filtering. The top enriched Gene Ontology (GO) terms from the categories Biological Process, Molecular Function, and Cellular Component are shown. Circle size reflects the number of genes per GO term, and color indicates the false discovery rate (FDR).

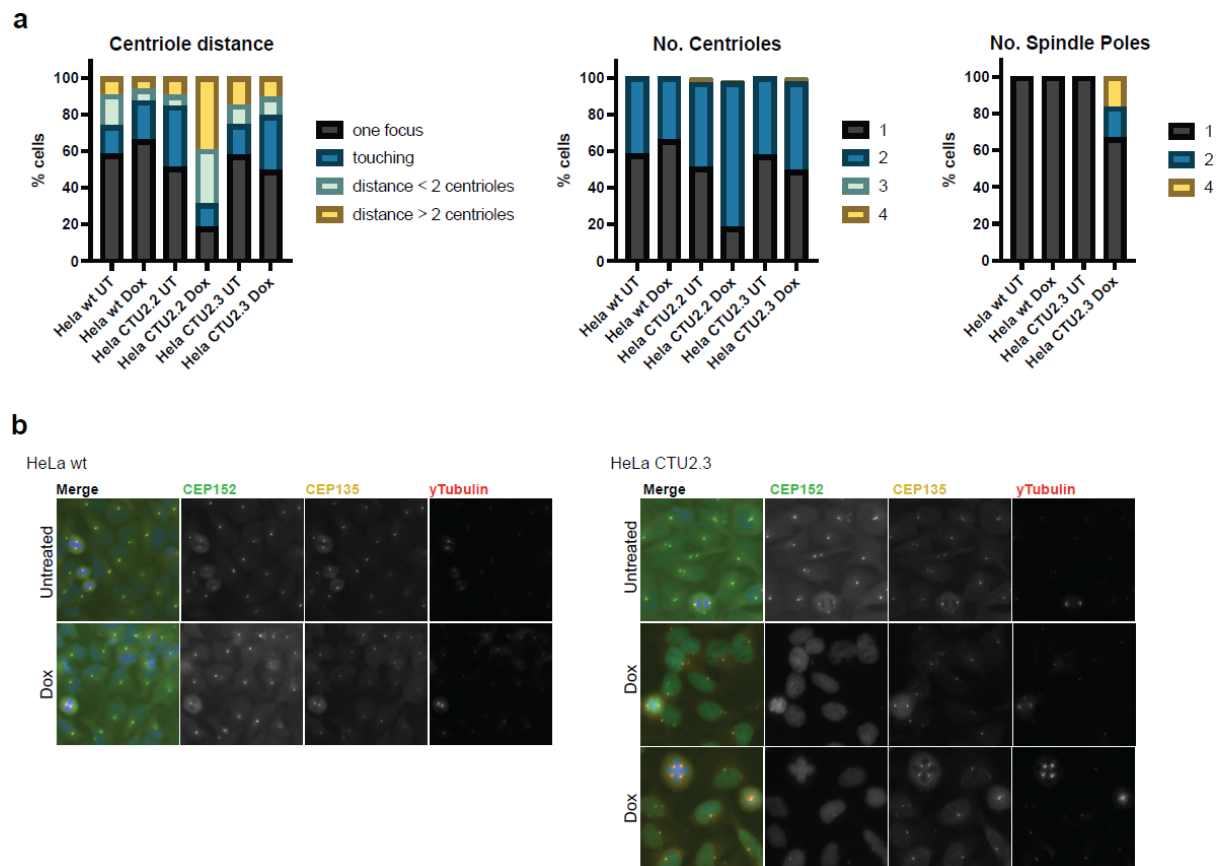
## Supplementary Fig. 4



**(a)** Western blot analysis of doxycycline (dox)-inducible CTU2 knockdown in RPE1 cells over time. Duration of dox treatment is indicated in days.

**(b)** Ribosome profiling in 96 h *CTU2*-depleted RPE1 cells compared with untreated controls. Normalized codon occupancy for all sense codons relative to untreated cells is shown.  $n = 2$  technical replicates.

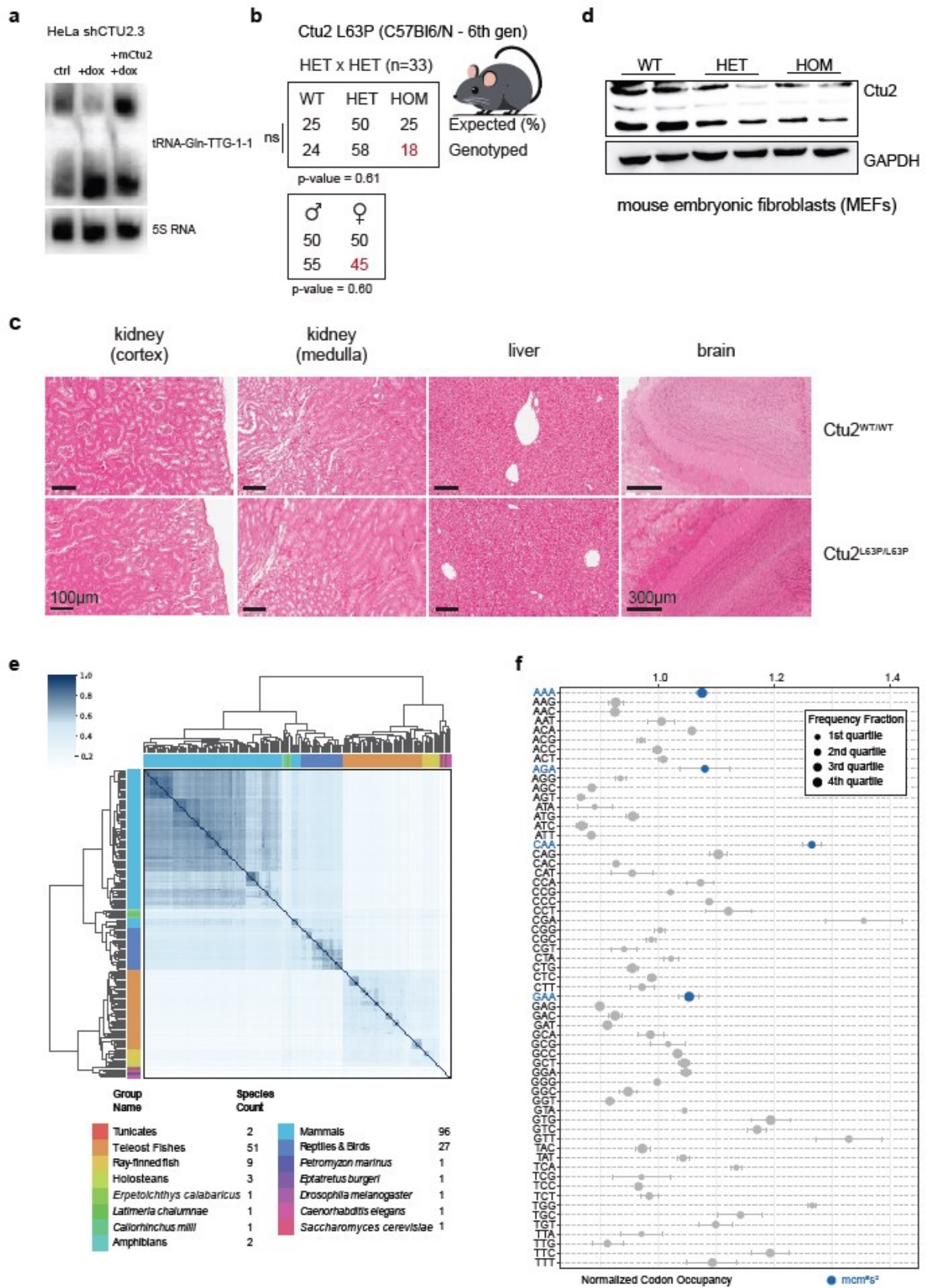
## Supplementary Fig. 5



**(a)** Analysis of centriole stainings by immunofluorescence in HeLa cells upon *CTU2*-depletion. The number and distance between centrioles, as well as the number of spindle poles during mitosis, were quantified. CEP152 (green) and CEP135 (grey) mark centrioles, and  $\gamma$ -tubulin (red) marks spindle poles.

**(b)** Representative images showing occasional multipolar spindle formation in a *CTU2*-depleted HeLa clone.

## Supplementary Fig. 6



- (a)** Cellular thiolation assay using murine CTU2 protein to modify human tRNA. tRNA<sup>Gln</sup><sub>UUG</sub> is shown representatively. 5S rRNA serves as a loading control.
- (b)** Breeding results of heterozygous *Ctu2*<sup>WT/L63P</sup> knock-in mice backcrossed for six generations to the C57Bl/6N background, born at Mendelian ratios. Chi-square goodness-of-fit test. p-values are indicated.
- (c)** Hematoxylin and eosin (H&E) staining of representative mouse organs commonly affected in DREAM-PL syndrome. Wildtype and *Ctu2*<sup>L63P/L63P</sup> mice are compared. Scale bars are indicated.
- (d)** Representative western blot analysis of CTU2 in *Ctu2*<sup>L63P/L63P</sup> mouse embryonic fibroblasts (MEFs).
- (e)** Cross-species comparison of A-ending codon frequency (AAA, GAA, CAA, AGA) in 197 species with annotated human homologs. Similarity scores were calculated using rank-biased overlap. Cluster group names and species counts are indicated below.
- (f)** Ribosome profiling in *Ctu2*<sup>L63P/L63P</sup> MEFs compared with wildtype cells. Normalized codon occupancy for all sense codons relative to wildtype is shown. n = 2 biological replicates. Respective codons of mcm<sup>5</sup>s<sup>2</sup> modified tRNAs are shown in blue.

## **METHODS**

### Cell culture

Fibroblasts (primary, MEFs) and cell lines (HeLa, hTERT-RPE1) were cultured in DMEM (Sigma, D5796), supplemented with 10% fetal bovine serum (Sigma, F7524) and 1% penicillin-streptomycin (Sigma, P4333). Cells were cultured at 37 °C and 5% CO<sub>2</sub>. STR profiling was performed for both HeLa and RPE1 (Microsynth). Cell lines were regularly tested for mycoplasma contamination by PCR.

### Western blotting

Cell pellets were lysed in RIPA buffer (50 mM Tris HCl pH8, 150 mM NaCl, 1% NP-40, 0.5% sodium deoxycholate, 0.1% SDS, 1X protease inhibitors (cOmplete EDTA-free Protease Inhibitor Cocktail, Merck). Samples were cleared and quantified using a BCA assay. 30-40µg of protein were loaded onto SDS-polyacrylamide gels (8-12%). The Mini-PROTEAN Tetra system (Bio-Rad) with Tris/Glycine/SDS buffer composition was used. A wet transfer was performed onto nitrocellulose membranes (Cytiva, GE10600002). Membranes were blocked with 5% non-fat dry milk in TBS-T. Antibodies were diluted in 1% milk in TBS-T and incubated overnight at 4°C while rotating. After washing, membranes were incubated with HRP-coupled secondary antibodies (Cell Signaling, mouse 7076, rabbit 7074) for 1 hour at room temperature. ECL Detection Reagent (Cytiva, RPN2235) was used as substrate. Chemiluminescent signal was detected on a ChemiDoc MP (Bio-Rad). When required, membranes were re-probed following antibody stripping for 2x 10 mins in mild stripping buffer (0.2M Glycine, 0.1% SDS, 1% Tween20, pH 2.2), washing and blocking.

### APM-northern blotting

RNA was isolated using TRIzol. 6µg of total RNA were loaded onto 7M urea-containing 8% polyacrylamide gels supplemented with 20µg/mL APM ([[(N-Acryloylamino)phenyl]mercuric Chloride (LGC Standards). RNA was transferred to positively charged nylon membranes (Hybond-N, Amersham) using a semi-dry apparatus. RNA was cross-linked to the membrane by UV light. Pre-hybridization was carried out in 6X SSC buffer with 10X Denhard's solution, 0.5% DMSO and 100µg/mL fish sperm (Merck) for 1 hour at 40°C while rotating. Membranes were hybridized overnight with radioactively labelled oligonucleotides (ATP, [ $\gamma$ -32P]). Following washes with SSC buffers decreasing in concentration, the membrane was wrapped in plastic and exposed to a storage phosphor screen overnight. Signal was detected with an Amersham Typhoon laser scanner (Cytiva).

Oligonucleotide sequences for human and mouse tRNAs were taken from (Lentini et al., 2018).

### Cell line generation

For CTU2 knockdown lines we utilized the GLTR system, an all-in-one lentiviral, doxycycline inducible short hairpin RNA (shRNA) expression vector (Addgene 55790, 58246). Cloning was done as described here (Sigl et al., 2014). For the constitutive overexpression of CTU2 the retroviral vector pMIG (pMSCV-IRES-GFP) was used (Addgene 9044). Lenti/Retroviral particles production was done by co-transfection with psPAX2 (Addgene 12260 – lentiviral) / gag-pol (Addgene 35614 – retroviral) and pMD2.G (both). Spin-infection was performed at 800 x g for 90 mins at 37°C. Infected cells were selected using Puromycin (GLTR) or cells were sorted by GFP signal using a Sony SH800 sorter.

### TPE-MI staining

Cells were seeded to reach 70% confluency overnight. After trypsinization and washing with PBS, cell pellets were resuspended in 50µM TPE-MI (a kind gift from Y. Hong) diluted in 50µL PBS and incubated for 30 mins at 37 °C in the incubator. Cells were washed with PBS and

analyzed with an LSR Fortessa Cell Analyzer (BD Biosciences). FCS files were analyzed using FlowJo v10.10. Statistical analysis was performed in Graphpad Prism version 10.0.3.

### AlphaFold predictions

AlphaFold 3 predictions were performed via the AlphaFold Server, using the amino acid sequences of human CTU1 (UniProt ID: Q7Z7A3), CTU2 (UniProt ID: Q2VPK5) and the sequence of tRNA<sup>Gln</sup><sub>UUG</sub> (GtRNAdb 2.0: chr6.trna179) at equal stoichiometric ratios. Structure predictions were carried out using default settings provided by the AlphaFold Server. The resulting models were inspected and used for visualization of the CTU1-CTU2-tRNA complex. Structural figures were prepared using ChimeraX software.

### Recombinant protein expression and purification

The codon-optimized ORFs of human CTU1 (UniProt ID: Q7Z7A3) and CTU2 (UniProt ID: Q2VPK5) were cloned into the pFASTBac vector to express proteins carrying N-terminal tags and a TEV-cleavage site to remove the tags. CTU1 was fused to 6xHis and Twin-Strep tags, whereas CTU2 was fused to a 6xHis tag, respectively. Mutated variants of CTU2 were generated by site-directed PCR mutagenesis using primers containing the desired mutation. Heterologous expression of the CTU1-CTU2 complex was performed using the Bac-to-Bac Baculovirus Expression System. In detail, the ORF-containing constructs were transformed into *E. coli* DH10Bac cells to generate recombinant bacmid DNA, which was subsequently transfected into Sf9 insect cells to produce recombinant baculoviruses. Individual baculoviruses and corresponding Sf9 baculovirus-infected insect cells (BiiC) were prepared separately for CTU1 and CTU2. For large-scale protein production, Hi5 cells were co-infected with CTU1 and CTU2 BiiC-derived viruses at a 1:1 virus ratio and cultured in HyClone SFM4 Insect cell medium supplemented with 0.5% fetal bovine serum (FBS) for 3 days at 27°C on a shaking platform and harvested afterwards. Cell pellets were lysed in lysis buffer (50 mM HEPES pH 7.5, 300 mM NaCl, 10% glycerol, 5 mM MgCl<sub>2</sub>, 0.1% NP-40, 1 mM TCEP supplemented with protease inhibitors cocktails and DNase I) by three freeze-thaw cycles in liquid nitrogen, followed by homogenization using an Emulsiflex C3 device (Avestin). The soluble fraction was obtained by centrifugation at 80,000 × g for 60 min. CTU1-CTU2 complexes were purified on a StrepTrap XT 5 mL affinity column (Cytiva) and eluted with elution buffer (50 mM HEPES pH 7.5, 300 mM NaCl, 5% glycerol, 1 mM TCEP, 50 mM biotin). The eluate was dialyzed overnight at 4°C against dialysis buffer (50 mM HEPES pH 7.5, 300 mM NaCl, 5% glycerol, 1 mM TCEP), using Slide-A-Lyzer dialysis cassette (Thermo Fisher Scientific). Tags were optionally cleaved with His-tagged TEV protease and removed by a second affinity purification step. Contamination and co-purifying nucleic acids were removed by using a HiTrap Heparin HP (Cytiva) affinity chromatography step. After binding the complexes were eluted with a linear gradient of heparin elution buffer (50 mM HEPES pH 7.5, 1 M KCl, 5% glycerol, 1 mM TCEP). The final eluate was concentrated using Amicon Ultra-15 centrifugal filters (30 kDa cut-off) and further separated on Superose 6 Increase 10/300 GL (Cytiva) size exclusion chromatography (SEC) column equilibrated in storage buffer (25 mM HEPES pH 7.5, 200 mM NaCl, 1 mM TCEP) to obtain pure and homogeneous protein samples. Samples were analyzed using denaturing SDS-PAGE (visualized by Coomassie Brilliant Blue) throughout all steps of the purification and complex containing SEC-fractions were pooled, concentrated, and either used for analyses or flash-frozen and stored at -80°C until further use.

### CTU2/CTU1 pull-down assays

Small scale pull-down assays were performed to evaluate expression levels, solubility, and complex formation of the human CTU1-CTU2 and mutated variants thereof. CTU1 carried an N-terminal Twin-strep tag that served as the bait protein for affinity purification of the entire complex. Hi5 insect cells (20 mL suspension cultures) were co-infected with CTU1 and CTU2 P2 baculoviruses at a 1:1 ratio and cultured under the same conditions as for large-scale expression. After three days of incubation at 27°C, cell pellets were collected and lysed by

three cycles of freezing and thawing in liquid nitrogen in lysis buffer (50 mM HEPES pH 7.5, 300 mM NaCl, 10% glycerol, 5 mM MgCl<sub>2</sub>, 0.1% NP-40, 1 mM TCEP supplemented with protease inhibitors cocktail and DNase I). Lysates were clarified by centrifugation at 20,000 × g for 15 min, and the supernatants were incubated with 20 µL of pre-washed and equilibrated in lysis buffer Strep-Tactin Sepharose beads (IBA Lifesciences), for 2h at 4°C with gentle mixing. The beads were collected by centrifugation at 500 × g for 3 min, washed three times with lysis buffer to remove non-specific proteins and resuspended in Laemmli sample buffer. Bound proteins were released by boiling at 95°C for 5 min. Protein expression, solubility, and stoichiometry of the complexes were analyzed by SDS-PAGE on Bolt™ 4-12% Bis-Tris Plus Gels (Thermo Fisher Scientific), visualized by Coomassie Brilliant Blue and documented using Chemidoc (Biorad).

### Microscale thermophoresis (MST)

Cy5-labeled, *in vitro* transcribed tRNA<sup>Gln</sup><sub>UUG</sub> at 50 nM was mixed with serially diluted purified human CTU1-CTU2 complex and mutants thereof in MST buffer (25 mM HEPES pH 7.5, 150 mM NaCl, 1 mM TCEP, 2 mM MgCl<sub>2</sub>, 0.025% Tween-20) and incubated at 20°C for 30 min. Samples were loaded into premium capillaries (MO-K025, NanoTemper Technologies) and measured using the Monolith Pico instrument (NanoTemper Technologies) equipped with MO.Control software (NanoTemper Technologies). Data from at least three independent experiments (n≥3) were analyzed with MO.Affinity Analysis software (NanoTemper Technologies), and K<sub>d</sub> values were determined based on the fitted, averaged binding curves. Graphs were plotted in OriginPro software (OriginLab).

### Transcriptomics

5x10<sup>5</sup> human dermal fibroblasts, from DREAM-PL patients or sex-matched healthy donor controls, were seeded into 10 cm dishes. After 48 hours, RNA was extracted from cultured fibroblasts using a kit according to manufacturer recommendations (Monarch Total RNA Miniprep Kit, New England Biolabs). RNA was polyA enriched and samples prepared for multiplexed. The library was sequenced on a NovaSeq X (Illumina) using paired end sequencing on an S4 flow cell with 300 cycles. Following demultiplexing, differential gene expression analysis using DEseq2 (1.18.1) was performed.

Gene Ontology (GO) enrichment analysis for biological processes was conducted with clusterProfiler (v3.6.0) using the human annotation database org.Hs.eg.db (v3.5.0). Significantly enriched GO terms were identified based on an FDR < 0.05, and visualization was performed using clusterProfiler's built-in plotting functions.

### Unfolded proteome identification

5x10<sup>5</sup> fibroblasts were seeded into 10cm dishes. After 24 hours, cells were harvested and transferred in PBS to 2 mL microcentrifuge tubes. Cells were collected, resuspended in 50µM TME in 300µL cysteine-free DMEM (Gibco, 21013024) and incubated for 30 mins at 37°C and 5% CO<sub>2</sub>. Cells were washed twice with PBS. Pellets were snap frozen in liquid nitrogen and stored at -80°C. Cell pellets were lysed for 30 mins at 37°C in lysis buffer (1x PBS, 1% SDS - Sigma, 71736, 2mM MgCl<sub>2</sub> - Invitrogen, AM9530G, 1x Protease inhibitors - Thermo, 78437, 1x Benzonase - Merck, 170746) and sonicated at 4°C (Bioruptor Pico, Diagenode, 90 sec ON – 30 sec OFF, 4 cycles). Lysates were cleared by centrifugation for 15 mins at 18.000 x g. Supernatants were transferred to lo-bind tubes (Eppendorf) and quantified (Thermo, 22660).

800µg of protein in 150µL lysis buffer were used for the Click reaction and further diluted with 450µL of potassium phosphate buffer (61.34mM K<sub>2</sub>HPO<sub>4</sub>\*3H<sub>2</sub>O - Sigma, P5504, 38.21mM KH<sub>2</sub>PO<sub>4</sub> - Sigma, P0662). Click reagents were added sequentially – biotin-PEG3-azide, freshly 1:2 mixed CuSO<sub>4</sub> - Sigma, C1297/ THPTA - Sigma, 762342, aminoguanidine HCl - Sigma, 396494, and sodium ascorbate - Roth, 3419.1 (final concentrations: 170µM, 230µM/1.15mM, 5mM, 5mM). The reaction was incubated for 1 hour at 25°C while rotating. Proteins were precipitated with ice cold acetone. The air-dried protein pellets were

resuspended in 1% SDS and resolubilized using an ultrasonic bath (Diagenode). Proteins were reduced by 4.5mM TCEP at 56°C for 1 hour while rotating, adjusted to a neutral pH and alkylated at 25°C for 30 mins using iodoacetamide. Enrichment of biotinylated proteins was done with PBS-equilibrated streptavidin-agarose beads (Thermo, 20353). Enrichment was carried out at 25°C for 1 hour while rotating. The beads were washed 16x using 8M urea in PBS. Beads were washed first with PBS then resuspended and washed with digestion buffer (50mM ammonium bicarbonate, 0.2M guanidine hydrochloride, 1mM calcium chloride, HPLC grade ddH<sub>2</sub>O). 1µg trypsin was added to each sample and left for 16 hours for off-bead digestion.

Peptides were harvested and purified using solid phase extraction. CPA and channel normalization was performed. Samples were labelled using isobaric TMTpro 16plex labels (Thermo Fisher) and pooled. On-tip high pH (10) fractionation was performed (5 fractions). 10µL were injected per fraction on an UltiMate 3000 RSLCnano system coupled to Orbitrap Fusion Lumos (Thermo Fisher), 5 x 190 min run, OTITOT (SPS-MS3 quantification). Data analysis was performed using Proteome Discoverer 2.4 SP1.

### Detection of ROS levels

The detection of ROS levels in fibroblasts was done according to manufacturer instructions (CellROX Deep Red Flow Cytometry Assay Kit, Invitrogen, C10491). Briefly, 1x10<sup>5</sup> fibroblasts were seeded to reach 70% confluency. Cells were harvested with trypsin, transferred to 1.5 mL microcentrifuge tubes, washed with PBS and resuspended in 250 µL of complete DMEM. CellROX Deep Red reagent was diluted 1:10 in DMSO and 1 µL added to each sample at a final concentration of 1µM and incubated for 30 mins at 37°C. After 15 mins 1 µL of 1:4 diluted Blue Dead Cell stain solution in PBS was added for the remaining 15 mins. Samples were acquired on an LSR Fortessa Cell Analyzer (BD Biosciences). FCS files were analyzed using FlowJo v10.10. Statistical analysis was performed in Graphpad Prism version 10.0.3.

### Annexin V

Cells were harvested and washed with PBS at relevant timepoints. Cell pellets were resuspended in 100 µL Annexin V Binding Buffer (422201, BioLegend). Samples were stained with 5 µL of FITC Annexin V antibody (640906, BioLegend) and 10 µL of propidium iodide for live cell gating (0.5 mg/mL) for 15 mins at RT in the dark. 400 µL of Annexin V Binding Buffer was added and samples were acquired on an LSR Fortessa Cell Analyzer (BD Biosciences). FCS files were analyzed using FlowJo v10.10. Statistical analysis was performed in Graphpad Prism version 10.0.3.

### Ribosome profiling

Libraries were prepared according to (Kim et. al., 2021) with minor modifications. Briefly, 3 OD<sub>260</sub> U of crude cell lysate were digested in 700µl of lysis buffer with 150U RNase I (AM2294, Invitrogen) for 1 h at 22 °C and 1400 rpm. The reaction was stopped with 5 µl of SUPERaseIn (AM2696, Invitrogen). To purify the digested monosomes, samples were separated by ultracentrifuging the extracts in a 10-50% sucrose gradient in a SW41 rotor at 35000 g for 3 h at 4 °C, and further fractionated using a Piston Gradient Fractionator (Biocomp). Monosome fractions were collected and RNA extracted from the sucrose using hot phenol/chloroform and separated by a 15 % TBE-urea gel. Subsequently ribosome protected fragments were excised from the gel. The fragments were dephosphorylated and ligated to an adaptor carrying 6 randomized positions prior to being reverse transcribed using a primer with 3 randomized positions. After cDNA synthesis, rRNA was depleted using a custom oligo pool. Finally, the depleted cDNA was circularized, and libraries were PCR-amplified and PAGE purified. Library quantification and sequencing were performed by the next generation sequencing platform of the University of Bern.

Sequencing data from ribosome profiling was pre-processed by removing the adapter and randomized nucleotides (three at the 5' end and 6 at the 3' end) using the FASTX\_toolkit

(Hannon, 2010). Non-coding reads were removed by mapping against non-coding RNA, including rRNAs, tRNAs, snoRNAs and other annotated lncRNAs using Bowtie (v1.2.3) (Langmead et al., 2009). The retained reads were mapped to all annotated open reading frames in humans (GRCh38) with unique mapping mode allowing at most one nucleotide mismatch using the parameters "-v 1 -m 1 -norc -best -strata". Codon translation speed was calculated as in (Nedialkova & Leidel, 2015) by normalizing the frequency of the A site codons to that in the +1, +2, +3 sites, followed by calculating the ratio of the translation rate between mutant and wild type. To focus the analysis on translation elongation, 15 codons were excluded at both end of the CDS.

## Proteomics

### Sample preparation - FASP + C18 cleanup

Cells were lysed in 0.4 mL lysis buffer (2% SDS, 50 mM HEPES, 1 mM PMFS, 1x protease inhibitor cocktail from Roche). Samples were resuspended and incubated at room temperature for 20 minutes before they were sonicated in a Branson ultrasonic processor with micro tip on ice (0.5 seconds on / 0.5 seconds off, 30 seconds total, 20% input). The lysate was centrifuged at 16,000 g for 10 minutes at 20°C and supernatants were transferred to a fresh tube. The protein concentration was measured with Pierce BCA Protein Assay (23227) according to manufacturer's instructions. The FASP protocol was employed for proteolytic digestion of 100 µg protein according to (Wiśniewski et al., 2009) with slight modifications. Shortly, DTT (83.3 mM) was added to the lysis buffer and incubated at 95°C for 5 minutes. Microcon 30 Ultracel YM-30 filter units were primed once with 200 µL urea buffer (8 M urea in 100 mM Tris/HCl, pH 8.5). Samples (100 µg) were loaded onto the filter units at 14,000 rcf at 20°C for 15 minutes, washed with UA solution (8 M Urea in 100 mM Tris/HCl, pH8.5). Alkylation was performed with 200 µl 50 mM Iodoacetamide in UA solution. Samples were again centrifuged (14,000 rcf, 10 minutes) after an incubation time of 30-minute incubation in the dark. Next, samples were washed twice with 100 µl UA and then twice with 100 µl 50 mM TEAB. Samples were then digested in 40 µl 50 mM TEAB, pH8.5, at a protein to enzyme ratio of 50:1. The spin columns were sealed and incubated at 37 °C overnight. On the next day, samples were spun down (14,000 rcf, 20 minutes) and the columns were washed once with 40 µL 50 mM TEAB and once with 50 µL 0.5M NaCl. The combined filtrate was acidified with 30% TFA until a pH below 3 was achieved. Samples were then subjected to C18 cleanup with Pierce™ Peptide Desalting spin columns according to manufacturer's instructions (ThermoFisher Scientific; 89851, 89852).

### Peptide quantification

Desalted peptides were reconstituted in LC-grade water, and peptide concentrations were determined using the Pierce™ Quantitative Fluorometric Peptide Assay (Thermo Fisher Scientific, 23290) according to manufacturer's instructions. Fluorescence measurements were performed on a SpectraMax® i3x Multi-Mode Microplate Reader (Molecular Devices).

### TMT labeling

Peptides were subsequently buffered to a final concentration of 50 mM HEPES, pH 8.5. Labeling was performed at a peptide concentration of  $\geq 1$  µg/µL using TMT reagent prepared in anhydrous acetonitrile at 16.7 µg/µL, applied at a TMT-to-peptide mass ratio of approximately 2:1 to 3:1. The final acetonitrile concentration during the labeling reaction was 35% (v/v). Samples were incubated for 1 hour at room temperature with gentle agitation (~600 rpm). Labeling reactions were subsequently quenched by the addition of 5% hydroxylamine solution in HEPES buffer to achieve a final hydroxylamine concentration of 0.2–0.4%, followed by incubation for 15 minutes at room temperature. Labeled peptides were pooled, dried by vacuum centrifugation, and reconstituted in 0.1% trifluoroacetic acid for subsequent processing. Labeling efficiency was routinely assessed following final analysis.

## Offline fractionation of TMT pool

Pooled TMT labelled sample was concentrated and desalted by using a Pierce Peptide Desalting Spin Columns (89851 and 89852) according to manufacturer's instructions with minor modifications: peptide elution was done in 2 steps: 40% ACN, 100mM TEAB and 70% ACN, 100 mM TEAB solution. Eluates were pooled and brought to dryness in a speedvac vacuum concentrator. Dry peptides were resuspended in 30ul 10mM ammonium formate (pH 10) and fractionated by reverse-phase chromatography at basic pH by using a Gemini-NX C18 (150 × 2 mm, 3 μm, 110 Å,) column (Phenomenex, Torrance, USA) on an Ultimate 3000 RSLC micro system (Thermo Fisher Scientific) equipped with a fraction collector. Peptides were separated at a flow rate of 50 μl/min in 10 mM ammonia formate buffer (pH 10.0) and eluted over a 70 min nonlinear gradient from 0 to 100% solvent B (90% acetonitrile, 10 mM ammonium formate, pH 10.0). Thirty-six concatenated fractions were collected in a time-based manner (at 30 s intervals) between minute 11.5 and 57. Fractions were immediately acidified by adding 5ul 30% TFA. After fractionation organics were removed in a vacuum concentrator and sample were stored at -20C until MS analysis.

## LC-ESI-MS/MS data acquisition

For MS analysis fractions were reconstituted in 150 ul 0.1% TFA and 5 μl were injected.

For proteomic data acquisition, a nanoflow LC-ESI-MS/MS setup comprised of a Dionex Ultimate 3000 RSLCnano system coupled to a Fusion Lumos mass spectrometer (both ThermoFisher Scientific) was used in positive ionization mode. MS data acquisition was performed in data-dependent acquisition (DDA) mode. For proteome analyses, peptides were delivered to a trap column (Acclaim™ PepMap™ 100 C18, 3 μm, 5 × 0.3 mm, Thermo Fisher Scientific) at a flowrate of 5 μL/min in HPLC grade water with 0.1% (v/v) TFA. After 10 min of loading, peptides were transferred to an analytical column (ReproSil Pur C18-AQ, 3 μm, Dr. Maisch, 500 mm × 75 μm, self-packed) and separated using a stepped gradient from minute 11 at 8% solvent B (0.4% (v/v) FA in 90% ACN) to minute 61 at 28% solvent B and minute 81 at 40% solvent B at 300 nL/min flow rate. The nano-LC solvent A was 0.4% (v/v) FA HPLC-grade water. MS1 spectra were recorded at a resolution of 60,000 using an automatic gain control target value of  $4 \times 10^5$  and a maximum injection time of 50 ms. The cycle time was set to 2 seconds. Only precursors with charge state 2 to 6 which fall in a mass range between 360 to 1300 Da were selected and dynamic exclusion of 30 s was enabled. Peptide fragmentation was performed using higher energy collision dissociation (HCD) and a normalized collision energy of 35%. The precursor isolation window width was set to 1.3 m/z. MS2 spectra were acquired at a resolution of 30,000 with an automatic gain control target value of  $5 \times 10^4$  and a maximum injection time of 54 ms. Using synchronous precursor selection, the top 10 fragment ions of the MS2 scans were isolated and subjected to HCD fragmentation in the linear ion trap using 55% normalized collision energy. MS3 spectra were acquired in the Orbitrap at a resolution of 50,000 over a scan range of 100 to 1000 Th, using an AGC target of  $1e5$  and a maximum injection time of 120 ms. The reagent tag type in the filer IsobaricTagExclusion was set to TMTpro.

## Data analysis

For all DDA measurements, MaxQuant (version 2.6.7.0) with its built-in search engine Andromeda was used for peptide identification and quantification (Cox et al., 2011; Tyanova, Temu, & Cox, 2016). MS2 spectra were searched against all Swiss-Prot canonical protein sequences obtained from UniProt (UP000005640, downloaded: 19 March 2025), supplemented with common contaminants (built-in option in MaxQuant). Trypsin/P was specified as the proteolytic enzyme. Precursor tolerance was set to 4.5 ppm, and fragment ion tolerance to 20 ppm. The minimal peptide length was defined as seven amino acids, and the "match-between-run" function was disabled. Quantification was performed on the MS3 level. "18plex" (TMTpro) was selected as isobaric labels and the reporter mass tolerance was set to 0.003 Da. For proteome analyses, carbamidomethylated cysteine was set as fixed

modification and oxidation of methionine and N-terminal protein acetylation as variable modifications. The FDR was set to 100%. These search results were then used as input files for oktoberfest (v.0.8.3) (Picciani et al., 2024). We performed Prosit rescoring and quantification via the picked-group-FDR approach (v.0.8.1) (Gessulat et al., 2019; The et al., 2022). The Prosit models Prosit\_2020\_irt\_TMT for retention time prediction and Prosit\_2020\_intensity\_TMT for intensity prediction were employed. The output files were filtered at 1% FDR.

Perseus was used for data analysis (Tyanova, Temu, Sinitcyn, et al., 2016). Briefly, "common contaminants", "reversed", and "only identified by site" were filtered out, intensities were log2-transformed, and median-centric normalized. Samples were then categorically annotated and the "Hawaii plot" function with default values was performed. The obtained matrix was exported for further investigations.

### Codon bias analysis

For the codon-bias analysis we ranked all human coding sequences (CDS) based on their content of AAA, GAA, CAA and AGA codons. In brief, we first downloaded a set of CDS nucleotide sequences from Ensembl (release 113) and subsequently counted the occurrences of all codons and computed the codon percentage for each CDS ( $\text{occurrence}(\text{codon}) / \text{sum}(\text{occurrences}(\text{CDS}))$ ). We then used the resulting codon frequencies to rank all CDS according to the sum of AAA, GAA, CAA and AGA codon frequencies and computed enrichments on the top 5% of the ranked CDS with gseapy's Enrichr API (Fang et al., 2023).

### Codon bias conservation analysis

All Ensembl release 113 species that had annotations of genes and their human homologs were compared with respect to their A-ending codons of interest AAA, GAA, CAA, AGA. In brief, we downloaded coding sequences (CDS) for 197 of the 310 species present in the Ensembl database release 113 and annotated the respective genes for their human homologs via Biomart using the API provided by gseapy 1.1.3. Only CDS with an annotated human homolog were retained. We then computed the percentage of A-ending codons of interest (AAA, GAA, CAA, AGA) for each coding sequence of each gene in each species. Subsequently, we utilized these data to compute species similarities by calculating the rank biased overlap of the top 10% highest ranking genes for each species (*i.e.* the top 10% of genes with the highest A-ending codon of interest content) implemented in rbo 0.1.3 (<https://github.com/changyaochen/rbo>). We then augmented this similarity matrix by clustering the accompanying Ensembl species tree with the UPGMA algorithm after pruning the tree to only contain the compared species. Finally, we plotted the resulting similarity matrix together with its species cluster annotation as a clustermap (*i.e.* rows and columns are clustered by UPGMA) using seaborn's clustermap implementation (version 0.13.2).

### Immunofluorescence

Cells were grown on coverslips and fixed in 1.5% paraformaldehyde and then in -20°C cold methanol for 4 minutes each. The samples were blocked for 1 hour in 2.5% FBS, 200 mM glycine, and 0.1% Triton X-100 in PBS and incubated with the respective primary antibodies in the same buffer for 1 hour. After washing, the cells were incubated with secondary antibodies (Invitrogen) and DAPI, washed and mounted in Prolong Gold Antifade (Life Technologies, P36930). Primary antibodies used were CEP135 (rabbit polyclonal, Alexa 555-conjugated, 1:500, (LoMastro et al., 2022)),  $\gamma$ -Tubulin (goat polyclonal, Alexa 647-conjugated, 1:500, (Levine et al., 2017)), CEP152 (rabbit polyclonal, Alexa 488-conjugated, 1:500, (LoMastro et al., 2022)), Acetyl- $\alpha$ -Tubulin (Rabbit polyclonal, Lys40 (D20G3) Cell Signaling 5335T, 1:1000). Cells were imaged using a DMi8 inverted microscope (Leica Microsystems) or a Thunder Imager (Leica Microsystems) with an Olympus 63 $\times$  1.42 NA oil objective.

## Generation of Ct<sub>u</sub>2<sup>L63P</sup> mice

The Ct<sub>u</sub>2<sup>L63P</sup> mouse strain was generated by mutating KH2 mouse embryonic stem cells *in vitro* using CRISPR/Cas9, followed by their injection into blastocysts. In brief, KH2 cells were co-electroporated with the pSpCas9(BB)-2A-GFP (PX458) vector (Addgene 48138) (Ran et al., 2013) encoding a guide RNA targeting the required locus (sgRNA: 5'GACCCGGTTCTTCCCAAGCA3') and a complementary ssDNA oligo repair template (ssDNA:

5'ACAGGGTTTGTTC AAGGCATTCTACGTT CACAAATTCcGgGcTATGCcTGGcAAGAAtC GGGTCATCTTCTCTGGGGAGAAGGTACGATGTGTGGT 3', with lowercase bases indicating mutations) (Bio-Rad GenePulse Xcell Electroporator). The repair template contained the mutation of interest and silent mutations for genotyping. GFP positive cells were sorted one day after electroporation (BD FACSAria™ III) and used to generate single cell clones. Clones were screened by PCR and validated by Sanger sequencing, before being injected into blastocysts and implanted into surrogate mothers. Germline transmission was confirmed by genotyping PCR (frw: 5'GCACGCCCTTTTCC3', rev: 5'gCCAgGCATaGCcCg3') and Sanger sequencing.

**Added retrospectively (01.12.2025)**

## Mouse Housing Conditions

Mice were specific pathogen free (SPF) according to FELASA recommendations (2014). All animals were housed in polysulfone Type IIL individually ventilated cages (Blue Line Classic, Tecniplast, Hohenpeissenberg, Germany), lined with heat-treated bedding (Lignocel Select, Rettenmaier Austria GmbH & Co. KG, Vienna, Austria) and enriched with nesting material (Pur-Zellin, Paul Hartmann GesmbH, Wiener Neudorf, Austria). Animals were maintained in a barrier rodent facility under controlled conditions (room temperature 21 ± 1 °C; relative humidity 50 ± 10%; photoperiod 12 h / light 12 h dark). Food (V1534, Ssniff Spezialdiäten GmbH, Soest, Germany) and chlorinated tap water (4 ppm) were available ad libitum.

## Ethics Statement

All animal procedures were discussed and approved by the Ethics and Animal Welfare Committee of the University of Veterinary Medicine Vienna and the national authority (Austrian Federal Ministry of Education, Science and Research) in accordance with §§ 26ff of the Austrian Animal Experiments Act (Tierversuchsgesetz 2012 – TVG 2012) under license numbers BMBWF-68.205/0010-V/3b/2019 and GZ 2025-0.597.528.

## REFERENCES

- Abbassi, N.-H., Jaciuk, M., Scherf, D., Böhnert, P., Rau, A., Hammermeister, A., Rawski, M., Indyka, P., Wazny, G., Chramiec-Głębik, A., Dobosz, D., Skupien-Rabian, B., Jankowska, U., Rappsilber, J., Schaffrath, R., Lin, T.-Y., & Glatt, S. (2024). Cryo-EM structures of the human Elongator complex at work. *Nature Communications*, *15*(1), 4094. <https://doi.org/10.1038/s41467-024-48251-y>
- Agris, P. F., Eruysal, E. R., Narendran, A., Väre, V. Y. P., Vangaveti, S., & Ranganathan, S. V. (2018). Celebrating wobble decoding: Half a century and still much is new. *RNA Biology*, *15*(4–5), 537–553. <https://doi.org/10.1080/15476286.2017.1356562>
- Alazami, A. M., Hijazi, H., Al-Dosari, M. S., Shaheen, R., Hashem, A., Aldahmesh, M. A., Mohamed, J. Y., Kentab, A., Salih, M. A., Awaji, A., Masoodi, T. A., & Alkuraya, F. S. (2013). Mutation in *ADAT3*, encoding adenosine deaminase acting on transfer RNA, causes intellectual disability and strabismus. *Journal of Medical Genetics*, *50*(7), 425–430. <https://doi.org/10.1136/jmedgenet-2012-101378>
- Al-Hamed, M. H., Kurdi, W., Khan, R., Tulbah, M., AlNemer, M., AlSahan, N., AlMugbel, M., Rafiullah, R., Assoum, M., Monies, D., Shah, Z., Rahbeeni, Z., Derar, N., Hakami, F., Almutairi, G., AlOtaibi, A., Ali, W., AlShammasi, A., AlMubarak, W., ... Imtiaz, F. (2022). Prenatal exome sequencing and chromosomal microarray analysis in fetal structural anomalies in a highly consanguineous population reveals a propensity of ciliopathy genes causing multisystem phenotypes. *Human Genetics*, *141*(1), 101–126. <https://doi.org/10.1007/s00439-021-02406-9>
- Alings, F., Scharmann, K., Eggers, C., Böttcher, B., Sokotowski, M., Shvetsova, E., Sharma, P., Roth, J., Rashiti, L., Glatt, S., Brunke, S., & Leidel, S. A. (2023). Ncs2\* mediates *in vivo* virulence of pathogenic yeast through sulphur modification of cytoplasmic transfer RNA. *Nucleic Acids Research*, gkad564. <https://doi.org/10.1093/nar/gkad564>
- Analysis of codon-specific translation by ribosome profiling. (2021). In Y. Kim, C. Eggers, E. Shvetsova, L. Kleemann, O. Sin, & S. A. Leidel, *Methods in Enzymology* (pp. 191–223). Elsevier. <https://doi.org/10.1016/bs.mie.2021.06.025>
- Bakunts, A., Orsi, A., Vitale, M., Cattaneo, A., Lari, F., Tadè, L., Sitia, R., Raimondi, A., Bachi, A., & Van Anken, E. (2017). Ratiometric sensing of BiP-client versus BiP levels by the unfolded protein response determines its signaling amplitude. *eLife*, *6*, e27518. <https://doi.org/10.7554/eLife.27518>
- Bento-Abreu, A., Jager, G., Swinnen, B., Rué, L., Hendrickx, S., Jones, A., Staats, K. A., Taes, I., Eykens, C., Nonneman, A., Nuyts, R., Timmers, M., Silva, L., Chariot, A., Nguyen, L., Ravits, J., Lemmens, R., Cabooter, D., Van Den Bosch, L., ... Robberecht, W. (2018). Elongator subunit 3 (ELP3) modifies ALS through tRNA modification. *Human Molecular Genetics*, *27*(7), 1276–1289. <https://doi.org/10.1093/hmg/ddy043>
- Birling, M.-C., Yoshiki, A., Adams, D. J., Ayabe, S., Beaudet, A. L., Bottomley, J., Bradley, A., Brown, S. D. M., Bürger, A., Bushell, W., Chiani, F., Chin, H.-J. G., Christou, S., Codner, G. F., DeMayo, F. J., Dickinson, M. E., Doe, B., Donahue, L. R., Fray, M. D., ... Murray, S. A. (2021). A resource of targeted mutant mouse lines for 5,061 genes. *Nature Genetics*, *53*(4), 416–419. <https://doi.org/10.1038/s41588-021-00825-y>
- Björk, G. R., Huang, B., Persson, O. P., & Byström, A. S. (2007). A conserved modified wobble nucleoside (mcm<sup>5</sup>s<sup>2</sup>U) in lysyl-tRNA is required for viability in yeast. *RNA*, *13*(8), 1245–1255. <https://doi.org/10.1261/rna.558707>
- Buhr, F., Jha, S., Thommen, M., Mittelstaet, J., Kutz, F., Schwalbe, H., Rodnina, M. V., & Komar, A. A. (2016). Synonymous Codons Direct Cotranslational Folding toward Different Protein Conformations. *Molecular Cell*, *61*(3), 341–351. <https://doi.org/10.1016/j.molcel.2016.01.008>

- Chan, P. P., & Lowe, T. M. (2016). GtRNADB 2.0: An expanded database of transfer RNA genes identified in complete and draft genomes. *Nucleic Acids Research*, *44*(D1), D184–D189. <https://doi.org/10.1093/nar/gkv1309>
- Chen, C., Tuck, S., & Byström, A. S. (2009). Defects in tRNA Modification Associated with Neurological and Developmental Dysfunctions in *Caenorhabditis elegans* Elongator Mutants. *PLoS Genetics*, *5*(7), e1000561. <https://doi.org/10.1371/journal.pgen.1000561>
- Chen, M. Z., Moily, N. S., Bridgford, J. L., Wood, R. J., Radwan, M., Smith, T. A., Song, Z., Tang, B. Z., Tilley, L., Xu, X., Reid, G. E., Pouladi, M. A., Hong, Y., & Hatters, D. M. (2017). A thiol probe for measuring unfolded protein load and proteostasis in cells. *Nature Communications*, *8*(1), 474. <https://doi.org/10.1038/s41467-017-00203-5>
- Cox, J., Neuhauser, N., Michalski, A., Scheltema, R. A., Olsen, J. V., & Mann, M. (2011). Andromeda: A Peptide Search Engine Integrated into the MaxQuant Environment. *Journal of Proteome Research*, *10*(4), 1794–1805. <https://doi.org/10.1021/pr101065j>
- Crick, F. H. C. (1966). Codon—anticodon pairing: The wobble hypothesis. *Journal of Molecular Biology*, *19*(2), 548–555. [https://doi.org/10.1016/S0022-2836\(66\)80022-0](https://doi.org/10.1016/S0022-2836(66)80022-0)
- DepMap, B. (2024). *DepMap 24Q4 Public* (p. 30825074613 Bytes) [Dataset]. Figshare+. <https://doi.org/10.25452/FIGSHARE.PLUS.27993248.V1>
- Dewez, M., Bauer, F., Dieu, M., Raes, M., Vandenhoute, J., & Hermand, D. (2008). The conserved Wobble uridine tRNA thiolase Ctu1–Ctu2 is required to maintain genome integrity. *Proceedings of the National Academy of Sciences*, *105*(14), 5459–5464. <https://doi.org/10.1073/pnas.0709404105>
- Durant, P. C., Bajji, A. C., Sundaram, M., Kumar, R. K., & Davis, D. R. (2005). Structural Effects of Hypermodified Nucleosides in the *Escherichia coli* and Human tRNA<sup>Lys</sup> Anticodon Loop: The Effect of Nucleosides s<sup>2</sup> U, mcm<sup>5</sup> U, mcm<sup>5</sup> s<sup>2</sup> U, mnm<sup>5</sup> s<sup>2</sup> U, t<sup>6</sup> A, and ms<sup>2</sup> t<sup>6</sup> A. *Biochemistry*, *44*(22), 8078–8089. <https://doi.org/10.1021/bi050343f>
- Elrick, H., Peterson, K. A., Willis, B. J., Lanza, D. G., Acar, E. F., Ryder, E. J., Teboul, L., Kasperek, P., Birling, M.-C., Adams, D. J., Bradley, A., Braun, R. E., Brown, S. D., Caulder, A., Codner, G. F., DeMayo, F. J., Dickinson, M. E., Doe, B., Duddy, G., ... Nutter, L. M. J. (2024). Impact of essential genes on the success of genome editing experiments generating 3313 new genetically engineered mouse lines. *Scientific Reports*, *14*(1), 22626. <https://doi.org/10.1038/s41598-024-72418-8>
- Esberg, A., Huang, B., Johansson, M. J. O., & Byström, A. S. (2006). Elevated Levels of Two tRNA Species Bypass the Requirement for Elongator Complex in Transcription and Exocytosis. *Molecular Cell*, *24*(1), 139–148. <https://doi.org/10.1016/j.molcel.2006.07.031>
- Fang, Z., Liu, X., & Peltz, G. (2023). GSEAPy: A comprehensive package for performing gene set enrichment analysis in Python. *Bioinformatics*, *39*(1), btac757. <https://doi.org/10.1093/bioinformatics/btac757>
- Gaik, M., Kojic, M., Stegeman, M. R., Öncü-Öner, T., Kościelniak, A., Jones, A., Mohamed, A., Chau, P. Y. S., Sharmin, S., Chramiec-Głąbik, A., Indyka, P., Rawski, M., Biela, A., Dobosz, D., Millar, A., Chau, V., Ünalp, A., Piper, M., Bellingham, M. C., ... Glatt, S. (2022). Functional divergence of the two Elongator subcomplexes during neurodevelopment. *EMBO Molecular Medicine*, *14*(7), e15608. <https://doi.org/10.15252/emmm.202115608>
- Gao, L., Behrens, A., Rodschinka, G., Forcelloni, S., Wani, S., Strasser, K., & Nedialkova, D. D. (2024). Selective gene expression maintains human tRNA anticodon pools during differentiation. *Nature Cell Biology*. <https://doi.org/10.1038/s41556-023-01317-3>
- Gessulat, S., Schmidt, T., Zolg, D. P., Samaras, P., Schnatbaum, K., Zerweck, J., Knaute, T., Rechenberger, J., Delanghe, B., Huhmer, A., Reimer, U., Ehrlich, H.-C., Aiche, S., Kuster, B., & Wilhelm, M. (2019). Prosit: Proteome-wide prediction of peptide tandem mass spectra by deep learning. *Nature Methods*, *16*(6), 509–518. <https://doi.org/10.1038/s41592-019-0426-7>

- Groza, T., Gomez, F. L., Mashhadi, H. H., Muñoz-Fuentes, V., Gunes, O., Wilson, R., Cacheiro, P., Frost, A., Keskivali-Bond, P., Vardal, B., McCoy, A., Cheng, T. K., Santos, L., Wells, S., Smedley, D., Mallon, A.-M., & Parkinson, H. (2023). The International Mouse Phenotyping Consortium: Comprehensive knockout phenotyping underpinning the study of human disease. *Nucleic Acids Research*, 51(D1), D1038–D1045. <https://doi.org/10.1093/nar/gkac972>
- Hannon, G. J. (2010). FASTX-toolkit: FASTQ/A short-reads pre-processing tools. *Repository Http://Hannonlab. Cshl. Edu/Fastx\_toolkit*.
- Helsmoortel, C., Vandeweyer, G., Ordoukhanian, P., Van Nieuwerburgh, F., Van Der Aa, N., & Kooy, R. F. (2015). Challenges and opportunities in the investigation of unexplained intellectual disability using family-based whole-exome sequencing. *Clinical Genetics*, 88(2), 140–148. <https://doi.org/10.1111/cge.12470>
- Hermann, J., Bortçen, T., Kalis, R., Kowar, A., Pechincha, C., Vogt, V., Schneider, M., Helm, D., Krijgsveld, J., Loayza-Puch, F., Zuber, J., & Palm, W. (2025). mTORC1 cooperates with tRNA wobble modification to sustain the protein synthesis machinery. *Nature Communications*, 16(1), 4201. <https://doi.org/10.1038/s41467-025-59185-4>
- Huang, B., Johansson, M. J. O., & Byström, A. S. (2005). An early step in wobble uridine tRNA modification requires the Elongator complex. *RNA*, 11(4), 424–436. <https://doi.org/10.1261/rna.7247705>
- Huang, B., Lu, J., & Byström, A. S. (2008). A genome-wide screen identifies genes required for formation of the wobble nucleoside 5-methoxycarbonylmethyl-2-thiouridine in *Saccharomyces cerevisiae*. *RNA*, 14(10), 2183–2194. <https://doi.org/10.1261/rna.1184108>
- Igloi, G. L. (1988). Interaction of tRNAs and of phosphorothioate-substituted nucleic acids with an organomercurial. Probing the chemical environment of thiolated residues by affinity electrophoresis. *Biochemistry*, 27(10), 3842–3849. <https://doi.org/10.1021/bi00410a048>
- Kojic, M., Abbassi, N. E. H., Lin, T.-Y., Jones, A., Wakeling, E. L., Clement, E., Nakou, V., Singleton, M., Dobosz, D., Kaliakatsos, M., Glatt, S., & Wainwright, B. J. (2023). A novel ELP1 mutation impairs the function of the Elongator complex and causes a severe neurodevelopmental phenotype. *Journal of Human Genetics*, 68(7), 445–453. <https://doi.org/10.1038/s10038-023-01135-3>
- Kojic, M., Gawda, T., Gaik, M., Begg, A., Salerno-Kochan, A., Kurniawan, N. D., Jones, A., Drożdżyk, K., Kościelniak, A., Chramiec-Głąbik, A., Hediye-Zadeh, S., Kasherman, M., Shim, W. J., Sinniah, E., Genovesi, L. A., Abrahamsen, R. K., Fenger, C. D., Madsen, C. G., Cohen, J. S., ... Wainwright, B. J. (2021). Elp2 mutations perturb the epitranscriptome and lead to a complex neurodevelopmental phenotype. *Nature Communications*, 12(1), 2678. <https://doi.org/10.1038/s41467-021-22888-5>
- Laguesse, S., Creppe, C., Nedialkova, D. D., Prévot, P.-P., Borgs, L., Huysseune, S., Franco, B., Duysens, G., Krusy, N., Lee, G., Thelen, N., Thiry, M., Close, P., Chariot, A., Malgrange, B., Leidel, S. A., Godin, J. D., & Nguyen, L. (2015). A Dynamic Unfolded Protein Response Contributes to the Control of Cortical Neurogenesis. *Developmental Cell*, 35(5), 553–567. <https://doi.org/10.1016/j.devcel.2015.11.005>
- Langmead, B., Trapnell, C., Pop, M., & Salzberg, S. L. (2009). Ultrafast and memory-efficient alignment of short DNA sequences to the human genome. *Genome Biology*, 10(3). <https://doi.org/10.1186/gb-2009-10-3-r25>
- Leiber, R.-M., John, F., Verhertbruggen, Y., Diet, A., Knox, J. P., & Ringli, C. (2010). The TOR Pathway Modulates the Structure of Cell Walls in *Arabidopsis*. *The Plant Cell*, 22(6), 1898–1908. <https://doi.org/10.1105/tpc.109.073007>
- Leidel, S., Pedrioli, P. G. A., Bucher, T., Brost, R., Costanzo, M., Schmidt, A., Aebersold, R., Boone, C., Hofmann, K., & Peter, M. (2009). Ubiquitin-related modifier Urm1 acts as a

- sulphur carrier in thiolation of eukaryotic transfer RNA. *Nature*, 458(7235), 228–232. <https://doi.org/10.1038/nature07643>
- Lentini, J. M., Ramos, J., & Fu, D. (2018). Monitoring the 5-methoxycarbonylmethyl-2-thiouridine (mcm5s2U) modification in eukaryotic tRNAs via the  $\gamma$ -toxin endonuclease. *RNA*, 24(5), 749–758. <https://doi.org/10.1261/rna.065581.118>
- Levine, M. S., Bakker, B., Boeckx, B., Moyett, J., Lu, J., Vitre, B., Spierings, D. C., Lansdorp, P. M., Cleveland, D. W., Lambrechts, D., Foijer, F., & Holland, A. J. (2017). Centrosome Amplification Is Sufficient to Promote Spontaneous Tumorigenesis in Mammals. *Developmental Cell*, 40(3), 313–322.e5. <https://doi.org/10.1016/j.devcel.2016.12.022>
- Linder, B., Sharma, P., Wu, J., Birbaumer, T., Eggers, C., Murakami, S., Ott, R. E., Fenzl, K., Vorgerd, H., Erhard, F., Jaffrey, S. R., Leidel, S. A., & Steinmetz, L. M. (2025). tRNA modifications tune m6A-dependent mRNA decay. *Cell*, 188(14), 3715–3727.e13. <https://doi.org/10.1016/j.cell.2025.04.013>
- Liu, Y., Vinyard, D. J., Reesbeck, M. E., Suzuki, T., Manakongtreecheep, K., Holland, P. L., Brudvig, G. W., & Söll, D. (2016). A [3Fe-4S] cluster is required for tRNA thiolation in archaea and eukaryotes. *Proceedings of the National Academy of Sciences*, 113(45), 12703–12708. <https://doi.org/10.1073/pnas.1615732113>
- LoMastro, G. M., Drown, C. G., Maryniak, A. L., Jewett, C. E., Strong, M. A., & Holland, A. J. (2022). PLK4 drives centriole amplification and apical surface area expansion in multiciliated cells. *eLife*, 11, e80643. <https://doi.org/10.7554/eLife.80643>
- Mahoney, D., Black, J., Dosa, N., Sakonju, A., & Lebel, R. (2023). P241: Expanding the phenotype of DREAM-PL: A case report. *Genetics in Medicine Open*, 1(1), 100269. <https://doi.org/10.1016/j.gimo.2023.100269>
- Monies, D., Vågbo, C. B., Al-Owain, M., Alhomaidi, S., & Alkuraya, F. S. (2019). Recessive Truncating Mutations in ALKBH8 Cause Intellectual Disability and Severe Impairment of Wobble Uridine Modification. *The American Journal of Human Genetics*, 104(6), 1202–1209. <https://doi.org/10.1016/j.ajhg.2019.03.026>
- Nediakova, D. D., & Leidel, S. A. (2015). Optimization of Codon Translation Rates via tRNA Modifications Maintains Proteome Integrity. *Cell*, 161(7), 1606–1618. <https://doi.org/10.1016/j.cell.2015.05.022>
- Nilsson, I., Sääf, A., Whitley, P., Gafvelin, G., Waller, C., & Von Heijne, G. (1998). Proline-induced disruption of a transmembrane  $\alpha$ -helix in its natural environment. *Journal of Molecular Biology*, 284(4), 1165–1175. <https://doi.org/10.1006/jmbi.1998.2217>
- Noma, A., Sakaguchi, Y., & Suzuki, T. (2009). Mechanistic characterization of the sulfur-relay system for eukaryotic 2-thiouridine biogenesis at tRNA wobble positions. *Nucleic Acids Research*, 37(4), 1335–1352. <https://doi.org/10.1093/nar/gkn1023>
- Pabis, M., Termathe, M., Ravichandran, K. E., Kienast, S. D., Krutyhołowa, R., Sokotowski, M., Jankowska, U., Grudnik, P., Leidel, S. A., & Glatt, S. (2020). Molecular basis for the bifunctional Uba4–Urm1 sulfur-relay system in tRNA thiolation and ubiquitin-like conjugation. *The EMBO Journal*, 39(19), e105087. <https://doi.org/10.15252/embj.2020105087>
- Picciani, M., Gabriel, W., Giurcoiu, V., Shouman, O., Hamood, F., Lautenbacher, L., Jensen, C. B., Müller, J., Kalhor, M., Soleymaniniya, A., Kuster, B., The, M., & Wilhelm, M. (2024). Oktoberfest: Open-source spectral library generation and rescoring pipeline based on ProSIT. *PROTEOMICS*, 24(8). <https://doi.org/10.1002/pmic.202300112>
- Ran, F. A., Hsu, P. D., Wright, J., Agarwala, V., Scott, D. A., & Zhang, F. (2013). Genome engineering using the CRISPR-Cas9 system. *Nature Protocols*, 8(11), 2281–2308. <https://doi.org/10.1038/nprot.2013.143>
- Ranjan, N., & Rodnina, M. V. (2017). Thio-Modification of tRNA at the Wobble Position as Regulator of the Kinetics of Decoding and Translocation on the Ribosome. *Journal of the American Chemical Society*, 139(16), 5857–5864. <https://doi.org/10.1021/jacs.7b00727>

- Rapino, F., Delaunay, S., Rambow, F., Zhou, Z., Tharun, L., De Tullio, P., Sin, O., Shostak, K., Schmitz, S., Piepers, J., Ghesquière, B., Karim, L., Charlotiaux, B., Jamart, D., Florin, A., Lambert, C., Rorive, A., Jerusalem, G., Leucci, E., ... Close, P. (2018). Codon-specific translation reprogramming promotes resistance to targeted therapy. *Nature*, *558*(7711), 605–609. <https://doi.org/10.1038/s41586-018-0243-7>
- Rapino, F., Zhou, Z., Roncero Sanchez, A. M., Joiret, M., Seca, C., El Hachem, N., Valenti, G., Latini, S., Shostak, K., Geris, L., Li, P., Huang, G., Mazzucchelli, G., Baiwir, D., Desmet, C. J., Chariot, A., Georges, M., & Close, P. (2021). Wobble tRNA modification and hydrophilic amino acid patterns dictate protein fate. *Nature Communications*, *12*(1), 2170. <https://doi.org/10.1038/s41467-021-22254-5>
- Ravichandran, K. E., Kaduhr, L., Skupien-Rabian, B., Shvetsova, E., Sokotowski, M., Krutyhotowa, R., Kwasna, D., Brachmann, C., Lin, S., Guzman Perez, S., Wilk, P., Kösters, M., Grudnik, P., Jankowska, U., Leidel, S. A., Schaffrath, R., & Glatt, S. (2022). E2 / E3 - independent ubiquitin-like protein conjugation by Urm1 is directly coupled to cysteine persulfidation. *The EMBO Journal*, *41*(20), e111318. <https://doi.org/10.15252/emj.2022111318>
- Rezgui, V. A. N., Tyagi, K., Ranjan, N., Konevega, A. L., Mittelstaet, J., Rodnina, M. V., Peter, M., & Pedrioli, P. G. A. (2013). tRNA tK<sup>UUU</sup>, tQ<sup>UUG</sup>, and tE<sup>UUC</sup> wobble position modifications fine-tune protein translation by promoting ribosome A-site binding. *Proceedings of the National Academy of Sciences*, *110*(30), 12289–12294. <https://doi.org/10.1073/pnas.1300781110>
- Schlieker, C. D., Van Der Veen, A. G., Damon, J. R., Spooner, E., & Ploegh, H. L. (2008). A functional proteomics approach links the ubiquitin-related modifier Urm1 to a tRNA modification pathway. *Proceedings of the National Academy of Sciences*, *105*(47), 18255–18260. <https://doi.org/10.1073/pnas.0808756105>
- Shaaban, A. I., Lotfy, F. M., Alharbi, M. S., Zaky, A. F., Al Sari, R. R., Mattar, R. K., Al Mubarak, H. A., Jama, A., Mousa, S. M., Borah, N. A., Alshami, F. M., Afandy, F. F., & Fadda, S. H. (2024). Extensive Phenotypic Variability in Syndrome Dysmorphic Facies, Renal Agenesis, Ambiguous Genitalia, Microcephaly, Polydactyly, and Lissencephaly (DREAM-PL): A Case Report Highlighting Diagnostic and Management Challenges. *Cureus*. <https://doi.org/10.7759/cureus.54043>
- Shaheen, R., Al-Salam, Z., El-Hattab, A. W., & Alkuraya, F. S. (2016). The syndrome dysmorphic facies, renal agenesis, ambiguous genitalia, microcephaly, polydactyly and lissencephaly (DREAM-PL): Report of two additional patients. *American Journal of Medical Genetics Part A*, *170*(12), 3222–3226. <https://doi.org/10.1002/ajmg.a.37877>
- Shaheen, R., Mark, P., Prevost, C. T., AlKindi, A., Alhag, A., Estwani, F., Al-Sheddi, T., Alobeid, E., Alenazi, M. M., Ewida, N., Ibrahim, N., Hashem, M., Abdulwahab, F., Bryant, E. M., Spinelli, E., Millichap, J., Barnett, S. S., Kearney, H. M., Accogli, A., ... Alkuraya, F. S. (2019). Biallelic variants in *CTU2* cause DREAM-PL syndrome and impair thiolation of tRNA wobble U34. *Human Mutation*, *40*(11), 2108–2120. <https://doi.org/10.1002/humu.23870>
- Shaheen, R., Patel, N., Shamseldin, H., Alzahrani, F., Al-Yamany, R., Al Moisher, A., Ewida, N., Anazi, S., Alnemer, M., Elsheikh, M., Alfaleh, K., Alshammari, M., Alhashem, A., Alangari, A. A., Salih, M. A., Kircher, M., Daza, R. M., Ibrahim, N., Wakil, S. M., ... Alkuraya, F. S. (2016). Accelerating matchmaking of novel dysmorphology syndromes through clinical and genomic characterization of a large cohort. *Genetics in Medicine*, *18*(7), 686–695. <https://doi.org/10.1038/gim.2015.147>
- Shigi, N. (2014). Biosynthesis and functions of sulfur modifications in tRNA. *Frontiers in Genetics*, *5*. <https://doi.org/10.3389/fgene.2014.00067>

- Sigl, R., Ploner, C., Shivalingaiah, G., Kofler, R., & Geley, S. (2014). Development of a Multipurpose GATEWAY-Based Lentiviral Tetracycline-Regulated Conditional RNAi System (GLTR). *PLoS ONE*, 9(5), e97764. <https://doi.org/10.1371/journal.pone.0097764>
- Simpson, C. L., Lemmens, R., Miskiewicz, K., Broom, W. J., Hansen, V. K., Van Vught, P. W. J., Landers, J. E., Sapp, P., Van Den Bosch, L., Knight, J., Neale, B. M., Turner, M. R., Veldink, J. H., Ophoff, R. A., Tripathi, V. B., Beleza, A., Shah, M. N., Proitsi, P., Van Hoecke, A., ... Al-Chalabi, A. (2009). Variants of the elongator protein 3 ( ELP3 ) gene are associated with motor neuron degeneration. *Human Molecular Genetics*, 18(3), 472–481. <https://doi.org/10.1093/hmg/ddn375>
- Slaugenhaupt, S. A., Blumenfeld, A., Gill, S. P., Leyne, M., Mull, J., Cuajungco, M. P., Liebert, C. B., Chadwick, B., Idelson, M., Reznik, L., Robbins, C. M., Makalowska, I., Brownstein, M. J., Krappmann, D., Scheidereit, C., Maayan, C., Axelrod, F. B., & Gusella, J. F. (2001). Tissue-Specific Expression of a Splicing Mutation in the Gene Causes Familial Dysautonomia. *The American Journal of Human Genetics*, 68(3), 598–605. <https://doi.org/10.1086/318810>
- Sokołowski, M., Kwasna, D., Ravichandran, K. E., Eggers, C., Krutyhotowa, R., Kaczmarczyk, M., Skupien-Rabian, B., Jaciuk, M., Walczak, M., Dahate, P., Pabis, M., Jemioła-Rzemińska, M., Jankowska, U., Leidel, S. A., & Glatt, S. (2024). Molecular basis for thiocarboxylation and release of Urm1 by its E1-activating enzyme Uba4. *Nucleic Acids Research*, 52(22), 13980–13995. <https://doi.org/10.1093/nar/gkac1111>
- Songe-Møller, L., Van Den Born, E., Leihne, V., Vågbø, C. B., Kristoffersen, T., Krokan, H. E., Kirpekar, F., Falnes, P. Ø., & Klungland, A. (2010). Mammalian ALKBH8 Possesses tRNA Methyltransferase Activity Required for the Biogenesis of Multiple Wobble Uridine Modifications Implicated in Translational Decoding. *Molecular and Cellular Biology*, 30(7), 1814–1827. <https://doi.org/10.1128/MCB.01602-09>
- Strug, L. J., Clarke, T., Chiang, T., Chien, M., Baskurt, Z., Li, W., Dorfman, R., Bali, B., Wirrell, E., Kugler, S. L., Mandelbaum, D. E., Wolf, S. M., McGoldrick, P., Hardison, H., Novotny, E. J., Ju, J., Greenberg, D. A., Russo, J. J., & Pal, D. K. (2009). Centrotemporal sharp wave EEG trait in rolandic epilepsy maps to Elongator Protein Complex 4 (ELP4). *European Journal of Human Genetics*, 17(9), 1171–1181. <https://doi.org/10.1038/ejhg.2008.267>
- Szklarczyk, D., Kirsch, R., Koutrouli, M., Nastou, K., Mehryary, F., Hachilif, R., Gable, A. L., Fang, T., Doncheva, N. T., Pyysalo, S., Bork, P., Jensen, L. J., & von Mering, C. (2023). The STRING database in 2023: Protein–protein association networks and functional enrichment analyses for any sequenced genome of interest. *Nucleic Acids Research*, 51(D1), D638–D646. <https://doi.org/10.1093/nar/gkac1000>
- The International Mouse Phenotyping Consortium, Dickinson, M. E., Flenniken, A. M., Ji, X., Teboul, L., Wong, M. D., White, J. K., Meehan, T. F., Weninger, W. J., Westerberg, H., Adissu, H., Baker, C. N., Bower, L., Brown, J. M., Caddle, L. B., Chiani, F., Clary, D., Cleak, J., Daly, M. J., ... Murray, S. A. (2016). High-throughput discovery of novel developmental phenotypes. *Nature*, 537(7621), 508–514. <https://doi.org/10.1038/nature19356>
- The, M., Samaras, P., Kuster, B., & Wilhelm, M. (2022). Reanalysis of ProteomicsDB Using an Accurate, Sensitive, and Scalable False Discovery Rate Estimation Approach for Protein Groups. *Molecular & Cellular Proteomics*, 21(12), 100437. <https://doi.org/10.1016/j.mcpro.2022.100437>
- Tsherniak, A., Vazquez, F., Montgomery, P. G., Weir, B. A., Kryukov, G., Cowley, G. S., Gill, S., Harrington, W. F., Pantel, S., Krill-Burger, J. M., Meyers, R. M., Ali, L., Goodale, A., Lee, Y., Jiang, G., Hsiao, J., Gerath, W. F. J., Howell, S., Merkel, E., ... Hahn, W. C. (2017). Defining a Cancer Dependency Map. *Cell*, 170(3), 564–576.e16. <https://doi.org/10.1016/j.cell.2017.06.010>

- Tükenmez, H., Xu, H., Esberg, A., & Byström, A. S. (2015). The role of wobble uridine modifications in +1 translational frameshifting in eukaryotes. *Nucleic Acids Research*, 43(19), 9489–9499. <https://doi.org/10.1093/nar/gkv832>
- Tyanova, S., Temu, T., & Cox, J. (2016). The MaxQuant computational platform for mass spectrometry-based shotgun proteomics. *Nature Protocols*, 11(12), 2301–2319. <https://doi.org/10.1038/nprot.2016.136>
- Tyanova, S., Temu, T., Sinitcyn, P., Carlson, A., Hein, M. Y., Geiger, T., Mann, M., & Cox, J. (2016). The Perseus computational platform for comprehensive analysis of (prote)omics data. *Nature Methods*, 13(9), 731–740. <https://doi.org/10.1038/nmeth.3901>
- Vendeix, F. A. P., Murphy, F. V., Cantara, W. A., Leszczyńska, G., Gustilo, E. M., Sproat, B., Malkiewicz, A., & Agris, P. F. (2012). Human tRNALys3UUU Is Pre-Structured by Natural Modifications for Cognate and Wobble Codon Binding through Keto–Enol Tautomerism. *Journal of Molecular Biology*, 416(4), 467–485. <https://doi.org/10.1016/j.jmb.2011.12.048>
- Walker, J., Kwon, S. Y., Badenhorst, P., East, P., McNeill, H., & Svejstrup, J. Q. (2011). Role of Elongator Subunit Etp3 in *Drosophila melanogaster* Larval Development and Immunity. *Genetics*, 187(4), 1067–1075. <https://doi.org/10.1534/genetics.110.123893>
- Waters, A. M., & Beales, P. L. (2011). Ciliopathies: An expanding disease spectrum. *Pediatric Nephrology*, 26(7), 1039–1056. <https://doi.org/10.1007/s00467-010-1731-7>
- Wiśniewski, J. R., Zougman, A., Nagaraj, N., & Mann, M. (2009). Universal sample preparation method for proteome analysis. *Nature Methods*, 6(5), 359–362. <https://doi.org/10.1038/nmeth.1322>
- Wu, J., Eggers, C., Sin, O., Koziej, Ł., Mancilla, H., Mollet, F., Schöler, H. R., Drexler, H., Ranff, T., Fufezan, C., Kraft, C., Glatt, S., Bruder, J. M., & Leidel, S. A. (n.d.). *Codon Pair-Specific Translation Defects Trigger Ribosome-Associated Quality Control to Avoid Proteotoxic Stress*.
- Xu, Y., Zhang, L., Ou, S., Wang, R., Wang, Y., Chu, C., & Yao, S. (2020). Natural variations of SLG1 confer high-temperature tolerance in indica rice. *Nature Communications*, 11(1), 5441. <https://doi.org/10.1038/s41467-020-19320-9>
- Yoshida, M., Kataoka, N., Miyauchi, K., Ohe, K., Iida, K., Yoshida, S., Nojima, T., Okuno, Y., Onogi, H., Usui, T., Takeuchi, A., Hosoya, T., Suzuki, T., & Hagiwara, M. (2015). Rectifier of aberrant mRNA splicing recovers tRNA modification in familial dysautonomia. *Proceedings of the National Academy of Sciences*, 112(9), 2764–2769. <https://doi.org/10.1073/pnas.1415525112>
- Zhang, S., Owyong, T. C., Sanislav, O., Englmaier, L., Sui, X., Wang, G., Greening, D. W., Williamson, N. A., Villunger, A., White, J. M., Heras, B., Wong, W. W. H., Fisher, P. R., & Hong, Y. (2025). Global analysis of endogenous protein disorder in cells. *Nature Methods*, 22(1), 124–134. <https://doi.org/10.1038/s41592-024-02507-z>
- Zinshteyn, B., & Gilbert, W. V. (2013). Loss of a Conserved tRNA Anticodon Modification Perturbs Cellular Signaling. *PLoS Genetics*, 9(8), e1003675. <https://doi.org/10.1371/journal.pgen.1003675>

## 2.2. Extended Results (Zebrafish)

To investigate the essentiality of tRNA thiolation in another major vertebrate species, apart from humans and mice, and to investigate possible organ-specific impact upon its dysfunction, we decided to study the loss of *urm1*, *ctu1* and *ctu2* also in zebrafish (*Danio rerio*).

## 2.3. Methods (Zebrafish)

Knockout fish lines were generated using a dual-guide CRISPR-Cas9 strategy. Single guide RNAs (sgRNAs) were designed to target specific genomic loci, the alteration of which would abrogate protein function (**Table 3**). Distinct targeting strategies were employed. For *urm1*, two sgRNAs were selected to specifically excise a region of 437 base pairs (bps) that contained Exon 1 and the translation initiation start codon (ATG). If successful, this prevents the synthesis of the Urm1 protein entirely. For *ctu1* and *ctu2*, sgRNAs were designed to remove large DNA fragments – 4.500 (Exon 2-3) and 22.000 (Exons 1-12) bps, respectively – that would introduce frameshift mutations or in case of in-frame repair would render the truncated protein dysfunctional.

Gene	sgRNA 1	sgRNA 2
<i>Urm1</i>	ACGCCCTCTCCGGTAAAATG	GCTGTGCGCGGCATTTGGAG
<i>Ctu1</i>	CCGGACTCTTTAATCGTGGA	CAAAGACCTGGAGTCCGTCA
<i>Ctu2</i>	GGAAGAGGATTATAATGGTC	GGGGTCTGTGGATCTAGTGG

**Table 3.** Single guide RNA (sgRNA) sequences used to create thiolation-null zebrafish lines

Embryos at the 1-cell stage were injected with a KCl-buffered master mix containing sgRNAs (25  $\mu$ M, Integrated DNA Technologies), Cas9 protein (25  $\mu$ M, IDT) and phenol-red using a standard microinjector and micromanipulator. At 24 hours post-fertilization, embryos were screened to validate the efficiency of the CRISPR-Cas9 editing. Genomic DNA was extracted from a subset of injected embryos, and the target loci amplified via PCR. Mutagenesis efficiency was assessed using the T7 Endonuclease assay. This assay detects heteroduplex DNA formed by the re-annealing of wildtype and mutated strands. The T7 endonuclease specifically cleaves mismatched DNA strands resulting from insertions or deletions introduced during the repair of double strand breaks. This fragmented bands pattern is visible on an agarose gel and is clearly distinguishable from an unedited DNA region that would run a single, sharp band. Following confirmation of editing activity, the remaining F0 siblings were raised to sexual maturity. These mosaic founder fish were subsequently out-crossed with wildtype zebrafish to eliminate potential off-target effects and to screen for germline transmission of the

mutations. F1 offspring were individually genotyped to identify heterozygous carriers, thereby establishing stable *urm1*, *ctu1*, and *ctu2* mutant lines for subsequent phenotypic analysis.

## 2.4. Results (Zebrafish)

Heterozygous fish did not show any overt phenotype. To test whether homozygous animals were viable or would recapitulate features of DREAM-PL syndrome, breeding of heterozygous animals were set up. Genotyping of the adult offspring confirmed the presence of homozygous mutants for all three genotypes (*urm1*<sup>-/-</sup>, *ctu1*<sup>-/-</sup>, *ctu2*<sup>-/-</sup>), albeit at much lower rates than expected from mammalian ratios. Contrary to expectations regarding the essential physiological role of tRNA thiolation, the homozygous null-mutants survived to adulthood. However, these animals were significantly smaller than wildtype and heterozygous counterparts (**Fig. 6**).

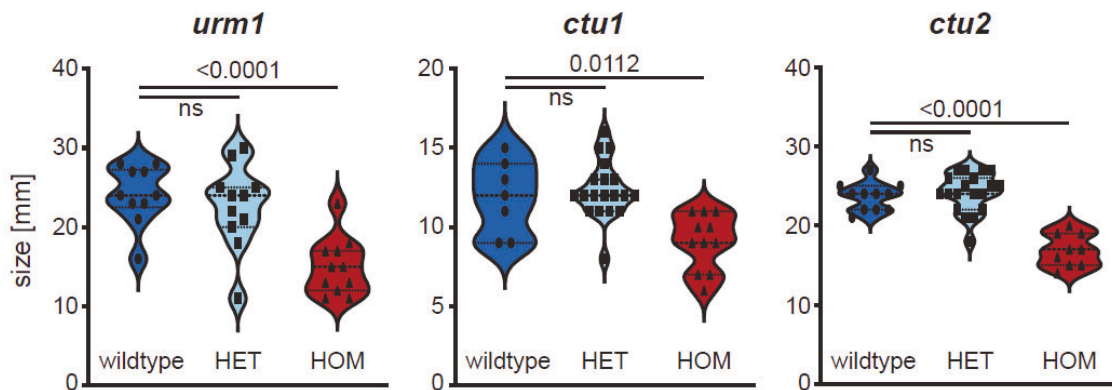


**Figure 6. Homozygous thiolation-incompetent mutants exhibit significantly reduced somatic growth.** Quantification of body length in adult zebrafish at 3 months post-fertilization (*urm1*, *ctu2*) and 1 month post-fertilization (*ctu1*). Homozygous knockout mutants are significantly smaller compared to wildtype and heterozygous siblings. Statistical significance was determined using an unpaired two-tailed Student's t-test, p-values are indicated.

RNA was extracted from these animals to validate the absence of tRNA thiolation using APM-Northern blotting (see Methods in manuscript above). Still surprisingly, this analysis confirmed the complete absence of tRNA thiolation in homozygous mutants (**Fig. 7**). Next, we performed mRNA sequencing (RNAseq) of *ctu1* mutants and wildtype littermates. Strikingly, several GO terms that describe groups of downregulated mRNAs described mitosis-related processes, such as mitotic sister chromatid segregation, cytoskeleton organization in mitosis and chromosome condensation (**Fig. 8**).

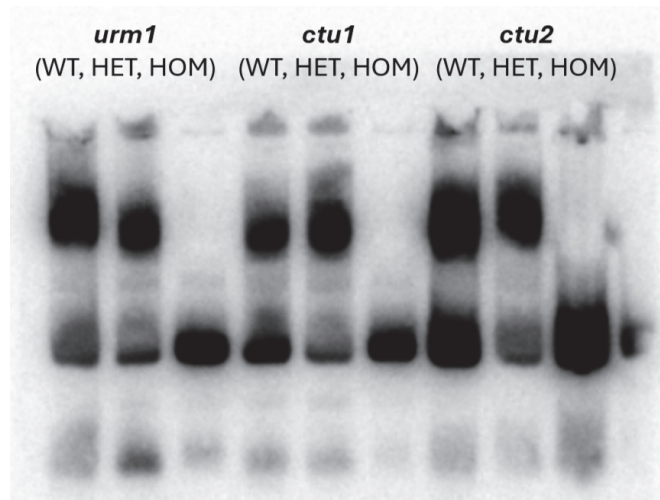


**Figure 7. Loss of tRNA thiolation in mutants confirmed by APM-Northern blotting.** Total RNA was isolated from adult wildtype (WT), heterozygous (HET), and homozygous mutant (HOM) zebrafish and separated on an APM-containing polyacrylamide gel. Thiolated tRNAs (upper band) migrate slower in the gel matrix. Homozygous mutants display a complete shift to the non-thiolated species (lower band), indicating the functional ablation of the tRNA thiolation machinery.

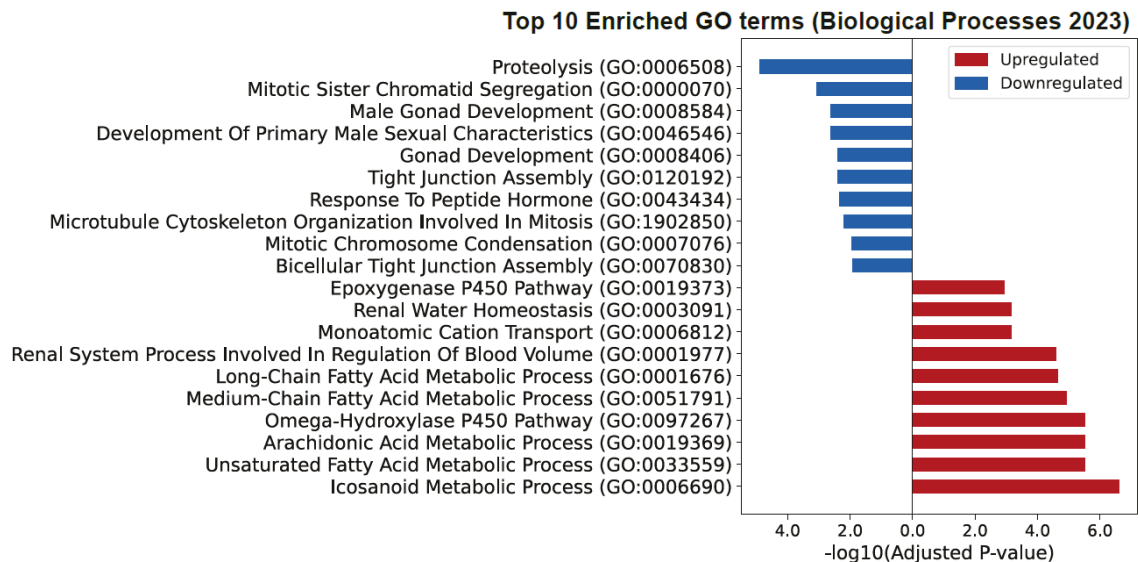


**Figure 8. Transcriptional downregulation of mitotic pathways in ctu1 knockout zebrafish.** Gene Ontology (GO) enrichment analysis of differentially expressed genes identified by RNAseq in ctu1 knockout compared to wildtype controls. The top 10 significantly downregulated (blue) and upregulated (red) biological process terms are shown. Bars represent the statistical significance of enrichment.

As these terms recapitulated our human thiolation-dependency pathway analysis quite well (see Results in manuscript above), we investigated whether loss of thiolation in fish functionally impacted ciliogenesis, a process closely linked to mitosis because cilia are anchored at centrioles, the organizers of microtubules. However, when visualizing cilia by

staining them with an acetylated  $\alpha$ -tubulin antibody, we found no changes in number or length (Fig. 9).

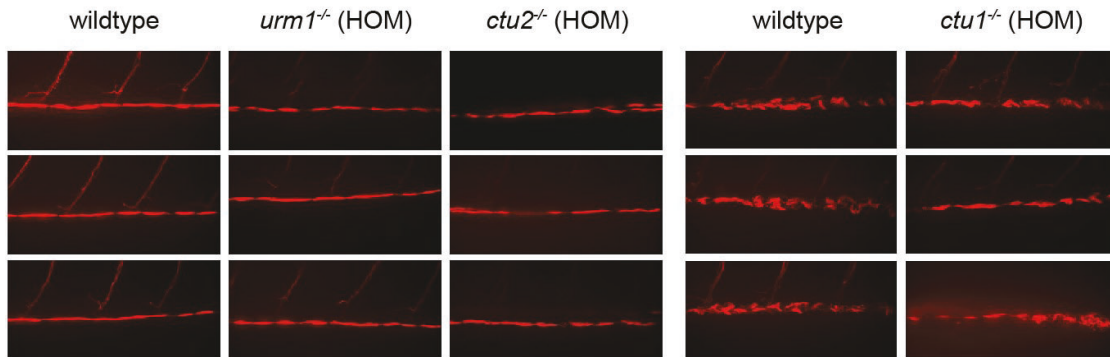


**Figure 9. Loss of tRNA thiolation does not markedly affect cilia formation in the pronephric duct.** Immunofluorescence stainings of  $\alpha$ -acetylated tubulin (red) in pronephric ducts. Representative images of biological triplicates are shown for homozygous *urm1*, *ctu1*, and *ctu2* knockout fish compared to wildtype littermates (left wildtype is an *urm1* littermate). No apparent differences in ciliation or duct structure was observed across genotypes.

## 2.5. Discussion (Zebrafish)

As we had previously found in mice, zebrafish do not depend on tRNA thiolation of wobble uridines for development or survival into adulthood. Compared to mice, however, thiolation-null zebrafish show stunted growth, which is in line with RNAseq data suggesting reduced cell division. Whether this growth defect stems directly from reduced translation efficiency of mitosis-related mRNAs enriched in thiolation-dependent codons remains to be investigated. Ribosomal stalling on these transcripts could trigger quality-control-mediated decay, explaining their downregulation. Future work will be needed to uncover why zebrafish are resilient to loss of thiolation, be it through shifted codon usage, rewired tRNA expression, or a yet unknown compensatory mechanism.

## 2.6. Acknowledgements (Zebrafish)

*Zebrafish models were planned in close collaboration with Univ.-Prof. Dr. Dirk Meyer's research group at the Leopold-Franzens Universität, Innsbruck (LFU). Animals were established, screened and studied by Sonja Töchterle, BSc. I thank them both, especially Sonja, for the exciting collaboration. Data acquisition for figures 6 and 9 was done by S.T., Fig. 7 and 8 by the author of this thesis.*

# **Chapter three**

### 3. Discussion

#### 3.1. DREAM-PL pathogenesis and ciliopathies: similarities and differences

Defective ciliogenesis or abrogated cilia-initiated signaling emerged as likely disease-causing events, due to the ciliopathy-like clinical patient presentation of DREAM-PL patients (*i.e.* microcephaly, polydactyly, kidney development). The highly biased mRNA codon-content (AAA/CAA/GAA/AGA) in structural and functional ciliogenesis genes, and our functional validation studies confirm reduced ciliation capacity in patient and murine model fibroblasts, which supports this concept. Impairment of primary cilia affects the development of both the brain and kidney (Hildebrandt *et al*, 2011). Molecularly this is explained by decreased sensing of morphogens such as Sonic hedgehog or WNT by cilia.

Nevertheless, additional candidate pathways may underly DREAM-PL syndrome. Kinetochore organization, mitotic spindle organization, mitotic microtubule organization and mitotic sister chromatid segregation all describe mitosis-related events centered around a function mitotic spindle assembly and functional centrosome. Indeed, HeLa cells acutely depleted of *CTU2* showed multiple instances of multipolar spindles and mitotic defects when analyzed by immunofluorescence imaging, staining for pericentriolar material ( $\gamma$ -tubulin) and centrioles (CEP135, CEP152). This should be investigated in more detail, as phenotypes like microcephaly and renal agenesis could be explained also by defects in cell division. In this context it is interesting to note that post-mitotic neurons seem to be particularly affected by the loss of tRNA thiolation. However rather than neuronal cell death, mitotic defects in precursors could explain microcephaly and lissencephaly.

#### 3.2. Species-specific divergence in the essentiality of tRNA thiolation

##### 3.2.1. Zebrafish

In light of our findings in zebrafish, the longstanding assumption that tRNA thiolation is essential for vertebrate development and survival needs to be challenged. Clearly, in zebrafish tRNA thiolation is not essential in a strict sense, as a full-body knockout (KO) of the modification machinery (*urm1*, *ctu1* and *ctu2*) is tolerated – albeit at the cost of a reduced body size. It is possible, maybe even likely, that these fish mutants have additional phenotypes. Interestingly, we did not see 25% homozygous offspring as expected from Mendelian inheritance, when breeding heterozygous animals of either genotype. This does suggest a negative impact of tRNA thiolation loss on the development of at least a subset of fish embryos.

This is indicative of a “developmental bottleneck”, which allows embryogenesis to complete once it is passed. In support of this, a recent study using morpholino antisense oligonucleotides targeting *ctu1* in zebrafish embryos found different developmental and adult phenotypes, ranging from enlarged brain ventricles and spine deformities, to angiogenesis defects and upregulated cell cycle genes (Yu *et al*, 2024). It is interesting that these fish with a transient antisense oligo-based *ctu1* knockdown (KD) were found to be more severely impacted than those with a CRISPR-Cas9 based full-body gene ablation. The authors did not quantify modification loss by northern blotting or mass spectrometry, which would have been valuable for comparison. It is possible that a morpholino strategy is a more rapid one, as injected Cas9 mRNA would need minutes to hours to be translated, before genetic editing can take place. Another explanation could be that full loss-of-function forces the developing organism to compensate by alternative means, while hypomethylation may not. It is interesting that the full KO that we generated shows reduced cell cycle gene expression at the mRNA level, whereas the opposite is reported upon KD. Theoretically, both morpholino and single-guide RNAs may have off-target effects explaining phenotypes, but as we targeted all three genes at the core thiolation pathway individually, *urm1*, *ctu1* and *ctu2*, this appears unlikely.

### 3.2.2. Mice

At the start of this project, several strategies of creating a DREAM-PL mouse model were considered. We opted against trying to establish a full-body *Ctu2* KO mouse, because of available data by the International Mouse Phenotyping Consortium (IMPC) ([www.mousephenotype.org](http://www.mousephenotype.org)) (Birling *et al*, 2021; Elrick *et al*, 2024; Groza *et al*, 2023; The International Mouse Phenotyping Consortium *et al*, 2016). This multi-center consortium seeks to study and describe the function of every protein-coding gene in the mouse by generating individual knockout animals. The KO of *Urm1*, *Ctu1* and *Ctu2* mice had been attempted by the IMPC, either through inserting a large cassette with a LacZ reporter and antibiotic resistance into mouse embryonic stem cells (mESCs) that disrupts the locus of interest (*Ctu2*), or by injecting sgRNAs and Cas9 directly into zygotes (*Urm1*, *Ctu1*) – analogous to our KO zebrafish. All mice were viable in the heterozygous state, with only a handful showing mild phenotypes in organ development or hematopoiesis, most notably an accumulation of eosinophils and basophils in heterozygous *Ctu2* KO animals. However, as no homozygous pups were recovered at the time of weaning, this genotype was classified as pre-weaning lethal with complete penetrance. Homozygous *Urm1* KO mice were even analyzed *in utero* and reported to show embryonic lethality at E12.5.

Consequently, we were left with two strategies, a conditional allele that would allow the mice to complete development before eliminating gene function in adulthood, and a knock-in allele with a predicted pathogenic mutation that would likely alter protein function and recapitulate a disease phenotype but allow for survival. To mitigate the risk of failure, we designed both a synthetic DNA locus with LoxP site-flanked *Ctu2* exon 3 to be introduced into zygotes by CRISPR-Cas9 and homologous recombination, as well as following the more conventional approach of knocking-in a DREAM-PL patient mutation by CRISPR-Cas9 into mESCs to be injected into blastocysts. The conditional allele strategy failed, as the synthetic construct was not incorporated into electroporated zygotes, likely because of the failure of one of the two sgRNAs used to exercise the endogenous locus. The DREAM-PL *Ctu2*<sup>L63P</sup> model was successfully established as described in the manuscript above. While tRNA thiolation was severely impacted, the mice however did not show other phenotypes reminiscent of DREAM-PL syndrome. The leucine-to-proline mutation at position 63 was chosen, because it was the only recurrently reported pathogenic point mutation in 3 patients (Helsmoortel *et al*, 2015; Shaheen *et al*, 2019, unpublished). Due to species-specific splicing events and diverging sequence contexts, we did not attempt to knock-in splice-site mutations.

The *Ctu2*<sup>L63P</sup> line, originally generated from mixed 129/Sv mESCs injected into C57BL/6 blastocysts, was backcrossed for six generations to establish a congenic C57BL/6N strain to eliminate confounding effects. However, also on a 99.22% BL/6N background, these mice showed no apparent phenotypic abnormalities, despite strongly reduced tRNA thiolation. Comparing these mouse models to zebrafish KOs, the lack of phenotypes could be explained by *Ctu2*<sup>L63P</sup> being a hypomorphic allele. The functional threshold of CTU2 required to maintain the modified tRNA pool, without triggering proteostasis defects, is unknown but appears to be quite low. Apart from a single report (Barrak *et al*, 2024), every DREAM-PL patient carried bi-allelic mutations, and every heterozygous mouse or zebrafish investigated throughout this project showed tRNA thiolation levels comparable to wildtype controls, confirming that 50% of the protein can sustain 100% of the thiolated pool. Since sulfur substitution at the wobble uridine represents the final step in a long enzymatic cascade, sulfur allocation likely prioritizes essential upstream pathways, such as reactive oxygen species detoxification via the glutathione system. However, if a minimal flux of sulfur is sufficient to sustain translational demands, this low threshold confers a distinct survival advantage. Given the combined carrier frequency of 1 in 871 of the two most common DREAM-PL mutations, but the very low disease incidence, these are not dominant-negative.

Intriguingly, and contrasting the observed pre-weaning lethality of mice lacking CTU1, CTU2 or URM1, a viable whole-body knockout mouse for ALKBH8, the methyltransferase completing the 5-methoxycarbonylmethyl modification of wobble uridine (mcm<sup>5</sup>), has been reported

(Songe-Møller *et al*, 2010). *Alkbh8* KO mice established by the IMPC were also viable, with the notable observation of abnormal kidney morphology in one tested animal, possibly representing a mild DREAM-PL phenotype (The International Mouse Phenotyping Consortium *et al*, 2016). In vertebrates, *mcm*<sup>5</sup> is a prerequisite of thiolation, requiring both a functional Elongator complex and ALKBH8 activity. Consequently, *Alkbh8*-null mice lack tRNA thiolation (Songe-Møller *et al*, 2010). The same is true for patients with bi-allelic *ALKBH8* mutations (Monies *et al*, 2019) (APM-northern blot data not shown by the authors). Apart from minor decreases in selenocysteine incorporation, these mice are healthy, although no long-term follow-up was conducted. It is possible that these animals show the same propensity to aging-specific loss of tissue homeostasis as *Ctu2*<sup>L63P/L63P</sup> mice.

Cumulatively, data from vertebrate models deficient in tRNA thiolation suggest that the mechanisms underlying DREAM-PL syndrome are either not evolutionarily conserved or efficiently compensated for in other species. The establishing of a conditional *Ctu1* or *Ctu2* knockout allele will be instrumental in answering this question.

### 3.3. Genomic architecture and physiological regulation of thiolated tRNAs

#### 3.3.1. Genomic redundancy and tRNA overexpression

The overexpression of exogenous tRNA genes has been one compensation or rescue strategy that is repeatedly employed in mutant *S. cerevisiae* that lack *mcm*<sup>5s2</sup> is (Bruch *et al*, 2020; Esberg *et al*, 2006; Leidel *et al*, 2009; Rezgui *et al*, 2013; Tyagi & Pedrioli, 2015). While the subsequently transcribed tRNAs are unmodified, their increased abundance normalizes translation dynamics, likely via mass action where ribosomal A-site rejection is compensated for by increasing the sampling frequency of these unmodified exogenous tRNAs. This results in the rescue of growth defects and even eliminates protein aggregation in yeast mutants (Nedialkova & Leidel, 2015). Ribosome pausing phenomena are often most severe on the AAA codon, which forms the weakest possible interaction when pairing with its UUU anticodon as it relies on the fewest possible hydrogen bonds. Intriguingly, some studies have found that solely overexpressing *Lys*<sup>UUU</sup> is sufficient to alleviate cellular phenotypes (Esberg *et al*, 2006).

**Table 4** shows a comparison of predicted endogenous tRNA genes present in the genomes of humans, mice and zebrafish. While humans and mice are comparable in number, zebrafish have 20 times more tRNA genes and a remarkable 31-fold higher number of genes encoding *Lys*<sup>UUU</sup> tRNA. Regarding the expression of predicted tRNA genes, a recent preprint, describing tissue specific tRNA expression in mice, reports close to 70% of the predicted unique tRNA genes to be actually expressed in at least one sampled tissue (Manning *et al*, 2025, bioRxiv).

Even if 30% of predicted genes are silenced, or regulated by different means, the drastic increase in expressed tRNAs in zebrafish compared to humans may explain the absence of severe phenotypes in *urm1*, *ctu1* and *ctu2* KO animals.

tRNA Species (genomic anticodon)	Human (GRCh38/hg38)	Mouse (GRCm39/mm39)	Zebrafish (GRCz11)	Factor (Zebrafish vs human)
tRNA-Arg (TCT)	6	5	132	22x
tRNA-Gln (TTG)	6	4	103	17x
tRNA-Glu (TTC)	8	11	192	24x
tRNA-Lys (TTT)	14	10	431	31x
Total tRNA genes	429	400	8676	20x

**Table 4.** Predicted genomic tRNA genes across different species. Genome reference assemblies are indicated above. Only tRNA genes with high prediction confidence are shown. Retrieved from gtrRNA database (data release 22) <https://gtrnadb.org/> (Chan & Lowe, 2016).

There have been no systematic studies that assess the individual impact of the four mammalian thiolated tRNAs on translation fidelity. This is understandable, as depleting single tRNA isodecoder families (e.g. all tRNA Gln species that recognize CAA/GAA codons, irrespective of tRNA body sequence diversity) is currently unfeasible, as all respective genomic tRNA loci would need to be edited to null-alleles (**Table 4**). In the age of synthetic biology, first attempts have been made to create “minimal yeast” with the smallest possible genome. Here, synthetic tRNA chromosomes have been designed and introduced into *S. cerevisiae*, but these cannot replace endogenous tRNA transcription yet (Schindler *et al*, 2023).

### 3.3.2. Tissue-specific tRNA expression

Nevertheless, functional heterogeneity of tRNAs is important to be studied, as certain tRNAs reproducibly show tissue-specific expression patterns (Manning *et al.*, 2025, bioRxiv). A famous example is the tRNA Arg<sup>UCU</sup> isodecoder, which is highly expressed in the mouse central nervous system. Studies in a mouse lacking a ribosomal recycling factor, showed that mutations in this isodecoder cause neurodegeneration (Ishimura *et al*, 2014). In human cells, the abundance of one specific species, tRNA-Arg-UCU-4-1, was also significantly elevated in neurons derived from induced pluripotent stem cells, when compared to undifferentiated stem cells (Gao *et al*, 2024). However, in contrast to the mouse study, when considering all isodecoders of the tRNA Arg<sup>UCU</sup> family, this upregulation was not significant.

Due to its thiolation status, tRNA Arg<sup>UCU</sup> is of high interest in DREAM-PL syndrome. As microcephaly is the consistent and fully penetrant feature across all documented cases, it is crucial to test for a correlation with tRNA Arg<sup>UCU</sup> abundance. Given this neurological phenotype, the most relevant cellular model would be neurons derived from induced

pluripotent stem cells differentiated from patient fibroblasts. It is unclear whether the selective neurological vulnerability in DREAM-PL syndrome stems from tissue-specific thiolation demands. However, we provide evidence for a conserved molecular mechanism, as the acute depletion of *CTU2* in hTERT-RPE1 cells caused the same striking ribosome pausing at the AGA codon, as observed in tRNA Arg<sup>UCU</sup> mutant mice (Ishimura *et al*, 2014).

### 3.3.3. The mammalian thiolation landscape

Although proven as early as 2015 in mass spec analyses (Yoshida *et al*, 2015), the presence of a 4<sup>th</sup> thiolated tRNA species in mammals has not been uniformly adopted by the broader research community. Additional work conducted for this thesis clearly shows in murine and human cells that tRNA Arg<sup>UCU</sup> carries the s<sup>2</sup> substitution – most likely in addition to mcm<sup>5</sup> (which has not been formally addressed). This neglect can be explained by the fact that in yeast, the indispensable backbone of tRNA modification research, thiolation is only found at U<sub>34</sub> of Lys<sup>UUU</sup>, Gln<sup>UUG</sup>, Glu<sup>UUC</sup>. While the modification landscape in *S. cerevisiae* is well characterized, grounded in the seminal work of Björk and Byström (Björk *et al*, 2007; Björk & Hagervall, 2014; Esberg *et al*, 2006; Huang *et al*, 2005) (Table 5), a comprehensive mcm<sup>5</sup>s<sup>2</sup> modification atlas, including wobbling potential, is still lacking for many organisms including humans.

Thiolation Status	Modification	tRNA Species (Anticodon)	Target Codons (A-ending)	Wobble Target (G-ending)	Amino Acid
Non-Thiolated	Ncm <sup>5</sup> Um	tRNA-Leu (UAA)	UUA	UUG (restricted)	Leucine (Leu)
	ncm <sup>5</sup> U	tRNA-Ser (UGA)	UCA	UCG	Serine (Ser)
		tRNA-Pro (UGG)	CCA	CCG	Proline (Pro)
		tRNA-Thr (UGU)	ACA	ACG	Threonine (Thr)
		tRNA-Val (UAC)	GUA	GUG	Valine (Val)
		tRNA-Ala (UGC)	GCA	GCG	Alanine (Ala)
	mcm <sup>5</sup> U	tRNA-Arg (UCU)	AGA	AGG	Arginine (Arg)
		tRNA-Gly (UCC)	GGA	GGG	Glycine (Gly)
Thiolated	Mcm <sup>5</sup> s <sup>2</sup> U	tRNA-Gln (UUG)	CAA	CAG	Glutamine (Gln)
		tRNA-Lys (UUU)	AAA	AAG	Lysine (Lys)
		tRNA-Glu (UUC)	GAA	GAG	Glutamic Acid (Glu)

**Table 5.** List of the 11 tRNA species in *Saccharomyces cerevisiae* that are (at least partially) modified at the wobble uridine (U<sub>34</sub>) by the Elongator complex and CTU1/CTU2. Target codons (A-ending) and wobble interactions (G-ending) are indicated for each species. Adapted from Björk & Hagervall, 2014.

List of the 11 tRNA species in *Saccharomyces cerevisiae* that are (at least partially) modified at the wobble uridine (U<sub>34</sub>) by the Elongator complex and CTU1/CTU2. Target codons (A-ending) and wobble interactions (G-ending) are indicated for each species. Adapted from Björk & Hagervall, 2014.

### 3.3.4. Expression and activity of the tRNA thiolation machinery

URM1, CTU1 and CTU2 are ubiquitously expressed across the human body – both on the mRNA and protein levels. The consensus dataset published by the Human Protein Atlas (Uhlén *et al*, 2015), which integrates GTEx (The GTEx Consortium *et al*, 2020) as well as their own data on mRNA expression, reports an average expression level of URM1 mRNA at 21.5 normalized transcripts per million (nTPM), which puts it at a moderate overall expression level. CTU2 and CTU1 are expressed at an average of 8 and 2.5 nTPM respectively, making CTU1 a rather lowly expressed gene. This correlates well with ubiquitous, but moderate-to-low protein expression. This ubiquitous mRNA expression is also seen in the mouse (Baldarelli *et al*, 2021).

tRNA transcription and modification is a dynamic process. Northern blot analyses conducted throughout this study in both murine and human cell lines show that at steady-state only 40-50% of respective tRNA molecules are thiolated. This could be explained by dilution effects when new tRNAs are transcribed, or by a low catalysis rate of the thiolation machinery. Since tRNAs are considered a very stable subtype of RNA, persisting for several days (Miller, 1973), it can be assumed that the pool of thiolated tRNA is actively maintained at a certain threshold. It is tempting to speculate that this depends on translational demand in each organ or tissue. Using APM-northern blotting, we tested thiolation levels in wildtype mouse livers, kidneys, spleens and brains, which are all organs with high protein synthesis rates (Shahbazian *et al*, 1987). However, we struggled to draw definitive conclusions, as the thiolated fractions compared to their unmodified counterpart appeared high in all organs but the spleen. Here, we saw a ratio closer to 50:50. To collect future conclusive evidence, controls of translationally “inert” tissues should be included. While *Ctu2*<sup>L63P/L63P</sup> animals exhibited the expected decrease in thiolated tRNAs, they surprisingly failed to show a corresponding shift toward the unmodified form, except for tRNA extracted from spleens. These data suggest a general reduction in tRNA abundance, implying that the unmodified tRNAs may be destabilized.

## 3.4. Prospective research directions

### 3.4.1. Resolving tissue-specific thiolation dependence

Crucial questions regarding organ-specific tRNA expression remain to be answered. As this is of high relevance for understanding DREAM-PL syndrome, establishing conditional *Ctu2* KO mice to address this has high priority. A *Cre-LoxP* approach – as we had originally designed and envisaged – would allow the exact pinpointing of which tissues are truly functionally dependent on tRNA thiolation, and which do not. The Cre recombinase excises DNA regions

upon recognizing distinctly arranged DNA sequences (LoxP sites), making it an excellent research tool to study conditional gene knockout.

First, major organs affected in DREAM-PL syndrome should be screened individually for developmental abnormalities. To that end, transgenic mice carrying *LoxP-flanked Ctug2* exons are crossed with different *Cre* lines, resulting in the organ-specific constitutive ablation of *Ctug2* expression in homozygous embryos. Possible *Cre* alleles include *Six2-Cre* for the kidney (Kobayashi *et al*, 2008), *Nestin-Cre* for the developing brain (Tronche *et al*, 1999) and *Tnnt2-Cre* for embryonic cardiomyocytes. Similar strategies using an inducible CreERT2 recombinase system, where DNA recombination only occurs upon the injection of Tamoxifen, can be employed to challenge adult mice with organ-specific or even whole-body loss of tRNA thiolation. In light of our findings in zebrafish and *Ctug2<sup>L63P/L63P</sup>* mice that tolerate tRNA hypothiolation, it will be interesting to see if adult mice show phenotypes upon acute impairment of tRNA thiolation. Furthermore, considering the propensity of aged *Ctug2<sup>L63P/L63P</sup>* mice to develop splenomegaly, such conditional KO mice should be screened for cancer phenotypes.

#### 3.4.2. Quantitative profiling of the tRNA modification landscape

A tissue atlas to understand steady state organ-specific modification levels would be a highly useful resource for the community. Currently this is most feasible in the mouse and has been attempted for tRNA expression (Manning *et al.*, 2025, bioRxiv). Because of our findings on aged animals, tRNAs extracted from young and old mice should be compared, as changes in modification levels may drive disease. To overcome the limitation of semi-quantitative APM-northern blotting, tRNA nucleoside mass spectrometry should be employed. One well-established protocol is NAIL-MS (Heiss *et al*, 2021). Here individual tRNA isodecoders can be enriched by using complementary DNA oligos immobilized to beads, digested into nucleosides and analyzed by liquid chromatography mass spectrometry (LC-MS). Using this approach, one run can provide quantitative information on the 4 canonical nucleosides (A, C, G and U) as well as 24 non-canonical, modified nucleosides (**Table 6**). By extracting and quantifying tRNA from different organs, this will reveal the modification landscape. By profiling cells from wildtype and *Ctug2<sup>L63P/L63P</sup>* mice – and DREAM-PL patient cells and healthy donor controls – spatiotemporal dependency of other modifications on tRNA thiolation can be addressed. Such a dependency for several anticodon modifications has recently been reported in a preprint on plants (Dannfald *et al.*, 2025, bioRxiv). If true also in humans, DREAM-PL patient tRNA should be screened for corresponding changes in modification levels.

Group	Modifications
Adenosine	m <sup>1</sup> A, m <sup>6</sup> A, m <sup>6</sup> Am, m <sup>6,6</sup> A, m <sup>6,6</sup> Am*, Am, i <sup>6</sup> A, t <sup>6</sup> A
Cytidine	m <sup>3</sup> C, m <sup>5</sup> C, Cm*, ac <sup>4</sup> C*
Guanosine	m <sup>1</sup> G, m <sup>2</sup> G, m <sup>2,2</sup> G, m <sup>7</sup> G, Gm, Q*, ManQ*, GalQ*
Uridine	m <sup>3</sup> U, m <sup>5</sup> U*, s <sup>2</sup> U, Um, acp <sup>3</sup> U*, D
Pseudouridine	Ψ, m <sup>1</sup> Ψ*
Wobble Uridines	mcm <sup>5</sup> U, ncm <sup>5</sup> U, cm <sup>5</sup> U*, mcm <sup>5</sup> s <sup>2</sup> U, ncm <sup>5</sup> s <sup>2</sup> U*
Inosine	I, m <sup>1</sup> I

**Table 6.** List of RNA modifications validated for detection via NAIL-MS. The table categorizes modified nucleosides by their parent canonical base. 28 modifications can be chromatographically separated and individually quantified in a single LC-MS/MS run using multiple reaction monitoring. Modification that have been technically validated are indicated with an \*.

### 3.4.3. Possible link between tRNA modifications and tumorigenesis

The role of hypothiolation on the formation of malignant disease requires further clarification. We reasoned that disease phenotypes may compound with age, as several studies have found that tRNA wobble modification levels change dynamically during stress (Ranjan & Rodnina, 2016). Based on our multi-omics analysis, the loss of functional CTU2 could sensitize cells to transformation by impairing the fidelity of chromosome segregation, yet it remains to be tested if signs of chromosomal instability can be found in cells that do not commit to apoptosis upon CTU2 depletion.

There is a relevant cancer connection to mcm<sup>5</sup>s<sup>2</sup> modifiers, as germline *ELP1* mutations are found in pediatric patients with a rare type of malignant brain tumor with constitutively active sonic hedgehog signaling (Waszak *et al*, 2020). As the loss of Elongator complex function impairs tRNA thiolation in humans, it is feasible that tRNA thiolation contributes to tumorigenesis in some settings. This would be in line with the observed downregulation of proteins enriched in AAA, GAA and CAA codons in these tumors (Waszak *et al*, 2020). This is reminiscent of a tRNA thiolation defect and matches the codon-biased proteome remodeling we describe upon acute hypothiolation in hTERT-RPE1 cells.

The opposing concept that tRNA modifiers are required for cancer progression, rather than CTU2 being a *bona fide* tumor suppressor – as data from this study could suggest – has been established in several different cancer types and for different tRNA modifiers. ELP3, CTU1 and CTU2 are upregulated in melanoma (Rapino *et al*, 2018) and breast cancer (Delaunay *et al*, 2016). Similarly, ALKBH1 was found to be required for the development of acute myeloid leukemia (Shen *et al*, 2025). In all three studies, the modification enzymes were needed to sustain cancer growth, metastasis or drug resistance and were linked to codon-biased translation.

It is possible that overexpression of modifiers is a late event in tumorigenesis that is beneficial for maintenance, whereas the loss of CTU2 may sensitize cells to transformation through chromosomal instability. Future studies will be required to determine whether the correlation between tRNA modifications and cancer predisposition represents a more generalizable concept.

#### **3.4.4. Non-canonical functions of CTU2**

An unresolved evolutionary question remains why eukaryotes need CTU2 at all. CTU2 does not contain the iron-sulfur cluster required for sulfur relay. Still, CTU2 is not predicted to be more dispensable than CTU1, the catalytic unit of the thiouridylases complex in the DepMap database (Tsherniak *et al*, 2017). While we propose a scaffolding role of CTU2 through tRNA backbone interactions, archaea do not require a second protein at all (Shigi, 2014). While this is purely speculative, the fact that eukaryotes have retained CTU2 in their genome could mean that it required other functions apart from tRNA thiolation. Genetic screens assessing “synthetic rescue” could identify such putative moonlighting functions in HeLa cells that depend on CTU2 for survival.

Another observation that could indicate additional contributions of CTU2 is that several studies have found the loss of wobble modifiers to show a minimal effect on protein translation (Rezgui *et al*, 2013). Using puromycin incorporation assays and fluorescent analogues for quantifying nascent translation, we find that DREAM-PL patient cells do not markedly slowdown of protein synthesis (data not shown). However, we see a clear phosphorylation signal of the eukaryotic initiation factor 2, eIF2 $\alpha$ , in DREAM-PL patient lymphoblasts. Canonically, this would decrease translation. While these observations could be explained by cellular adaptation phenomena, it may also suggest that tRNA thiolation is not only important for proteostasis but also essential for other cellular processes.

### **3.5. Theoretical intervention concepts**

DREAM-PL syndrome is a devastating disease without treatment. Currently, patient care in severe cases revolves around the relieving and managing of symptoms, for example by providing respiratory support. As the disease is caused by developmental defects, it is doubtful whether therapeutic intervention could sufficiently restore organ function after birth. However, genetic testing could identify carriers in high-risk populations and possibly suggest therapeutic measures, once available. Before that, studies in mouse models could address the feasibility of experimental treatments. The best treatment strategy would be to correct the mutation, for example by using prime editing (Chen & Liu, 2023). However, this is currently limited by delivery systems and off-target considerations – although prime editing guide RNAs are highly

specific and do not cause double strand breaks. Another strategy, based on findings in yeast, is the overexpression of tRNAs that could compensate for loss of tRNA thiolation. tRNA genes are good candidates for gene therapy, as they are indistinguishable from endogenous genes and are very short at approximately 110 bps (5' leader, coding body with internal promoter and 3' terminator). This is beneficial for delivery and would likely not cause adverse effects. Suppressor tRNAs that cause premature stop codon readthrough have shown promise in gene therapy in human cells and in mice (Wang *et al*, 2022). Here adenovirus-encapsulated tRNA was delivered systemically by tail vein injection into knock-in mice modelling Mucopolysaccharidosis type I. Within 10 weeks, the impaired enzymatic function in the livers and hearts of these mice was partially restored and maintained over the follow-up period of 6 months. While such results in animal models are encouraging, in the case of DREAM-PL syndrome, gene therapy would need to be started as early as possible *in utero*. This is technically feasible, and a promising first study on *in utero* enzyme-replacement therapy has shown promise (Cohen *et al*, 2022). Nevertheless, further research to combine this with gene therapy is required.

For now, expanded genetic testing and counseling could help affect families and the broad public to identify disease risk. Affected parents may consider screening for heterozygous embryos to be used in *in vitro* fertilization.

### 3.6. Conclusion

The research presented in this thesis sought to define the physiological and pathophysiological role of sulfur substitution at the wobble uridine of tRNA in higher organisms. It complements the seminal research in yeast that established the field of “Epitranscriptomics”.

To address our primary aims of defining the molecular consequences of modification loss and identifying disease-causing pathways, we characterized cells of patients affected by DREAM-PL syndrome. Furthermore, to investigate organismal vulnerability *in vivo*, we established a comprehensive toolkit of cellular and animal models, approaching the tRNA thiolation cascade from different angles. This includes acute *CTU2* depletion by inducible short-hairpin RNAs, disease-specific knock-in strategies in mice, and the constitutive knockout in zebrafish.

Our findings reveal a striking biological divergence among vertebrates regarding the requirement of tRNA thiolation for healthy development and survival. This implies the existence of species-specific compensatory mechanisms.

These validated tools, now published and shared with the broader research community, will be instrumental in investigating tissue-specific contexts and resolving remaining evolutionary questions. Ultimately, we hope they pave the way for future breakthroughs in treating DREAM-PL syndrome.

*We thank the patients and families who participated in this and similar studies. Their trust and willingness to contribute are essential to the advancement of medical research.*

# Chapter four

## 4. Materials and methods

A detailed description of the experimental procedures, reagents, and statistical analyses used in this study is provided in the preprint included in **Chapter two**. The full text is also available online at [www.biorxiv.org](http://www.biorxiv.org).

.

## References

- Abbassi N-H, Jaciuk M, Scherf D, Böhnert P, Rau A, Hammermeister A, Rawski M, Indyka P, Wazny G, Chramiec-Głąbik A, *et al* (2024) Cryo-EM structures of the human Elongator complex at work. *Nat Commun* 15: 4094
- Abouelhoda M, Sobahy T, El-Kalioby M, Patel N, Shamseldin H, Monies D, Al-Tassan N, Ramzan K, Imtiaz F, Shaheen R, *et al* (2016) Clinical genomics can facilitate countrywide estimation of autosomal recessive disease burden. *Genet Med Off J Am Coll Med Genet* 18: 1244–1249
- Agris PF (2008) Bringing order to translation: the contributions of transfer RNA anticodon-domain modifications. *EMBO Rep* 9: 629–635
- Alings F, Scharmann K, Eggers C, Böttcher B, Sokołowski M, Shvetsova E, Sharma P, Roth J, Rashiti L, Glatt S, *et al* (2023) Ncs2\* mediates *in vivo* virulence of pathogenic yeast through sulphur modification of cytoplasmic transfer RNA. *Nucleic Acids Res*: gkad564
- Armache J-P, Jarasch A, Anger AM, Villa E, Becker T, Bhushan S, Jossinet F, Habeck M, Dindar G, Franckenberg S, *et al* (2010) Localization of eukaryote-specific ribosomal proteins in a 5.5-Å cryo-EM map of the 80S eukaryotic ribosome. *Proc Natl Acad Sci U S A* 107: 19754–19759
- Baldarelli RM, Smith CM, Finger JH, Hayamizu TF, McCright IJ, Xu J, Shaw DR, Beal JS, Blodgett O, Campbell J, *et al* (2021) The mouse Gene Expression Database (GXD): 2021 update. *Nucleic Acids Res* 49: D924–D931
- Barrak MM, Al-Aidy SR, & Morteza Bonyadi (2024) Unraveling DREAM-PL: A Case Report on Challenges and Management. *Univ Thi-Qar J Sci* 11: 33–35
- Bauer F, Matsuyama A, Candiracci J, Dieu M, Scheliga J, Wolf DA, Yoshida M & Hermand D (2012) Translational Control of Cell Division by Elongator. *Cell Rep* 1: 424–433
- Beenstock J & Sicheri F (2021) The structural and functional workings of KEOPS. *Nucleic Acids Res* 49: 10818–10834
- Bento-Abreu A, Jager G, Swinnen B, Rué L, Hendrickx S, Jones A, Staats KA, Taes I, Eykens C, Nonneman A, *et al* (2018) Elongator subunit 3 (ELP3) modifies ALS through tRNA modification. *Hum Mol Genet* 27: 1276–1289
- Berg MD & Brandl CJ (2021) Transfer RNAs: diversity in form and function. *RNA Biol* 18: 316–339
- Biela A, Hammermeister A, Kaczmarczyk I, Walczak M, Koziej L, Lin T-Y & Glatt S (2023) The diverse structural modes of tRNA binding and recognition. *J Biol Chem* 299: 104966
- Biela AD, Nowak JS, Biela AP, Mukherjee S, Moafinejad SN, Maiti S, Chramiec-Głąbik A, Mehta R, Jeżowski J, Dobosz D, *et al* (2025) Determining the effects of pseudouridine incorporation on human tRNAs. *EMBO J*
- Birling M-C, Yoshiki A, Adams DJ, Ayabe S, Beaudet AL, Bottomley J, Bradley A, Brown SDM, Bürger A, Bushell W, *et al* (2021) A resource of targeted mutant mouse lines for 5,061 genes. *Nat Genet* 53: 416–419
- Björk GR & Hagervall TG (2014) Transfer RNA Modification: Presence, Synthesis, and Function. *EcoSal Plus* 6: 10.1128/ecosalplus.ESP-0007–2013
- Björk GR, Huang B, Persson OP & Byström AS (2007) A conserved modified wobble nucleoside (mcm<sup>5</sup>s<sup>2</sup>U) in lysyl-tRNA is required for viability in yeast. *RNA* 13: 1245–1255

- Brandman O, Stewart-Ornstein J, Wong D, Larson A, Williams CC, Li G-W, Zhou S, King D, Shen PS, Weibezahn J, *et al* (2012) A Ribosome-Bound Quality Control Complex Triggers Degradation of Nascent Peptides and Signals Translation Stress. *Cell* 151: 1042–1054
- Braun DA, Rao J, Mollet G, Schapiro D, Daugeron M-C, Tan W, Gribouval O, Boyer O, Revy P, Jobst-Schwan T, *et al* (2017) Mutations in KEOPS-complex genes cause nephrotic syndrome with primary microcephaly. *Nat Genet* 49: 1529–1538
- Brenner S, Jacob F & Meselson M (1961) An Unstable Intermediate Carrying Information from Genes to Ribosomes for Protein Synthesis. *Nature* 190: 576–581
- Brito Querido J, Díaz-López I & Ramakrishnan V (2024) The molecular basis of translation initiation and its regulation in eukaryotes. *Nat Rev Mol Cell Biol* 25: 168–186
- Bruch A, Laguna T, Butter F, Schaffrath R & Klassen R (2020) Misactivation of multiple starvation responses in yeast by loss of tRNA modifications. *Nucleic Acids Res*
- Cairo LV, Hong X, Müller MBD, Yuste-Checa P, Jagadeesan C, Bracher A, Park S-H, Hayer-Hartl M & Hartl FU (2024) Stress-dependent condensate formation regulated by the ubiquitin-related modifier Urm1. *Cell* 187: 4656-4673.e28
- Cavarelli J, Eriani G, Rees B, Ruff M, Boeglin M, Mitschler A, Martin F, Gangloff J, Thierry JC & Moras D (1994) The active site of yeast aspartyl-tRNA synthetase: structural and functional aspects of the aminoacylation reaction. *EMBO J* 13: 327–337
- Chan PP & Lowe TM (2016) GtRNADB 2.0: an expanded database of transfer RNA genes identified in complete and draft genomes. *Nucleic Acids Res* 44: D184–D189
- Chen D, Nemazanyy I, Peulen O, Shostak K, Xu X, Tang SC, Wathieu C, Turchetto S, Tielens S, Nguyen L, *et al* (2022) Elp3-mediated codon-dependent translation promotes mTORC2 activation and regulates macrophage polarization. *EMBO J* 41
- Chen PJ & Liu DR (2023) Prime editing for precise and highly versatile genome manipulation. *Nat Rev Genet* 24: 161–177
- Chujo T & Tomizawa K (2021) Human transfer RNA modopathies: diseases caused by aberrations in transfer RNA modifications. *FEBS J* 288: 7096–7122
- Claude A (1946) FRACTIONATION OF MAMMALIAN LIVER CELLS BY DIFFERENTIAL CENTRIFUGATION. *J Exp Med* 84: 61–89
- Cohen JL, Chakraborty P, Fung-Kee-Fung K, Schwab ME, Bali D, Young SP, Gelb MH, Khaledi H, DiBattista A, Smallshaw S, *et al* (2022) In Utero Enzyme-Replacement Therapy for Infantile-Onset Pompe's Disease. *N Engl J Med* 387: 2150–2158
- Collart MA & Weiss B (2020) Ribosome pausing, a dangerous necessity for co-translational events. *Nucleic Acids Res* 48: 1043–1055
- Crick FH (1958) On protein synthesis. *Symp Soc Exp Biol* 12: 138–163
- Crick FH, Barnett L, Brenner S & Watts-Tobin RJ (1961) General nature of the genetic code for proteins. *Nature* 192: 1227–1232
- Crick FHC (1966) Codon—anticodon pairing: The wobble hypothesis. *J Mol Biol* 19: 548–555
- Damon JR, Pincus D & Ploegh HL (2015) tRNA thiolation links translation to stress responses in *Saccharomyces cerevisiae*. *Mol Biol Cell* 26: 270–282

- Dannfald A, Cadoudal A, Carpentier M-C, Merret R, Rigal Q, Vialaret J, Attina A, Kindermans J, Berrissou C, Koprivova A, *et al* (2025) Loss of tRNA uridine thiolation affects mRNA translation, protein production, and sulfur-compound metabolism in Arabidopsis. doi:10.1101/2025.09.25.678457 [PREPRINT]
- Delaunay S, Helm M & Frye M (2024) RNA modifications in physiology and disease: towards clinical applications. *Nat Rev Genet* 25: 104–122
- Delaunay S, Rapino F, Tharun L, Zhou Z, Heukamp L, Termathe M, Shostak K, Klevernic I, Florin A, Desmecht H, *et al* (2016) Elp3 links tRNA modification to IRES-dependent translation of LEF1 to sustain metastasis in breast cancer. *J Exp Med* 213: 2503–2523
- Demeshkina N, Jenner L, Westhof E, Yusupov M & Yusupova G (2012) A new understanding of the decoding principle on the ribosome. *Nature* 484: 256–259
- Dever TE, Dinman JD & Green R (2018) Translation Elongation and Recoding in Eukaryotes. *Cold Spring Harb Perspect Biol* 10: a032649
- Dewez M, Bauer F, Dieu M, Raes M, Vandenhoute J & Hermand D (2008) The conserved Wobble uridine tRNA thiolase Ctu1–Ctu2 is required to maintain genome integrity. *Proc Natl Acad Sci* 105: 5459–5464
- Drabkin HJ, Estrella M & Rajbhandary UL (1998) Initiator-Elongator Discrimination in Vertebrate tRNAs for Protein Synthesis. *Mol Cell Biol* 18: 1459–1466
- Durant PC, Bajji AC, Sundaram M, Kumar RK & Davis DR (2005) Structural Effects of Hypermodified Nucleosides in the *Escherichia coli* and Human tRNA<sup>Lys</sup> Anticodon Loop: The Effect of Nucleosides s<sup>2</sup> U, mcm<sup>5</sup> U, mcm<sup>5</sup> s<sup>2</sup> U, mnm<sup>5</sup> s<sup>2</sup> U, t<sup>6</sup> A, and ms<sup>2</sup> t<sup>6</sup> A. *Biochemistry* 44: 8078–8089
- Elrick H, Peterson KA, Willis BJ, Lanza DG, Acar EF, Ryder EJ, Teboul L, Kasperek P, Birling M-C, Adams DJ, *et al* (2024) Impact of essential genes on the success of genome editing experiments generating 3313 new genetically engineered mouse lines. *Sci Rep* 14: 22626
- Esberg A, Huang B, Johansson MJO & Byström AS (2006) Elevated Levels of Two tRNA Species Bypass the Requirement for Elongator Complex in Transcription and Exocytosis. *Mol Cell* 24: 139–148
- Franz M, Hagenau L, Jensen LR & Kuss AW (2020) Role of transfer RNA modification and aminoacylation in the etiology of congenital intellectual disability. *J Transl Genet Genomics*
- Fu D, Brophy JAN, Chan CTY, Atmore KA, Begley U, Paules RS, Dedon PC, Begley TJ & Samson LD (2010) Human AlkB Homolog ABH8 Is a tRNA Methyltransferase Required for Wobble Uracil Modification and DNA Damage Survival. *Mol Cell Biol* 30: 2449–2459
- Gaik M, Kojic M, Stegeman MR, Öncü-Öner T, Kościelniak A, Jones A, Mohamed A, Chau PYS, Sharmin S, Chramiec-Głębik A, *et al* (2022) Functional divergence of the two Elongator subcomplexes during neurodevelopment. *EMBO Mol Med* 14: e15608
- Gao L, Behrens A, Rodschinka G, Forcelloni S, Wani S, Strasser K & Nedialkova DD (2024) Selective gene expression maintains human tRNA anticodon pools during differentiation. *Nat Cell Biol*
- Giege R, Sissler M & Florentz C (1998) Universal rules and idiosyncratic features in tRNA identity. *Nucleic Acids Res* 26: 5017–5035
- Groza T, Gomez FL, Mashhadi HH, Muñoz-Fuentes V, Gunes O, Wilson R, Cacheiro P, Frost A, Kesivali-Bond P, Vardal B, *et al* (2023) The International Mouse Phenotyping Consortium: comprehensive knockout phenotyping underpinning the study of human disease. *Nucleic Acids Res* 51: D1038–D1045

- Gupta R, Walvekar AS, Liang S, Rashida Z, Shah P & Laxman S (2019) A tRNA modification balances carbon and nitrogen metabolism by regulating phosphate homeostasis. *eLife* 8: e44795
- Guy MP, Shaw M, Weiner CL, Hobson L, Stark Z, Rose K, Kalscheuer VM, Gecz J & Phizicky EM (2015) Defects in tRNA Anticodon Loop 2'-O-Methylation Are Implicated in Nonsyndromic X-Linked Intellectual Disability due to Mutations in *FTSJ1*. *Hum Mutat* 36: 1176–1187
- Hammermeister A, Gaik M, Dahate P & Glatt S (2025) Structural Snapshots of Human tRNA Modifying Enzymes. *J Mol Biol*: 169106
- Hansen JL, Schmeing TM, Moore PB & Steitz TA (2002) Structural insights into peptide bond formation. *Proc Natl Acad Sci U S A* 99: 11670–11675
- Heiss M, Borland K, Yoluç Y & Kellner S (2021) Quantification of Modified Nucleosides in the Context of NAIL-MS. *Methods Mol Biol Clifton NJ* 2298: 279–306
- Hellen CUT (2018) Translation Termination and Ribosome Recycling in Eukaryotes. *Cold Spring Harb Perspect Biol* 10: a032656
- Helsmoortel C, Vandeweyer G, Ordoukhanian P, Van Nieuwerburgh F, Van Der Aa N & Kooy RF (2015) Challenges and opportunities in the investigation of unexplained intellectual disability using family-based whole-exome sequencing. *Clin Genet* 88: 140–148
- Hermann J, Bortçen T, Kalis R, Kowar A, Pechincha C, Vogt V, Schneider M, Helm D, Krijgsveld J, Loayza-Puch F, *et al* (2025) mTORC1 cooperates with tRNA wobble modification to sustain the protein synthesis machinery. *Nat Commun* 16: 4201
- Hetz C, Zhang K & Kaufman RJ (2020) Mechanisms, regulation and functions of the unfolded protein response. *Nat Rev Mol Cell Biol* 21: 421–438
- Hildebrandt F, Benzing T & Katsanis N (2011) Ciliopathies. *N Engl J Med* 364: 1533–1543
- Hoagland MB, Stephenson ML, Scott JF, Hecht LI & Zamecnik PC (1958) A soluble ribonucleic acid intermediate in protein synthesis. *J Biol Chem* 231: 241–257
- Holley RW, Apgar J, Everett GA, Madison JT, Marquisee M, Merrill SH, Penswick JR & Zamir A (1965) Structure of a Ribonucleic Acid. *Science* 147: 1462–1465
- Huang B, Johansson MJO & Byström AS (2005) An early step in wobble uridine tRNA modification requires the Elongator complex. *RNA* 11: 424–436
- Huang B, Lu J & Byström AS (2008) A genome-wide screen identifies genes required for formation of the wobble nucleoside 5-methoxycarbonylmethyl-2-thiouridine in *Saccharomyces cerevisiae*. *RNA* 14: 2183–2194
- Ibba M & Soll D (2000) Aminoacyl-tRNA synthesis. *Annu Rev Biochem* 69: 617–650
- Ingolia NT, Ghaemmaghami S, Newman JRS & Weissman JS (2009) Genome-Wide Analysis in Vivo of Translation with Nucleotide Resolution Using Ribosome Profiling. *Science* 324: 218–223
- Ishimura R, Nagy G, Dotu I, Zhou H, Yang X-L, Schimmel P, Senju S, Nishimura Y, Chuang JH & Ackerman SL (2014) Ribosome stalling induced by mutation of a CNS-specific tRNA causes neurodegeneration. *Science* 345: 455–459
- Jaciuk M, Scherf D, Kaszuba K, Gaik M, Rau A, Kościelniak A, Krutyholowa R, Rawski M, Indyka P, Graziadei A, *et al* (2023) Cryo-EM structure of the fully assembled Elongator complex. *Nucleic Acids Res* 51: 2011–2032

- Jäger G, Nilsson K & Björk GR (2013) The Phenotype of Many Independently Isolated +1 Frameshift Suppressor Mutants Supports a Pivotal Role of the P-Site in Reading Frame Maintenance. *PLoS ONE* 8: e60246
- Johansson MJO, Esberg A, Huang B, Björk GR & Byström AS (2008) Eukaryotic Wobble Uridine Modifications Promote a Functionally Redundant Decoding System. *Mol Cell Biol* 28: 3301–3312
- Johansson MJO, Xu F & Byström AS (2018) Elongator—a tRNA modifying complex that promotes efficient translational decoding. *Biochim Biophys Acta BBA - Gene Regul Mech* 1861: 401–408
- Karczewski KJ, Francioli LC, Tiao G, Cummings BB, Alföldi J, Wang Q, Collins RL, Laricchia KM, Ganna A, Birnbaum DP, *et al* (2020) The mutational constraint spectrum quantified from variation in 141,456 humans. *Nature* 581: 434–443
- Karikó K, Buckstein M, Ni H & Weissman D (2005) Suppression of RNA Recognition by Toll-like Receptors: The Impact of Nucleoside Modification and the Evolutionary Origin of RNA. *Immunity* 23: 165–175
- Karikó K, Muramatsu H, Welsh FA, Ludwig J, Kato H, Akira S & Weissman D (2008) Incorporation of Pseudouridine Into mRNA Yields Superior Nonimmunogenic Vector With Increased Translational Capacity and Biological Stability. *Mol Ther* 16: 1833–1840
- Karlsborn T, Tükenmez H, Mahmud AKMF, Xu F, Xu H & Byström AS (2014) Elongator, a conserved complex required for wobble uridine modifications in Eukaryotes. *RNA Biol* 11: 1519–1528
- Kearse MG & Wilusz JE (2017) Non-AUG translation: a new start for protein synthesis in eukaryotes. *Genes Dev* 31: 1717–1731
- Keffer-Wilkes LC, Veerareddygarri GR & Kothe U (2016) RNA modification enzyme TruB is a tRNA chaperone. *Proc Natl Acad Sci* 113: 14306–14311
- Kimura S & Waldor MK (2019) The RNA degradosome promotes tRNA quality control through clearance of hypomodified tRNA. *Proc Natl Acad Sci* 116: 1394–1403
- Klassen R, Bruch A & Schaffrath R (2017) Independent suppression of ribosomal +1 frameshifts by different tRNA anticodon loop modifications. *RNA Biol* 14: 1252–1259
- Klassen R, Bruch A & Schaffrath R (2020) Induction of protein aggregation and starvation response by tRNA modification defects. *Curr Genet* 66: 1053–1057
- Klassen R, Grunewald P, Thüring KL, Eichler C, Helm M & Schaffrath R (2015) Loss of Anticodon Wobble Uridine Modifications Affects tRNALys Function and Protein Levels in *Saccharomyces cerevisiae*. *PLOS ONE* 10: e0119261
- Kobayashi A, Valerius MT, Mugford JW, Carroll TJ, Self M, Oliver G & McMahon AP (2008) Six2 Defines and Regulates a Multipotent Self-Renewing Nephron Progenitor Population throughout Mammalian Kidney Development. *Cell Stem Cell* 3: 169–181
- Kojic M, Gawda T, Gaik M, Begg A, Salerno-Kochan A, Kurniawan ND, Jones A, Drożdżyk K, Kościelniak A, Chramiec-Głąbik A, *et al* (2021) Elp2 mutations perturb the epitranscriptome and lead to a complex neurodevelopmental phenotype. *Nat Commun* 12: 2678
- Konevega AL, Soboleva NG, Makhno VI, Semenkov YP, Wintermeyer W, Rodnina MV & Katunin VI (2004) Purine bases at position 37 of tRNA stabilize codon–anticodon interaction in the ribosomal A site by stacking and Mg<sup>2+</sup>-dependent interactions. *RNA* 10: 90–101

- Kruger K, Grabowski PJ, Zaugg AJ, Sands J, Gottschling DE & Cech TR (1982) Self-splicing RNA: autoexcision and autocyclization of the ribosomal RNA intervening sequence of *Tetrahymena*. *Cell* 31: 147–157
- de Crécy-Lagard V, Boccaletto P, Mangleburg CG, Sharma P, Lowe TM, Leidel SA & Bujnicki JM (2019) Matching tRNA modifications in humans to their known and predicted enzymes. *Nucleic Acids Res* 47: 2143–2159
- Laguesse S, Creppe C, Nedialkova DD, Prévot P-P, Borgs L, Huysseune S, Franco B, Duysens G, Krusy N, Lee G, *et al* (2015) A Dynamic Unfolded Protein Response Contributes to the Control of Cortical Neurogenesis. *Dev Cell* 35: 553–567
- Laxman S, Sutter BM, Wu X, Kumar S, Guo X, Trudgian DC, Mirzaei H & Tu BP (2013) Sulfur Amino Acids Regulate Translational Capacity and Metabolic Homeostasis through Modulation of tRNA Thiolation. *Cell* 154: 416–429
- Leidel S, Pedrioli PGA, Bucher T, Brost R, Costanzo M, Schmidt A, Aebersold R, Boone C, Hofmann K & Peter M (2009) Ubiquitin-related modifier Urm1 acts as a sulphur carrier in thiolation of eukaryotic transfer RNA. *Nature* 458: 228–232
- Leimkühler S (2025) 2-Thiouridine formation in *Escherichia coli*: a critical review. *J Bacteriol* 207: e00420-24
- Leimkühler S, Bühning M & Beilschmidt L (2017) Shared Sulfur Mobilization Routes for tRNA Thiolation and Molybdenum Cofactor Biosynthesis in Prokaryotes and Eukaryotes. *Biomolecules* 7: 5
- Lin BY, Chan PP & Lowe TM (2019) tRNAviz: explore and visualize tRNA sequence features. *Nucleic Acids Res* 47: W542–W547
- Liu Y, Vinyard DJ, Reesbeck ME, Suzuki T, Manakongtreecheep K, Holland PL, Brudvig GW & Söll D (2016) A [3Fe-4S] cluster is required for tRNA thiolation in archaea and eukaryotes. *Proc Natl Acad Sci* 113: 12703–12708
- Lomakin IB & Steitz TA (2013) The initiation of mammalian protein synthesis and mRNA scanning mechanism. *Nature* 500: 307–311
- Mahoney D, Black J, Dosa N, Sakonju A & Lebel R (2023) P241: Expanding the phenotype of DREAM-PL: A case report. *Genet Med Open* 1: 100269
- Manning AC, Chan PP & Lowe TM Diverse expression and modification of tRNAs and tRNA-derived RNAs in 19 mouse tissues.
- Martinis SA & Boniecki MT (2010) The balance between pre- and post-transfer editing in tRNA synthetases. *FEBS Lett* 584: 455–459
- Miller BG (1973) THE BIOLOGICAL HALF-LIVES OF RIBOSOMAL AND TRANSFER RNA IN THE MOUSE UTERUS. *J Endocrinol* 59: 81–85
- Monies D, Vågbø CB, Al-Owain M, Alhomaidi S & Alkuraya FS (2019) Recessive Truncating Mutations in ALKBH8 Cause Intellectual Disability and Severe Impairment of Wobble Uracil Modification. *Am J Hum Genet* 104: 1202–1209
- Nakai Y, Nakai M, Lill R, Suzuki T & Hayashi H (2007) Thio Modification of Yeast Cytosolic tRNA Is an Iron-Sulfur Protein-Dependent Pathway. *Mol Cell Biol* 27: 2841–2847
- Nedialkova DD & Leidel SA (2015) Optimization of Codon Translation Rates via tRNA Modifications Maintains Proteome Integrity. *Cell* 161: 1606–1618

- Nilsson I, Sääf A, Whitley P, Gafvelin G, Waller C & Von Heijne G (1998) Proline-induced disruption of a transmembrane  $\alpha$ -helix in its natural environment. *J Mol Biol* 284: 1165–1175
- Nirenberg M (2004) Historical review: Deciphering the genetic code – a personal account. *Trends Biochem Sci* 29: 46–54
- Nirenberg M, Caskey T, Marshall R, Brimacombe R, Kellogg D, Doctor B, Hatfield D, Levin J, Rottman F, Pestka S, *et al* (1966) The RNA Code and Protein Synthesis. *Cold Spring Harb Symp Quant Biol* 31: 11–24
- Nirenberg M & Leder P (1964) RNA Codewords and Protein Synthesis: The Effect of Trinucleotides upon the Binding of sRNA to Ribosomes. *Science* 145: 1399–1407
- Nirenberg MW & Matthaei JH (1961) The dependence of cell-free protein synthesis in *E. coli* upon naturally occurring or synthetic polyribonucleotides. *Proc Natl Acad Sci* 47: 1588–1602
- Nissen P, Hansen J, Ban N, Moore PB & Steitz TA (2000) The structural basis of ribosome activity in peptide bond synthesis. *Science* 289: 920–930
- Noma A, Sakaguchi Y & Suzuki T (2009) Mechanistic characterization of the sulfur-relay system for eukaryotic 2-thiouridine biogenesis at tRNA wobble positions. *Nucleic Acids Res* 37: 1335–1352
- Numata T, Ikeuchi Y, Fukai S, Suzuki T & Nureki O (2006) Snapshots of tRNA sulphuration via an adenylated intermediate. *Nature* 442: 419–424
- Oerum S, Dégut C, Barraud P & Tisné C (2017) m1A Post-Transcriptional Modification in tRNAs. *Biomolecules* 7: 20
- Oniya O, Neves K, Ahmed B & Konje JC (2019) A review of the reproductive consequences of consanguinity. *Eur J Obstet Gynecol Reprod Biol* 232: 87–96
- Otero G, Fellows J, Li Y, De Bizemont T, Dirac AMG, Gustafsson CM, Erdjument-Bromage H, Tempst P & Svestrup JQ (1999) Elongator, a Multisubunit Component of a Novel RNA Polymerase II Holoenzyme for Transcriptional Elongation. *Mol Cell* 3: 109–118
- Pabis M, Termathe M, Ravichandran KE, Kienast SD, Krutyhołowa R, Sokołowski M, Jankowska U, Grudnik P, Leidel SA & Glatt S (2020) Molecular basis for the bifunctional Uba4–Urm1 sulfur-relay system in tRNA thiolation and ubiquitin-like conjugation. *EMBO J* 39: e105087
- Palade GE (1955) A SMALL PARTICULATE COMPONENT OF THE CYTOPLASM. *J Cell Biol* 1: 59–68
- Pan T (2018) Modifications and functional genomics of human transfer RNA. *Cell Res* 28: 395–404
- Phizicky EM & Hopper AK (2023) The life and times of a tRNA. *RNA* 29: 898–957
- Pisarev AV, Skabkin MA, Pisareva VP, Skabkina OV, Rakotondrafara AM, Hentze MW, Hellen CUT & Pestova TV (2010) The role of ABCE1 in eukaryotic posttermination ribosomal recycling. *Mol Cell* 37: 196–210
- Ranjan N & Rodnina MV (2016) tRNA wobble modifications and protein homeostasis. *Translation* 4: e1143076
- Rapino F, Delaunay S, Rambow F, Zhou Z, Tharun L, De Tullio P, Sin O, Shostak K, Schmitz S, Piepers J, *et al* (2018) Codon-specific translation reprogramming promotes resistance to targeted therapy. *Nature* 558: 605–609

- Rapino F, Zhou Z, Roncero Sanchez AM, Joiret M, Seca C, El Hachem N, Valenti G, Latini S, Shostak K, Geris L, *et al* (2021) Wobble tRNA modification and hydrophilic amino acid patterns dictate protein fate. *Nat Commun* 12: 2170
- Ravichandran KE, Kaduhr L, Skupien-Rabian B, Shvetsova E, Sokołowski M, Krutyholowa R, Kwasna D, Brachmann C, Lin S, Guzman Perez S, *et al* (2022) E2 / E3 -independent ubiquitin-like protein conjugation by Urm1 is directly coupled to cysteine persulfidation. *EMBO J* 41: e111318
- Rezgui VAN, Tyagi K, Ranjan N, Konevega AL, Mittelstaet J, Rodnina MV, Peter M & Pedrioli PGA (2013) tRNA tK<sup>UUU</sup>, tQ<sup>UUG</sup>, and tE<sup>UUC</sup> wobble position modifications fine-tune protein translation by promoting ribosome A-site binding. *Proc Natl Acad Sci* 110: 12289–12294
- Rogalski M, Karcher D & Bock R (2008) Superwobbling facilitates translation with reduced tRNA sets. *Nat Struct Mol Biol* 15: 192–198
- Rosselló-Tortella M, Llinàs-Arias P, Sakaguchi Y, Miyauchi K, Davalos V, Setien F, Calleja-Cervantes ME, Piñeyro D, Martínez-Gómez J, Guil S, *et al* (2020) Epigenetic loss of the transfer RNA-modifying enzyme TYW2 induces ribosome frameshifts in colon cancer. *Proc Natl Acad Sci* 117: 20785–20793
- Rosu A, El Hachem N, Rapino F, Rouault-Pierre K, Jorssen J, Somja J, Ramery E, Thiry M, Nguyen L, Jacquemyn M, *et al* (2021) Loss of tRNA-modifying enzyme Elp3 activates a p53-dependent antitumor checkpoint in hematopoiesis. *J Exp Med* 218: e20200662
- Rubio Gomez MA & Ibba M (2020) Aminoacyl-tRNA synthetases. *RNA* 26: 910–936
- Sabatini DD (1999) George E. Palade: charting the secretory pathway. *Trends Cell Biol* 9: 413–417
- Sanger F & Tuppy H (1951) The amino-acid sequence in the phenylalanyl chain of insulin. 1. The identification of lower peptides from partial hydrolysates. *Biochem J* 49: 463–481
- Schaffrath R & Leidel SA (2017) Wobble uridine modifications—a reason to live, a reason to die?! *RNA Biol* 14: 1209–1222
- Schimmel P & De Poupiana LR (1995) Transfer RNA: From minihelix to genetic code. *Cell* 81: 983–986
- Schindler D, Walker RSK, Jiang S, Brooks AN, Wang Y, Müller CA, Cockram C, Luo Y, García A, Schraivogel D, *et al* (2023) Design, construction, and functional characterization of a tRNA neochromosome in yeast. *Cell* 186: 5237-5253.e22
- Schlieker CD, Van Der Veen AG, Damon JR, Spooner E & Ploegh HL (2008) A functional proteomics approach links the ubiquitin-related modifier Urm1 to a tRNA modification pathway. *Proc Natl Acad Sci* 105: 18255–18260
- Selvadurai K, Wang P, Seimetz J & Huang RH (2014) Archaeal Elp3 catalyzes tRNA wobble uridine modification at C5 via a radical mechanism. *Nat Chem Biol* 10: 810–812
- Shahbazian FM, Jacobs M & Lajtha A (1987) Rates of protein synthesis in brain and other organs. *Int J Dev Neurosci* 5: 39–42
- Shaheen R, Al-Salam Z, El-Hattab AW & Alkuraya FS (2016a) The syndrome dysmorphic facies, renal agenesis, ambiguous genitalia, microcephaly, polydactyly and lissencephaly (DREAM-PL): Report of two additional patients. *Am J Med Genet A* 170: 3222–3226
- Shaheen R, Mark P, Prevost CT, AlKindi A, Alhag A, Estwani F, Al-Sheddi T, Alobeid E, Alenazi MM, Ewida N, *et al* (2019) Biallelic variants in *CTU2* cause DREAM-PL syndrome and impair thiolation of tRNA wobble U34. *Hum Mutat* 40: 2108–2120

- Shaheen R, Patel N, Shamseldin H, Alzahrani F, Al-Yamany R, Al Moisher A, Ewida N, Anazi S, Alnemer M, Elsheikh M, *et al* (2016b) Accelerating matchmaking of novel dysmorphology syndromes through clinical and genomic characterization of a large cohort. *Genet Med* 18: 686–695
- Shao S, Murray J, Brown A, Taunton J, Ramakrishnan V & Hegde RS (2016) Decoding Mammalian Ribosome-mRNA States by Translational GTPase Complexes. *Cell* 167: 1229–1240.e15
- Shen C, Che Y, Zhou K, Wang K, Li W, Xue D, Wu T, Yang L, Chen M, Sheng Y, *et al* (2025) ALKBH1 Drives Tumorigenesis and Drug Resistance via tRNA-decoding Reprogramming and Codon-biased Translation. *Cancer Discov* 15: 2298–2325
- Shi H & Moore PB (2000) The crystal structure of yeast phenylalanine tRNA at 1.93 Å resolution: a classic structure revisited. *RNA N Y N* 6: 1091–1105
- Shigi N (2014) Biosynthesis and functions of sulfur modifications in tRNA. *Front Genet* 5
- Shinoda S, Kitagawa S, Nakagawa S, Wei F-Y, Tomizawa K, Araki K, Araki M, Suzuki T & Suzuki T (2019) Mammalian NSUN2 introduces 5-methylcytidines into mitochondrial tRNAs. *Nucleic Acids Res* 47: 8734–8745
- Siekevitz P & Palade GE (1958) A Cytochemical Study on the Pancreas of the Guinea Pig. *J Cell Biol* 4: 557–566
- Singer MF (1968) 1968 Nobel Laureate in Medicine or Physiology. *Science* 162: 433–436
- Smith TJ, Giles RN & Koutmou KS (2024) Anticodon stem-loop tRNA modifications influence codon decoding and frame maintenance during translation. *Semin Cell Dev Biol* 154: 105–113
- Söll D, Ohtsuka E, Jones DS, Lohrmann R, Hayatsu H, Nishimura S & Khorana HG (1965) Studies on polynucleotides, XLIX. Stimulation of the binding of aminoacyl-sRNA's to ribosomes by ribotrinucleotides and a survey of codon assignments for 20 amino acids. *Proc Natl Acad Sci* 54: 1378–1385
- Songe-Møller L, Van Den Born E, Leihne V, Vågbø CB, Kristoffersen T, Krokan HE, Kirpekar F, Falnes PØ & Klungland A (2010) Mammalian ALKBH8 Possesses tRNA Methyltransferase Activity Required for the Biogenesis of Multiple Wobble Uridine Modifications Implicated in Translational Decoding. *Mol Cell Biol* 30: 1814–1827
- Suzuki T, Nagao A & Suzuki T (2011) Human Mitochondrial tRNAs: Biogenesis, Function, Structural Aspects, and Diseases. *Annu Rev Genet* 45: 299–329
- The GTEx Consortium, Aguet F, Anand S, Ardlie KG, Gabriel S, Getz GA, Graubert A, Hadley K, Handsaker RE, Huang KH, *et al* (2020) The GTEx Consortium atlas of genetic regulatory effects across human tissues. *Science* 369: 1318–1330
- The International Mouse Phenotyping Consortium, Dickinson ME, Flenniken AM, Ji X, Teboul L, Wong MD, White JK, Meehan TF, Weninger WJ, Westerberg H, *et al* (2016) High-throughput discovery of novel developmental phenotypes. *Nature* 537: 508–514
- Thommen M, Holtkamp W & Rodnina MV (2017) Co-translational protein folding: progress and methods. *Curr Opin Struct Biol* 42: 83–89
- Tiefenbacher S, Pezo V, Marlière P, Roberts TM & Panke S (2024) Systematic analysis of tRNA transcription unit deletions in *E. coli* reveals insights into tRNA gene essentiality and cellular adaptation. *Sci Rep* 14: 24102
- Torres AG, Rodríguez-Escribà M, Marcet-Houben M, Santos Vieira HG, Camacho N, Catena H, Murillo Recio M, Rafels-Ybern À, Reina O, Torres FM, *et al* (2021) Human tRNAs with inosine

- 34 are essential to efficiently translate eukarya-specific low-complexity proteins. *Nucleic Acids Res* 49: 7011–7034
- Tronche F, Kellendonk C, Kretz O, Gass P, Anlag K, Orban PC, Bock R, Klein R & Schütz G (1999) Disruption of the glucocorticoid receptor gene in the nervous system results in reduced anxiety. *Nat Genet* 23: 99–103
- Tsherniak A, Vazquez F, Montgomery PG, Weir BA, Kryukov G, Cowley GS, Gill S, Harrington WF, Pantel S, Krill-Burger JM, *et al* (2017) Defining a Cancer Dependency Map. *Cell* 170: 564–576.e16
- Tükenmez H, Xu H, Esberg A & Byström AS (2015) The role of wobble uridine modifications in +1 translational frameshifting in eukaryotes. *Nucleic Acids Res* 43: 9489–9499
- Tuorto F, Legrand C, Cirzi C, Federico G, Liebers R, Müller M, Ehrenhofer-Murray AE, Dittmar G, Gröne H & Lyko F (2018) Queuosine-modified tRNAs confer nutritional control of protein translation. *EMBO J* 37: e99777
- Tyagi K & Pedrioli PGA (2015) Protein degradation and dynamic tRNA thiolation fine-tune translation at elevated temperatures. *Nucleic Acids Res* 43: 4701–4712
- Uhlén M, Fagerberg L, Hallström BM, Lindskog C, Oksvold P, Mardinoglu A, Sivertsson Å, Kampf C, Sjöstedt E, Asplund A, *et al* (2015) Tissue-based map of the human proteome. *Science* 347: 1260419
- Vendeix FAP, Murphy FV, Cantara WA, Leszczyńska G, Gustilo EM, Sproat B, Malkiewicz A & Agris PF (2012) Human tRNA<sup>Lys</sup>3UUU Is Pre-Structured by Natural Modifications for Cognate and Wobble Codon Binding through Keto–Enol Tautomerism. *J Mol Biol* 416: 467–485
- Wang J, Zhang Y, Mendonca CA, Yukselen O, Muneeruddin K, Ren L, Liang J, Zhou C, Xie J, Li J, *et al* (2022) AAV-delivered suppressor tRNA overcomes a nonsense mutation in mice. *Nature* 604: 343–348
- Waszak SM, Robinson GW, Gudenas BL, Smith KS, Forget A, Kojic M, Garcia-Lopez J, Hadley J, Hamilton KV, Indersie E, *et al* (2020) Germline Elongator mutations in Sonic Hedgehog medulloblastoma. *Nature* 580: 396–401
- Waters AM & Beales PL (2011) Ciliopathies: an expanding disease spectrum. *Pediatr Nephrol* 26: 1039–1056
- Wathieu C, Lavergne A, Xu X, Rolot M, Nemazany I, Shostak K, El Hachem N, Maurizy C, Leemans C, Close P, *et al* (2024) Loss of Elp3 blocks intestinal tuft cell differentiation via an mTORC1–Atf4 axis. *EMBO J*
- Watson JD & Crick FHC (1953) Molecular Structure of Nucleic Acids: A Structure for Deoxyribose Nucleic Acid. *Nature* 171: 737–738
- Weixlbaumer A, Murphy FV, Dziergowska A, Malkiewicz A, Vendeix FAP, Agris PF & Ramakrishnan V (2007) Mechanism for expanding the decoding capacity of transfer RNAs by modification of uridines. *Nat Struct Mol Biol* 14: 498–502
- Westhof E, Yusupov M & Yusupova G (2019) The multiple flavors of GoU pairs in RNA. *J Mol Recognit* 32: e2782
- Wu J, Eggers C, Sin O, Koziej Ł, Mancilla H, Mollet F, Schöler HR, Drexler H, Ranff T, Fufezan C, *et al* Codon Pair-Specific Translation Defects Trigger Ribosome-Associated Quality Control to Avoid Proteotoxic Stress.

- Xu S, Zhan M, Jiang C, He M, Yang L, Shen H, Huang S, Huang X, Lin R, Shi Y, *et al* (2019) Genome-wide CRISPR screen identifies ELP5 as a determinant of gemcitabine sensitivity in gallbladder cancer. *Nat Commun* 10: 5492
- Yared M-J, Marcelot A & Barraud P (2024) Beyond the Anticodon: tRNA Core Modifications and Their Impact on Structure, Translation and Stress Adaptation. *Genes* 15: 374
- Yoshida M, Kataoka N, Miyauchi K, Ohe K, Iida K, Yoshida S, Nojima T, Okuno Y, Onogi H, Usui T, *et al* (2015) Rectifier of aberrant mRNA splicing recovers tRNA modification in familial dysautonomia. *Proc Natl Acad Sci* 112: 2764–2769
- Yu F, Tanaka Y, Yamashita K, Suzuki T, Nakamura A, Hirano N, Suzuki T, Yao M & Tanaka I (2011) Molecular basis of dihydrouridine formation on tRNA. *Proc Natl Acad Sci* 108: 19593–19598
- Yu Y, Wang C, Wang Y, Shi H, Hu H, Du Y & Zhou Z (2024) The conserved wobble uridine tRNA thiolase Ctu1 is required for angiogenesis and embryonic development. *PLOS ONE* 19: e0315854
- Zinshteyn B & Gilbert WV (2013) Loss of a Conserved tRNA Anticodon Modification Perturbs Cellular Signaling. *PLoS Genet* 9: e1003675

Google DeepMind (2025) Gemini 3 (November 2025 version) [Large language model]. Available at: <https://gemini.google.com>

OpenAI (2025) ChatGPT with GPT-5 (October 2025 version) [Large language model]. Available at: <https://chat.openai.com>

# Appendix

## Prologue II

The following publication is included to fulfill the official regulations of the Medical University of Vienna requiring a first-author publication for the doctoral degree. As this research represents a distinct line of inquiry unrelated to the primary thesis focus on tRNA modification and human disease, it is not discussed in detail within the main body of this thesis.

The attached study, published in *Nature Communications*, characterizes a previously unstudied gene termed *FAME* (Factor Associated with Metabolism and Energy). Using comparative genomics and knockout mouse models, we identify *Fame/FAME* as a kidney-enriched, membrane-bound protein with significant evolutionary divergence. The work links *FAME* and metabolic regulation, demonstrating that its ablation leads to altered energy expenditure.

This project was initiated by Dr. Julian Petersen and Prof. Igor Adameyko at the Center for Brain Research at the Medical University of Vienna in 2016. It marks the first scientific project the author of this thesis undertook, spanning seven years – starting with his Bachelor’s thesis, continuing through his employment as a research assistant and his Master’s studies in Vienna. It was a particular pleasure to complete the final experiments and revisions during his doctoral studies at CeMM. This publication represents a major milestone: the author’s first project carried out from inception to completion. It is presented here with pride for the interested reader.

# A previously uncharacterized Factor Associated with Metabolism and Energy (FAME/C14orf105/CCDC198/1700011H14Rik) is related to evolutionary adaptation, energy balance, and kidney physiology

Received: 24 September 2021

Accepted: 11 May 2023

Published online: 29 May 2023

 Check for updates

A list of authors and their affiliations appears at the end of the paper

In this study we use comparative genomics to uncover a gene with uncharacterized function (*1700011H14Rik/C14orf105/CCDC198*), which we hereby name *FAME* (Factor Associated with Metabolism and Energy). We observe that *FAME* shows an unusually high evolutionary divergence in birds and mammals. Through the comparison of single nucleotide polymorphisms, we identify gene flow of *FAME* from Neandertals into modern humans. We conduct knockout experiments on animals and observe altered body weight and decreased energy expenditure in *Fame* knockout animals, corresponding to genome-wide association studies linking *FAME* with higher body mass index in humans. Gene expression and subcellular localization analyses reveal that *FAME* is a membrane-bound protein enriched in the kidneys. Although the gene knockout results in structurally normal kidneys, we detect higher albumin in urine and lowered ferritin in the blood. Through experimental validation, we confirm interactions between *FAME* and ferritin and show co-localization in vesicular and plasma membranes.

Through natural selection, major animal groups have developed unique mechanisms for adaptations to the environment. The genetic landscape corresponds to developmental, morphological, and physiological adaptations<sup>1</sup>. Gene regulatory regions undergo rapid evolutionary change to tune the production of mRNAs encoding the actual effectors of adaptation, the proteins. The gene products also undergo natural selection, which shapes them according to various benefits derived from their functions<sup>2</sup>. Importantly, not all such products, including mainly proteins, are essential for basic embryonic development and the mere survival of animals. Numerous gene knockout experiments in mice have highlighted a cohort of proteins that are functionally important to some extent, and yet the animals can live perfectly without them under beneficial circumstances<sup>3</sup>. These non-essential proteins convey an adaptive advantage to their hosts when

the animals are exposed to the diversity of challenging natural environments<sup>4</sup>.

Furthermore, these seemingly non-essential genes might become a basis for diverse pathologies or loss of fitness<sup>5,6</sup>. Finally, similar to essential genes, non-essential genes might be a perfect substrate for evolution, especially for tuning metabolic, stress- and energy-related features. Being non-essential, such genes can evolve much faster to provide the necessary evolvability under intense selective pressure. In extreme cases, the evolution of proteins (especially when it comes to a non-essential group) might result in a complete change of function<sup>7,8</sup> or a pseudogenization, which occurs in genes involved in dental genesis in birds, turtles, and toothless mammals<sup>9</sup>.

The comparative genomics approach<sup>10</sup> is perfectly designed to elucidate genomic protein-coding and non-coding regions responsible

✉ e-mail: [julian.petersen@medizin.uni-leipzig.de](mailto:julian.petersen@medizin.uni-leipzig.de); [igor.adameyko@meduniwien.ac.at](mailto:igor.adameyko@meduniwien.ac.at)

for different animal groups' divergence and adaptive radiation<sup>11,12</sup>. For instance, such analyses brought forward the genomic changes associated with "birdness" or "mammalness". Many identified regions appeared to be involved in the evolution of egg production, placental development, or genital shaping<sup>11,12</sup>. Indeed, the divergence of major vertebrate groups such as birds, reptiles, and mammals resulted in heavy modifications of metabolism<sup>13,14</sup>, reproduction<sup>15</sup>, and excretion<sup>16</sup>, together with associated genomic changes and adapting protein structures. For example, the processes of water and nutrient re-absorption in birds and mammals differ dramatically at structural, cellular, and molecular levels, including genetics. Birds and reptiles predominantly excrete uric acid instead of the urea used by mammals and, thus, rely on negligible amounts of water for nitrogen excretion<sup>17</sup>.

Although many of the comparative studies pinpointed well-characterized genes that can be analyzed in the context of functional networks involved in the diverging organ systems and physiological functions, the uncharacterized genes remained enigmatic in this evolutionary paradigm. Although the human and mouse genomes contain around 20,000 protein-coding genes, not all of these are identified, annotated, and characterized in terms of their expression and biological function<sup>18–20</sup>. Characterizing such genes functionally and investigating their evolutionary roles are essential to complete the holistic picture of genome transformations through time.

Here we uncovered an uncharacterized protein-coding *170001IH14Rik/C14orf105/CCDC198* gene hereby named *FAME* (*Factor Associated with Metabolism and Energy*), that evolves at an exceptional rate in birds and mammals. Specific alleles of *FAME* flow from Neandertals into modern humans, highlighting its involvement in our fitness. We addressed the expression, subcellular localization, molecular structure, functional roles, and potential disease association of *FAME*. Our results establish *FAME* as a fast-evolving gene modulating iron exchange, excretion, energy expenditure, and processes potentially associated with cancer progression.

## Results

### **FAME sequence evolves at an extra-high rate during the divergence of reptiles, birds, and mammals**

To identify previously identified genes with uncharacterized function that could ensure diverging adaptations in major amniote groups, we took advantage of the comparative genomics approach. Evolutionary pressure on proteins are often quantified by the ratio of substitution rates at non-synonymous and synonymous sites. To elucidate proteins co-evolving with major vertebrate groups, we compared the ratio of the number of non-synonymous substitutions per non-synonymous site (dN) to the number of synonymous substitutions per synonymous site (dS) (dN/dS signature) for 27, 16, and 28 pairs of genomes of birds, reptiles and mammals, respectively (Supplementary Data 1 and 2). We started with 20 pairs of mammals and birds and added 8 more pairs of mammals and 7 more pairs of birds to increase diversity. We had difficulty finding pairs for reptiles because of fewer available genomes and fewer branches on their evolutionary tree, but included several selected pairs from different clades of reptiles.

We identified 312 proteins, which showed significantly different dN/dS ratios between reptiles and birds (FDR < 0.001) (Supplementary Data 3). Among them, 129 genes had significantly higher dN/dS in reptiles, and 183 proteins had significantly higher dN/dS in birds. Interestingly, when performing bidirectional comparisons to identify proteins with the most flexible sequence in reptiles, only three proteins (STOX1, CEP126, and CCDC198) had a mean of identity of less than 60% (Fig. 1a, b and Supplementary Data 4). Two of them have been previously described. STOX1 is a protein involved in free radical equilibrium and mitochondrial function<sup>21</sup>, whereas CEP126 is a centrosomal protein involved in primary cilium formation<sup>22</sup>. The third protein, CCDC198/C14orf105 in humans or 170001IH14Rik in mice (hereafter called *FAME*, Factor Associated with Metabolism and

Energy), however, has not been characterized yet. *FAME* demonstrated a higher average of dN/dS in mammals and birds than in reptiles: 0.3912, 0.4235, and 0.2779, respectively, which indicates a high evolutionary rate in mammals and birds (Fig. 1b and Supplementary Data 4).

Despite the high rate of evolutionary changes, this protein did not undergo pseudogenization in any of the studied clades (Supplementary Fig. 1a). Next, we tested how this gene's evolution coincided with the animals' lifestyles. For this, we created the matrix of lifestyles based on the Thera-base database (<https://esapubs.org/archive/ecol/E090/184/metadata.htm> ("PanTHERIA\_I-0\_WR93\_Aug2008.txt")) with 42 recorded parameters for species with known and published genomes. Then we tested correlations between these parameters and protein alignments, but also with the selection of specific regions in the alignments (Fig. 1c, Supplementary Fig. 2a). The result suggested that specific portions of *FAME* co-evolved with metabolic and excretion traits (Fig. 1d, Supplementary Fig. 2b). This indicated that *FAME* might be involved in the control of water and nutrient exchange. To test this, we created our own matrix based on the animals' habitats, including desert-living species and water-dwelling mammals such as whales (Supplementary Data 5).

Interestingly, scanning for the highest correlation of intracellular location suggested the importance of the N-terminal region within the protein. A more in-depth sequence analysis revealed a possible N-myristoylation site and several phosphorylation sites (Supplementary Fig. 3a–d, Supplementary Data 6). This analysis also showed correlations of the *FAME* structure with the habitat (Supplementary Fig. 3e). Furthermore, no homologs in any of the explored genomes were evident, whereas a domain with unknown function DUF4619 was present.

To test if evolutionary changes of *FAME* also occurred in humans, we next analyzed the evolutionary modifications in *FAME* since the split between modern humans and Neandertals. Although some contact may have occurred<sup>23</sup>, Neandertals and modern humans evolved independently before the major out-of-Africa dispersal ~70,000 years ago<sup>24,25</sup>. During ~0.5 million years, these two lineages accumulated mutations that reached fixation, or near fixation in their genome, in both groups. To explore the recent evolution in *FAME* we investigated all single-nucleotide polymorphisms (SNPs) for which 108 Nigerian Yorubans (representing the modern human)<sup>26</sup> carry one allele in a homozygous form and three high-coverage Neandertals<sup>27–29</sup> homozygously carry a different allele. In this region encompassing *FAME* and 50 kb upstream and downstream (chr14:57886018–58010575, hg19), which we compared with the ancestral allele, we found 23 such SNPs (Fig. 1e, f, Supplementary Fig. 1b, c). For 20 of these SNPs, modern humans carry the ancestral allele, and for three SNPs Neandertals carry the ancestral allele. That more alleles are derived from the Neanderthal lineage is compatible with the lower effective population size of Neandertals<sup>30</sup>, and the fact that we only have three high-coverage Neandertals and 108 Yorubans bias us to detect alleles that are derived on the Neanderthal lineage.

Overall, these results indicate evidence for gene flow from Neandertals at the locus encompassing *FAME*. However, there are two alternative scenarios as to why the Neanderthal-like alleles in Fig. 1f could be found among present-day people. These alleles were present in the shared ancestral population between Neandertals and modern humans, or these alleles were introduced by gene flow from Neandertals when these two groups met<sup>31</sup>. In the geneflow scenario, we expect to find these alleles on long Neanderthal-like haplotypes because meiotic recombination has not had time to break these DNA segments down to shorter pieces during the time since the gene flow took place (~50,000 years). To explore these two scenarios, we calculated the linkage disequilibrium between the 23 SNPs in Fig. 1f. We found that 14 of these alleles are inherited together ( $r^2 > 0.8$ ) among the individuals ( $n = 2504$ ) in the 1000 Genomes Project

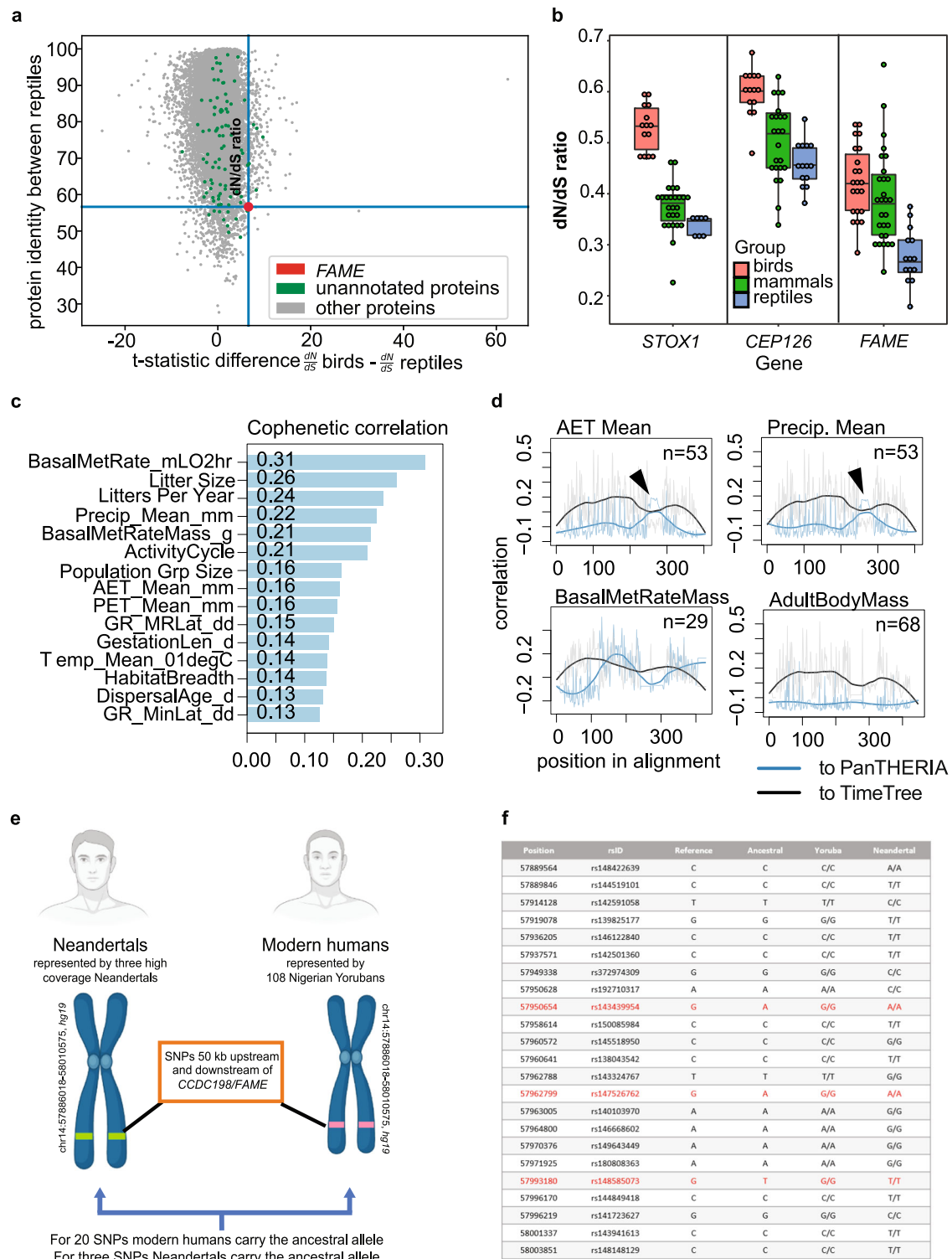
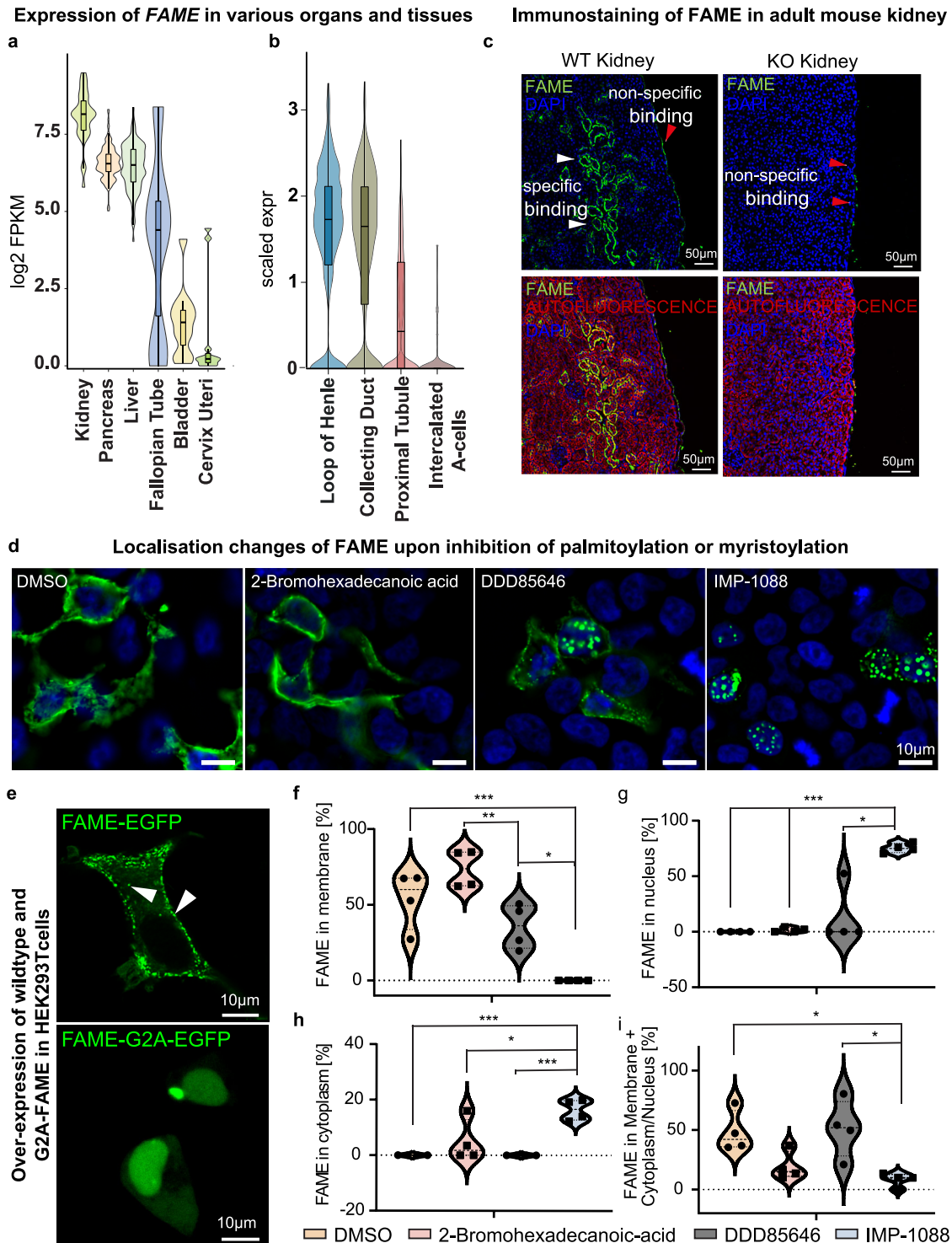


**Fig. 1 | FAME sequence changes during the evolutionary divergence of reptiles, birds, and mammals.** **a** Identification of FAME in a screen for evolutionary diverging proteins corresponding to the split of major vertebrate groups. **b** Comparison of dN/dS ratios of unannotated proteins of low protein identity between reptiles. Mean  $\pm$  SEM and *n* (genome pairs): *STOX1* birds  $0.5297 \pm 0.0120$  *n* = 14 mammals  $0.3733 \pm 0.0095$  *n* = 26 reptiles  $0.3369 \pm 0.0071$  *n* = 7. *CEP126* birds  $0.5982 \pm 0.0126$  *n* = 14 mammals  $0.5026 \pm 0.0159$  *n* = 23 reptiles  $0.4581 \pm 0.0116$  *n* = 14. *FAME* birds  $0.4235 \pm 0.0150$  *n* = 22 mammals  $0.3912 \pm 0.0176$  *n* = 28 reptiles  $0.2779 \pm 0.0144$  *n* = 14. Descriptive statistics can be accessed in Supplementary Data 13. **c** Cophenetic correlation between dendrograms obtained from amino acid sequence alignments and dendrograms based on PanTHERIA scores of different ecological

factors. The longest protein sequences were obtained for 68 mammalian species using biomaRt (Ensembl). **d** correlation between 2-mer alignment regions to ecological (PanTHERIA) and phylogenetic (TimeTree) dendrograms. The species count with both ecological data and orthologue sequence available is indicated in the top right corner. Regions with trends ties are marked with arrows. These regions are likely connected with ecological factors. Other examples are shown in Supplementary Fig. 2. Notably, there are different shapes of trends and positions of the ties. **e, f** Single nucleotide polymorphisms (SNPs) for which Neandertals (*n* = 3) and Yorubans (*n* = 108) homozygously carry different alleles. Genomic coordinates are in hg19. The ancestral alleles were taken from Ensembl<sup>90</sup> and the Neandertal alleles from previously published genomes<sup>27,28</sup>.



(Supplementary Fig. 1b). This haplotype, tagged by rs149643449-G, has a length of -87 kb (chr14:57958614-58046101) and includes the promoter region and the first two exons of FAME (Supplementary Fig. 1c), as well as the first four exons of the neighboring gene SLC35F4. We investigated if a haplotype this length could have survived since the time of the common ancestor as previously described<sup>32</sup>, i.e., using the equation  $1 - \text{GammaCDF}(m, \text{shape} = 2, \text{rate} = 1/L)$ , where  $m$  is the measured haplotype length and  $L$  the expected length given by the equation  $L = 1/(r \times t)$ . Here  $r$  is the recombination rate per generation and  $t$  is the length of the human and Neanderthal branches since divergence. Furthermore, we used the local recombination rate (1.47 cM per Mb)<sup>33</sup>, and previously published estimates of branch

lengths and generation time<sup>32</sup>. Under this assumption, the probability of a haplotype of this length surviving since the common ancestor of modern humans and Neanderthals is low ( $p = 3.7 \times 10^{-6}$ ). We thus conclude that this haplotype has been introduced in the gene pool of present-day people by gene flow from Neanderthals. In the 1000 Genomes data set<sup>26</sup>, these haplotypes are found at low frequencies in Asia, reaching a maximum allele frequency of 1.0% among Han Chinese ( $n = 208$ ) and in admixed Americans, where it reaches an allele frequency of 0.8% in people of Mexican ancestry ( $n = 64$ ).

**FAME is a membrane-associated protein enriched in the kidney, pancreas, liver, and fallopian tube.** Using Genotype-Tissue

**Fig. 2 | FAME is highly expressed in kidneys and localises to the cell membranes and vesicles.** **a** Analysis of *FAME* expression in various human tissues based on Genotype-Tissue Expression data. *FAME* expression is particularly high in the kidney, pancreas, liver, and fallopian tube. Mean  $\pm$  SEM and *n* (GTEx samples): kidney (8.071  $\pm$  0.1468 *n* = 32) pancreas (6.575  $\pm$  0.0392 *n* = 171) liver (6.447  $\pm$  0.06853 *n* = 119) fallopian tube (4.702  $\pm$  1.230 *n* = 5) bladder (1.414  $\pm$  0.3387 *n* = 11) cervix uteri (0.9330  $\pm$  0.5028 *n* = 11). **b** Detailed expression analysis of *Fame* using Tabula Muris, a single-cell atlas of the mouse. The data demonstrate high expression in kidney epithelial cell types, the loop of Henle and collecting duct cells, but also in the proximal tubules. Mean  $\pm$  SEM and *n* (single mouse cells): loop of Henle (1.546  $\pm$  0.03942 *n* = 471) collecting duct (1.403  $\pm$  0.04278 *n* = 443) proximal tubule (0.6419  $\pm$  0.02091 *n* = 1198) intercalated A-cells (0.07076  $\pm$  0.03823 *n* = 45). **c** Immunofluorescence of the adult wild type and knockout mouse kidney stained for FAME and imaged together with auto fluorescence. Representative image from 3 different animals is shown. See Supplementary Fig. 5 for additional stainings. **d** Validation of the FAME N-myristoylation site. Visualization of overexpressed fluorescently tagged FAME-EGFP in HEK293T cells upon treatment with the N-myristoylation inhibitors DDD85646 and IMP-1088 and the palmitoylation inhibitor 2-bromohexadecanoic acid (2-BP) as control. Data from 4 independent experiments is shown. **e** Overexpression of the fusion protein in HEK293T cells

shows the localisation of FAME in the plasma membrane and intracellular vesicles (white arrows). **f–i** Quantification of localisation changes of overexpressed FAME-GFP upon N-myristoylation inhibition in cellular compartments. **f** Violin plots of the percentage of FAME-EGFP localised in the plasma membrane upon treatment with the indicated inhibitors. Mean  $\pm$  SEM and *n*: DMSO (53.78  $\pm$  9.491 *n* = 4) 2-BP (73.71  $\pm$  6.262 *n* = 4) DDD85646 (35.62  $\pm$  7.446 *n* = 4) IMP-1088 (0.00  $\pm$  0.00 *n* = 4), *p*-value DMSO vs IMP-1088 = 0.0013, *p*-value 2-BP vs DDD85646 = 0.0078, *p*-value DDD85646 vs IMP-1088 = 0.0030. **g** Violin plots for nuclear FAME localization upon treatment. Mean  $\pm$  SEM and *n*: DMSO (0.00  $\pm$  0.00 *n* = 4) 2-BP (1.622  $\pm$  1.029 *n* = 4) DDD85646 (13.10  $\pm$  13.10 *n* = 4) IMP-1088 (75.36  $\pm$  2.151 *n* = 4), *p*-value DMSO vs IMP-1088 = 0.0001, *p*-value 2-BP vs IMP-1088 = 0.0001. **h** Violin plots for cytoplasmic FAME localization upon treatment. Mean  $\pm$  SEM and *n*: DMSO (0.00  $\pm$  0.00 *n* = 4) 2-BP (4.882  $\pm$  3.806 *n* = 4) DDD85646 (0.00  $\pm$  0.00 *n* = 4) IMP-1088 (16.38  $\pm$  1.882 *n* = 4), *p*-value DMSO vs IMP-1088 = 0.0001, *p*-value 2-BP vs IMP-1088 = 0.0351, *p*-value DDD85646 vs IMP-1088 = 0.0001. **i** Violin plots for membranous and cytoplasmic/nuclear FAME localisation upon treatment. Mean  $\pm$  SEM and *n*: DMSO (48.09  $\pm$  8.612 *n* = 4) 2-BP (19.05  $\pm$  5.971 *n* = 4) DDD85646 (51.34  $\pm$  12.16 *n* = 4) IMP-1088 (8.255  $\pm$  2.894 *n* = 4), *p*-value DMSO vs IMP-1088 = 0.0046, *p*-value DDD85646 vs IMP-1088 = 0.0137. Source data are provided as a Source Data file.

Expression (GTEx) data, we discovered that the expression of *FAME* was particularly high in the kidney and to a smaller extent in the pancreas, liver, and fallopian tube (Fig. 2a and Supplementary Fig. 4a). The analysis of publicly available single-cell transcriptomics data of the mouse kidney<sup>34,35</sup> further confirmed the specific expression in kidney epithelial cell types. This includes the loop of Henle and collecting duct cells, proximal tubules, and minor expression in intercalated A cells (Fig. 2b and Supplementary Fig. 4b).

By utilizing publicly available mass spectrometry data, we found evidence for the presence of FAME at the protein level in different tissues and species. For instance, FAME protein is detected in ProteomicsDB [<https://www.proteomicsdb.org>], Phosphomouse [<https://phosphomouse.hms.harvard.edu>] and PeptideAtlas [<https://db.systemsbio.org/sbeams/cgi/PeptideAtlas/Search>] public mass spectrometry databases<sup>36–39</sup>. Strong experimental evidence for FAME protein production exists in both the human<sup>40</sup> and mouse kidney<sup>37</sup>. Furthermore, FAME protein was detected in cultured murine collecting duct cells<sup>41</sup>, validating the presence of FAME protein in a cell type shown to produce its mRNA in vivo (Fig. 2b).

Therefore, we next focused on the kidney and validated the presence of FAME protein in the proximal tubules by immunohistochemistry. This is supported by the fact that we did not detect FAME in samples from knockout animals (Fig. 2c and Supplementary Fig. 5). Importantly, we ensured that our antibody is functional and specific via detecting FAME as a part of FAME-EGFP fusion in cultured cells that do not produce FAME endogenously (Supplementary Figs. 5 and 6). However, although we validated the functionality of the antibody, we must also acknowledge its limitations connected to potential low sensitivity, which results in inability to detect FAME in western blot without overexpressing FAME, which we discussed in detail in the method section.

With the help of molecular cloning and overexpression in HEK293T cells, we found that FAME localizes to plasma membranes as well as to small cytoplasmic vesicles (Fig. 2d, e, and Supplementary Fig. 4c). To further validate the predicted myristoylation site (Supplementary Fig. 3c), we treated HEK293T cells overexpressing FAME-EGFP with IMP-1088 (an inhibitor of the human N-myristoyltransferases NMT1 and NMT2) and DDD85646 (an inhibitor of *T. brucei* N-myristoyltransferase (TbNMT)), as well as, 2-Bromohexadecanoic acid as a negative control (a non-selective inhibitor of lipid metabolism) (Fig. 2d, f–i). These results show that once HEK293T cells are treated with myristoylation-specific inhibitors, the localization of FAME shifts from the plasma membrane toward the nucleus (Fig. 2f–i). DMSO treatment or the non-selective inhibition of lipid metabolism did not alter the localisation of FAME. These results

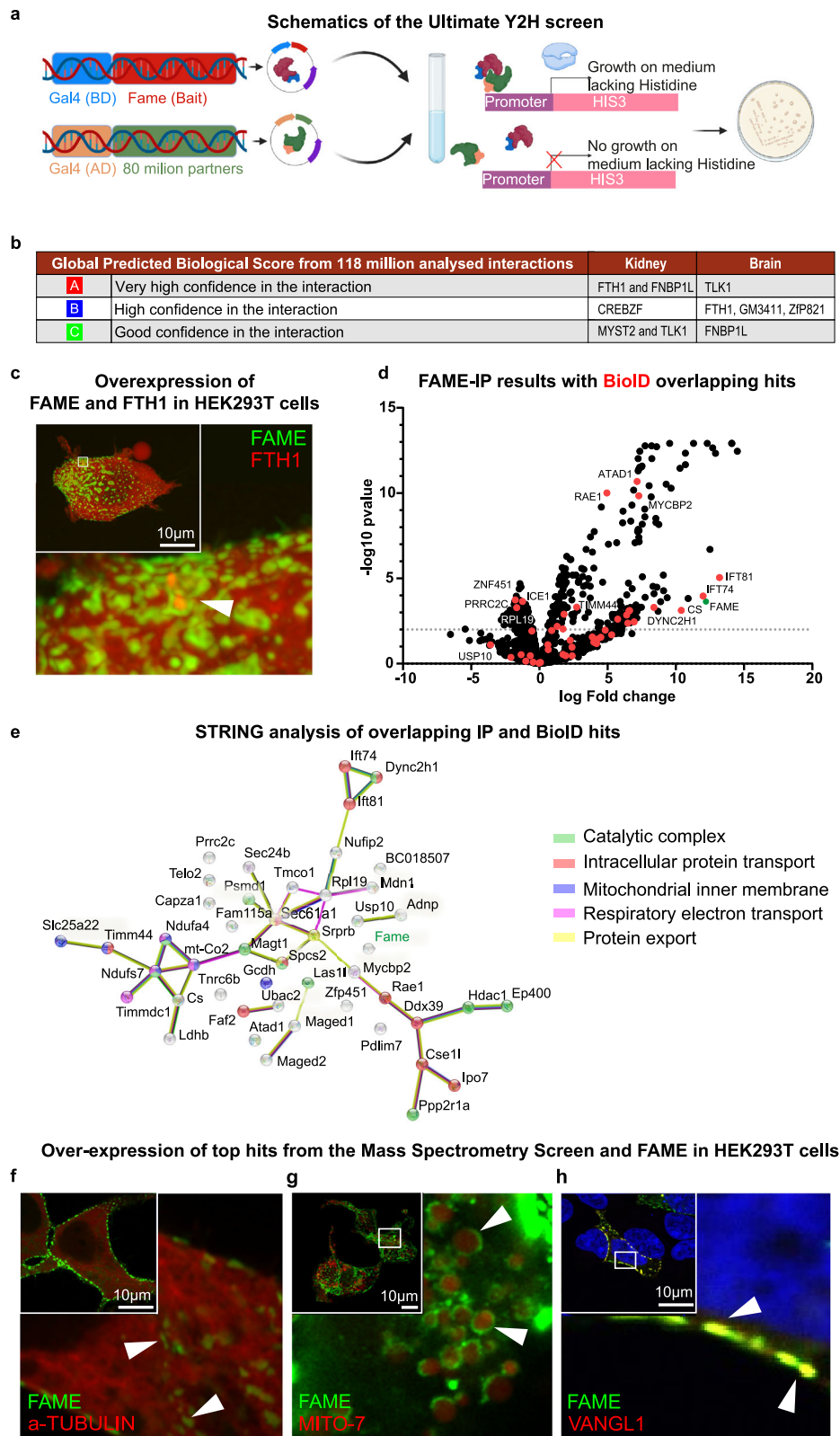
support the existence of a myristoylation site in FAME. In addition, mutating the amino-terminal glycine residue (site of myristoylation) to alanine also resulted in the nuclear localisation of the protein (Fig. 2e). Live-cell imaging experiments revealed fast trafficking of FAME in the membranes and exocytosis-related or exosome transport from transfected to non-transfected cells, as well as membrane sharing (Supplementary Fig. 4c–e and Supplementary Movie 1).

Overall, these data show a high expression and vesicular nature of FAME in the mouse kidney, suggesting a link to cellular/membrane transport.

**Binding partners of FAME suggest a role in iron metabolism and cell cycle-association.** To elucidate the molecular binding partners of FAME, we performed a yeast two-hybrid screen. For this, we used two different libraries (mouse kidney embryo from E18.5 and mouse brain embryo mix of E10.5 and E12.5) to cover more possible interaction partners (Fig. 3a). Both screens identified Ferritin Heavy Chain 1 (FTH1), Formin Binding Protein 1 Like (FNBPI), as well as Tousled Like Kinase 1 (TLK1) as top hits (Fig. 3b). *Fth1* encodes the heavy subunit of ferritin, the major intracellular iron storage protein in prokaryotes and eukaryotes. A main function of ferritin is the storage of iron in a soluble nontoxic state and further iron uptake in capsule cells of the developing kidney<sup>42</sup>. FNBPI, on the other hand, is required to coordinate membrane tubulation with the reorganization of the actin cytoskeleton during endocytosis<sup>43,44</sup>. TLK1 has several diverse substrates and is active when phosphorylated. Activation by phosphorylation is cell cycle-dependent with its peak activity in S-phase. Overexpression of TLK1 protein causes severe growth defects and cell cycle arrest in the G2/M phase with apoptosis<sup>45</sup>. Our yeast-two-hybrid screen also detected FAME interactions with transcription factors and proteins with histone H4-specific acetyltransferase activity, including CREB/ATF BZIP Transcription Factor (CREBZF) and Lysine Acetyltransferase 7 (MYST2). Both CREBZF and MYST2 are associated with cell cycle progression and replication. CREBZF arrests the growth of osteosarcoma cells by displacing MDM2 and stabilizing p53<sup>46</sup>, whereas MYST2 has crucial functions in transcription, replication, and DNA repair<sup>47</sup>.

However, since FAME was not located in the nucleus (Fig. 2d, e), the putative Y2H interaction partners in the nucleus (Fig. 3b) must be considered with caution. Nevertheless, we confirmed the interaction with FTH1 using mCherry-labelled FTH1 expressed in HEK293T cells co-transfected with GFP-tagged FAME (Fig. 3c).

To obtain a better picture of the interactome of FAME we performed a proximity-dependent biotin identification (Bio-ID) experiment together with classical immunoprecipitation followed by mass



spectrometry (Fig. 3d and Supplementary Data 7, 8). The FAME-IP results are visualized in Fig. 3d together with overlapping hits from the BioID experiment. STRING analysis of these overlapping hits revealed a strong association of FAME with the catalytic complex, intracellular protein transport, mitochondrial inner membrane, respiratory electron transport, and protein export (Fig. 3e). These data are supported by gene correlation data from publicly available single-cell

transcriptomics data of various tissues (Supplementary Fig. 7). From these positive correlations, we could show the co-localization of genes specific for the microtubule, mitochondria, and PCP-pathway association of the FAME protein (Fig. 3f-h).

**FAME controls the excretion of nutrients and iron.** To understand the functional role of FAME in general development, the morphology

**Fig. 3 | Binding partners of FAME suggest a role in iron metabolism.** **a** Graphical representation of the ULTImate Y2H™ screen performed by Hybrigenics. Mouse FAME bait was cloned into the pB27 (N-LexA-AKR2-C fusion) vector, and used for screening using mouse kidney embryo\_RP1 and mouse embryo Brain\_RP2 fragment libraries as prey. The interaction of two proteins reconstitutes an active transcription factor and enables yeast growth. **b** Top scoring interaction partners for kidney embryo and embryo brain libraries are indicated. In total, 118 million interactions were tested. **c** Validation of FTH1 as top FAME interaction partner from the ULTImate Y2H™ screen. FAME-EGFP was overexpressed together with FTH1-mCherry to visualize the heavy subunit of ferritin in HEK293T cells. The white arrow points towards encapsulated FTH1 by FAME. Representative image of 3 independent experiments. **d** Visualization of FAME interaction partners identified by both

immunoprecipitation (IP)/mass spectrometry and proximity-dependent biotin identification analysis (BioID). **e** STRING analysis from all overlapping IP and BioID hits. **f–h** Validation of top FAME interaction partners from the mass spectrometry analysis. Representative image of 3 independent experiments. **f** Overexpression of FAME-EGFP together with  $\alpha$ -Tubulin-mCherry in HEK293 cells for the visualization of microtubules. White arrows point at FAME co-localising with  $\alpha$ -Tubulin. **g** Overexpression of FAME-EGFP together with MITO-7-mCherry to identify mitochondria. White arrows highlight the membranous localisation of FAME in mitochondria. **h** Overexpression of FAME-EGFP and VANGL1-myc visualized with an anti-VANGL1 antibody. White arrows show co-localization of both proteins within the plasma membrane.

of organs, and its physiology, we generated *Fame* knockout mice using an *FVB/Ant* genetic background. CRISPR/Cas9 was used to create these knockout mice by inserting a double STOP codon downstream of the initiator ATG (see Methods section). These mice appeared viable without major developmental, morphological, or behavioural defects. We could effectively propagate the colony in the homozygous knockout state.

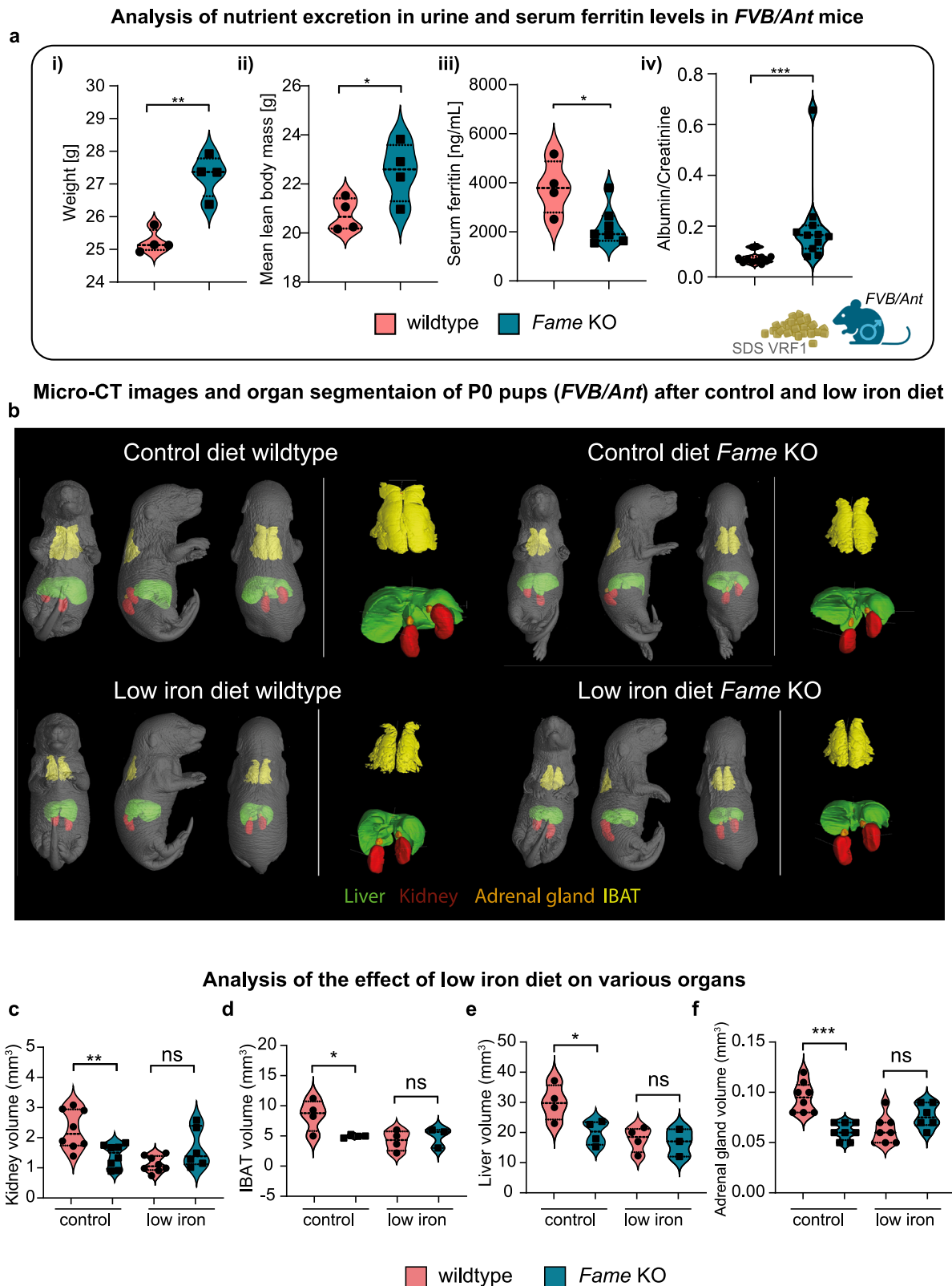
Interestingly, body weight and mean lean body mass were significantly altered in *FVB/Ant Fame* knockout mice (Fig. 4a(i, ii)). When analysing serum ferritin levels, we revealed a significant decrease in ferritin in knockout animals compared to the control (Fig. 4a(iii)). Furthermore, we found an unusually high amount of albumin in the urine of knockout animals (Fig. 4a(iv)). To examine this phenotype in more detail, we carefully investigated the kidneys of control and knockout animals. Analysis of the kidney volumes of adult, 12-week old mice and the amount and size of the filtering glomeruli did not show any differences (Supplementary Fig. 8a). Histological analyses of Periodic acid–Schiff (PAS) sections showed normal histomorphology in both wild type and *Fame* knockout mice, without any signs of pathological alterations of glomeruli, vessels, or the tubulointerstitium (Supplementary Fig. 8b). As consequences of kidney malfunction, particularly proteinuria, can be affected by changes only visible at the ultrastructural level, we also analysed the kidneys using transmission electron microscopy. The analysis showed an intact and normally developed filtration barrier of the glomeruli (Supplementary Fig. 8b), with regularly shaped podocyte foot processes, regular glomerular basal membrane, and thin fenestrated endothelium of glomerular capillaries. Also, the tubular cells showed a normal ultrastructural appearance with a prominent brush border in proximal tubules and high amounts of mitochondria. No signs of metabolic stress were observed, including no signs of intracellular accumulations of lipids or glycogen, increased vesicles, or high lysosomal activity.

Because adult homozygous knockout animals did not show any structural phenotype at the level of the kidney, we hypothesized that FAME might convey specific adaptive highly tunable functions and is important for the competitiveness of animals in different ecological niches. To address the role of FAME in adverse environmental conditions and to challenge the developing systems of organs, we tested the effect of a low iron diet during embryonic development of wild type and knockout mice (*FVB/Ant* background). For this, we kept females on a low-iron or control diet for four weeks before mating. New-born pups were then analysed using microCT coupled with 3D segmentation. All *Fame* (*FVB/Ant*) knockout mice on the control diet showed a size reduction of the kidneys, adrenal glands, interscapular brown adipose tissue, and liver compared to the wild type mice on a control diet. This phenotype was comparable with control pups being on a low-iron diet. *Fame* (*FVB/Ant*) knockout mice on a low-iron diet showed no further changes in organ size (Fig. 4b–f). These findings suggest that FAME is important for scaling the inner organs in response to adverse conditions, including the energy storages observed by the reduced interscapular brown adipose tissue.

To dig deeper into the function of FAME, particularly in the kidney, we performed single-cell RNA sequencing of wild type and knockout kidney samples (*FVB/Ant* background) (Fig. 5a–c and Supplementary Fig. 9). The data confirmed the presence of two consecutive stop codons in the protein-coding region of *Fame* mRNA in individual cells from the knockout condition (Supplementary Fig. 10a). As a main result, the single-cell transcriptomics analysis confirmed the presence of all cell populations in knockout kidneys, with only minor compositional changes (Fig. 5a, b). By analyzing the gene expression within clusters in more detail, we identified only a few significant differentially expressed genes (Fig. 5c and Supplementary Fig. 10b–e), including the previously identified FAME-binding, iron-transporting *Fth1* and *Slc25a39*—a mitochondrial membrane transporter involved in biosynthesis and potentially iron homeostasis<sup>48</sup>. This suggests that the knockout phenotype has a molecular nature without noticeable defects at tissue organization levels.

Next, to investigate if such metabolism tuning roles of FAME depend on the genetic background<sup>49,50</sup> and additional modifications of experimental conditions, we created and tested a second mouse knockout model using a *C57BL/6Ncr1* background. Although the excretion of albumin in the urine and serum ferritin levels were not altered in these mice with knocked out *Fame*, the body weight and lean body mass were significantly changed (Supplementary Fig. 11). These two knockout models on different genetic backgrounds revealed that depending on the exact genetic background, the body weight and lean body mass show different significant alterations compared to the controls of the same background. The reason for these differences can be multifaceted and might include the complex and divergent context of differentially expressed interacting molecules. For instance, the controls of different backgrounds showed differences in the excretion of albumin and serum levels at steady state (compare Fig. 4a and Supplementary Fig. 11). Furthermore, the differences in fine movement and the changed metabolic status in both animal groups can cause differences in body weight and lean body mass. Interestingly, despite the differences in weight changes in the two knockout models, the level of the energy balance influencing hormones ghrelin and leptin were not significantly changed in either mouse model (Supplementary Fig. 12). Furthermore, analysis of multiple additional blood parameters did not show significant differences, except a decreased platelet count in knockout females with an *FVB/Ant* background (Supplementary Fig. 13) and lower eosinophil number in females with a *C57BL/6Ncr1* background (Supplementary Fig. 14).

**Knockout of *Fame* influences metabolic parameters and activity of the animals.** To elucidate the metabolic phenotype of the knockout animals, we performed metabolic phenotyping. Measurements were performed on 75-day old male mice with an *FVB/Ant* background, four wild type and four *Fame* knockout mice, after a three-day training phase in specific metabolic cages. For the *C57BL/6Ncr1* experimental group of similar age, we had eight wild type and ten knockout males and seven wild type and five knockout females, that underwent metabolic phenotyping. Food and water intake, locomotor activity, O<sub>2</sub>



consumption, and  $\text{CO}_2$  production of the mice were monitored for 48 h. Before and after the measurement, body composition analysis of the mice was carried out by EchoMRI (Fig. 6a). As stated above, knockout animals with *FVB/Ant* genetic backgrounds showed a significantly higher average body weight as compared to the wild types (Fig. 4a). Interestingly, the effect was reversed in the *C57BL/6Ncr1* background group (Supplementary Fig. 11). These differences in body

weight suggest that *Fame* deletion alters energy homeostasis in a way depending on different genetic backgrounds.

When we investigated food intake and normalized it to total body weight, only the food intake of the knockout mice with *FVB/Ant* background was significantly lower during the daytime (Fig. 6b).

In addition, the energy expenditure of the *FVB/Ant* *Fame* knockout animals normalized for total body weight (Fig. 6b), as well as Z-activity,

**Fig. 4 | *Fame* is involved in the excretion of proteins and participates in the scaling of inner organs under adverse conditions such as nutrient deficiency.**

**a** (i) Violin plots showing the differences in weight between male wildtype and *Fame* knockout (KO) animals on an *FVB/Ant* background. Mean  $\pm$  SEM and *n* for each group: WT (27.26  $\pm$  0.3204 *n* = 4), KO (25.24  $\pm$  0.1775 *n* = 4), *p*-value WT vs KO = 0.0015. (ii) Comparison of mean lean body mass. Mean  $\pm$  SEM and *n*: WT (20.75  $\pm$  0.3303 *n* = 4) KO (22.50  $\pm$  0.5986 *n* = 4), *p*-value WT vs KO = 0.0436. (iii) Comparison of serum ferritin levels. Mean  $\pm$  SEM and *n*: WT (3817  $\pm$  548.6 *n* = 4) KO (2238  $\pm$  295.5 *n* = 7), *p*-value WT vs KO = 0.0206. (iv) Comparison of urine albumin to creatinine ratio. Mean  $\pm$  SEM and *n*: WT (0.07496  $\pm$  0.007053 *n* = 11) KO (0.1983  $\pm$  0.04809 *n* = 11), *p*-value Mann-Whitney test WT vs KO < 0.0001. **b** Micro-CT images of P0 pups with control and low iron diet, containing 178.58 mg iron/kg or 5.16 mg iron/kg, respectively. The kidney (red), interscapular brown adipose tissue (IBAT) (yellow), liver (green) and adrenal glands (orange) are segmented

using 3D Visualization software and superimposed onto the pups. **c–f** Violin plots comparing inner organ scaling amongst P0 wildtype and knockout pups on different diets. **c** Kidney volume. Mean  $\pm$  SEM and *n*: WT control (2.261  $\pm$  0.2301, *n* = 8), KO control (1.401  $\pm$  0.1354, *n* = 8), *p*-value WT control vs KO control = 0.0062, WT low iron (1.120  $\pm$  0.0973, *n* = 8), KO low iron (1.642  $\pm$  0.2669, *n* = 6). **d** IBAT volume. Mean  $\pm$  SEM and *n*: WT control (8.44  $\pm$  1.299, *n* = 4), KO control (4.955  $\pm$  0.1169, *n* = 4), *p*-value WT control vs KO control = 0.037, WT low iron (4.210  $\pm$  0.8292, *n* = 4), KO low iron (4.897  $\pm$  0.9432, *n* = 3). **e** Liver volume. Mean  $\pm$  SEM and *n*: WT control (29.94  $\pm$  2.959, *n* = 4), KO control (19.90  $\pm$  1.988, *n* = 4), *p*-value WT control vs KO control = 0.0304, WT low iron (17.72  $\pm$  2.049, *n* = 4), KO low iron (16.72  $\pm$  2.632, *n* = 3). **f** Adrenal gland volume. Mean  $\pm$  SEM and *n*: WT control (0.095  $\pm$  0.005345, *n* = 8), KO control (0.06125  $\pm$  0.002950, *n* = 8), *p*-value WT control vs KO control < 0.0001, WT low iron (0.06250  $\pm$  0.00491, *n* = 8), KO low iron (0.07667  $\pm$  0.004944, *n* = 6). Source data are provided as a Source Data file.

a measure for exploratory behaviour, of *C57BL/6Ncr1* knockout animals differed significantly compared to wild type mice of their corresponding genetic background (Fig. 6c and Supplementary Fig. 15).

Of note, we detected a noticeable tendency for changes in fine activity in the *FVB/Ant* background mice: the knockout animals showed fewer fine movements at night, and their average fine movements were fewer as compared to the wild types (Fig. 6b).

Since both mouse models exhibited slightly different metabolic profiles, we challenged them using different approaches to further validate the previously observed phenotypes. To exclude the effect of food on energy expenditure and the potential impact of the differing daytime food intake between the genotypes on a *FVB/Ant* background, we repeated the experiment upon fasting. For this, we removed the food from the cage, and started the measurement after an 8-hour-long fasting period without the further addition of food. During this setup, the same parameters as in the experiments before were monitored for 24 h.

Similar to the experiment before, we observed differences between the two groups of *FVB/Ant* mice in activity at the beginning of the night-time. Both fine and Z-activity differed significantly early during the 12-hour dark period (Supplementary Fig. 16a–d). In line with this, the energy expenditure of the *FVB/Ant* knockout mice was significantly less between 7 and 9 PM as compared to controls of the same background (Supplementary Fig. 16e, f). These data indicate that the food-seeking activity of the *FVB/Ant* knockout animals was less pronounced compared to wild types. These time points early during the dark period overlap with the intensive food-seeking activity of *FVB/Ant* wild type mice, indicating that the significantly higher energy expenditure of the *FVB/Ant* wild type animals is due to the higher locomotor activity. On the other hand, it is worth mentioning that the energy expenditure of the *FVB/Ant* knockout mice stayed below the energy expenditure of *FVB/Ant* wild type mice during the whole measurement. Overall, *FVB/Ant* knockout mice had higher body weight with higher lean body mass. Furthermore, *FVB/Ant* knockout mice seemed to be less hungry after 8-hour fasting periods resulting in less intense food-seeking behavior. The energy expenditure of the *FVB/Ant* knockout mice was significantly lower due to their decreased locomotor activity.

Next, we challenged *C57BL/6Ncr1* mice by exposing them to a first warm and then cold environment to study effects on energy expenditure of knockout animals. While effects on energy expenditure were small, we did find that depending on the sex of the animals, different measured parameters, such as Z-activity, food intake and to a low degree energy expenditure, were altered differently between females (Supplementary Fig. 17) and males (Supplementary Fig. 18). This suggests that *FAME* has a sex-specific role.

These results support the evolutionary diverging and plastic role of *FAME* in tuning the energy expenditure balance in various animal groups and different genetic backgrounds.

In humans, the analysis of genome-wide association studies (GWAS) showed a correlation of mutations in *FAME* with higher body

mass index and diabetes-related pathologies as well as macular degeneration (Supplementary Fig. 19). These results are in line with our previous findings, fitting that iron homeostasis and age are factors related to macular degeneration<sup>51</sup>, together with the role of iron in diabetes and body mass indexes<sup>52</sup>.

To investigate this further, we examined the phenotypic effects of recent evolutionary changes in *CCDC198* (*FAME*) on the modern human lineage. Of the three mutations derived from the modern human lineage (rs143439954, rs147526762, rs148585073) (Fig. 1f), only rs147526762 has an ancestral allele still present among Europeans (allele frequency ~0.1%). Given that the vast majority of genetic association studies have been carried out on Europeans, we explored whether rs147526762 had any phenotypic effects relating to the phenotypes discussed above (metabolic syndromes, kidney-related disorders, and macular degeneration). We examined possible associations using PhenoScanner<sup>53</sup>, and although no association passed correction for multiple comparisons, the hit with the lowest *p*-value was an association with high-density lipoprotein (*p* = 0.02, beta = 0.74, inverse normally transformed units) from the UK Household Longitudinal Study<sup>54</sup>. For this association, the ancestral allele increased the HDL levels. We also investigated any association between rs147526762 and 1,400 broad phenotypes among 400,000 Britons (using UK BioBank data and PheWeb (PheWeb, n.d.)). The association with the lowest *p*-value was against hypertensive chronic kidney disease, for which the ancestral Neanderthal-like allele increases the risk (*p* = 0.04, beta = 6.6, log odds units). Although these associations did not pass correction for multiple comparisons, we note that the tentative associations match the here suggested role of *CCDC198* (*FAME*). The low allele frequency of the ancestral allele makes phenotypic analyses challenging. Future, more extensive studies, particularly among Southern Han Chinese people, where 3% carry the ancestral allele<sup>26</sup>, are needed to corroborate these putative associations.

**Correlation of *FAME* with cancer.** Due to the metabolic phenotypes observed in *FAME* knockout mice, we became interested in the role of *FAME* in tumors, where energy expenditure and metabolism are altered. Indeed, the expression of *FAME* appeared stably maintained in all tumor types derived from healthy human *FAME*<sup>+</sup> tissues and cell types according to our analysis of public TCGA and GTEx datasets (Fig. 7a, b and Supplementary Fig. 20a). The survival probability of different types of cancer can be stratified by low or high *FAME* expression (Supplementary Fig. 20b). To test this in vitro, we over-expressed *FAME* in HEK293T and A549 cells (human adenocarcinoma from the lung), which led to a decrease in proliferation (Fig. 7c, d). The knockout of *FAME* in HEK293T cells by CRISPR-Cas9 genome editing did not lead to a change in proliferation (data not shown). This is likely because *Fame* is not endogenously expressed in HEK293T cells, as confirmed by qPCR (Supplementary Fig. 20c) and according to human protein atlas data. Conversely, the knockout of

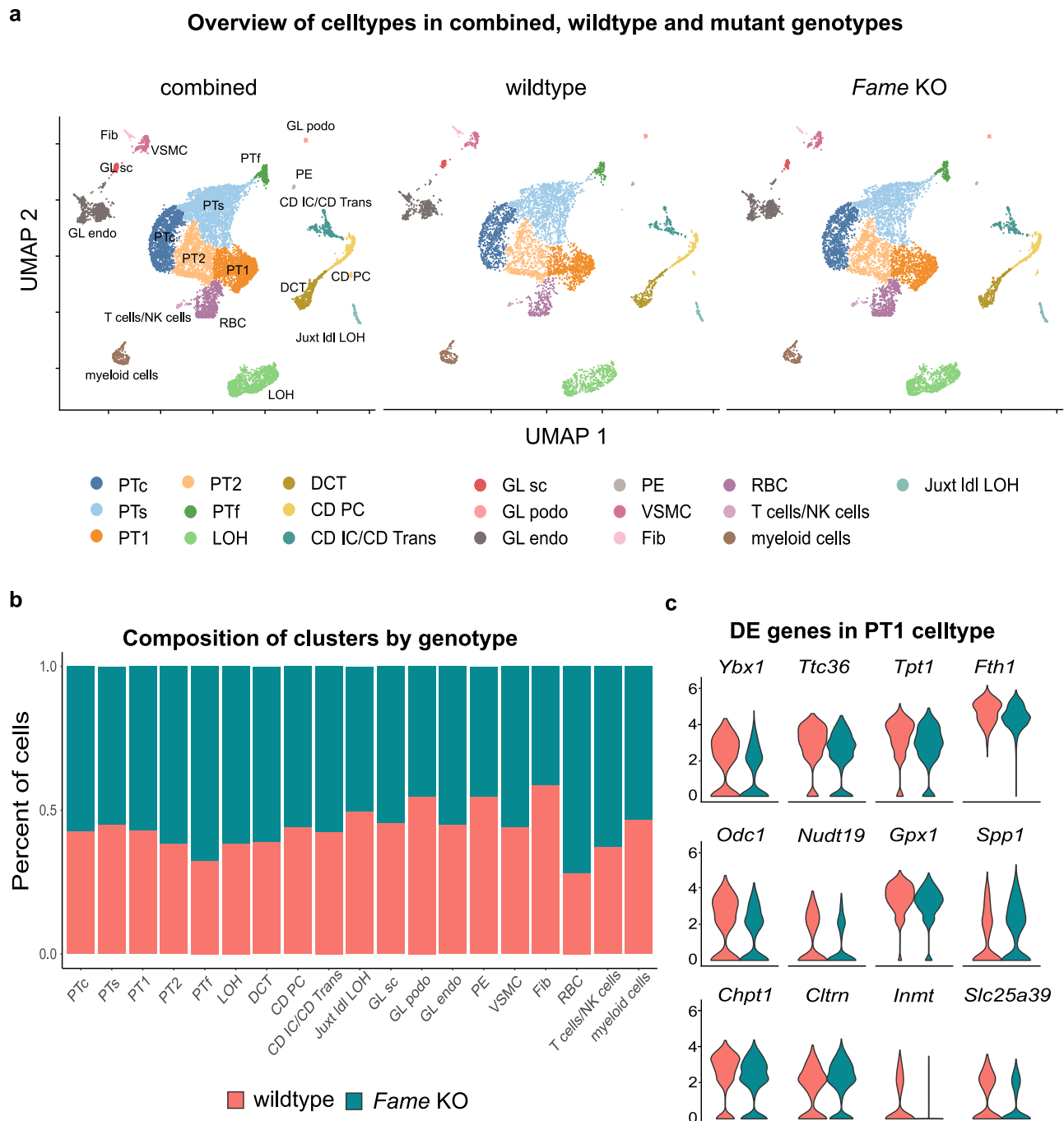


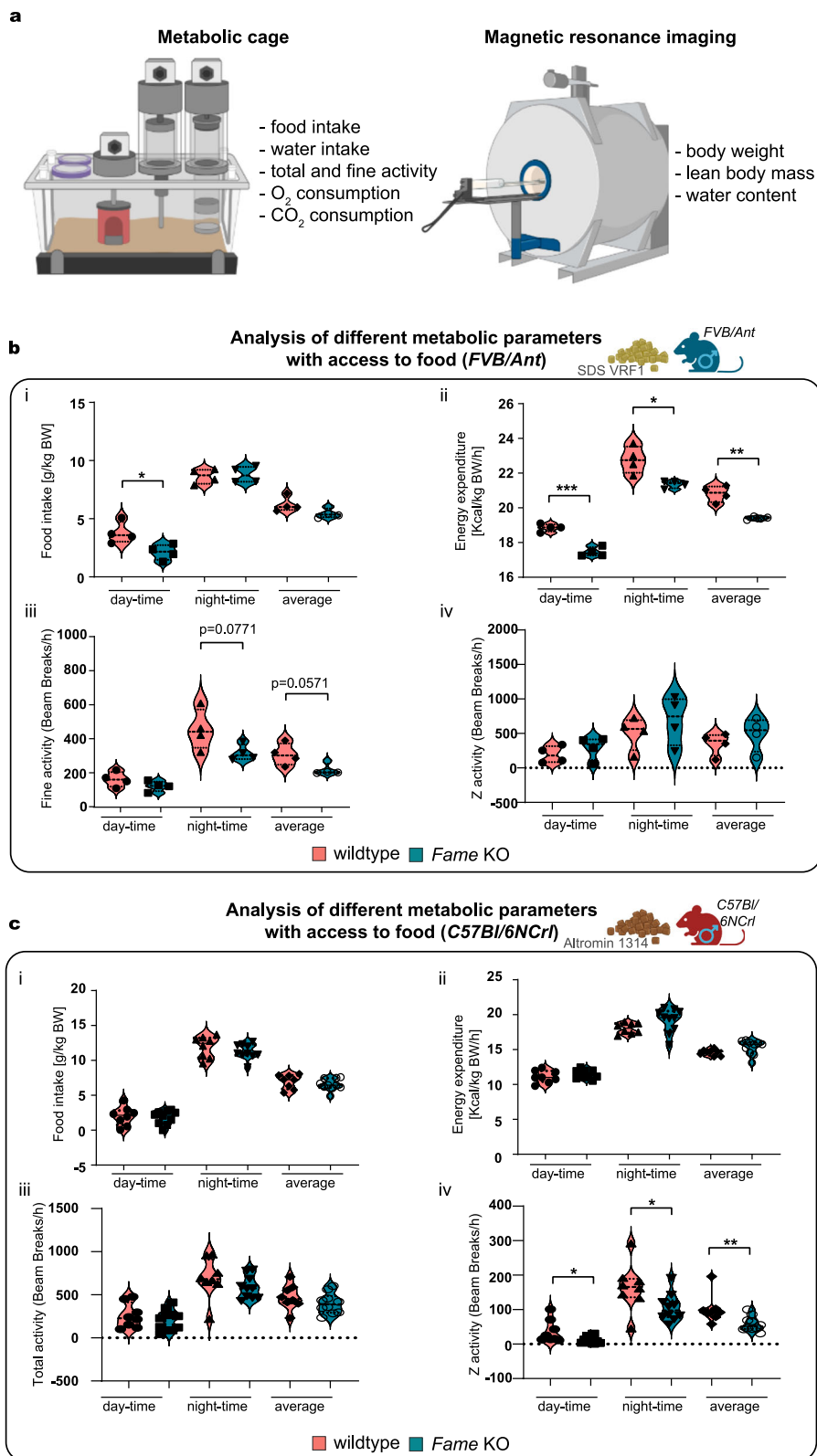
**Fig. 5 | Single-cell sequencing reveals minor molecular changes in *Fame* knockout kidneys. **a** UMAP embedding of the adult mouse kidney scRNA-seq combined dataset, with the distribution of wildtype and *Fame* KO cells. Cell types are indicated. PTc proximal convoluted tubules, PTs proximal straight tubule, PTF female-specific cells, PT1 unidentified subcluster of PT, PT2 unidentified subcluster of PT, GL endo endothelial cells in glomeruli, GL podo podocytes in glomeruli, GL sc putative stem cells, LOH loop of Henle, DCT distal convoluted tubule, CD PC**

collecting duct principal cells, CD IC/CD Trans collecting duct intercalated cells and transitional cells, VSMC vascular smooth muscle cells, Juxt ldl LOH long descending limb of the loop of Henle in juxtamedullary nephrons, PE parietal epithelium in glomeruli, Fib fibroblasts, RBC red blood cells. **b** Stacked bar plots of combined dataset illustrating the composition of cell types by genotype. **c** Violin plots of significantly differentially expressed genes in the PT1 cluster.

*FAME* in A549 cells that express it at high endogenous levels resulted in a proliferation increase, as shown in two independent knockout cell lines (Fig. 7e, f).

To get a better picture of FAME in relation to cancer, we aimed to check the localization of the protein in different tumor cell types. For this, we used two tumor cell lines, A549 and 786-O (human renal cell adenocarcinoma) that also expresses *FAME* at high endogenous levels. FAME was highly present in these cells in membranous

protrusions and appeared specifically enriched during cell division (Supplementary Fig. 21a, b). Next, the immunohistochemistry analysis on cryo-slices of human renal healthy and tumor tissues showed that FAME localized predominantly to the plasma membrane of healthy cells. In contrast, it appeared heavily internalized in malignant tissue (Supplementary Fig. 21c). This might indicate the role and trafficking activity of this protein during an altered metabolic state of tumor cells.



Comparing the survival probability of patients with kidney renal papillary cell carcinoma (KIRP) and kidney renal clear cell carcinoma (KIRC) indicated a tendency towards a higher survival of patients with higher expression levels of *FAME* with a *p*-value of 0.08 and 0.071, respectively (Supplementary Fig. 20b). Along this line we tested whether cells with lowered *FAME* protein levels—given its interaction with iron-storing *FTH1*—could be specifically targeted using Ferroptosis

inducing drugs. However, this does not seem to be the case in human A549 KO cells (Supplementary Fig. 21d). Yet, our single-cell transcriptomics experiment revealed that *FAME* knockout kidneys show significant downregulation of genes associated with epithelial to mesenchymal transition (EMT) (Fig. 5c and Supplementary Data 9). Among those were: *Ybx1*<sup>55</sup>, *Tpt1*<sup>56</sup>, *Odc1*<sup>57</sup>, *Gpx1*<sup>58</sup>, and *Spp1*<sup>59</sup>. Correspondingly, the analysis of a public single-cell transcriptomics atlas of

**Fig. 6 | Knock out of *Fame* influences metabolic parameters and activity.**

a Graphical representation of the performed metabolic cage and magnetic resonance imaging experiments. Measured parameters are listed. **b** (i-iv) Metabolic cage experiments using 75-day old male mice. Wildtype and *Fame* KO animals on *FVB/Ant* background are compared. 12-hour light (day) and dark (night) periods and 24-hour averages are shown. (i) Food intake normalized to body weight. Mean  $\pm$  SEM and *n* for each group: WT day-time ( $3.780 \pm 0.4648$  *n* = 4), KO day-time ( $2.120 \pm 0.3283$  *n* = 4), *p*-value (day-time WT vs KO) = 0.0267, WT night-time ( $8.648 \pm 0.3195$  *n* = 4), KO night-time ( $8.785 \pm 0.3498$  *n* = 4), WT average ( $6.215 \pm 0.3284$  *n* = 4), KO average ( $5.453 \pm 0.2056$  *n* = 4). (ii) Energy expenditure, normalized by body weight. Mean  $\pm$  SEM and *n* for each group: WT day-time ( $18.85 \pm 0.1104$  *n* = 4), KO day-time ( $17.46 \pm 0.1311$  *n* = 4), *p*-value (day-time WT vs KO) = 0.0002, WT night-time ( $22.77 \pm 0.3909$  *n* = 4), KO night-time ( $21.36 \pm 0.1067$  *n* = 4), *p*-value (night-time WT vs KO) = 0.0130, WT average ( $20.81 \pm 0.2344$  *n* = 4), KO average ( $19.41 \pm 0.04249$  *n* = 4), *p*-value (average WT vs KO) = 0.0011. (iii) Fine activity. Mean  $\pm$  SEM and *n* for each group: WT day-time ( $152.0 \pm 22.28$  *n* = 4), KO day-time ( $111.6 \pm 15.09$  *n* = 4), WT night-time ( $444.2 \pm 59.6$  *n* = 4), KO night-time ( $307.4 \pm 23.88$  *n* = 4), *p*-value (night-time WT vs KO) = 0.0771, WT average ( $298.1 \pm 32.48$  *n* = 4), KO average ( $209.5 \pm 17.0$  *n* = 4), *p*-value Mann-Whitney test (average WT vs KO) = 0.0571. (iv) Z-activity. Mean  $\pm$  SEM and *n* for each group: WT day-time ( $193.9 \pm 61.34$  *n* = 4), KO day-time ( $291.7 \pm 83.16$  *n* = 4), WT night-time ( $504.4 \pm 120.1$  *n* = 4), KO night-time ( $691.0 \pm 176.1$  *n* = 4), WT

average ( $349.2 \pm 81.28$  *n* = 4), KO average ( $491.4 \pm 122.9$  *n* = 4). **c** (i-iv) Metabolic cage experiments using 70-day old male mice. Wildtype and *Fame* KO animals on *C57BL/6NcrJ* background are compared. 12-hour light (day) and dark (night) periods and 24-hour averages are shown. (i) Food intake normalized to body weight. Mean  $\pm$  SEM and *n* for each group: WT day-time ( $1.996 \pm 0.4721$  *n* = 8), KO day-time ( $1.834 \pm 0.3098$  *n* = 10), WT night-time ( $11.92 \pm 0.5476$  *n* = 8), KO night-time ( $11.24 \pm 0.3413$  *n* = 10), WT average ( $6.958 \pm 0.3622$  *n* = 8), KO average ( $6.535 \pm 0.2606$  *n* = 10). (ii) Energy expenditure, normalized to body weight. Mean  $\pm$  SEM and *n* for each group: WT day-time ( $11.13 \pm 0.3114$  *n* = 8), KO day-time ( $11.44 \pm 0.1955$  *n* = 10), WT night-time ( $18.04 \pm 0.2678$  *n* = 8), KO night-time ( $19.19 \pm 0.5414$  *n* = 10), WT average ( $14.59 \pm 0.1513$  *n* = 8), KO average ( $15.31 \pm 0.3281$  *n* = 10). (iii) Total activity (fine movements and beam breaks). Mean  $\pm$  SEM and *n* for each group: WT day-time ( $256.6 \pm 50.68$  *n* = 8), KO day-time ( $214.6 \pm 37.37$  *n* = 10), WT night-time ( $691.9 \pm 82.49$  *n* = 8), KO night-time ( $584.6 \pm 41.67$  *n* = 10), WT average ( $474.4 \pm 50.82$  *n* = 8), KO average ( $399.5 \pm 37.80$  *n* = 10). (iv) Z-activity. Mean  $\pm$  SEM and *n* for each group: WT day-time ( $36.63 \pm 11.72$  *n* = 8), KO day-time ( $11.90 \pm 3.136$  *n* = 10), *p*-value (day-time WT vs KO) = 0.0388, WT night-time ( $164.9 \pm 24.29$  *n* = 8), KO night-time ( $105.8 \pm 12.59$  *n* = 10), *p*-value (night-time WT vs KO) = 0.0359, WT average ( $100.8 \pm 14.47$  *n* = 8), KO average ( $58.80 \pm 6.772$  *n* = 10), *p*-value Mann-Whitney test (average WT vs KO) = 0.0059. Source data are provided as a Source Data file.

mouse neural crest development<sup>60</sup> showed that *FAME* is explicitly expressed during epithelial-to-mesenchymal transition (EMT), which we validated with immunohistochemistry (Supplementary Fig. 5e, f). Thus, a potential role of *FAME* in the process of EMT may be linked to local invasion and metastasis during cancer progression, which warrants further investigations.

## Discussion

The elucidations of the role of uncharacterized protein-coding genes in the mammalian genome have been fairly uncommon in recent years. Despite the early genome sequencing efforts that have fuelled waves of massive characterizations<sup>61</sup>, some proteins have avoided close attention, and 170001H14Rik/C14orf105/CCDC198 has remained such a “lost in a genome” exception.

During this study, we initially aimed to find proteins conveying specific molecular adaptations behind the grand evolutionary splits between reptiles, birds, and mammals in different environments. Using a sophisticated comparative genomics screen, we identified a range of such proteins, among them, we spotted 170001H14Rik/C14orf105/CCDC198, which we named *FAME* (Factor Associated with Metabolism and Energy). This protein appeared to be one of a kind, without additional paralogs in the genome. The phylogenetic analysis revealed a fast evolutionary pace with specific and distinct divergence in the corresponding gene structure in birds and mammals identified by comparing dN/dS ratios. Furthermore, we wanted to establish if the evolutionary divergence in specific parts within the protein structure can be linked to the lifestyles of various mammals. This could give a hint of the role of the protein itself. By performing such correlation analyses, we found specific regions in this protein where evolutionary changes coincided with land-based, water-based, desert-dwelling, or other specific modalities of life. Altogether, these correlations suggested the possible role of *FAME* in balancing energy expenditure and excretion.

Furthermore, the involvement of *FAME* in fitness control is supported by allele flow from Neandertals into modern humans. Compelled by the fact that the function of this protein has remained unknown, we decided to proceed with molecular and functional characterization of the protein in vivo and in vitro systems.

The analysis of expression patterns suggested a role of *FAME* in inner organs, including the kidney, pancreas, fallopian tube, and liver. The prominent expression in kidneys led us to investigate these in more detail. Here, the knockout of *Fame* in mice with an *FVB/Ant* background confirmed that the excretory function of kidneys was

failing, leading to a decline of ferritin levels in the blood and excessive excretion of protein in the urine. These data related to the effects of *FAME* on iron homeostasis might be important in the context of reports that show how an iron deficiency in humans influences a variety of body functions, such as brain activity and energy expenditure<sup>62</sup>. This also connects to the fact that the regulation of iron metabolism by ferritin sustains organismal redox homeostasis. In this way, ferritin is essential to support organismal energy expenditure and thermogenesis<sup>63</sup>.

Interestingly, knockout mice with a *C57BL/6NcrJ* background did not exhibit a kidney excretion phenotype. We can only speculate about the reasons for these differences. One such reason could be the default differences in ferritin and albumin measurements in wild type *FVB/Ant* and *C57BL/6NcrJ* mice. For instance, *FVB/Ant* wild type mice show ten times more ferritin in serum as compared to *C57BL/6NcrJ* wild type mice. Additionally, *C57BL/6NcrJ* mice excrete albumin two times as much as compared to *FVB/Ant* mice.

On the other hand, knockout models with two different genetic backgrounds (*FVB/Ant* and *C57BL/6NcrJ*) revealed significant effects as compared to the same background wild type controls in metabolic cage experiments, including a different BMI of knockout animals, variation in day/night activity, and general differences in food intake and energy expenditure. At the same time, the adult knockout animals stayed morphologically normal and fertile, with kidneys histologically and anatomically indistinguishable from wild type controls. This picture fits our predictions about the possible evolutionary fine-tuning role of *FAME* in the diversification and adaptation of amniotes.

To determine if adverse environmental conditions can be tolerated differently with and without *FAME*, we subjected pregnant *FVB/Ant* *FAME* knockout females to iron deficit. This resulted in different developing embryos compared to the wild type genotype, with altered sizes of inner organs and interscapular brown adipose tissue. Overall, the tuning role of *FAME* appears to be pleiotropic and might be important during both embryonic development and adulthood. This variety of molecular roles is supported by our results showing that *FAME* can interact not only with proteins involved in iron homeostasis (or regulate their expression), such as *FTH1*<sup>64</sup> and *SLC25A39*<sup>48</sup>, but also with those involved in metabolic/mitochondrial processes, signaling molecules and transcriptional factors, as supported by IP and Bio-ID analysis of potential interactors. Finally, since *FAME* is expressed in other inner organs, such as the pancreas and liver, which play rather dominant roles in metabolism<sup>65</sup>, it is critical to focus on these organs and corresponding interacting molecules in future studies in more detail.

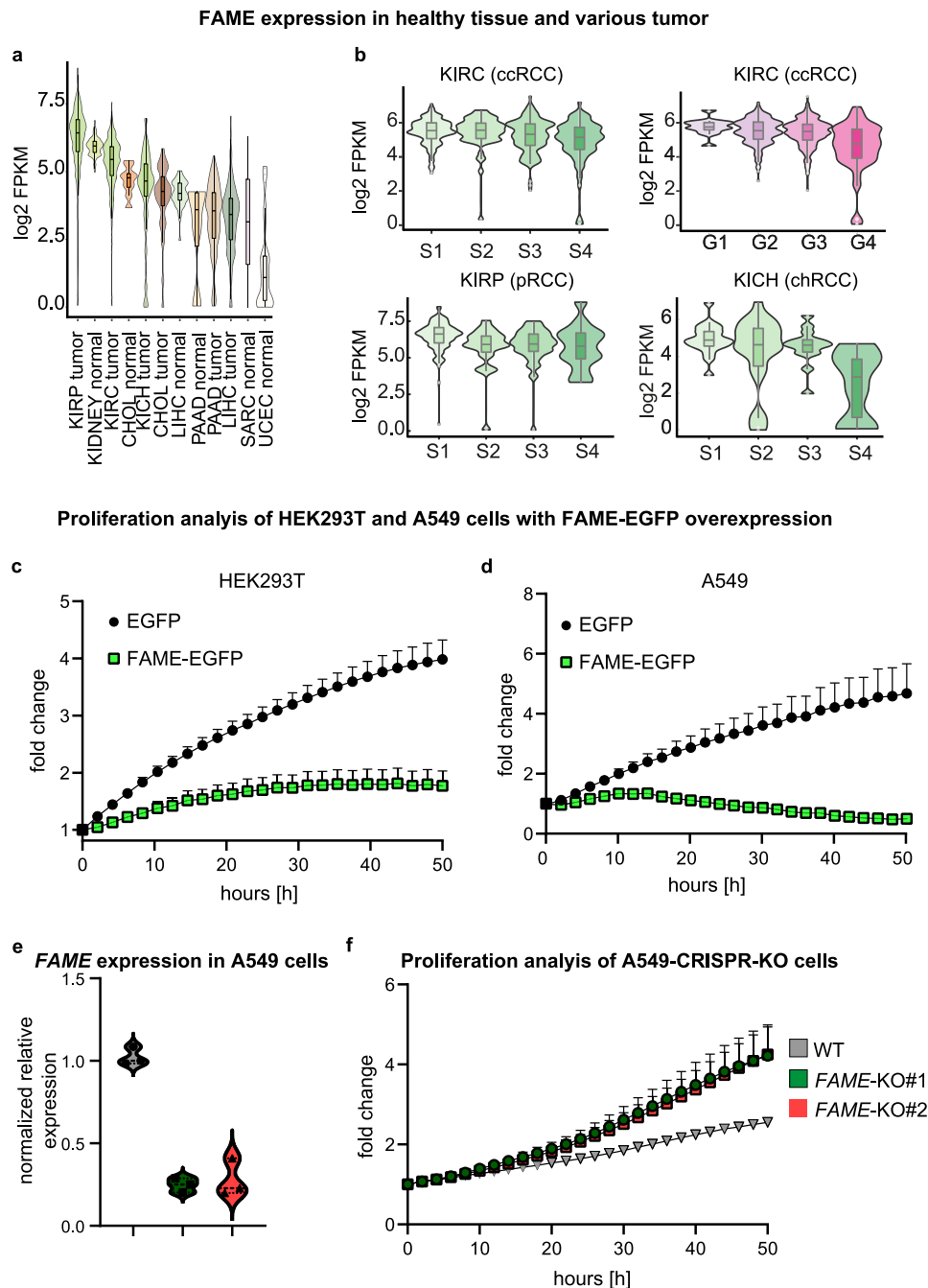


**Fig. 7 | Association of FAME with cancer.** **a** Analysis of *FAME* expression in various tumors and healthy tissues using RNAseq data obtained from The Cancer Genome Atlas (TCGA) Program. Mean  $\pm$  SEM and *n* (tumor or healthy tissue samples): KIRP tumor ( $6.251 \pm 0.0671$   $n = 289$ ) kidney normal ( $5.916 \pm 0.0301$   $n = 126$ ) KIRC tumor ( $5.309 \pm 0.0418$   $n = 530$ ) CHOL normal ( $4.663 \pm 0.1816$   $n = 9$ ) KICH tumor ( $4.331 \pm 0.1988$   $n = 65$ ) CHOL tumor ( $4.056 \pm 0.2020$   $n = 36$ ) LIHC normal ( $4.199 \pm 0.0688$   $n = 50$ ) PAAD normal ( $2.872 \pm 0.9882$   $n = 4$ ) PAAD tumor ( $3.319 \pm 0.0996$   $n = 178$ ) LIHC tumor ( $3.255 \pm 0.0623$   $n = 373$ ) SARC normal ( $3.145 \pm 3.145$   $n = 2$ ) UCEC normal ( $1.295 \pm 0.2736$   $n = 24$ ). **b** *FAME* expression in kidney tumors (TCGA data) stratified by tumor grade (G)/stage (S). The expression is maintained in all tumor types derived from *FAME* expressing tissue. Mean  $\pm$  SEM and *n* (tumor samples): KIRC S1 ( $5.437 \pm 0.0472$   $n = 266$ ) KIRC S2 ( $5.451 \pm 0.1307$   $n = 57$ ) KIRC S3 ( $5.236 \pm 0.0894$   $n = 123$ ) KIRC S4 ( $4.905 \pm 0.1459$   $n = 81$ ) KIRP S1 ( $6.455 \pm 0.0737$   $n = 172$ ) KIRP S2 ( $5.816 \pm 0.3306$   $n = 22$ ) KIRP S3 ( $5.811 \pm 0.1692$   $n = 51$ ) KIRP S4 ( $5.743 \pm 0.3829$   $n = 15$ ) KICH S1 ( $4.917 \pm 0.1813$   $n = 20$ ) KICH S2 ( $4.200 \pm 0.3868$   $n = 25$ ) KICH S3 ( $4.541 \pm 0.2704$   $n = 14$ ) KICH S4 ( $2.438 \pm 0.8041$   $n = 6$ ). **c** Proliferation analysis of HEK293T cells overexpressing FAME-EGFP or an EGFP control plasmid. EGFP<sup>+</sup> cells were included in the analysis. Mean values of 5 independent cell clones per condition with positive error bars (SEM) are shown. Figure **d** as in **c** using human A549 cells. **e** Normalized RNA expression levels of *FAME* in A549 cells measured by qPCR. Technical replicates ( $n = 3$ ) of two independent KO clones and one wildtype clone are shown. **f** Proliferation analysis of A549 clones in which *FAME* was knocked out using the CRISPR-Cas9 system. As control (WT), a FAME-sgRNA-transduced, but unedited clone in the locus of interest, was included. Mean values from 3 independent experiments with 2 replicates each per KO or WT clone ( $n = 6$ ), with positive error bars (SEM), are shown. Source data are provided as a Source Data file. **c**, **d**, **f** Error bars are shown as positive SEM from the mean. Some bars are smaller than data symbols.

The fine-tuning and pleiotropic functions of FAME discovered in animal models suggested that FAME might be associated with human tumor development. The analysis of expression levels of FAME in human kidney tumors differentially correlated with patient survival trends with a *p*-value close to significance in some cases. Although this analysis of survival curves of cancer patients did not result in predictions of strong effects, our experimental analysis of FAME localization in healthy versus tumor tissues suggested the potential importance of FAME in kidney tumors. Furthermore, our experiments with knockout and overexpression of FAME in human cell lines (HEK293T and A549), with and without endogenous expression of FAME, showed a role of FAME in controlling cell proliferation. Further, they supported the potential role of FAME in cancer. However, to answer the direct question if FAME represents a cancer progression suppressor or driver (and not a passenger molecule, being only a part of the prognostic signature) in specific tumors or heterogeneous tumor cell populations, further experiments in rodents involving patient-derived xenograft models are required. Furthermore, we identified FAME as a gene associated with neural crest epithelial mesenchymal transition (EMT) and interacting with several proteins involved in the EMT process. These results are consistent with a previous report showing that metabolic activity affects the EMT of neural crest cells<sup>66</sup>. Additionally, according to the Yeast two-hybrid data, ferritin, the interacting partner of FAME is involved in controlling cancer cell growth<sup>67</sup>. Furthermore, it is interesting to note that the additional putative interaction partners revealed by our screening (TLK1, CREBZF, and MYST2) are mostly involved in cell cycle regulation. Since our functional experiments, including overexpression and knockout in two cell lines, strongly indicate that FAME plays a role in cell proliferation, we do not want to neglect the possibility of these interactions being important. However, this is subject to further experiments that are not part of this manuscript.

At last, the genetic and pharmacological experiments revealed that the membranous localization of FAME is maintained due to N-myristoylation<sup>68</sup>. Interestingly, the localization of FAME changed from membranous to vesicle-forming structures in the malignant tissue. This pattern of FAME redistribution during tumor formation follows a well-known phenomenon of increased membrane-associated protein trafficking in tumor growth<sup>69</sup>.

In conclusion, FAME appears to be a non-essential gene involved in tuning the metabolism, energy expenditure, and excretion processes. Being a fine-tuning and fast-evolving factor, it influences the evolutionary diversification of amniote animal groups. It shows diverse effects depending on the animals' genetic background, metabolic needs, and sexes. As a result, the high evolutionary speed of changes observed in FAME structure and its correlation with bird speciation might be defined by specifics of the bird's metabolism, excretion, and anatomy. For instance, birds excrete uric acid (unlike mammals excreting water-soluble urea), show the presence of a renal portal vein, and do not have a bladder. Last but not least, FAME might be a potential confounder of tumor progression and human metabolic disorders, according to our experimental data and published GWAS analysis.

## Methods

### Statement on ethical considerations

All animal work was approved and permitted by the Local Ethical Committee on Animal Experiments and conducted according to the Guidelines for Animal Experimentation recommendations (ARRIVE guidelines). In particular, mouse work related to *C57BL/6NcrJ* mice was approved and permitted by the Institute of Molecular Genetics of the Czech Academy of Sciences (licence: 45/2017 AVCR). Mouse work related to *FVB/Ant* by the BMBWF-V/3b (Animal experimentation and genetic engineering, Austria) (licence: BMWFV-66.009/0018-WF/V/3b/2017).

Mice were sacrificed by isoflurane overdose. In all instances, apart from blood drawing, cervical dislocation was carried out additionally.

### Antibodies

The following antibodies were used in this study:

Mouse monoclonal anti-170001H14Rik/FAME (B-1) antibody (Santa Cruz, sc-398907, 1:50) (the limitations of this antibody are discussed below, validation is shown in Supplementary Figs. 5 and 6)

Fluorescein-labeled Lotus Tetragonolobus Lectin (Vector Laboratories, FL13212, 1:200), Mouse monoclonal VANGL1 (E-3) antibody (Santa Cruz, sc-166844, 1:200), Chicken polyclonal anti-GFP antibody (Abcam, ab13970, 1:250), Normal mouse IgG (1 μg) (I2-371, Merck), Alexa Fluor 555, Donkey anti-Mouse IgG secondary antibody (Invitrogen, A-31570, 1:1000), Alexa Fluor 647, Donkey anti-Chicken IgY secondary antibody (Invitrogen, A-78952, 1:1000).

**Discussion of limitation of the anti-FAME antibody.** Given that FAME was an uncharacterized protein, we were limited in the number of commercially available antibodies. We tested several antibodies for immunohistochemistry and western blot applications. Of the 4 tested antibodies (Santa Cruz mouse monoclonal SC-398907, Santa Cruz goat polyclonal SC-245243, Invitrogen rabbit polyclonal PA5-70922 and St. John's Lab rabbit polyclonal STJ195864), only the Santa Cruz mouse monoclonal SC-398907 antibody provided consistent and specific results in immunohistochemistry on mouse wild type tissues, and did not show a similar signal in FAME knockout tissues. Notably, FAME antibody did not stain all proximal tubules in the mouse kidney sections in Fig. 2c. We were unable to determine the reason for this, but it might be due to differences in *Fame* expression levels within the tubules depending on the region of the kidney and section plane. Furthermore, while being able to detect FAME in an overexpression setting, we were not able to detect endogenous FAME protein by western blot. It is possible that the used antibody can only detect a certain threshold of FAME preferably in non-denaturing conditions, and the concentration of FAME in total kidney extract is low because the protein is produced only in few cell types associated with tubules. This suggestion corresponds well to our immunohistochemistry results on kidney sections. NOTE: This antibody has not been validated to detect the human variant of FAME.

**Comparative genomics approach.** Protein and CDS sequences from different Amniota organisms were obtained from the NCBI database. For dN/dS analysis, organisms were paired up in their classes, and in each pair bidirectional Blastp was performed. We chose pairs of mammalian and bird genomes based on the criteria that the median dS between a pair of organisms would be 0.27–0.47 to obtain a similar evolutionary distance between species and avoid redundancy and to not repeat the species. Then for each pair, we aligned proteins by using MUSCLE<sup>70</sup>, then we aligned the CDS to the protein sequences by tranalign, and finally obtained the dN/dS ratio by using PAML. To group orthologous pairs, we also aligned each of them to *Homo sapiens* or *Gallus gallus* by bidirectional blast.

To compensate for non-ideal genomes, we used many pairs for bird, reptile, and mammal genomes. We used the Ensembl database to access gene sequence data and only kept 1-to-1 orthologues for our analysis. Of the 94 amino acid sequences we used, only 4 were fewer than 200 amino acids long and were labelled as partial. These partial sequences likely resulted from genome sequence incompleteness but should not affect our results overall.

### Expression analysis (Genotype-Tissue Expression (GTEx)/*Tabula muris*)

Gene expression data from 8555 samples from 30 different human tissues were obtained from the Genotype Tissue Expression Project (GTEx) repository (release V6p) [<https://www.gtexportal.org/home/>]<sup>71</sup>.

Gene transcript level expression data was calculated as reads per kilobase million (RPKM).

Gene expression data from single mouse cells were obtained from the Tabula Muris consortium<sup>34</sup> and [<https://github.com/czbiohub/tabula-muris>]. Mouse tissue scaled gene expression values, as processed by the Seurat software<sup>72</sup>, were obtained from 55,656 cells from 12 different tissues classified into 55 different cell types.

### Microscopy

**Staining of tissue on paraffin.** Tissue samples were collected and fixed in 4% paraformaldehyde for 24 h at 4 degrees under rotation. The fixed tissue samples were then dehydrated with graded series of ethanol, cleared with xylene, and finally embedded in paraffin. The embedded tissue blocks were then sectioned into 5 µm sections using a microtome. The sections were mounted on positively charged glass slides and allowed to dry at room temperature. Antigen retrieval was performed using Dako Target Retrieval Solution, pH 9, 1x concentration. Briefly, the slides were immersed in DAKO solution and heated in a pressure cooker for 60 min. After cooling to room temperature, the slides were washed with phosphate-buffered saline (PBS) to remove any residual solution. The slides were then incubated with the primary antibody diluted in 1:50 concentration for 1 h at room temperature. After washing with PBS, the slides were incubated with the appropriate secondary antibody conjugated with a fluorochrome for 1 h at room temperature. The slides were then counterstained with DAPI to visualize the cell nuclei.

**Immunocytochemistry (ICC).** Coverslips in 24-well plates were treated with Collagen I (rat tail, 50 µg/ml, Gibco) for 1 h at room temperature. After 3 PBS washes, HEK293T cells were cultured overnight, followed by transfection of 250 ng of FAME-pEGFP-N1 using Lipofectamine LTX<sup>®</sup> and Plus<sup>™</sup> Reagent (Invitrogen). After overnight incubation, the cells were fixed using 4% paraformaldehyde in PBS for 20 min at room temperature. After 3 PBS washes, cells were either directly stained with primary anti-1700011H14Rik/FAME antibody (Santa Cruz) and subsequent donkey anti-mouse 555 secondary antibody (Invitrogen), or treated with 1x Dako Target Retrieval Solution, pH 9 (Agient) for 40 min in a steamer at 97 °C. Next, cells were washed 3 times with PBS-T and stained sequentially with primary anti-FAME and anti-GFP (Abcam, ab13970) diluted in a mixture of 5% donkey serum, 20% dimethyl sulfoxide (DMSO) (Sigma) and 75% PBS for one hour, followed by 3 PBS-T washes. Secondary antibody staining with Donkey anti-mouse 555 (Alexa Fluor<sup>™</sup>) and donkey anti-chicken 647 (Invitrogen) was done for 1 h. Following 3 PBS-T washes, cells were stained with 4',6-Diamidino-2-phenylindole (DAPI) at a 1:10,000 dilution and mounted with Mowiol mounting medium (Sigma). Fluorescence images were obtained by Leica DMi8 automated fluorescence microscopy.

**Staining of embryonic/tissue cryo-sections.** Embryos/tissue were harvested and fixed in 4% PFA for 4 h at 4 °C while rotating and subsequently put into a 30% sucrose (VWR, C27480) solution for 24 h. The embryos/tissue were then embedded in OCT (Sakura, 4566) and sectioned at 25 µm on a Cryostar NX70 cryostat (Thermo Fisher). For staining, the tissue was encircled with a hydrophobic pen (Agilent, S2002). Slides were washed with PBS-T and incubated with primary antibody diluted in Dako Antibody Diluent (Agilent, S3022) for 1 h at room temperature or at 4 °C overnight. Slides were washed in PBS-T and incubated with secondary antibody diluted in PBS-T for 1 h at room temperature. The tissue was washed with PBS-T, counterstained with DAPI, washed and mounted using Mowiol mounting medium (Sigma).

**Staining of tissue on paraffin.** Tissue samples were collected and fixed in 4% paraformaldehyde for 24 h at 4 degrees under rotation. The fixed tissue samples were then dehydrated with graded series of ethanol,

cleared with xylene, and finally embedded in paraffin. The embedded tissue blocks were then sectioned into 5 µm sections using a microtome. The sections were mounted on positively charged glass slides and allowed to dry at room temperature. Antigen retrieval was performed using Dako Target Retrieval Solution, pH 9, 1x concentration. Briefly, the slides were immersed in DAKO solution and heated in a pressure cooker for 60 min. After cooling to room temperature, the slides were washed with phosphate-buffered saline (PBS) to remove any residual solution. The slides were then incubated with the primary antibody diluted in 1:50 concentration for 1 h at room temperature. After washing with PBS, the slides were incubated with the appropriate secondary antibody conjugated with a fluorochrome for 1 h at room temperature. The slides were then counterstained with DAPI to visualize the cell nuclei. The stained slides were observed and images were acquired using a fluorescence microscope equipped with appropriate filters. The images were captured using a camera and processed using image analysis software.

**Confocal microscopy.** Images were acquired using a Zeiss LSM880 Airyscan confocal microscope. The 488, 555, and 647 nm Alexa fluor conjugated secondary antibodies were excited using 488, 561, and 633 nm VIS lasers, respectively. For the visualization of DAPI in cell culture experiments, a UV laser exciting at 405 nm was utilized. The corresponding filters channeling the emitted light were 493–556 nm (488 excitations), 562–624 nm (555), 638–755 nm (633), and 412–474 nm (405). The C-Apochromat 40x/1.2 W Korr FCS M27 objective was used for live-cell imaging and fixed ICC. Imaging of sections was performed at the highest available magnification with the Plan-Apochromat 63x/1.4 Oil objective.

Imaris 8.3 by Bitplane was used for image analysis.

**Live-cell imaging.** pEGFP-N1-FAME was transfected into HEK293T cells as described above and imaged using a confocal microscope. The localization and possible movement of the protein of interest was to be determined. The resolution was kept low, allowing images to be taken within milliseconds. Every second, two images were captured. Cells were tracked for 7 min, on average, until the sample was bleached.

### Cell culture

**Cell lines.** HEK293T and A549 were cultured in DMEM (Sigma, D5796), supplemented with 10% fetal bovine serum (Sigma, F7524), 1% Penicillin-Streptomycin (Sigma, P4333), and 1% L-Glutamate (Sigma, G7513). Cells were cultured in humidified incubators at 37 °C and 5% atmospheric CO<sub>2</sub>. Both cell lines are classified as commonly misidentified by the ICLAC. HEK293T were purchased from ATCC (CRL-3216). A549 cells were authenticated by autosomal STR profiling by Microsynth Austria, matching 100% the DNA profile of ATCC CRM-CCL-185.

**Plasmids for overexpression experiments.** For overexpression studies 1700011H14Rik/Fame (Dharmacon, MMM1013-202768062), Vangl1-myc (Addgene), Fth1 (Biocat, BC012314-TCM1004-GVO-TRI), pPAmCherry-α-tubulin (Addgene, 31930), mCherry-Mito-7 (Addgene, 55148), were either cloned into pEGFP-N1 (Clontech) or mCherry-expressing vectors (mCherry2-Cl, Addgene, 54563). Cloning was done using restriction enzymes. Restriction sites were introduced by PCR primers. For creation of a glycine to alanine (G2A) *Fame* mutant, respective changes were introduced by primers. Primers were ordered from Sigma Aldrich. Restriction enzymes and ligase were purchased from ThermoFisher. Plasmids were validated by sequencing.

**Myristylation inhibition.** Coverslips in a 24-well plate were treated with Collagen I (50 µg/ml, Gibco) for 1 hour at room temperature. After washing 3 times with PBS, HEK293T-cells were cultured overnight, followed by treatment of DMSO, 2-BP bromohexadecanoic acid

(100  $\mu$ M), IMP-1088 (100 nM) or DDD85646 (1  $\mu$ M) 30 min before transfection. The transfection was performed with 250 ng of RIK-pEGFP-N1 using Lipofectamine LTX<sup>®</sup> and Plus<sup>™</sup> Reagent (Invitrogen). After overnight incubation, the cells were fixed using 4% PFA for 20 min at room temperature, washed 3 times with PBS and stained with DAPI. Imaging and counting was performed using a Thunder System (Leica). Violin charts were generated using Prism Software v 9.0 (Graphpad).

### Interaction partners

**Yeast Two-Hybrid Y2H Screening.** The ULTimate Y2H screening was performed by Hybrigenics Services (Paris, France; [www.hybrigenics-services.com](http://www.hybrigenics-services.com)) following previously described methods<sup>73,74</sup>. The mouse 1700011H14Rik (aa 1-294) bait was PCR-amplified, sequenced, cloned in the pB27 (N-LexA-AKR2-C fusion) vector, and used for screening using mouse kidney embryo\_RP1 and mouse embryo Brain\_RP2 fragment libraries as prey. A total of 174 and 94 prey fragments, respectively, of the positive clones, were amplified by PCR and sequenced at their 50 and 30 junctions. The resulting sequences were used to identify the corresponding interacting proteins in the GenBank database (NCBI) using a fully automated procedure.

**Bio-ID.** The Proximity-dependent Biotin Identification (BioID) experiments were performed using the PROFACGEN Service ([www.profacgen.com](http://www.profacgen.com)). The Detailed report, as well as RAW data, are available under [<https://datadryad.org/stash/share/ojRXiYXvS3yzg5SZwdrXHoggtgeQBDaSgPvhRBdU8Yw>].

**Immunoprecipitation (IP) and MS/MS analysis of peptides.** HEK293T cells were transfected with a plasmid encoding untagged mouse 1700011H14Rik/FAME. The day after transfection, cells were washed with PBS, scraped in ice-cold PBS, and pelleted by 200  $\times$  g, 4  $^{\circ}$ C centrifugation. Cells were lysed in 1 ml of cold lysis buffer (0.5% NP40, 50 mM Tris buffer, pH 7.4; 300 mM NaCl; 1 mM EDTA) supplemented with protease inhibitors (Roche, 11836145001) and 0.1 mM dithiothreitol (Sigma, E3876). After 15 min, the lysate was cleared by centrifugation at 16000  $\times$  g for 15 min. 1  $\mu$ g of mouse monoclonal 1700011H14Rik antibody or normal mouse IgG as negative control (Merck, 12-371) was used per sample and incubated overnight at 4  $^{\circ}$ C on a rotating wheel. 40  $\mu$ l of protein G-Sepharose beads slurry (GE Healthcare, 17-0618-05) was washed in 1 ml of lysis buffer and 200  $\times$  g centrifugation. Equilibrated beads were added to the lysates with antibodies, and incubated at 4  $^{\circ}$ C on a rotating wheel for 4 h. The beads were washed 6 times in lysis buffer by centrifugation. The last two washes were done in buffer without detergent.

Following IP washes, bead bound protein complexes were digested directly on the beads by adding of 1  $\mu$ g trypsin (Promega, sequencing grade) in 50 mM NaHCO<sub>3</sub> buffer. Beads were mixed and incubated at 37  $^{\circ}$ C with mild agitation for two hours. Beads were vortexed and removed, while the released protein complexes were further incubated at 37  $^{\circ}$ C overnight (16 h) without agitation. The resulting peptides were extracted in LC-MS vials by 2.5% formic acid (FA) in 50% acetonitrile (ACN) and 100% ACN with the addition of polyethylene glycol (PEG-20.000; final concentration 0.001%) and concentrated in a SpeedVac concentrator (ThermoFisher) to a final volume of 15  $\mu$ l.

Six independent replicates were analyzed by mass spectrometry (Supplementary Figs. 23 and 24).

LC-MS/MS analyses of peptide mixtures were done using an Ultimate 3000 RSLCnano system connected to an Orbitrap Elite hybrid spectrometer (Thermo Fisher Scientific). Prior to LC separation, tryptic digests were online concentrated and desalted using a trapping column (100  $\mu$ m  $\times$  30 mm) filled with 3.5- $\mu$ m X-Bridge BEH 130 C18 sorbent (Waters). After washing of the trapping column with 0.1% FA, the peptides were eluted (flow rate 300 nl/min) from the trapping

column onto an analytical column (Acclaim Pepmap100 C18, 3  $\mu$ m particles, 75  $\mu$ m  $\times$  500 mm; Thermo Fisher Scientific) by a 100 min nonlinear gradient program (1–56% of mobile phase B; mobile phase A: 0.1% FA in water; mobile phase B: 0.1% FA in 80% ACN). Equilibration of the trapping column and analytical column was done prior to sample injection to sample loop. The analytical column outlet was directly connected to the Digital PicoView 550 (New Objective) ion source with a PicoTip emitter SilicaTip (New Objective, FS360-20-15-N-20-C12). ABIRD (Active Background Ion Reduction Device) was installed.

MS data were acquired in a data-dependent strategy selecting up to top 10 precursors based on precursor abundance in the survey scan ( $m/z$  350–2000). The resolution of the survey scan was 60 000 ( $m/z$  400) with a target value of  $1 \times 10^6$  ions, one microscan and maximum injection time of 200 ms. HCD MS/MS spectra were acquired with a target value of 50 000 and resolution of 15 000 ( $m/z$  400). The maximum injection time for MS/MS was 500 ms. Dynamic exclusion was enabled for 45 s after one MS/MS spectra acquisition and early expiration was disabled. The isolation window for MS/MS fragmentation was set to 2  $m/z$ .

For data evaluation, the MaxQuant software (2.0.1.0)<sup>75</sup> with inbuilt Andromeda search engine was used using default settings unless otherwise noted. Search was done against UniProtKB proteome database for *Homo sapiens* (downloaded from [[https://ftp.uniprot.org/pub/databases/uniprot/current\\_release/knowledgebase/reference\\_proteomes/Eukaryota/UP000005640/UP000005640\\_9606.fasta.gz](https://ftp.uniprot.org/pub/databases/uniprot/current_release/knowledgebase/reference_proteomes/Eukaryota/UP000005640/UP000005640_9606.fasta.gz)], version from 2021-06-16, 20,600 protein sequences), a separate fasta file containing the mouse C14orf105/FAME Q9CPZ1 (CNI05\_MOUSE) sequence and the cRAP contaminants database (112 sequences, version from 2018-11-22, downloaded from [<http://www.thegpm.org/crap>]). Modifications were set as follows for the database search: oxidation (M), deamidation (N, Q), and acetylation (Protein N-term) as variable modifications, with carbamidomethylation (C) as a fixed modification. Enzyme specificity was tryptic/P with two permissible miscleavages. Second peptides and match between runs (MBR) features were enabled. Only peptides and proteins with false discovery rate threshold under 0.01 were considered. Data are publicly available in the PRIDE database with the identifier PXD039259.

The proteinGroups.txt file, the resulting output from MaxQuant, was further processed in R, v. 4.1.1. using the Differential Enrichment of Proteomics Data (DEP) R package<sup>76</sup>. In the workflow, firstly contaminant hits were filtered out and protein intensities were log<sub>2</sub> transformed. Only proteins with intensity > 0 in more than 4/6 samples of at least one condition were retained. Intensities were normalized using LoessF normalization, and missing values were imputed using minimal value. Finally, limma test with Benjamini-Hochberg adjustment for multiple comparison was used to test for the differentially expressed proteins. Proteins were denoted as upregulated when passing the threshold of log<sub>2</sub> fold change > 1 and adjusted *p*-value < 0.05. Corresponding cellular localizations of upregulated proteins were visualized using the Human Cell Map resource<sup>77</sup> (Supplementary Fig. 23c).

### Mouse models

The original *FVB/Ant* colony was a kind gift from the University of Antwerp, Belgium. The colony was refreshed from the Jackson Laboratory [<https://www.jax.org/strain/004828>] several times. All experiments were performed in accordance with the Institutional Ethical Codex, Hungarian Act of Animal Care and Experimentation (2013, 40/2013) and the European Union guidelines (Directive 2010/63/EU), and with the approval of the Institutional Animal Care and Use Committee of the Institute of Experimental Medicine. Mice were maintained on a 12-hour light/dark cycle, and food and water were provided *ad libitum* behind a SPF barrier according to FELASA recommendation. All mice were healthy with no obvious behavioral phenotypes. Low iron (C1038) and control diet (C1000) were obtained from Altromin.

All *C57BL/6NCrl* animals were bred and housed at the Czech Center for Phenogenomics, Vestec, which is accredited by the Ministry of Agriculture of the Czech Republic. Mice were housed under standard conditions (12:12 - light:dark cycle) in the individually ventilated cages (Tecniplast green line) and had free access to standard chow (Altromin 1310) and purified chlorinated water. Laboratory animal facility ventilation is set for optimal air quality (HEPA filtration) and quantity for animal and working staff comfort and stable temperature (in range 19–21 °C) and humidity (45–65%). All animal experiments were approved by the Animal Care and Use Committee of the Institute of Molecular Genetics of the Czech Academy of Sciences, Prague, in accordance with guidelines and practices established by the Directive 2010/63/EU of the European Parliament on the Protection of Animals Used for Scientific Purposes.

**Generation of *Fame* KO mice.** For *FVB/Ant* transgenic mice generation, we co-injected Cas9 protein (30 ng/μl), the gRNA (GGAACACA GGGCCAGTTGA(GGG)) (50 ng/μl), and ssODN donor (CAGTCTCGTGA ATGAGCTTTCTTCTCCAGTTCGATTCAATGCAAAGAACACAGGG CCTCACTAGGGTGTCTCTGTTCTTGGCTTGTAAGGTG) (15 ng/μl) into *FVB/Ant* fertilized eggs. Injected embryos were transplanted into the oviduct of B6CBAF1 pseudopregnant females. The genotyping of the new-born mice was carried out by a PCR-based strategy, where we could detect the correct modification by using specific primers for the modified sequence.

**Generation of the *Ccdc198/Fame* knockout model.** The *Ccdc198/Fame* KO mouse (*C57BL/6NCrl-Ccdc198 em1(IMPC)Cpcpz*) was generated on a *C57BL/6NCRL* background (Charles River Laboratories) by deletion of a critical exon, specifically exon 3 of the *Ccdc198/Fame* gene (ENSMUSG00000021850) by using the CRISPR/Cas9 system. The guide RNAs (gRNAs) of highest score and specificity were designed using CRISPOR. The following guide RNAs were selected to generate the exon deletion: gRNAs, 5'-AAGGACCTGAATCTAGCACT-3' and 5'-CATTTCAGTACAGACTAGT-3'. The gRNAs were assembled into a ribonucleoprotein (RNP) complex with Cas9 protein (Integrated DNA Technologies, 1081058, 1072532), electroporated into 1-cell zygotes, and transferred into pseudopregnant foster females (*CrI:CD1(ICR)*). Putative founders were analyzed by PCR and sequencing. A founder harboring a 661 bp deletion overlapping the entire exon 3 of the *Ccdc198/Fame* gene was chosen for subsequent breeding. Genotyping was performed by PCR with the forward primer 5'-GCTGAACTGT GGAGCAGGTA-3' and reverse primer 5'-CAATCCACCCCAATACC CC-3'.

**Tissue contrasting and X-ray computed microtomography measurements.** To increase the contrast of soft tissues for X-ray computed microtomography (microCT), the samples were stained with 1% iodine. After embryo dissection in ice-cold PBS, the samples were fixed in 4% formaldehyde in PBS solution for 24 h at 4 °C with slow rotation. Subsequently, samples were dehydrated in incrementally increasing ethanol concentrations (30%, 50%, 70%), 1 day in each concentration. Samples were transferred into 1% iodine in 90% methanol for tissue contrasting. The iodine-methanol solution was changed after 3 days. P0 pups were stained for 7 days. The contrasting procedure was followed by rehydration of the samples by incubation in ethanol series (90%, 70%, 50%, and 30%). Then, the rehydrated embryos were embedded in 1% agarose gel (Sigma-Aldrich, A5304) and placed in polypropylene conical tubes to avoid motion artifacts during microCT scanning. The microCT measurements were conducted using the system GE phoenix v|tome|x L 240 (GE Sensing and Inspection Technologies) with a 180 kV/15 W maximum power nano focus X-ray tube and flat panel dynamic 41|100: 4000 × 4000 px, with pixel size 100 × 100 μm. The exposure time was 900 ms and 2000 projections were taken over 360°. Three

projections in every position were averaged for reduction of the noise in the data. The utilized acceleration voltage and current were 60 kV and 200 μA. X-ray spectrum was filtered by 0.2 mm of aluminum plate. The voxel size of the reconstructed data was 12 μm for P0 pups, 5.8 μm for the whole kidneys, and 1.3 μm for sections of the kidneys. The tomographic reconstructions were performed using GE phoenix dataview 2.0 3D computed tomography software (GE Sensing and Inspection Technologies). For 3D visualization, the segmentation was done by an operator using a combination of software Avizo (ThermoFisher Scientific) and VG Studio MAX (Volume Graphics).

**Urine and blood analyses.** Urine was collected for each mouse at the same time in the morning. To collect urine, the mouse was held over a Petri dish. The urine was transferred into a collection tube and stored at 4 °C or directly used for further analysis.

Blood collection was performed from the tail vein of the mice. Subsequently, the serum was isolated by centrifugation for 20 min at 2500 rpm. The serum was then transferred into a clean tube and used for immediate analysis. The following kits were used according to the manufacturer's instruction. Mouse Creatinine Assay Kit (Crystalchem, 80350), Mouse Albumin ELISA Kit (Crystalchem, 80630), Mouse Ferritin ELISA Kit (Crystalchem, 80636), Sodium Assay Kit (Crystalchem, 80179), Potassium Assay Kit (Crystalchem, 80169).

**Transmission electron microscopy.** Kidney tissue was cut in small pieces and fixed in 3% glutaraldehyde in PBS. Samples were washed in 0.1 M Soerensen's phosphate buffer (Merck), post-fixed in 1% OsO<sub>4</sub> (Roth, Karlsruhe, Germany) in 25 mM sucrose buffer (Merck) and dehydrated by ascending ethanol series (30, 50, 70, 90 and 100%) for 10 min each. The last step was repeated 3 times. Dehydrated specimens were incubated in propylene oxide (Serva) for 30 min, in a mixture of Epon resin (Serva) and propylene oxide (1:1) for 1 h, and finally in pure Epon for 1 h. Samples were embedded in pure Epon. Epon polymerization was performed at 90 °C for 2 h. Ultrathin sections (70–100 nm) were cut by ultramicrotome (Reichert Ultracut S, Leica) with a diamond knife (Leica) and picked up on Cu/Rh grids (HR23 Maxtaform, Plano). The contrast was enhanced by staining with 0.5% uranyl acetate and 1% lead citrate (both EMS). Samples were examined using a Zeiss Leo 906 transmission electron microscope (Carl Zeiss) operating at an acceleration voltage of 60 kV.

**Single-cell preparation from adult kidneys.** Control and mutant littermate mice (male and female) were used for single-cell transcriptomic and morphological analysis of the adult kidney. Mice were anesthetized with isoflurane overdose and transcardially perfused with PBS. Kidneys were dissected. One kidney per mouse was fixed in 4% PFA at 4 °C overnight to be used for morphological analysis. The second kidney was chopped in small pieces and digested with 2 mg/ml Collagenase P for 10 min at 37 °C, an equal volume of 0.10% trypsin/EDTA was added, and tissue was digested for an additional 10 min at 37 °C. Following enzymatic digestion, tissue was triturated using a wide-bore pipette tip, and clumps were mechanically dissociated using a 100 μm mesh and a syringe plunger.

Cell suspensions were washed twice with PBS/10% FBS and resuspended at a concentration of 1,000 cells/μl for processing with a 10x controller (10x Genomics).

**Library preparation and sequencing.** Library preparation was performed using a 10x controller (10x Genomics) with the Single Cell 3' v3 chemistry. Sequencing was performed using a HiSeq 3000 (Illumina) at the Biomedical Scientific Facility (BSF), Vienna, Austria.

Single-cell RNA sequencing of the five samples (KO female, KO male, KO mix, WT female, WT mix) resulted in 103,554,203 reads (86.30% and 67.90% of them were confidently mapped to the genome

and the transcriptome, respectively) for KO female; 58,088,304 reads (87.30% and 69.10%) for KO male; 73,512,818 (90.30% and 75.00%); 75,266,219 reads (86.40% and 65.40%) for WT female; and 58,636,386 reads (92.50% and 77.90%) for WT mix. The insert size for each sequencing was 350 bp.

To check whether DE genes between wildtype and knockout are not sex-specific, we compared them with the list of the corresponding DE genes between female and male proximal tubule (PT) samples from<sup>78</sup>. The genes whose adjusted *p*-values are less than 0.01 were excluded from the comparative analysis. Both lists have a little intersection; moreover, in the case of these few intersected genes, the most significant DE genes between wildtype and KO were not even in the top 40 sex-specific genes. The exceptions are *Inmt* (male-specific) and *Spp1* (female-specific) genes. The most intriguing findings are that the FAME-binding iron-transporting *Fth1* and potentially iron homeostasis associated *Slc25a39* gene seem to be gender neutral. These Data are now outlined in Supplementary Data 10.

**Single-cell RNAseq analysis.** Raw files were processed, mapped, and counted to the Cell Ranger mm10-2020-A genome and its corresponding annotation by Cell Ranger version 4.0.0. The output count matrices for each sample were further processed with the Seurat package pipeline (v.3.2.2.9001)<sup>79</sup>. Each dataset was filtered to remove genes expressed in less than three cells and to remove cells that had fewer than 1000 mRNA counts per cell and more than 50 % of mitochondrial counts (accounting for the high metabolic rate observed in the kidney)<sup>35</sup>. Putative doublet cells were predicted by Scrublet before the filtration and log-normalization steps<sup>80</sup>. For further comparative analysis, five datasets were integrated into one joint dataset. To improve downstream dimensionality reduction and clustering, the mitochondrial gene content was regressed out by using the ScaleData function from the Seurat package. The first 40 principal components and 30 nearest neighbors were used for graph-based clustering and further visualization by UMAP. Each cluster was assigned a cell type based on the marker genes reported in previous studies<sup>35,78,81–83</sup> and Supplementary Fig. 9. To estimate the difference in genotype compositional content, the exact Fisher test was applied. Identification of differentially expressed genes in wild type and mutant genotypes in each cluster was done by the FindMarkers function that implemented Wilcoxon rank-sum test and used a cutoff for minimum log FC difference (0.25). More details can be found online [https://github.com/ipooverennaya/RIK\\_paper](https://github.com/ipooverennaya/RIK_paper).

**Metabolic cage experiments (FVB/Ant).** To examine the effect of the absence of *1700011H14Rik/Fame* gene on the metabolism of adult mice, metabolic phenotyping was carried out by using the PhenoMaster System (TSE Systems). Mice were placed individually into metabolic training cages to habituate to the new environment for 3 days. After that, the body composition, including total body weight, total and free water content, fat and lean body mass of the animals were determined by an EchoMRI whole-body magnetic resonance analyzer (Zinsser Analytic). During phenotyping, the water and food intake (g), the locomotor activity (counts/hour), and the calorimetric parameters, like O<sub>2</sub> consumption (*V*O<sub>2</sub>), CO<sub>2</sub> production (*V*CO<sub>2</sub>) of the animals were continuously monitored for 24 or 48 h. The energy expenditure (kcal/h) was calculated according to the Weir equation<sup>84</sup>. The resting energy expenditure was estimated from the energy expenditure data in specific time points when a mouse individually moved less than 1% of its maximum ambulatory value for the last 30 min and ate less than 0.1g for the last 1h<sup>85</sup>. The respiratory exchange ratio is the ratio of CO<sub>2</sub> produced and O<sub>2</sub> used (*V*CO<sub>2</sub>/*V*O<sub>2</sub>). At the end of the metabolic measurement, the body composition analysis was repeated. All RAW Data from these measurements can be found in Supplementary Data 11.

**Metabolic cage experiments (C57BL/6NcrJ).** A PhenoMaster (TSE Systems) system was used for the indirect calorimetry. The software used in the PhenoMaster PC was TSE PhenoMaster v.7.1.2. Before the start of the indirect calorimetry measurements, a complete calibration protocol for the gas analyzers was performed according to the manufacturer's recommendations using normal air-compressed, CO<sub>2</sub> 1% and N<sub>2</sub> 100%. The mice were individually housed in a multiplex system with 8 cages plus a reference cage. The sampling frequency to measure the CO<sub>2</sub> and O<sub>2</sub> gas measurements were every 15 min. All measurements were initiated in the morning between 9:00 and 11:00.

We provided every cage ad libitum access to water and food, a standard chow diet (Altromin, 1314). Wooden chips bedding volume was limited to approximately 125 ml during indirect calorimetry measurements to properly detect the locomotor activity of the mice by an infrared beam break frame surrounding the cage in the horizontal plane.

The environmental conditions inside the climatic chamber were 55% relative humidity and a light cycle of 12 h of light (6:00 to 18:00) and 12 h of darkness (18: to 6:00) synchronized with the animal facility where the mice were previously housed. For the indirect calorimetry measurement, the temperature was set up as follows: at 23 °C for 48 h, and after that, we kept the mice in thermoneutrality (30 °C) for approximately 24 h, in total 36 h.

For indirect calorimetry using a cold challenge, the temperature was set up as follows: We started the indirect calorimetry measurement using 23 °C for 7 h. At 17:00 the climate chamber was warming up the environment to 30 °C for 7 h. At 00:00 the temperature started to decrease gradually to reach 4 °C. At approx. 8:00, we kept 4 °C for 4 h, and at 12:00 the temperature was increased back to 23 °C and remained at 23 °C for approx. 22 h when the calorimetry finished, after a total of 48 h. This allowed us to evaluate whether the cold challenge produced a metabolic carry over effect.

The indirect calorimetry recorded the CO<sub>2</sub> production and O<sub>2</sub> consumption. From these values, the Energy Expenditure (EE) and Respiratory exchange ratio (RER) was calculated. Moreover, measurements for locomotor activity and food and water intake were recorded every 15 min. When the indirect calorimetry protocol ended, the experiment was stopped, and the mice were weighed and placed into their original cages. All RAW Data from these measurements can be found in Supplementary Data 12.

#### Expression analysis—tumor data

The Cancer Genome Atlas (TCGA) gene expression data were downloaded from the Genomic Data Commons (GDC) portal in December 2018 [<https://portal.gdc.cancer.gov/>]. Replicates and samples flagged by the Pan-Cancer Atlas initiative (PanCanAtlas; [gdc.cancer.gov/about-data/publications/pancanatlas](https://gdc.cancer.gov/about-data/publications/pancanatlas)) were removed, yielding 9,510 tumors and 713 matched normal tissue samples from 31 different tissue sites. Gene expression values represent upper quantile normalized HTSeq-acquired Fragments Per Kilobase per Million reads mapped (FPKM) processed by the TCGA IlluminaHiSeq\_RNASeqV2 platform. Pathologic tumor stage data for kidney tumors were obtained from the PanCanAtlas project site.

#### Generation of FAME KO cell lines

CRISPR-Cas9 based gene editing was used to create *FAME* KO lines in A549 cells. Single Guide RNAs (sgRNAs) were designed using CRISPOR<sup>86</sup> and cloned into lentiCRISPR v2 (Addgene #52961) following the Zheng lab protocol<sup>87</sup> (sgRNA: AAGTCCACACGCCAGCCGA). Plasmids were validated by sequencing. Lentiviral particles were produced in HEK293T cells by co-transfection of 2.4 μg of psPAX2 (Addgene #12260), 1.8 μg MD2.G (Addgene #12259) and 3.6 μg lentiCRISPR v2-sgRNA construct using polyethyleneimine (PEI, 25 K, Polysciences) at a 1:3 DNA:PEI (1 μg/μl) ratio. Supernatants were harvested 48 h post-infection. For knocking out *FAME*, 1 × 10<sup>5</sup> cells were seeded

into 6-well plates, virus-particle containing supernatant was added, and protamine sulfate (Merck) at 8 µg/mL was added. Cells were transduced by spinfection at 800 × g for 60 min. Selection of infected cells was started 24 h post-transduction using 2 µg/mL puromycin (Cayman Chemical). Single-cell clones were obtained by limiting dilution. Genomic DNA was extracted using the Monarch gDNA Purification Kit (New England Biolabs) according to manufacturer instructions. *FAME* KO was validated by sequencing of the *FAME* locus with the sequencing primers (Microsynth): sgRNA KO locus, fwd 5' GCCAT-GAAGGAAATGACTGCT 3', revs 5' TCAAACCACAAAGTCTGGTGC 3'. The validation of these knockouts can be found in Supplementary Fig. 22.

**Proliferation analysis of *FAME* KO cell lines.** For proliferation assays,  $5 \times 10^4$  A549 or HEK293T cells were seeded into 12-well plates. The next day, cells were transfected with 1 µg of pEGFP-N1 as control or pEGFP-N1-*FAME* using Lipofectamine 3000 (Invitrogen) and placed into an Incucyte S3 Live-Cell Analysis Instrument (Sartorius). Images of transmitted light and green fluorescence were taken every 2 h. After -95 h, the image acquisition was stopped. Green area confluence was analyzed using the Incucyte Base Analysis Software (Sartorius) and Prism 9 (Graphpad).

**KO validation.** RNA isolation was performed using the Nucleospin RNA II kit (Macherey-Nagel). The concentration of RNA was measured using a NanoDrop ND-1000 system (Thermo Fisher Scientific). RNA quality and integrity were assessed by the TapeStation 2200 system (Agilent Technologies). For qRT-PCR expression analysis, the RNA was reverse transcribed using the Verso cDNA Synthesis Kit (Thermo Fisher Scientific) according to the manufacturer's instructions. Quantitative expression analysis was performed using the QuantStudio 5 Real-Time PCR instrument and predesigned TaqMan gene expression assays (Thermo Fisher Scientific): C14ORF105 (Taqman probe Hs00216847\_m1). GAPDH expression was used as an internal control. Relative quantification was performed according to the  $\Delta\Delta CT$  method<sup>88</sup>.

### Statistics and reproducibility

Statistical analysis was performed using appropriate software (Graphpad Prism 9). Descriptive statistics are displayed as mean ± standard error of the mean (SEM). All data following Gaussian distribution were analyzed by unpaired *t*-tests (two-tailed). *p*-values smaller than 0.05 were considered statistically significant ( $*p < 0.05$ ,  $**p < 0.01$ ,  $***p < 0.001$ ). All *p*-values without additional indication stem from *t*-tests. Nonparametric data were analyzed by Mann-Whitney test and specifically indicated in the figure legends.

### Reporting summary

Further information on research design is available in the Nature Portfolio Reporting Summary linked to this article.

### Data availability

Two knockout mice strains were generated for this manuscript. Mice on a *C57BL/6NCRl* background will be available through the International Mouse Phenotyping Consortium [<https://www.mousephenotype.org/data/search?term=CCDC198&type=gene>] whereas *FVB/Ant* are deposited to the Jackson Laboratory (JAX Stock No. 038293). All the information necessary to reproduce the single cell analysis is presented in the Methods Section. All other relevant data supporting the key findings of this study are available within the article and its Supplementary Information files or from the corresponding author upon request. SNP data for ancestral alleles (108 Nigerian Yorubans, YRI) was taken from the 1000 Genomes Project deposited in Ensembl [<https://www.ensembl.org/info/genome/variation/species/populations.html>]. The Neanderthal genomes were published previously<sup>27</sup>: [<http://ftp.eva.mpg.de/neandertal/Chagyrskaya/VCF/>]<sup>28</sup>, European Nucleotide Archive (ENA) PRJEB21157 [<https://bioinf.eva.mpg.de/jbrowse/>]<sup>29</sup>, 2014 ENA ERP002097 [<http://cdna.eva.mpg.de/neandertal/altai/>]. The RAW mass spectrometry can be accessed through PRIDE with the identifier PXD039259. RAW Single cell sequencing files can be downloaded from GEO with the accession number GSE206860. RAW Yeast-Two-Hybrid data can be accessed through [<https://datadryad.org/stash/share/ojrxixYXvS3yzg5SZwdrXHoggtgeQBDaSgPvhRBdU8Yw>]. Protein and CDS sequences from different amniota organisms were obtained from NCBI database (Supplementary Fig. 3). The Cancer Genome Atlas Program (TCGA, December 2018, [<https://portal.gdc.cancer.gov/>]) and Genotype-Tissue Expression (GTEx) project datasets (release V6p) [<https://www.gtexportal.org/home/>] were used to collect data for Fig. 7a, b and Supplementary Fig. 4a. Tabula muris [<https://tabula-muris.ds.czbiohub.org/>] was used to obtain data for Fig. 2a and Supplementary Fig. 4b and downloaded from [[https://figshare.com/projects/Tabula\\_Muris\\_Transcriptomic\\_characterization\\_of\\_20\\_organisms\\_and\\_tissues\\_from\\_Mus\\_musculus\\_at\\_single\\_cell\\_resolution/27733](https://figshare.com/projects/Tabula_Muris_Transcriptomic_characterization_of_20_organisms_and_tissues_from_Mus_musculus_at_single_cell_resolution/27733)]. GWAS<sup>89</sup> was used to generate data from Supplementary Fig. 19. Source data are provided with this paper.

de/neandertal/Chagyrskaya/VCF/]<sup>28</sup>, European Nucleotide Archive (ENA) PRJEB21157 [<https://bioinf.eva.mpg.de/jbrowse/>]<sup>29</sup>, 2014 ENA ERP002097 [<http://cdna.eva.mpg.de/neandertal/altai/>]. The RAW mass spectrometry can be accessed through PRIDE with the identifier PXD039259. RAW Single cell sequencing files can be downloaded from GEO with the accession number GSE206860. RAW Yeast-Two-Hybrid data can be accessed through [<https://datadryad.org/stash/share/ojrxixYXvS3yzg5SZwdrXHoggtgeQBDaSgPvhRBdU8Yw>]. Protein and CDS sequences from different amniota organisms were obtained from NCBI database (Supplementary Fig. 3). The Cancer Genome Atlas Program (TCGA, December 2018, [<https://portal.gdc.cancer.gov/>]) and Genotype-Tissue Expression (GTEx) project datasets (release V6p) [<https://www.gtexportal.org/home/>] were used to collect data for Fig. 7a, b and Supplementary Fig. 4a. Tabula muris [<https://tabula-muris.ds.czbiohub.org/>] was used to obtain data for Fig. 2a and Supplementary Fig. 4b and downloaded from [[https://figshare.com/projects/Tabula\\_Muris\\_Transcriptomic\\_characterization\\_of\\_20\\_organisms\\_and\\_tissues\\_from\\_Mus\\_musculus\\_at\\_single\\_cell\\_resolution/27733](https://figshare.com/projects/Tabula_Muris_Transcriptomic_characterization_of_20_organisms_and_tissues_from_Mus_musculus_at_single_cell_resolution/27733)]. GWAS<sup>89</sup> was used to generate data from Supplementary Fig. 19. Source data are provided with this paper.

### Code availability

All custom-made scripts used in the analysis are available at: [[https://github.com/ipoverennaya/RIK\\_paper](https://github.com/ipoverennaya/RIK_paper)].

### References

- Jones, F. C. et al. The genomic basis of adaptive evolution in threespine sticklebacks. *Nature* **484**, 55–61 (2012).
- Bustamante, C. D. et al. Natural selection on protein-coding genes in the human genome. *Nature* **437**, 1153–1157 (2005).
- Wang, T. et al. Identification and characterization of essential genes in the human genome. *Science* **350**, 1096–1101 (2015).
- Lieben, L. Evolution: Redefining gene essentiality. *Nat. Rev. Genet.* **17**, 66 (2016).
- Manuylov, N. L., Manuylova, E., Avdoshina, V. & Tevosian, S. Serdin1/Lrrc10 is dispensable for mouse development. *Genesis* **46**, 441–446 (2008).
- Brody, M. J. & Lee, Y. The Role of Leucine-Rich Repeat Containing Protein 10 (LRRC10) in Dilated Cardiomyopathy. *Front Physiol.* **7**, 337 (2016).
- Strasser, B. et al. Evolutionary origin and diversification of epidermal barrier proteins in amniotes. *Mol. Biol. Evol.* **31**, 3194–3205 (2014).
- Kawasaki, K., Lafont, A. G. & Sire, J. Y. The evolution of milk casein genes from tooth genes before the origin of mammals. *Mol. Biol. Evol.* **28**, 2053–2061 (2011).
- Meredith, R. W., Gatesy, J. & Springer, M. S. Molecular decay of enamel matrix protein genes in turtles and other edentulous amniotes. *BMC Evol. Biol.* **13**, 20 (2013).
- Ellegren, H. Comparative genomics and the study of evolution by natural selection. *Mol. Ecol.* **17**, 4586–4596 (2008).
- Zhang, G. et al. Comparative genomics reveals insights into avian genome evolution and adaptation. *Science* **346**, 1311–1320 (2014).
- Jarvis, E. D. et al. Whole-genome analyses resolve early branches in the tree of life of modern birds. *Science* **346**, 1320–1331 (2014).
- Seebacher, F. The evolution of metabolic regulation in animals. *Comp. Biochem. Physiol. B Biochem. Mol. Biol.* **224**, 195–203 (2018).
- Hedrick, M. S. & Hillman, S. S. What drove the evolution of endothermy? *J. Exp. Biol.* **219**, 300–301 (2016).
- Roberts, R. M., Green, J. A. & Schulz, L. C. The evolution of the placenta. *Reproduction* **152**, R179–R189 (2016).
- Vize, P. D. & Smith, H. W. A Homeric view of kidney evolution: A reprint of H.W. Smith's classic essay with a new introduction.

- Evolution of the kidney. 1943. *Anat. Rec. A Disco. Mol. Cell Evol. Biol.* **277**, 344–354 (2004).
17. Poulson, T. L., McNabb, F. M. & Folk, R. L. Uric acid: the main nitrogenous excretory product of birds. *Science* **170**, 98–99 (1970).
  18. Galperin, M. Y. & Koonin, E. V. From complete genome sequence to ‘complete’ understanding? *Trends Biotechnol.* **28**, 398–406 (2010).
  19. Galperin, M. Y. & Koonin, E. V. ‘Conserved hypothetical’ proteins: prioritization of targets for experimental study. *Nucleic Acids Res* **32**, 5452–5463 (2004).
  20. Pawlowski, K. Uncharacterized/hypothetical proteins in biomedical ‘omics’ experiments: is novelty being swept under the carpet? *Brief. Funct. Genom. Proteomic* **7**, 283–290 (2008).
  21. Doridot, L. et al. Nitroso-redox balance and mitochondrial homeostasis are regulated by STOX1, a pre-eclampsia-associated gene. *Antioxid. Redox Signal* **21**, 819–834 (2014).
  22. Bonavita, R. et al. Cep126 is required for pericentriolar satellite localisation to the centrosome and for primary cilium formation. *Biol. Cell* **106**, 254–267 (2014).
  23. Chen, L., Wolf, A. B., Fu, W., Li, L. & Akey, J. M. Identifying and Interpreting Apparent Neanderthal Ancestry in African Individuals. *Cell* **180**, 677–687.e616 (2020).
  24. Posth, C. et al. Pleistocene Mitochondrial Genomes Suggest a Single Major Dispersal of Non-Africans and a Late Glacial Population Turnover in Europe. *Curr. Biol.* **26**, 827–833 (2016).
  25. Rito, T. et al. A dispersal of Homo sapiens from southern to eastern Africa immediately preceded the out-of-Africa migration. *Sci. Rep.* **9**, 4728 (2019).
  26. Genomes Project, C. et al. A global reference for human genetic variation. *Nature* **526**, 68–74 (2015).
  27. Mafessoni, F. et al. A high-coverage Neandertal genome from Chagyrskaya Cave. *Proc. Natl Acad. Sci. USA* **117**, 15132–15136 (2020).
  28. Prufer, K. et al. A high-coverage Neandertal genome from Vindija Cave in Croatia. *Science* **358**, 655–658 (2017).
  29. Prufer, K. et al. The complete genome sequence of a Neandertal from the Altai Mountains. *Nature* **505**, 43–49 (2014).
  30. Mafessoni, F. & Prufer, K. Better support for a small effective population size of Neandertals and a long shared history of Neandertals and Denisovans. *Proc. Natl Acad. Sci. USA* **114**, E10256–E10257 (2017).
  31. Green, R. E. et al. A draft sequence of the Neandertal genome. *Science* **328**, 710–722 (2010).
  32. Huerta-Sanchez, E. et al. Altitude adaptation in Tibetans caused by introgression of Denisovan-like DNA. *Nature* **512**, 194–197 (2014).
  33. Kong, A. et al. Fine-scale recombination rate differences between sexes, populations and individuals. *Nature* **467**, 1099–1103 (2010).
  34. Tabula Muris, C. et al. Single-cell transcriptomics of 20 mouse organs creates a Tabula Muris. *Nature* **562**, 367–372 (2018).
  35. Park, J. et al. Single-cell transcriptomics of the mouse kidney reveals potential cellular targets of kidney disease. *Science* **360**, 758–763 (2018).
  36. Deutsch, E. W. The PeptideAtlas Project. *Methods Mol. Biol.* **604**, 285–296 (2010).
  37. Huttlin, E. L. et al. A tissue-specific atlas of mouse protein phosphorylation and expression. *Cell* **143**, 1174–1189 (2010).
  38. Schmidt, T. et al. ProteomicsDB. *Nucleic Acids Res* **46**, D1271–D1281 (2018).
  39. Wang, D. et al. A deep proteome and transcriptome abundance atlas of 29 healthy human tissues. *Mol. Syst. Biol.* **15**, e8503 (2019).
  40. Li, S. et al. Digging More Missing Proteins Using an Enrichment Approach with ProteoMiner. *J. Proteome Res* **16**, 4330–4339 (2017).
  41. Rinschen, M. M. et al. Quantitative phosphoproteomic analysis reveals vasopressin V2-receptor-dependent signaling pathways in renal collecting duct cells. *Proc. Natl Acad. Sci. USA* **107**, 3882–3887 (2010).
  42. MacKenzie, E. L., Iwasaki, K. & Tsuji, Y. Intracellular iron transport and storage: from molecular mechanisms to health implications. *Antioxid. Redox Signal* **10**, 997–1030 (2008).
  43. Ho, H. Y. et al. Toca-1 mediates Cdc42-dependent actin nucleation by activating the N-WASP-WIP complex. *Cell* **118**, 203–216 (2004).
  44. Kakimoto, T., Katoh, H. & Negishi, M. Regulation of neuronal morphology by Toca-1, an F-BAR/EFC protein that induces plasma membrane invagination. *J. Biol. Chem.* **281**, 29042–29053 (2006).
  45. Lee, J., Kim, M. S., Park, S. H. & Jang, Y. K. Tousel-like kinase 1 is a negative regulator of core transcription factors in murine embryonic stem cells. *Sci. Rep.* **8**, 334 (2018).
  46. Zhang, R., Thamm, D. H. & Misra, V. The effect of Zhangfei/CREBZF on cell growth, differentiation, apoptosis, migration, and the unfolded protein response in several canine osteosarcoma cell lines. *BMC Vet. Res* **11**, 22 (2015).
  47. Pardo, M. et al. Myst2/Kat7 histone acetyltransferase interaction proteomics reveals tumour-suppressor Niam as a novel binding partner in embryonic stem cells. *Sci. Rep.* **7**, 8157 (2017).
  48. Nilsson, R. et al. Discovery of genes essential for heme biosynthesis through large-scale gene expression analysis. *Cell Metab.* **10**, 119–130 (2009).
  49. Tschop, M. H. et al. A guide to analysis of mouse energy metabolism. *Nat. Methods* **9**, 57–63 (2011).
  50. West, D. B., Boozer, C. N., Moody, D. L. & Atkinson, R. L. Dietary obesity in nine inbred mouse strains. *Am. J. Physiol.* **262**, R1025–R1032 (1992).
  51. Dunaief, J. L. Iron induced oxidative damage as a potential factor in age-related macular degeneration: the Cogan Lecture. *Invest Ophthalmol. Vis. Sci.* **47**, 4660–4664 (2006).
  52. Sypes, E. E. et al. Higher Body Mass Index Is Associated with Iron Deficiency in Children 1 to 3 Years of Age. *J. Pediatr.* **207**, 198–204.e191 (2019).
  53. Kamat, M. A. et al. PhenoScanner V2: an expanded tool for searching human genotype-phenotype associations. *Bioinformatics* **35**, 4851–4853 (2019).
  54. Prins, B. P. et al. Genome-wide analysis of health-related biomarkers in the UK Household Longitudinal Study reveals novel associations. *Sci. Rep.* **7**, 11008 (2017).
  55. Gopal, S. K. et al. YBX1/YB-1 induces partial EMT and tumorigenicity through secretion of angiogenic factors into the extracellular microenvironment. *Oncotarget* **6**, 13718–13730 (2015).
  56. Tang, J. et al. Knockdown of TPT1-AS1 inhibits cell proliferation, cell cycle G1/S transition, and epithelial-mesenchymal transition in gastric cancer. *Bosn. J. Basic Med. Sci.* **21**, 39–46 (2021).
  57. Ye, Z. et al. ODC1 promotes proliferation and mobility via the AKT/GSK3beta/beta-catenin pathway and modulation of acidotic microenvironment in human hepatocellular carcinoma. *Onco Targets Ther.* **12**, 4081–4092 (2019).
  58. Meng, Q. et al. Abrogation of glutathione peroxidase-1 drives EMT and chemoresistance in pancreatic cancer by activating ROS-mediated Akt/GSK3beta/Snail signaling. *Oncogene* **37**, 5843–5857 (2018).
  59. Xu, C. et al. SPP1, analyzed by bioinformatics methods, promotes the metastasis in colorectal cancer by activating EMT pathway. *Biomed. Pharmacother.* **91**, 1167–1177 (2017).
  60. Soldatov, R. et al. Spatiotemporal structure of cell fate decisions in murine neural crest. *Science* **364**, eaas9536 (2019).
  61. Guan, C., Ye, C., Yang, X. & Gao, J. A review of current large-scale mouse knockout efforts. *Genesis* **48**, 73–85 (2010).
  62. Wenger, M. J., DellaValle, D. M., Murray-Kolb, L. E. & Haas, J. D. Effect of iron deficiency on simultaneous measures of behavior, brain activity, and energy expenditure in the performance of a cognitive task. *Nutr. Neurosci.* **22**, 196–206 (2019).
  63. Blankenhau, B. et al. Ferritin regulates organismal energy balance and thermogenesis. *Mol. Metab.* **24**, 64–79 (2019).

64. Bogdan, A. R., Miyazawa, M., Hashimoto, K. & Tsuji, Y. Regulators of Iron Homeostasis: New Players in Metabolism, Cell Death, and Disease. *Trends Biochem Sci.* **41**, 274–286 (2016).
65. Wasserman, D. H., O'Doherty, R. M. & Zinker, B. A. Role of the endocrine pancreas in control of fuel metabolism by the liver during exercise. *Int J. Obes. Relat. Metab. Disord.* **19**, S22–S30 (1995).
66. Bhattacharya, D., Azambuja, A. P. & Simoes-Costa, M. Metabolic Reprogramming Promotes Neural Crest Migration via Yap/Tead Signaling. *Dev. Cell* **53**, 199–211.e196 (2020).
67. Manz, D. H., Blanchette, N. L., Paul, B. T., Torti, F. M. & Torti, S. V. Iron and cancer: recent insights. *Ann. N. Y Acad. Sci.* **1368**, 149–161 (2016).
68. Yuan, M. et al. N-myristoylation: from cell biology to translational medicine. *Acta Pharm. Sin.* **41**, 1005–1015 (2020).
69. Lin, C. Y. et al. Membrane protein-regulated networks across human cancers. *Nat. Commun.* **10**, 3131 (2019).
70. Edgar, R. C. MUSCLE: multiple sequence alignment with high accuracy and high throughput. *Nucleic Acids Res* **32**, 1792–1797 (2004).
71. Carithers, L. J. et al. A Novel Approach to High-Quality Postmortem Tissue Procurement: The GTEx Project. *Biopreserv Biobank* **13**, 311–319 (2015).
72. Butler, A., Hoffman, P., Smibert, P., Papalexis, E. & Satija, R. Integrating single-cell transcriptomic data across different conditions, technologies, and species. *Nat. Biotechnol.* **36**, 411–420 (2018).
73. Formstecher, E. et al. Protein interaction mapping: a Drosophila case study. *Genome Res.* **15**, 376–384 (2005).
74. Rain, J. C. et al. The protein-protein interaction map of *Helicobacter pylori*. *Nature* **409**, 211–215 (2001).
75. Cox, J. & Mann, M. MaxQuant enables high peptide identification rates, individualized p.p.b.-range mass accuracies and proteome-wide protein quantification. *Nat. Biotechnol.* **26**, 1367–1372 (2008).
76. Zhang, X. et al. Proteome-wide identification of ubiquitin interactions using UbiA-MS. *Nat. Protoc.* **13**, 530–550 (2018).
77. Go, C. D. et al. A proximity-dependent biotinylation map of a human cell. *Nature* **595**, 120–124 (2021).
78. Ransick, A. et al. Single-Cell Profiling Reveals Sex, Lineage, and Regional Diversity in the Mouse Kidney. *Dev. Cell* **51**, 399–413.e397 (2019).
79. Stuart, T. et al. Comprehensive Integration of Single-Cell Data. *Cell* **177**, 1888–1902.e1821 (2019).
80. Wolock, S. L., Lopez, R. & Klein, A. M. Scrublet: Computational Identification of Cell Doublets in Single-Cell Transcriptomic Data. *Cell Syst.* **8**, 281–291.e289 (2019).
81. Wilson, P. C. et al. The single-cell transcriptomic landscape of early human diabetic nephropathy. *Proc. Natl Acad. Sci. USA* **116**, 19619–19625 (2019).
82. Chung, J. J. et al. Single-Cell Transcriptome Profiling of the Kidney Glomerulus Identifies Key Cell Types and Reactions to Injury. *J. Am. Soc. Nephrol.* **31**, 2341–2354 (2020).
83. Schroeder, A. W. et al. NOVEL HUMAN KIDNEY CELL SUBSETS IDENTIFIED BY MUX-SEQ. *Transplantation* **104**, S85 (2020).
84. Weir, J. B. New methods for calculating metabolic rate with special reference to protein metabolism. *J. Physiol.* **109**, 1–9 (1949).
85. Even, P. C., Mokhtarian, A. & Pele, A. Practical aspects of indirect calorimetry in laboratory animals. *Neurosci. Biobehav Rev.* **18**, 435–447 (1994).
86. Concordet, J. P. & Haeussler, M. CRISPOR: intuitive guide selection for CRISPR/Cas9 genome editing experiments and screens. *Nucleic Acids Res* **46**, W242–W245 (2018).
87. Shalem, O. et al. Genome-scale CRISPR-Cas9 knockout screening in human cells. *Science* **343**, 84–87 (2014).
88. Livak, K. J. & Schmittgen, T. D. Analysis of relative gene expression data using real-time quantitative PCR and the 2(-Delta Delta C(T)) Method. *Methods* **25**, 402–408 (2001).
89. Beck, T., Rowlands, T., Shorter, T. & Brookes, A. J. GWAS Central: an expanding resource for finding and visualising genotype and phenotype data from genome-wide association studies. *Nucleic Acids Res* **51**, D986–D993 (2023).
90. Howe, K. L. et al. Ensembl 2021. *Nucleic Acids Res* **49**, D884–D891 (2021).

## Acknowledgements

We would like to thank Vendula Novosadova (Institute of Molecular Genetics of the Czech Academy of Sciences) and Roldan Medina De Guia (Institute of Molecular Genetics of the Czech Academy of Sciences) for feedback on the statistics as well as clinical chemistry. M.T., M.K., T.Z., and J.K. acknowledge CzechNanoLab Research Infrastructure supported by MEYS CR (LM2018110). M.T. acknowledges the Brno City Municipality as a Brno Ph.D. Talent Scholarship Holder and Martina Roeselova Memorial Fellowship. R.S. was supported by the Czech Academy of Sciences RVO 68378050 and by LM2018126, Czech Centre for Phenogenomics, provided by the Ministry of Education, Youth and Sports of the Czech Republic. CIISB, Instruct-CZ Centre of Instruct-ERIC EU consortium, funded by MEYS CR infrastructure project LM2023042 and European Regional Development Fund-Project „JP CIISB“ (No. CZ.02.1.01/0.0/0.0/18\_046/0015974), is gratefully acknowledged for the financial support of the measurements at the CEITEC Proteomics Core Facility. Computational resources for the IP LC-MS/MS data processing were provided by the e-INFRA CZ project (ID:90140), supported by the Ministry of Education, Youth and Sports of the Czech Republic. I.A. was supported by Bertil Hallsten Research Foundation, Medical University of Vienna and Gustafsson's Foundation Prize 2021, T.B. was supported by a grant from the Austrian Science Fund M2688-B28, J.K. was supported by the Grant Agency of Masaryk University (MUNI/H/1615/2018). I.P. was supported by the European Union's Horizon 2020 Research and Innovation Program under Marie Skłodowska-Curie (grant agreement No. 860635, ITN NEUcrest), P.B. was supported by the German Research Foundation (DFG, Project IDs 322900939, 454024652, 432698239 & 445703531), European Research Council (ERC Consolidator Grant No 101001791), and the Federal Ministry of Education and Research (BMBF, STOP-FSGS-01GM2202C). The work of J.K. was supported by Czech Science Foundation (22-02794 S). Parts of Figs. 1, 3, 6 and Supplementary Figs 6, 11 – 18 were created with BioRender.com. OG and RD were supported by Ministry of Science and Higher Education of the Russian Federation grant 075-15-2021-1344 and Japan Society for the Promotion of Science (JSPS) KAKENHI JP23H02226.

## Author contributions

J.Pe., L.E., A.A., I.P., R.M., T.B., M.T., R.D., A.S.S., E.E.A., D.P.R., H.Z., M.K., M.E.K., J.Kr., T.R., K.G., S.K., D.P., Z.Z., R.S.G., A.G., M.E.B., M.i.K., H.A., and D.L. acquired all biological data and performed the relevant analysis. R.K. and C.K. provided human samples and gave feedback on experimental aspects. J.Pe., I.A., T.Z., F.E., Z.M., G.S., T.K., V.B., T.H., K.F., J.Ka., P.B., C.F., J.R., P.K., J.P.R., R.S. and O.G. gave feedback on experimental aspects, supervised experimental approaches, and implemented the data interpretation. J.Pe., L.E. and I.A. made all figures containing data and resulting analysis. J.Pe. and I.A. designed the study, organized the experimental work, and wrote the manuscript. All authors provided feedback on figures, manuscript composition, and structure.

## Funding

Open access funding provided by Karolinska Institute.

## Competing interests

The authors declare no competing interests.

## Additional information

**Supplementary information** The online version contains supplementary material available at <https://doi.org/10.1038/s41467-023-38663-7>.

**Correspondence** and requests for materials should be addressed to Julian Petersen or Igor Adameyko.

**Peer review information** *Nature Communications* thanks Erich Jarvis and the other, anonymous, reviewer(s) for their contribution to the peer review of this work. A peer review file is available.

**Reprints and permissions information** is available at <http://www.nature.com/reprints>

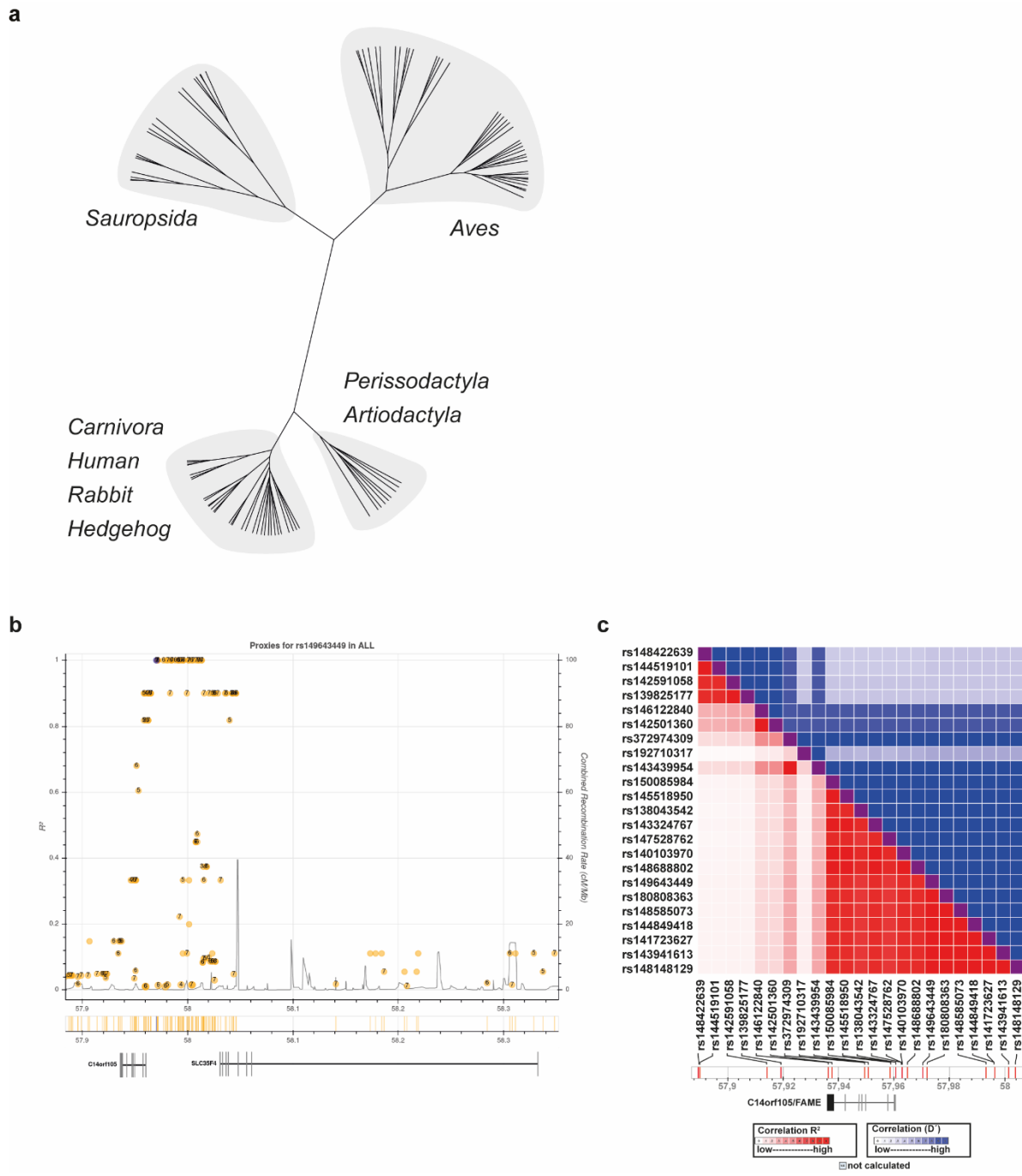
**Publisher's note** Springer Nature remains neutral with regard to jurisdictional claims in published maps and institutional affiliations.

**Open Access** This article is licensed under a Creative Commons Attribution 4.0 International License, which permits use, sharing, adaptation, distribution and reproduction in any medium or format, as long as you give appropriate credit to the original author(s) and the source, provide a link to the Creative Commons license, and indicate if changes were made. The images or other third party material in this article are included in the article's Creative Commons license, unless indicated otherwise in a credit line to the material. If material is not included in the article's Creative Commons license and your intended use is not permitted by statutory regulation or exceeds the permitted use, you will need to obtain permission directly from the copyright holder. To view a copy of this license, visit <http://creativecommons.org/licenses/by/4.0/>.

© The Author(s) 2023, corrected publication 2023

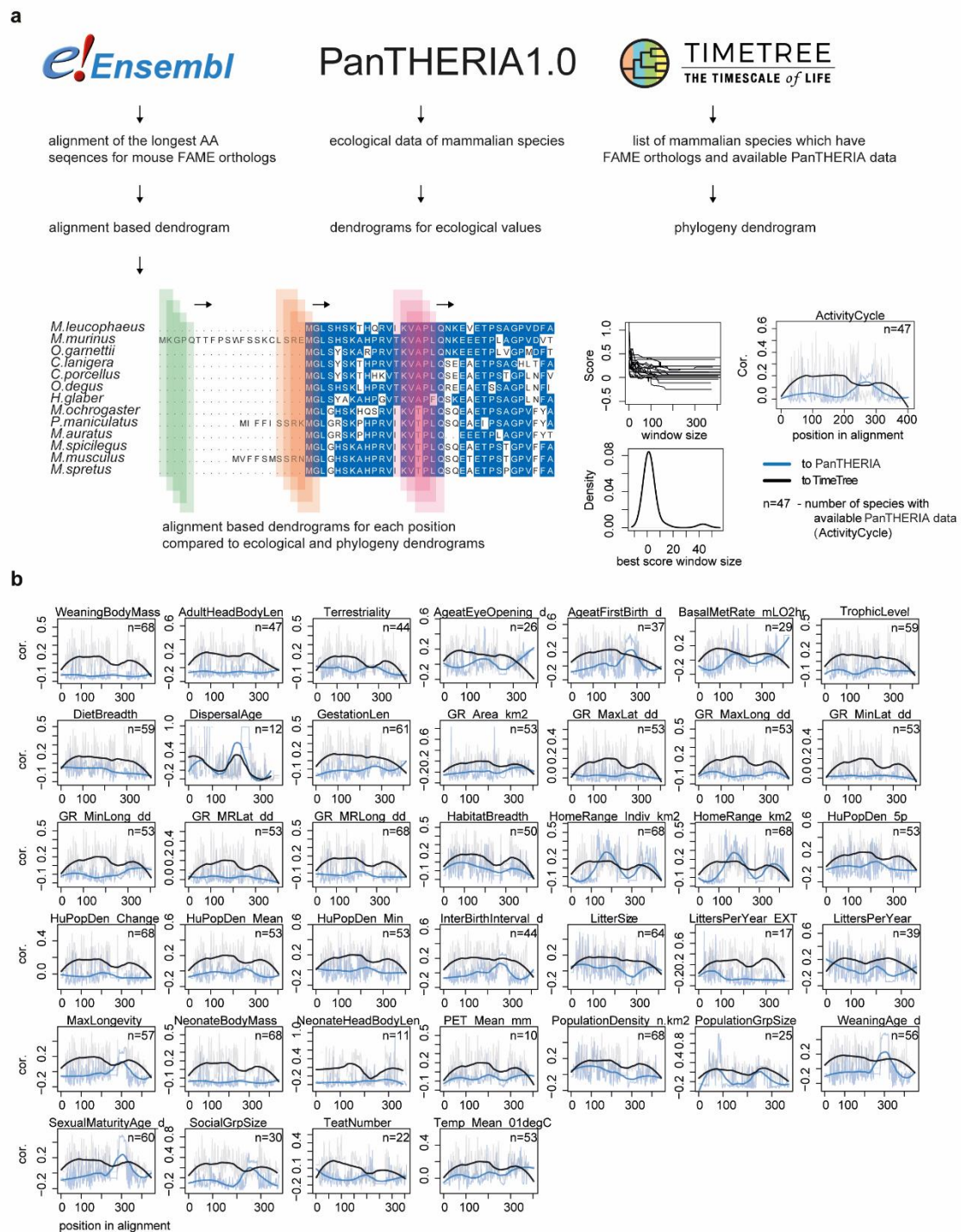
Julian Petersen<sup>1,25</sup>✉, Lukas Englmaier<sup>2,3,25</sup>, Artem V. Artemov<sup>4</sup>, Irina Poverennaya<sup>4</sup>, Ruba Mahmoud<sup>1</sup>, Thibault Boudierlique<sup>4</sup>, Marketa Tesarova<sup>5</sup>, Ruslan Deviatiiarov<sup>6,7</sup>, Anett Szilvasy-Szabo<sup>8</sup>, Evgeny E. Akkuratov<sup>9,10</sup>, David Pajuelo Reguera<sup>11</sup>, Hugo Zeberg<sup>12,13</sup>, Marketa Kauccka<sup>14</sup>, Maria Eleni Kastriti<sup>4,13</sup>, Jan Krivanek<sup>15</sup>, Tomasz Radaszkiewicz<sup>16</sup>, Kristina Gomoryova<sup>16</sup>, Sarah Knauth<sup>1</sup>, David Potesil<sup>17</sup>, Zbynek Zdrahal<sup>17</sup>, Ranjani Sri Ganji<sup>17</sup>, Anna Grabowski<sup>4</sup>, Miriam E. Buhl<sup>18</sup>, Tomas Zikmund<sup>5</sup>, Michaela Kavkova<sup>5,15</sup>, Hakan Axelson<sup>19</sup>, David Lindgren<sup>19</sup>, Rafael Kramann<sup>20</sup>, Christoph Kuppe<sup>20</sup>, Ferenc Erdelyi<sup>21</sup>, Zoltan Mate<sup>21</sup>, Gabor Szabo<sup>21</sup>, Till Koehne<sup>1</sup>, Tibor Harkany<sup>22</sup>, Kaj Fried<sup>13</sup>, Jozef Kaiser<sup>5</sup>, Peter Boor<sup>18</sup>, Csaba Fekete<sup>8</sup>, Jan Rozman<sup>11,23</sup>, Petr Kasperek<sup>11</sup>, Jan Prochazka<sup>11</sup>, Radislav Sedlacek<sup>11</sup>, Vitezslav Bryja<sup>16</sup>, Oleg Gusev<sup>6,24</sup> & Igor Adameyko<sup>4,13</sup>✉

<sup>1</sup>Department of Orthodontics, University Leipzig Medical Center, Leipzig, Germany. <sup>2</sup>CeMM Research Center for Molecular Medicine of the Austrian Academy of Sciences, 1090 Vienna, Austria. <sup>3</sup>Ludwig Boltzmann Institute for Rare and Undiagnosed Diseases, 1090 Vienna, Austria. <sup>4</sup>Department of Neuroimmunology, Center for Brain Research, Medical University Vienna, Vienna, Austria. <sup>5</sup>Central European Institute of Technology, Brno University of Technology, Brno, Czech Republic. <sup>6</sup>Regulatory Genomics Research Center, Institute of Fundamental Medicine and Biology, Kazan Federal University, Kazan, Russia. <sup>7</sup>Endocrinology Research Center, Moscow, Russia. <sup>8</sup>Laboratory of Integrative Neuroendocrinology, Institute of Experimental Medicine, 1083 Budapest, Hungary. <sup>9</sup>Department of Applied Physics, Royal Institute of Technology, Science for Life Laboratory, 171 65, Stockholm, Sweden. <sup>10</sup>University of Oxford, MRC Weatherall Institute of Molecular Medicine, Radcliffe Department of Medicine, Oxford OX3 9DS, UK. <sup>11</sup>Institute of Molecular Genetics of the Czech Academy of Science, Czech Centre for Phenogenomics, Vestec, Czech Republic. <sup>12</sup>Department of Neuroscience, Karolinska Institutet, Stockholm, Sweden. <sup>13</sup>Department of Physiology and Pharmacology, Karolinska Institutet, Stockholm, Sweden. <sup>14</sup>Max Planck Institute for Evolutionary Biology, Plon 24306, Germany. <sup>15</sup>Department of Histology and Embryology, Faculty of Medicine, Masaryk University, Brno, Czech Republic. <sup>16</sup>Institute of Experimental Biology, Faculty of Science, Masaryk University, Brno, Czech Republic. <sup>17</sup>Central European Institute of Technology, Masaryk University, Brno, Czech Republic. <sup>18</sup>Institute of Pathology & Electron Microscopy Facility, RWTH Aachen University Hospital, Aachen, Germany. <sup>19</sup>Translational Cancer Research, Department of Laboratory Medicine, Lund University, Medicon Village, Scheelevagen 2, Lund, Sweden. <sup>20</sup>Institute of Experimental Medicine and Systems Biology, RWTH Aachen University, Aachen, Germany. <sup>21</sup>Medical Gene Technology Unit, Institute of Experimental Medicine, Budapest, Hungary. <sup>22</sup>Department of Molecular Neurosciences, Center for Brain Research, Medical University Vienna, Vienna, Austria. <sup>23</sup>Luxembourg Centre for Systems Biomedicine, University of Luxembourg, 6, avenue du Swing, 4367 Belvaux, Luxembourg. <sup>24</sup>Intractable Disease Research Center, Graduate School of Medicine, Juntendo University, Tokyo, Japan. <sup>25</sup>These authors contributed equally: Julian Petersen, Lukas Englmaier. ✉ e-mail: [julian.petersen@medizin.uni-leipzig.de](mailto:julian.petersen@medizin.uni-leipzig.de); [igor.adameyko@meduniwien.ac.at](mailto:igor.adameyko@meduniwien.ac.at)



**Supplementary Figure 1: Comparative genomics analysis of FAME/C14orf105**

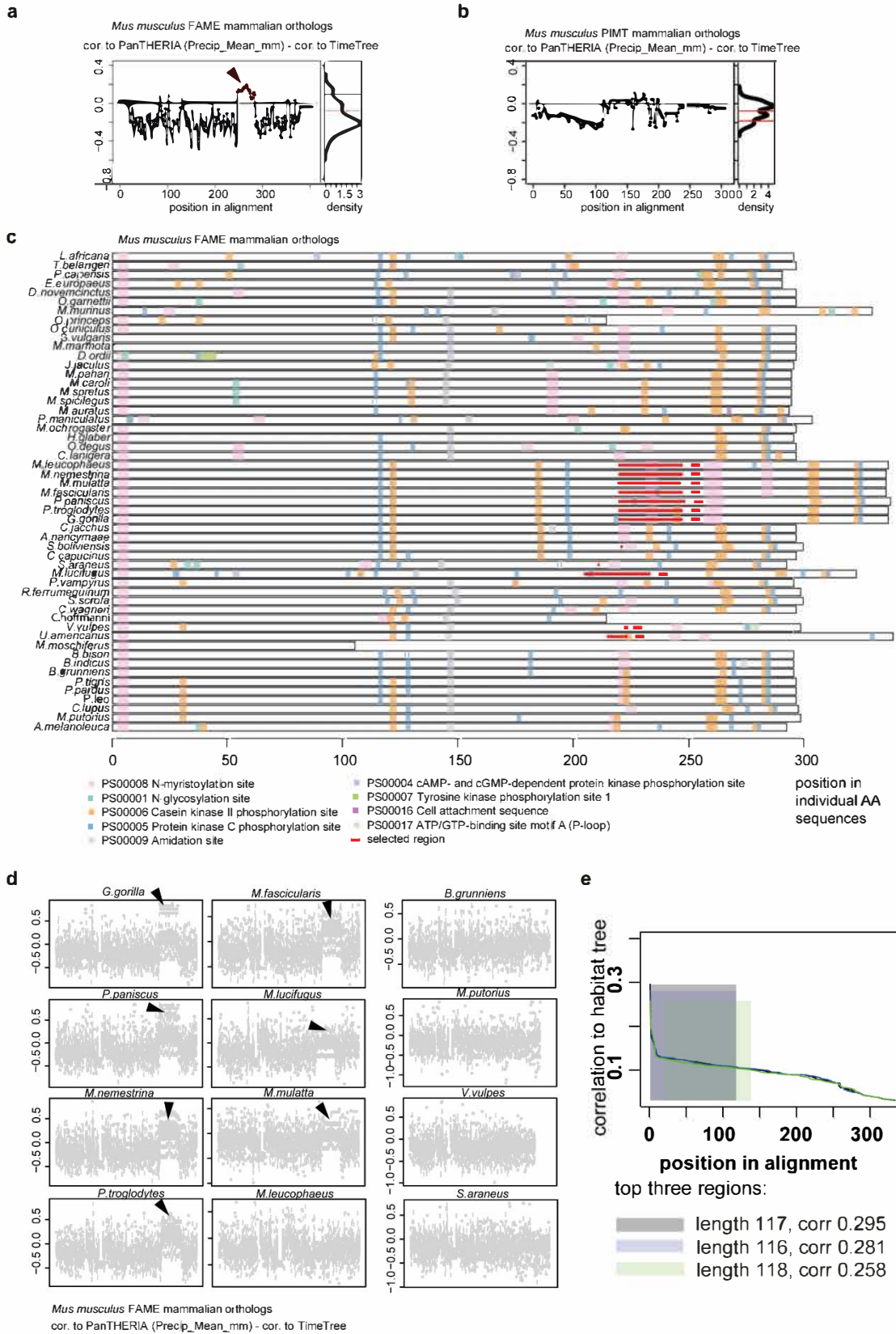
(a) Phylogenetic tree for FAME orthologs of diverse species. (b) Linkage disequilibrium between the polymorphisms in **Figure 1f**. Fourteen of these alleles form a block with linkage disequilibrium  $r^2 > 0.8$ . (c) Introgressed Neanderthal haplotype encompassing *C14orf105*. 58 SNPs form a haplotype ( $r^2 > 0.8$ ), which is tagged by rs149643449, spanning the genomic region chr14:57958614-58046101. (b-c) Figure generated using LDlink (Machiela and Chanock 2015) using data from the 1000 Genomes Project (Genomes Project, Auton et al. 2015). The abscissa gives genomic coordinates on chromosome 14 (*hg19*).



## Supplementary Figure 2: FAME evolution with animal lifestyle

(a) Basic scheme of the correlation pipeline. Orthologous gene IDs for *Mus musculus* FAME were obtained from Ensembl. For each gene and species, the longest amino acid (AA) sequences were downloaded through biomaRt. Ecological data for mammalian species were obtained from PanTHERIA1.0. Phylogenetic distances of species used as controls were obtained from TimeTree database. For each condition in PanTHERIA (n=44) a subset of species with available data was extracted and an ecologic dendrogram was built based on the feature scores. A subset of the phylogenetic tree was created for selected species. Amino acid alignments were created for the subset list. The window size was analyzed to provide the

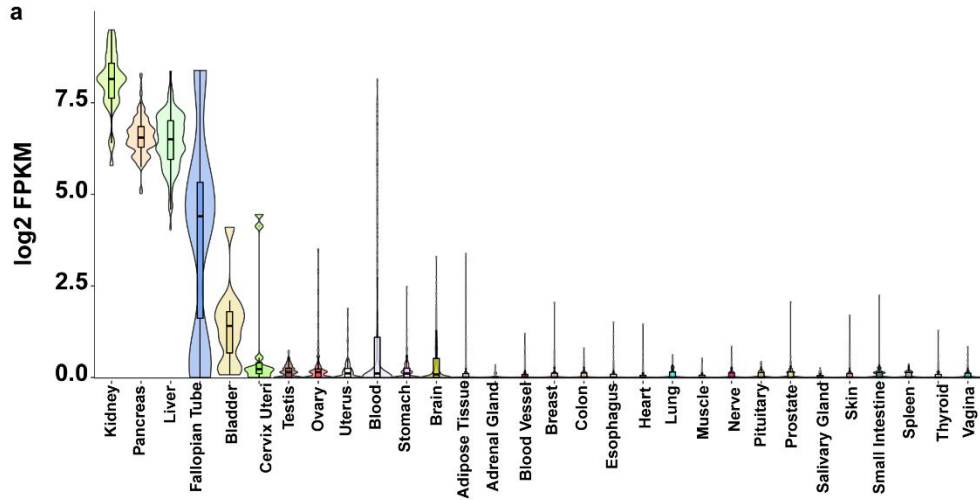
highest difference between cophenetic correlation of the alignment k-mer dendrogram with ecologic and phylogenetic dendrograms. As expected, this score drops with increasing k-mer length and, in most cases, the shortest 2-mer window provides the highest difference (density plot). Scanning the alignment subset (n=47) with the 2 AA window for the feature "ActivityCycle" resulted in trends overlapping with phylogeny. **(b)** Further examples of correlation trends are shown. Detailed explanation of ecologic factors titles can be accessed under [<https://esapubs.org/archive/ecol/E090/184/metadata.htm>]. Interestingly, the sites of ties can be the same or different and trends in general have different trajectories leading to functional significance or insignificance of protein domains in relation to ecological factor.



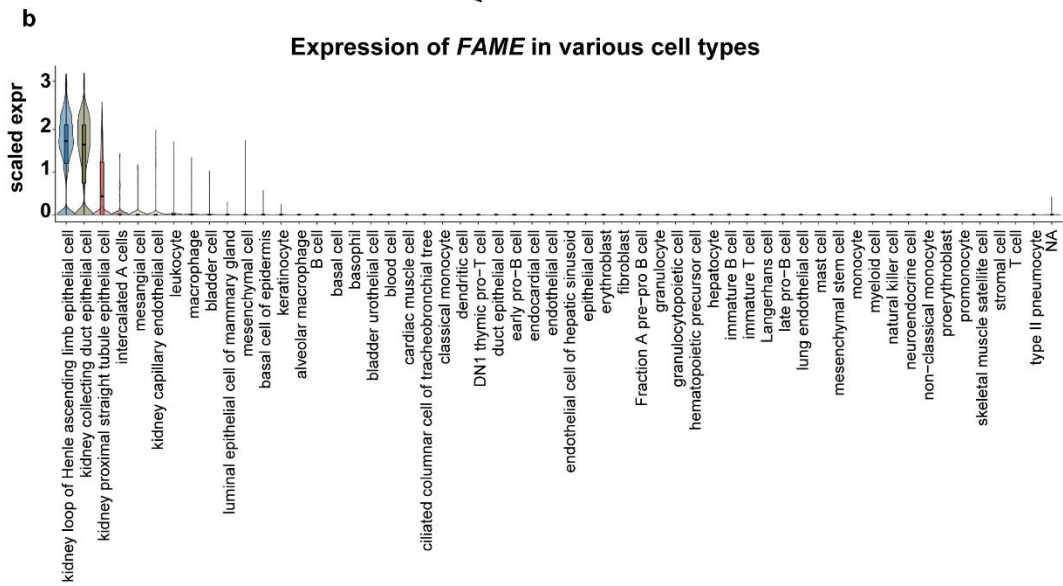
### Supplementary Figure 3: Comparison of FAME orthologs

(a) FAME orthologs contain high scoring regions (2-mer alignment based dendrogram cor. to PanTHERIA - cor. to TimeTree) between 200 and 300 AA of the alignment. We extracted these positions by selecting minimums for density of positions and using the highest minimum as a threshold (0.095, top red line). (b) Mammalian PIMT orthologs (n=52) were selected as negative controls and checked for difference between correlation profiles. In general, score values are lower and most of them are close to zero (highest threshold matches with negative score value -0.075, top red line). This can be explained as an absence of functional connections of any PIMT domains with precipitation. (c) Transferring of selected region from the alignment to individual molecules. Prosite domains are annotated and labeled as boxes with different colors. Red color indicates the highest scoring region. Approximately 10 proteins contain this annotated region, and it overlaps with Prosite domains. Overlap significance (Fisher's exact test) highlights the match with the N-myristylation site (PS00008) for the majority of proteins (Supplementary Data 6). (d) Repeating the experiment with 100 bootstraps for 10 random sequences. Arrows points out the high scoring region of individual molecules. (e) Correlation between alignments and habitat tree for the top three windows.

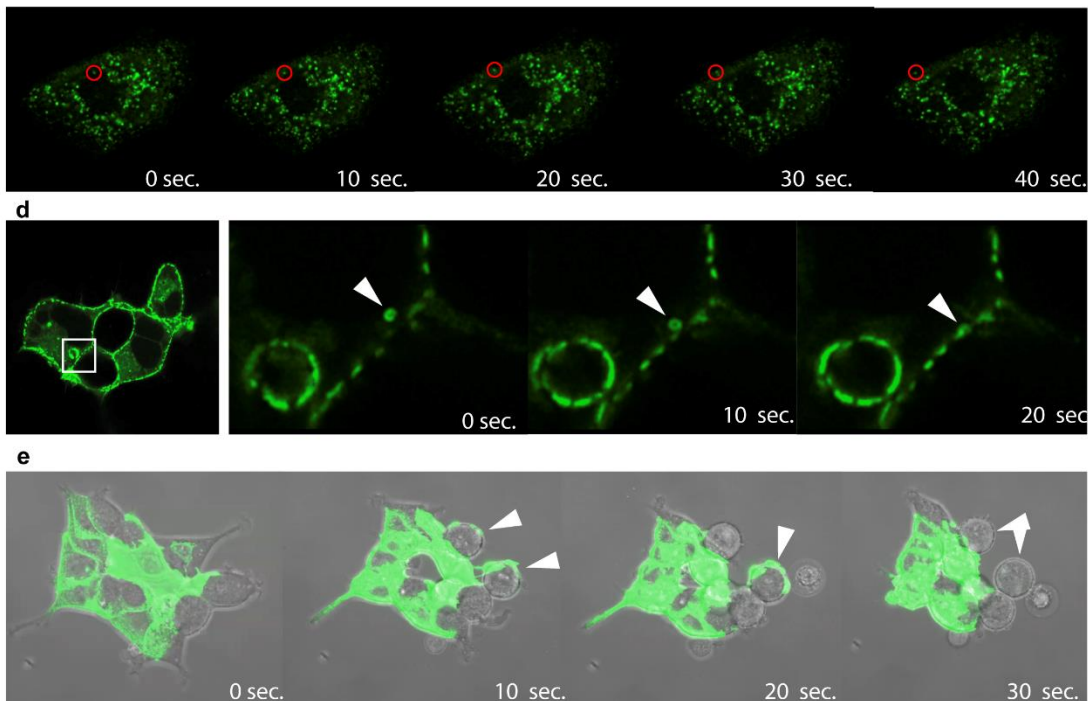
**Expression of *FAME* in various organs and tissues**



**Expression of *FAME* in various cell types**



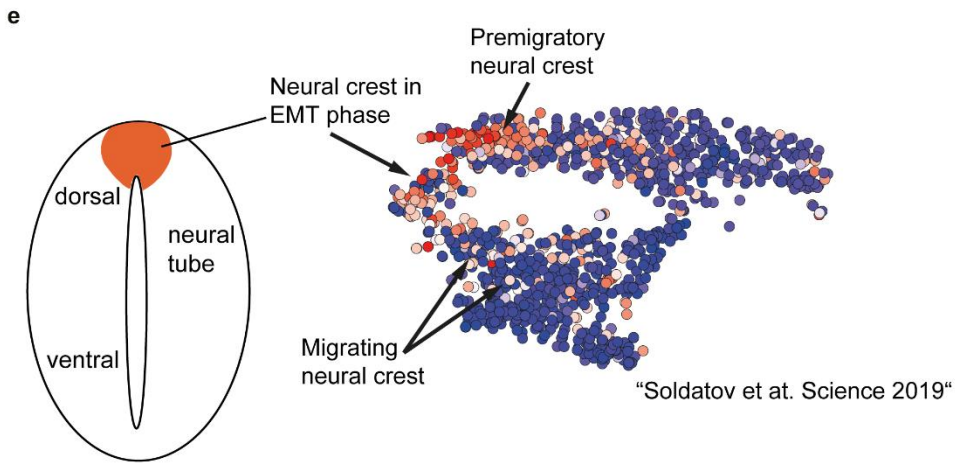
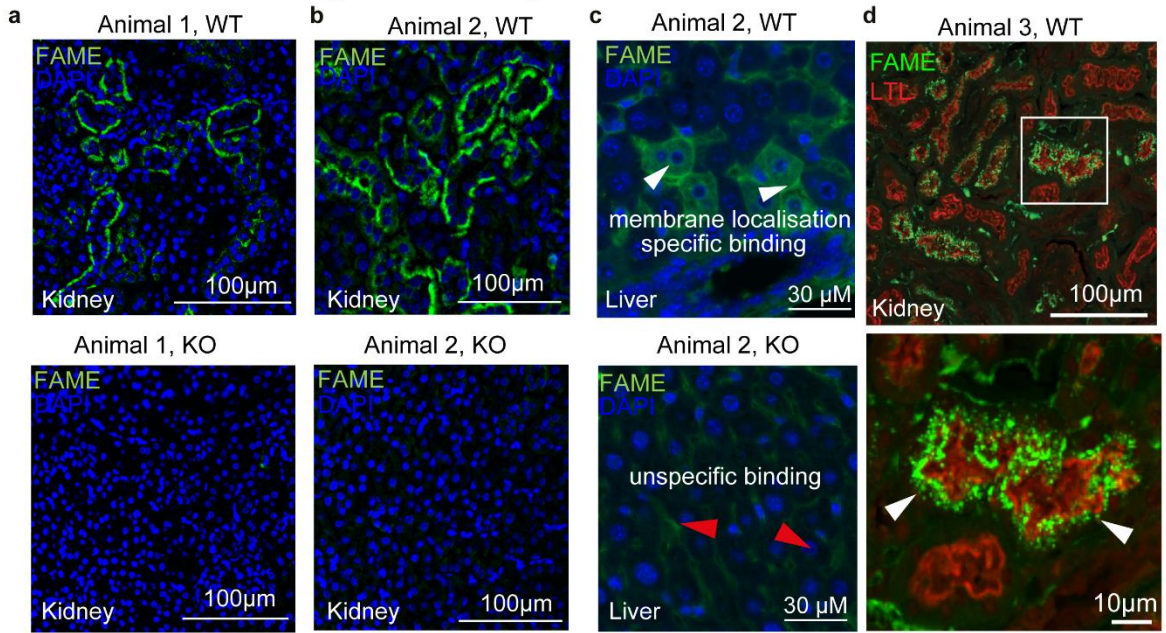
**Live cell imaging of HEK293T cells expressing FAME-EGFP**



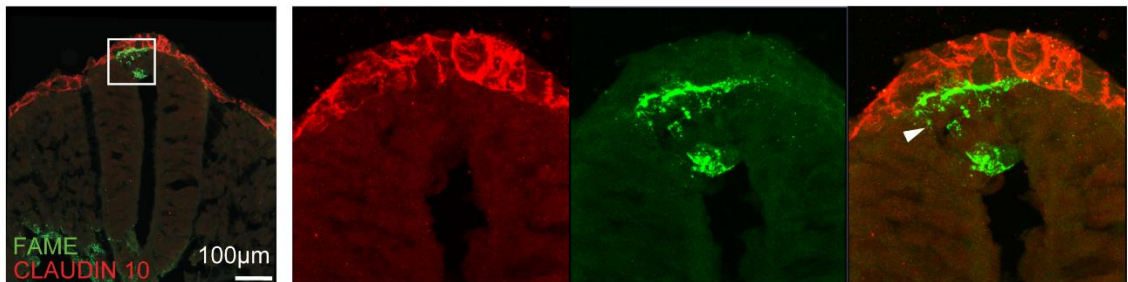
**Supplementary Figure 4: *FAME* expression in tissues and protein localization upon overexpression**

(a) Analysis of *FAME* expression in various human tissues based on Genotype-Tissue Expression data. (b) Detailed expression analysis of *Fame* in different mouse cell types using Tabula muris, a recently derived mouse single cell atlas. (a-b) Descriptive statistics can be accessed in Supplementary Data 13. (c-e) Live cell imaging of overexpressed FAME tagged with EGFP in HEK293T cells (c) FAME protein localizes to fast trafficking vesicular structures. Red circle follows a single vesicle over time. (d) FAME positive vesicle are transported amongst cells (white arrow). (e) FAME<sup>+</sup> cells share membranes with FAME cells (white arrows).

Immunostaining of FAME in kidney and liver from WT and KO animals



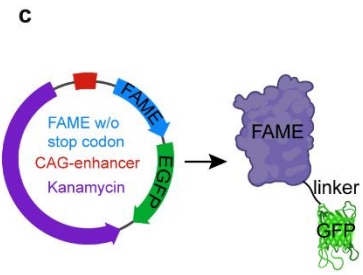
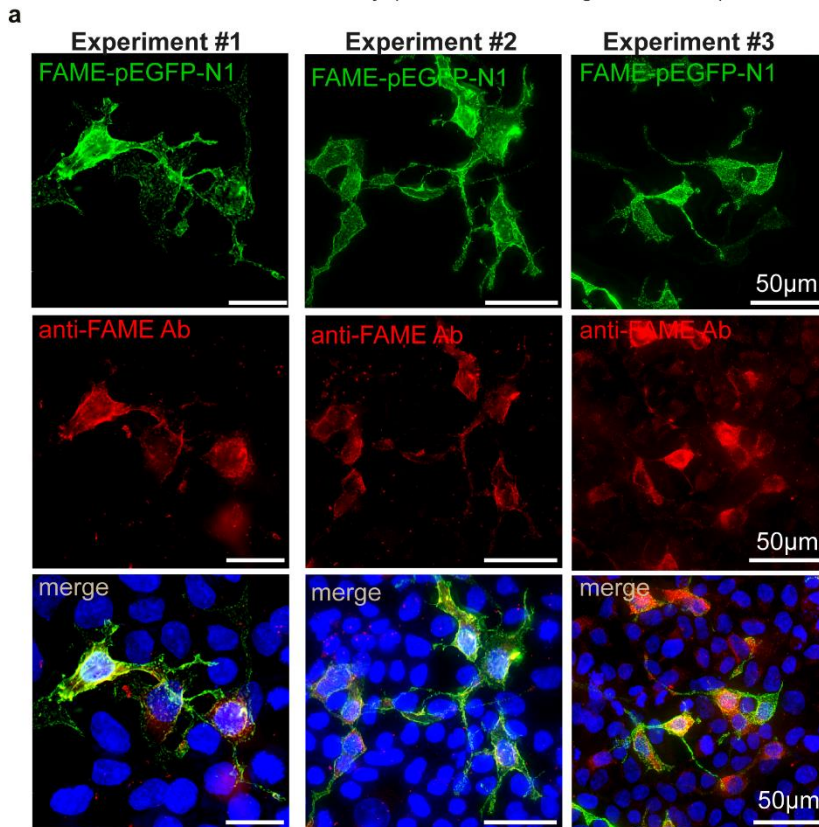
**f** Immunostaining of FAME in the neural tube of an E9.5 embryo, animal 4, WT



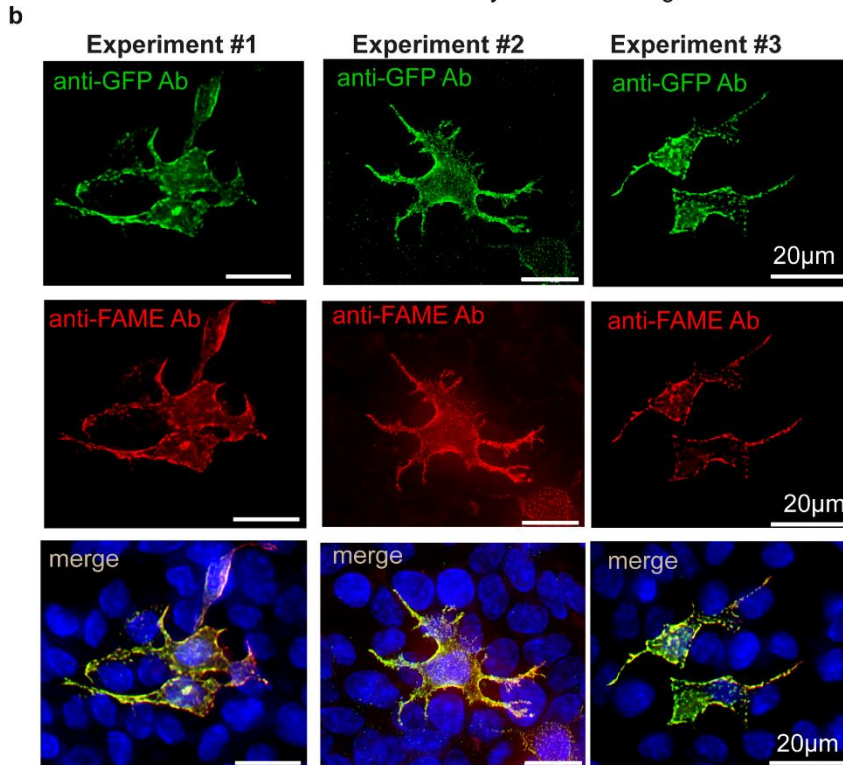
### **Supplementary Figure 5: Endogenous localization and appearance of FAME in the adult mouse and developing embryo**

**(a-b)** Knockout validation of the used FAME mouse monoclonal antibody. Protein specificity of the antibody is shown by immunohistochemistry on paraffin embedded tissue sections. Note the absence of signal in the two independent knockout (KO) animals. DAPI (blue), FAME (green) **(c)** Unspecific signal, often in the form of pronounced puncta, was frequently observed both in wild type in KO animals. **(a-c)** Representative images from 3 individual animals for each genotype. **(d)** Cell type specific staining was confirmed in high-magnification images, as shown here in the mouse kidney counterstained with lotus tetragonolobus lectin (LTL, red) visualizing proximal tubules. Note the vesicular appearance of FAME that corresponds to overexpression data. **(e)** Single cell analysis of murine neural crest and experimental validations associate *Fame* with epithelial-to-mesenchymal transition (EMT) (Soldatov, Kaucka et al. 2019). Schematic representation of the neural tube during development. **(f)** Transversal cryosection of an E9.5 mouse embryo with an immunofluorescence staining of the neural tube for FAME and CLAUDIN10. The white arrow points to an area of high FAME expression within the dorsal neural tube. Representative image from 3 tissue sections.

HEK293T cells transfected with FAME-pEGFP-N1 and stained with anti-FAME Antibody (without heat antigen retrieval)

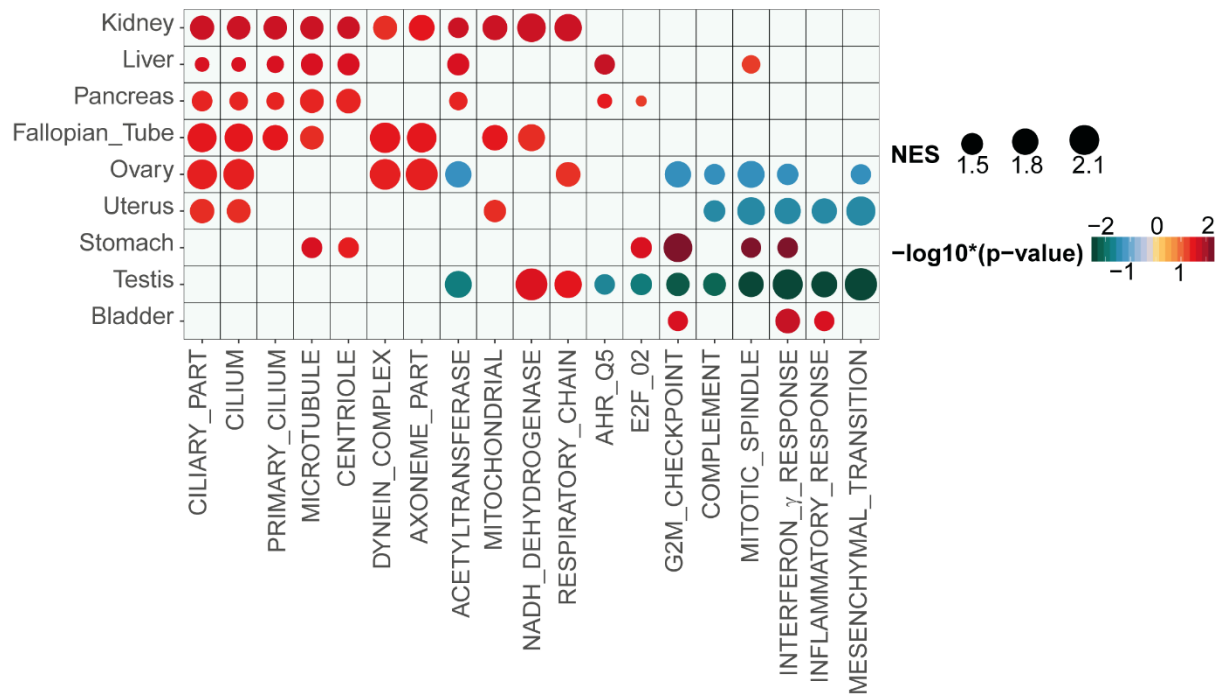


HEK293T cells transfected with FAME-pEGFP-N1 and stained with anti-GFP and anti-FAME Antibody after heat antigen retrieval



### **Supplementary Figure 6: FAME antibody validation and staining optimization in cells**

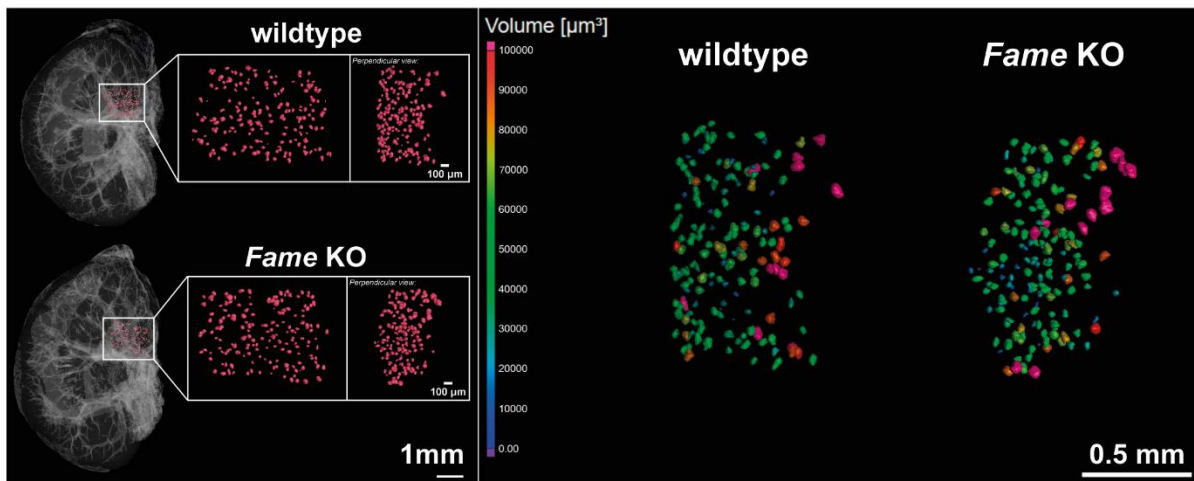
**(a)** Validation of the used mouse monoclonal antibody by immunocytochemistry. FAME fused to the green fluorescent protein EGFP was overexpressed in HEK293T cells. The same cells were stained with the used FAME-specific antibody. Note that only cells expressing FAME-EGFP show a signal in the red antibody-stained channel. There is no background staining observed in HEK293T cells that do not express FAME endogenously. **(b)** as (a) with additional heat-based antigen retrieval. Antigen retrieval leads to a near-perfect co-localisation suggesting increased performance of the used antibody. **(a-b)** Representative images from 3 independent experiments are shown. **(c)** Schematic vector map of the used pEGFP-N1 plasmid with the inserted FAME cDNA. The stop codon was removed to create a fusion protein with EGFP.



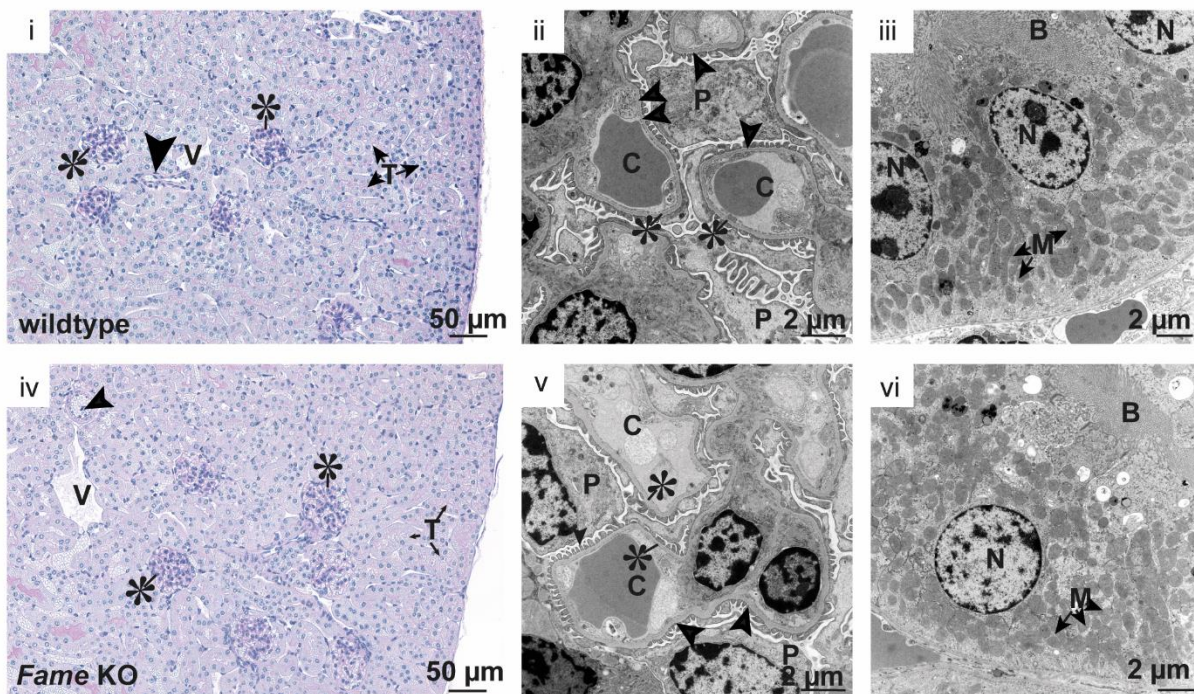
**Supplementary Figure 7: Gene correlation enrichment analysis using Genotype-Tissue Expression data**

Gene correlation enrichment analysis using Genotype-Tissue Expression data. The human tissues with highest *FAME* expression are ordered in a descending manner.

**a** micro-CT image of adult mouse kidney (*FVB/Ant*) and segmentation of glomeruli



**b** Histological and ultrastructural analyses of adult mouse kidney (*FVB/Ant*)



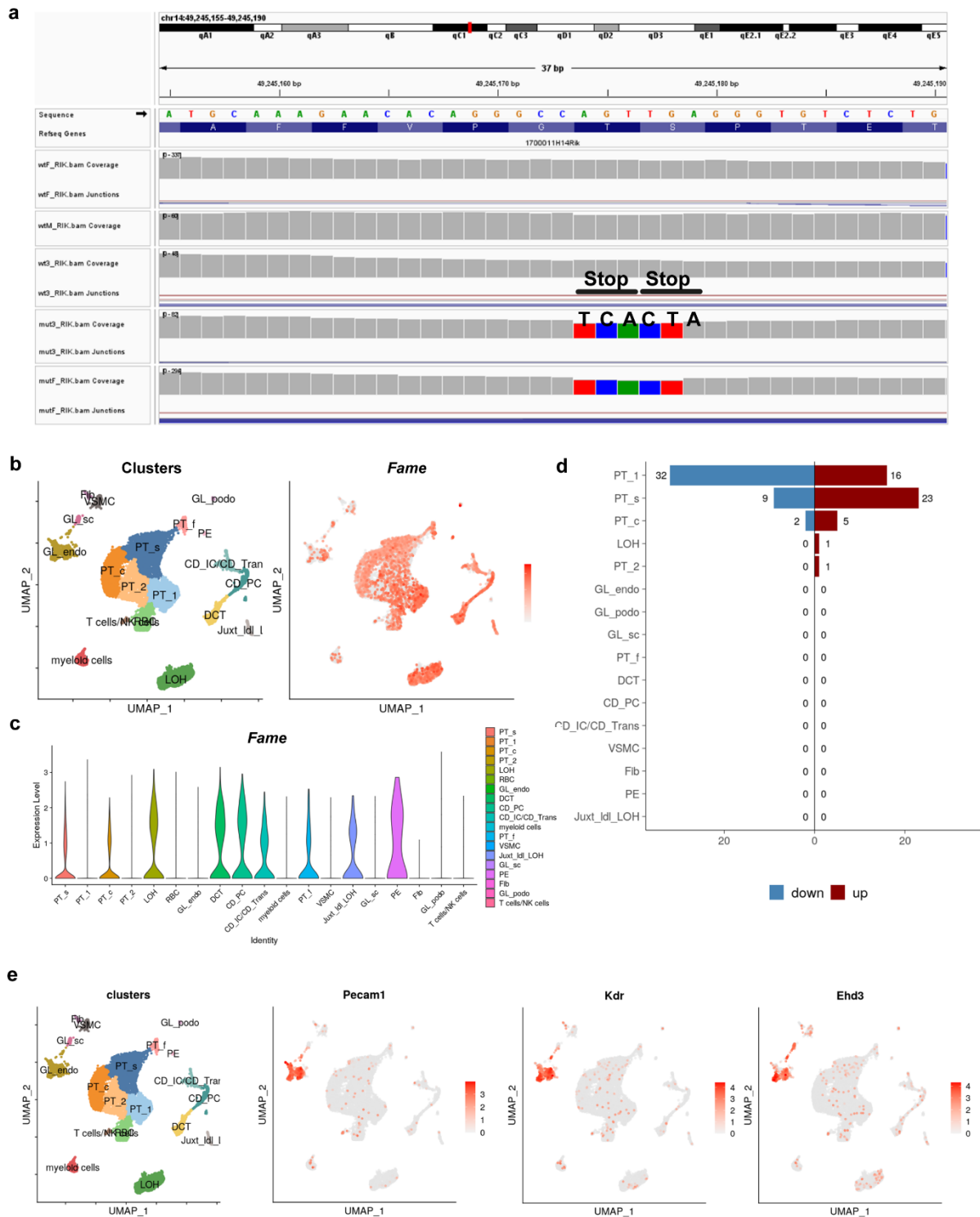
**Supplementary Figure 8: Structural analyses of *Fame* KO kidneys**

(a) Micro-CT images of wild type and *Fame* KO kidneys. Glomeruli were segmented and visualized in dark red. The right panel shows the volume analysis of the segmented glomeruli. No statistically significant differences were observed. (b) Histological (i, iv) and ultrastructural analyses (ii, iii, v, vi) show no morphological changes in *Fame* KO mice. (a-b) Representative images from 3 independent experiments are shown. (i, iv) PAS-stained paraffin sections of wild type and *Fame* KO mice show regularly developed kidneys. (T= tubuli, V= vein, arrow= artery, asterisk= glomeruli) (ii, v) Ultrastructural analyses by transmission electron microscopy of glomeruli show intact glomerular filtration barriers with regularly shaped podocyte foot processes (arrows), glomerular basal membrane (asterisks) and thin fenestrated endothelium of glomerular capillaries (C). (P= podocyte body) (iii, vi) The tubular cells show typical differentiated morphology with a prominent brush border (B) and several mitochondria (M).



### **Supplementary Figure 9: Marker genes of cell types found in the adult mouse kidney**

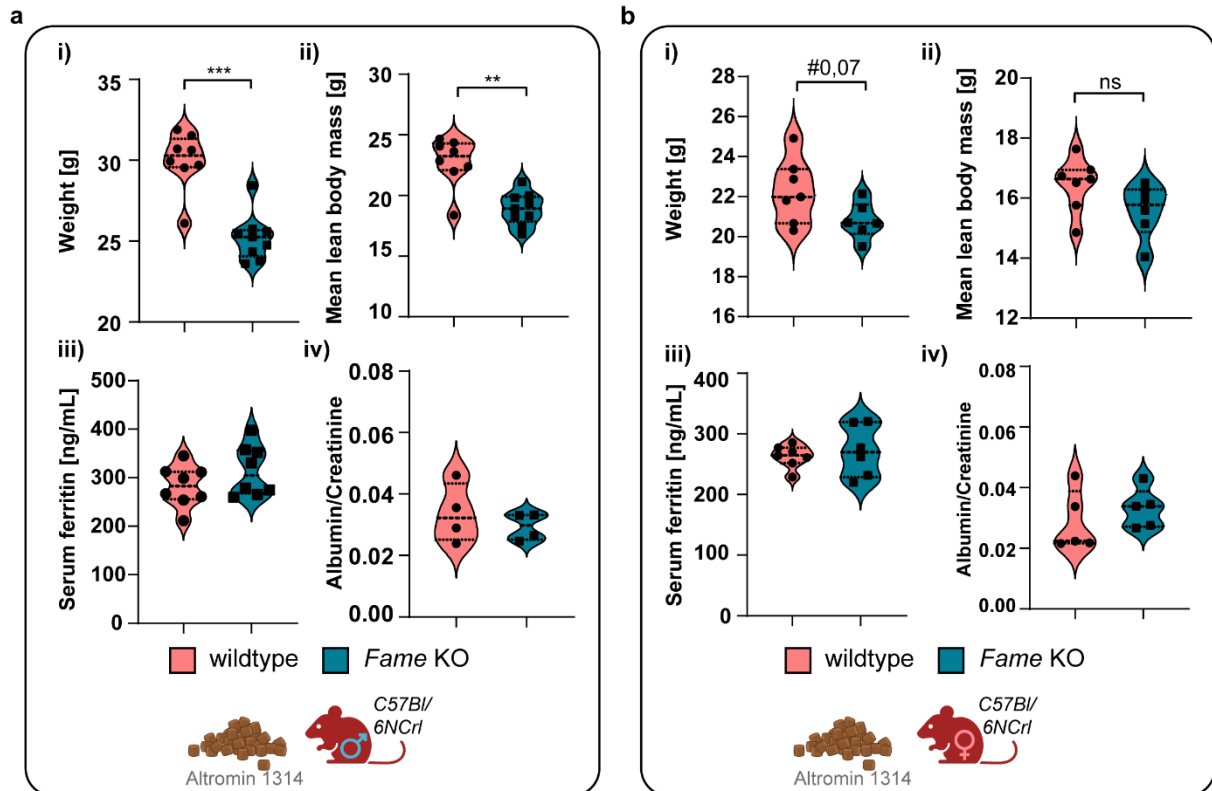
Dot plot of marker genes for identification of the cell types corresponding to each cluster in the adult mouse kidney scRNA-seq combined dataset. PTc= proximal convoluted tubules (segment S1), PTs= proximal straight tubule, PTf= female-specific cells from segment S3, PT1= unidentified subcluster of PT, PT2= unidentified subcluster of PT, GL endo= endothelial cells in glomeruli, GL podo= podocytes in glomeruli, GL sc= putative stem cells, LOH= loop of Henle, DCT= distal convoluted tubule, CD PC= collecting duct principal cells, CD IC/CD Trans= collecting duct intercalated cells and transitional cells, VSMC= vascular smooth muscle cells, Juxt ldl LOH= long descending limb of the loop of Henle in juxtamedullary nephrons, PE= parietal epithelium in glomeruli, Fib= fibroblasts, RBC= red blood cells.



**Supplementary Figure 10: Single-cell transcriptomics data of *Fame* KO kidneys**

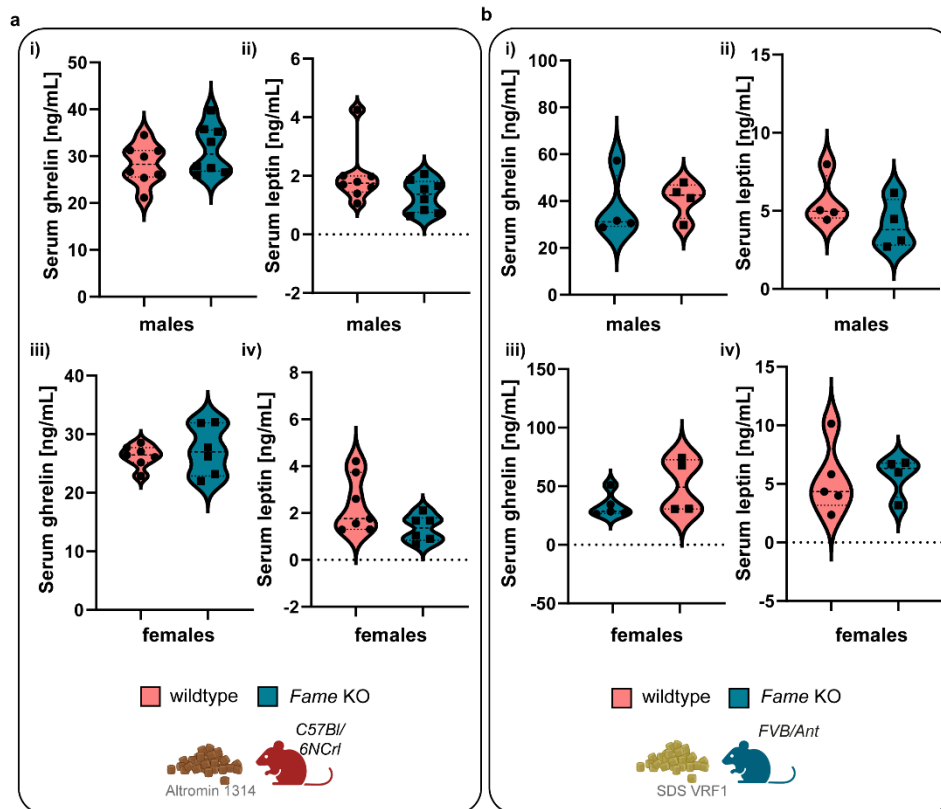
(a) Validation of *Fame* KO mouse (*FVB/Ant* background). Genomic DNA sequences of the indicated locus on chromosome 14 are shown. Note the insertion of a tandem stop codon in *Fame* KO animals. The sequencing reads are visualized by the IGV desktop application (Robinson, Thorvaldsdottir et al. 2011). (b) UMAP embedding of single-cell RNA sequencing data and the expression pattern of *Fame* are shown. (c) Violin plots of *Fame* expression levels in different cell types/clusters. *Fame* is expressed in all cluster with highest levels in the proximal tubules, collecting duct, loop of Henle, and distal convoluted tubule-associated

clusters. **(d)** Butterfly plot of up- and downregulated genes between wild type and *Fame* KO conditions in different clusters (adjusted p-values <0.01). PT1 contains the most differentially expressed genes between wild type and KO conditions. **(e)** Cluster annotation and expression patterns of *Pecam1*, *Kdr* and the glomerular endothelial cell specific marker *Ehd3* in the GL endo cluster.



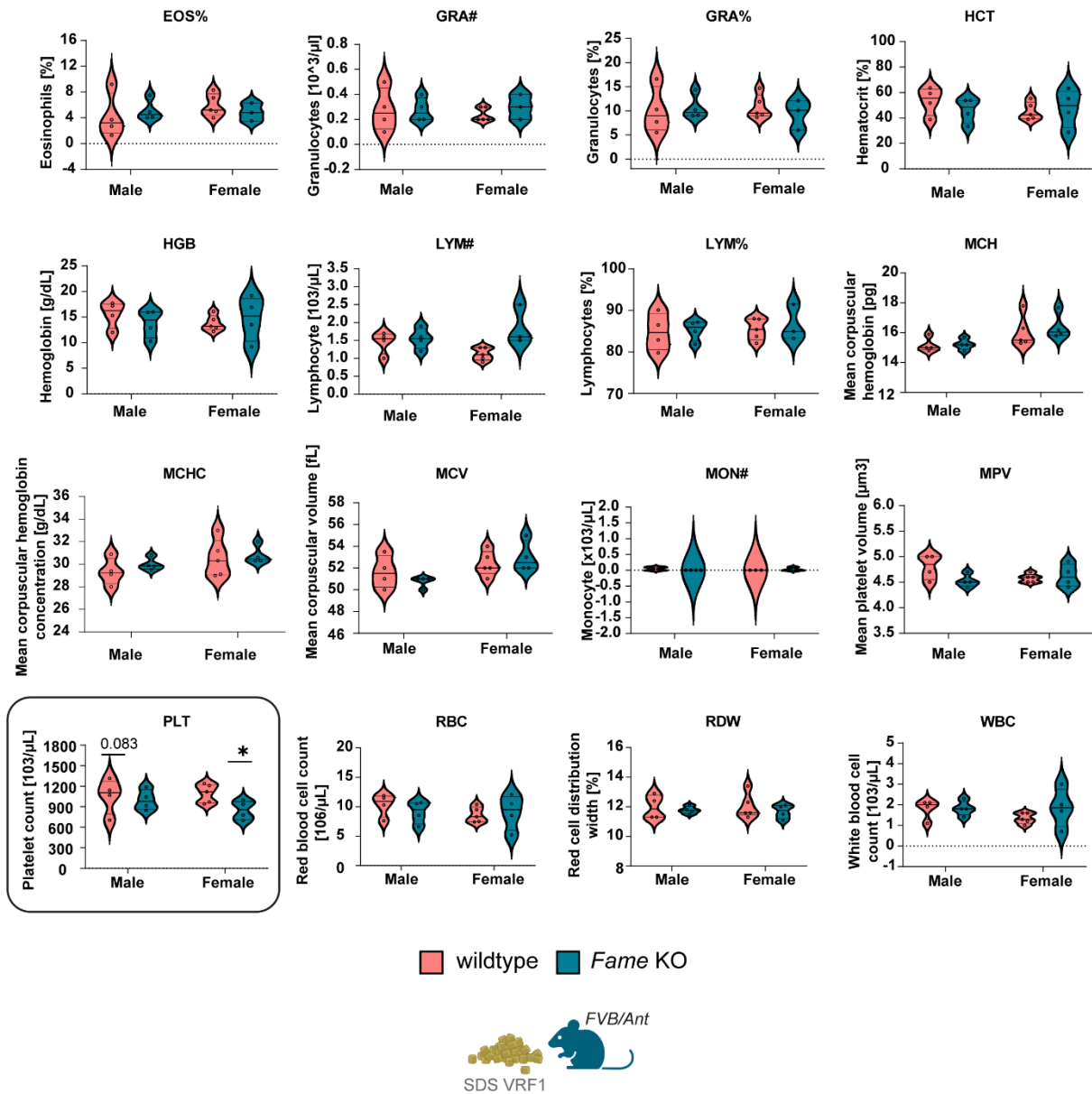
**Supplementary Figure 11: Phenotype comparison of *Fame* KO mice (*C57Bl/6Ncr*)**

**(a-b)** Phenotype comparison of the second *Fame* KO mouse model on *C57Bl/6Ncr* genetic background. Serum was collected at sacrificing at the 18-week timepoint. **(a)** 10-week-old male mice on indicated diet. **(i)** Body weight. Mean  $\pm$  SEM and n: WT ( $30.01 \pm 0.6319$  n=8), KO ( $25.22 \pm 0.481$  n=9), p-value WT vs KO  $<0.001$  **(ii)** Mean lean body mass. Mean  $\pm$  SEM and n: WT ( $22.79 \pm 0.7147$  n=8), KO ( $18.90 \pm 0.4462$  n=9), p-value Mann Whitney test WT vs KO=0.0016 **(iii)** Serum ferritin. Mean  $\pm$  SEM and n: WT ( $282.7 \pm 14.95$  n=8), KO ( $314.6 \pm 18.28$  n=8) **(iv)** Urine albumin to creatinine ratio. Urine was collected from 14-week-old mice. WT ( $0.03362 \pm 0.004791$  n=4), KO ( $0.02939 \pm 0.002206$  n=4) **(b)** 10-week-old female mice on indicated diet. **(i)** Body weight. Mean  $\pm$  SEM and n: WT ( $22.27 \pm 0.6043$  n=7), KO ( $20.80 \pm 0.3696$  n=6), p-value WT vs KO= 0.0721 **(ii)** Mean lean body mass. Mean  $\pm$  SEM and n: WT ( $16.44 \pm 0.3369$  n=7), KO ( $15.58 \pm 0.365$  n=6) **(iii)** Serum ferritin. Mean  $\pm$  SEM and n: WT ( $262.7 \pm 7.028$  n=7), KO ( $271.8 \pm 17.31$  n=6) **(iv)** Urine albumin to creatinine ratio. WT ( $0.02866 \pm 0.004448$  n=5), KO ( $0.03312 \pm 0.002937$  n=5). Source data are provided as a Source Data file.



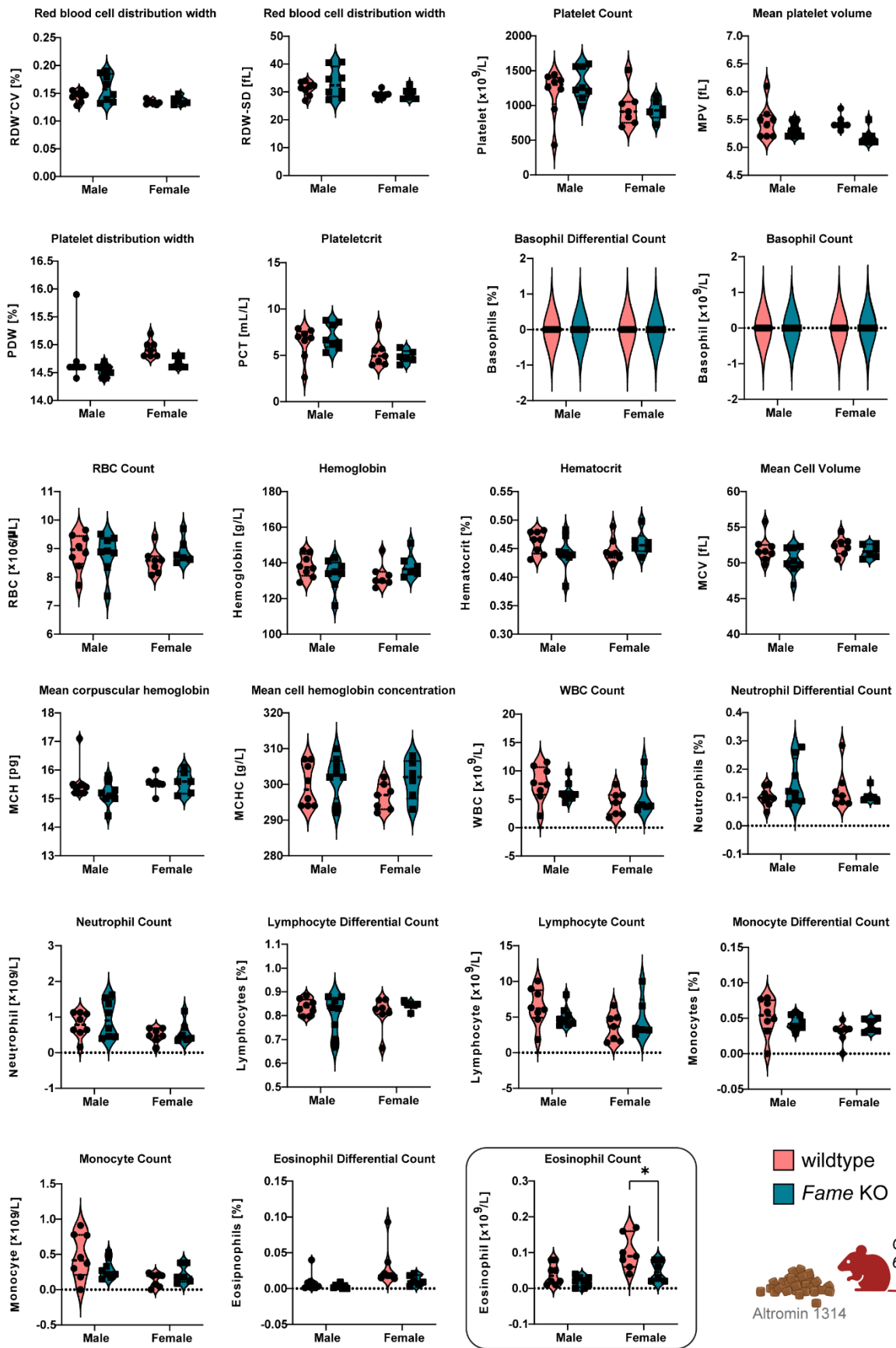
### Supplementary Figure 12: Analysis of ghrelin and leptin serum levels

**(a-b)** Levels of the energy balance influencing hormones ghrelin and leptin compared between *Fame* KO mice on different genetic backgrounds. Serum was collected at sacrificing at the 18-week timepoint. **(a)** Male and female *C57Bl/6NCr* *Fame* KO mice. **(i)** Serum ghrelin in male mice. Mean  $\pm$  SEM and n: WT ( $28.27 \pm 1.495$  n=8), KO ( $31.46 \pm 1.827$  n=8) **(ii)** Serum leptin in male mice. Mean  $\pm$  SEM and n: WT ( $1.975 \pm 0.3443$  n=8), KO ( $1.314 \pm 0.1929$  n=8) **(iii)** Serum ghrelin in female mice. Mean  $\pm$  SEM and n: WT ( $26.27 \pm 0.7028$  n=7), KO ( $27.18 \pm 1.731$  n=6) **(iv)** Serum leptin in female mice. Mean  $\pm$  SEM and n: WT ( $2.350 \pm 0.4543$  n=7), KO ( $1.345 \pm 0.2288$  n=6) **(b)** Male and female *FVB/Ant* *Fame* KO mice. **(i)** Serum ghrelin in male mice. Mean  $\pm$  SEM and n: WT ( $37.06 \pm 6.763$  n=4), KO ( $40.68 \pm 3.886$  n=4) **(ii)** Serum leptin in male mice. Mean  $\pm$  SEM and n: WT ( $5.590 \pm 0.8075$  n=4), KO ( $4.113 \pm 0.7777$  n=4) **(iii)** Serum ghrelin in female mice. Mean  $\pm$  SEM and n: WT ( $33.51 \pm 4.621$  n=5), KO ( $50.83 \pm 11.73$  n=4) **(iv)** Serum leptin in female mice. Mean  $\pm$  SEM and n: WT ( $5.330 \pm 1.324$  n=5), KO ( $5.663 \pm 0.8480$  n=4). Source data are provided as a Source Data file.



**Supplementary Figure 13: Whole blood count of *Fame* KO mice (*FVB/Ant*)**

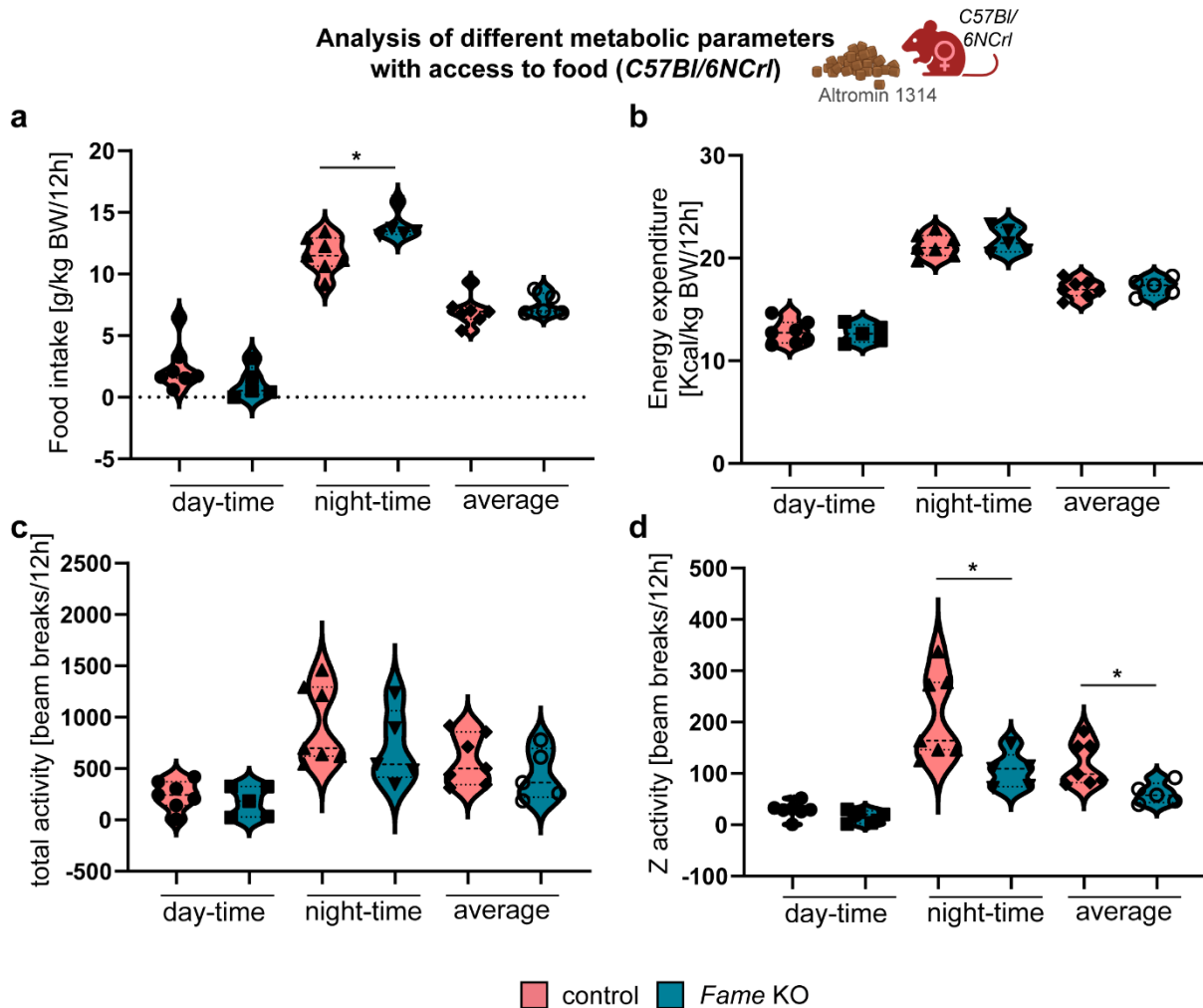
*Fame* KO mice on an *FVB/Ant* background do not exhibit signs of anaemia and present with a normal blood count except of reduced platelet numbers in females. Platelet count. Mean  $\pm$  SEM and n: WT male ( $1057 \pm 128.3$  n=4), KO male ( $997.8 \pm 74.94$  n=4). WT female ( $1094 \pm 60.52$  n=5), KO female ( $845.8 \pm 70.39$  n=4), p-value female WT vs KO=0.0310. Descriptive statistics of the tested parameters that were not found to be significantly altered can be accessed in Supplementary Data 13. Source data are provided as a Source Data file.



#### **Supplementary Figure 14: Whole blood count of *Fame* KO mice (*C57Bl/6CrI*)**

*Fame* KO mice on a *C57Bl/6NCrI* background show a normal blood count except for decreased numbers of eosinophils in female animals. Platelets of knockout animals differ in size from those of wild type animals. Eosinophil count. Mean  $\pm$  SEM and n: WT male ( $0.04 \pm 0.0104$  n=8), KO male ( $0.01875 \pm 0.00515$  n=8), WT female ( $0.100 \pm 0.0184$  n=7), KO female ( $0.0483 \pm 0.0117$  n=6), p-value female WT vs KO= 0.0437, p-value male WT vs KO=0.0874; Mean platelet volume. Mean  $\pm$  SEM and n: WT male ( $5.463 \pm 0.1068$  n=8), KO male ( $5.325 \pm 0.0453$  n=8), WT female ( $5.443 \pm 0.0481$  n=7), KO female ( $5.20 \pm 0.0633$  n=6), p-value female WT vs KO= 0.0227 (Mann-Whitney test); Platelet distribution width. Mean  $\pm$  SEM and n: WT male ( $14.75 \pm 0.1669$  n=8), KO male ( $14.54 \pm 0.0375$  n=8), WT female ( $14.93 \pm 0.0565$  n=7), KO female ( $14.68 \pm 0.0401$  n=6), p-value female WT vs KO=0.0117 (Mann-Whitney test). Descriptive statistics of the tested parameters that were not found to be significantly altered can be accessed in Supplementary Data 13. Source data are provided as a Source Data file.

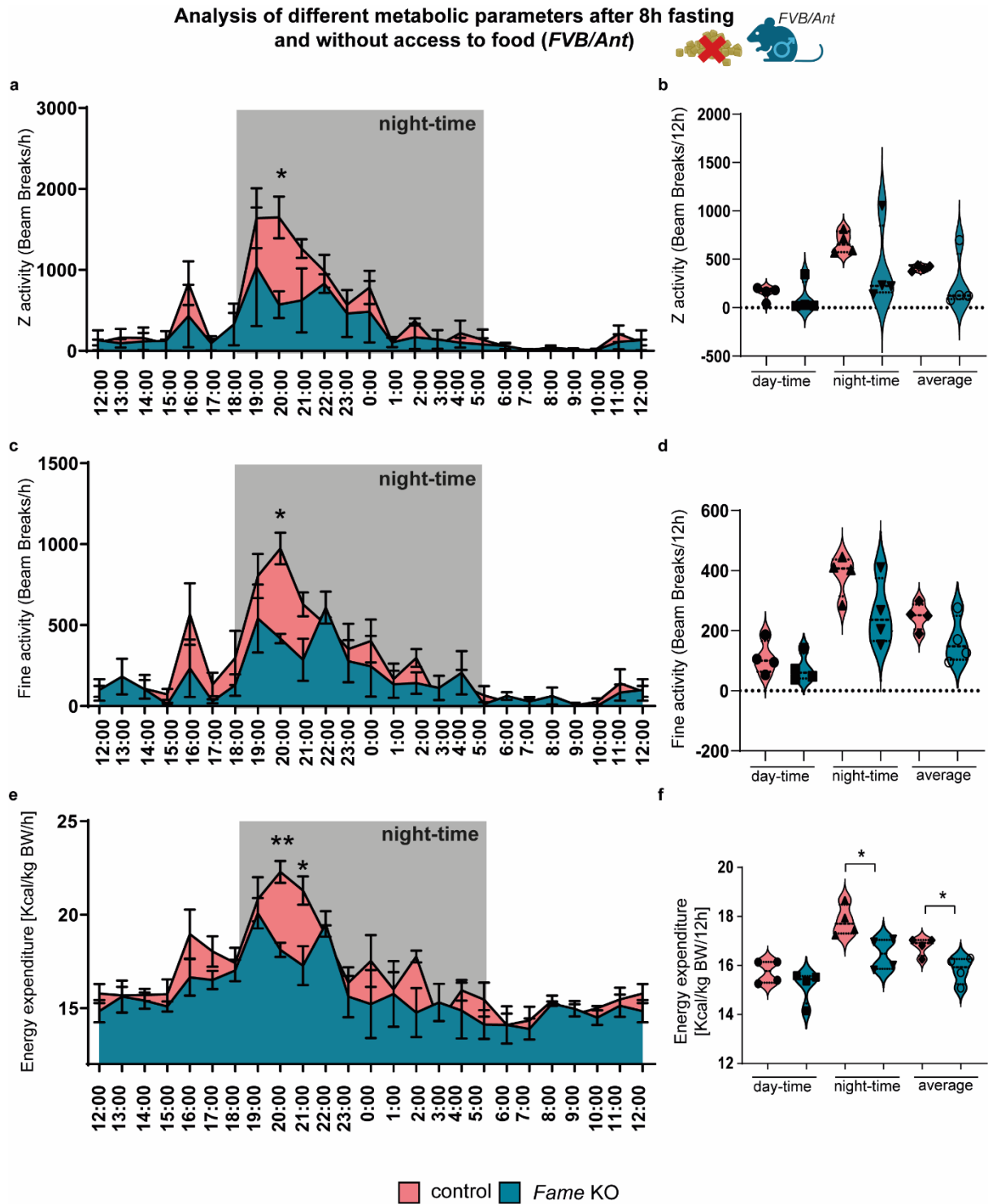
Lorem ipsum



**Supplementary Figure 15: Metabolic parameters and activity of female *Fame* KO mice (*C57Bl/6NCrI*)**

(a-d) Violin plots for metabolic cage experiments with 10-week-old female *C57Bl/6NCrI* wild type and *Fame* KO mice averaged on day-time (6:00-18:00), night-time (18:00-6:00) and average (06:00 – 06:00). (a) Food intake of control and *Fame* KO animals normalized to body weight. Female *Fame* KO mice on a *C57Bl/6NCrI* background have a higher food intake at night than wild type counterparts. Day-time WT ( $2.476 \pm 0.7255$  n=7) or KO ( $1.152 \pm 0.5717$  n=5), night-time WT ( $11.58 \pm 0.5474$  n=7) or KO ( $13.89 \pm 0.5058$  n=5), average WT ( $7.029 \pm 0.4530$  n=7) or KO ( $7.524 \pm 0.3914$  n=5), p-value night-time WT vs KO=0.0101 (Mann-Whitney test) (b) Energy expenditure of control and *Fame* KO animals normalized to body weight. Day-time WT ( $12.78 \pm 0.4252$  n=7) or KO ( $12.66 \pm 0.3955$  n=5), night-time WT ( $21.26 \pm 0.4142$  n=7) or KO ( $21.73 \pm 0.5472$  n=5), average WT ( $17.02 \pm 0.3280$  n=7) or KO ( $17.20 \pm 0.3788$  n=5). (c) Total activity of control and *Fame* KO mice. Day-time WT ( $242 \pm 53.30$  n=7) or KO ( $178.3 \pm 66.51$  n=5), night-time WT ( $924.8 \pm 144.4$  n=7) or KO ( $700.4 \pm 161.3$  n=5), average WT ( $583.4 \pm 92.39$  n=7) or KO ( $439.4 \pm 111.5$  n=5). (d) Z-activity of control and *Fame* KO mice. Female *Fame* KO mice show a significant reduction in Z-activity during night-time. Day-time WT ( $28.61 \pm 5.647$  n=7) or KO ( $16.02 \pm 5.639$  n=5), night-time WT ( $209.8 \pm 31.67$  n=7)

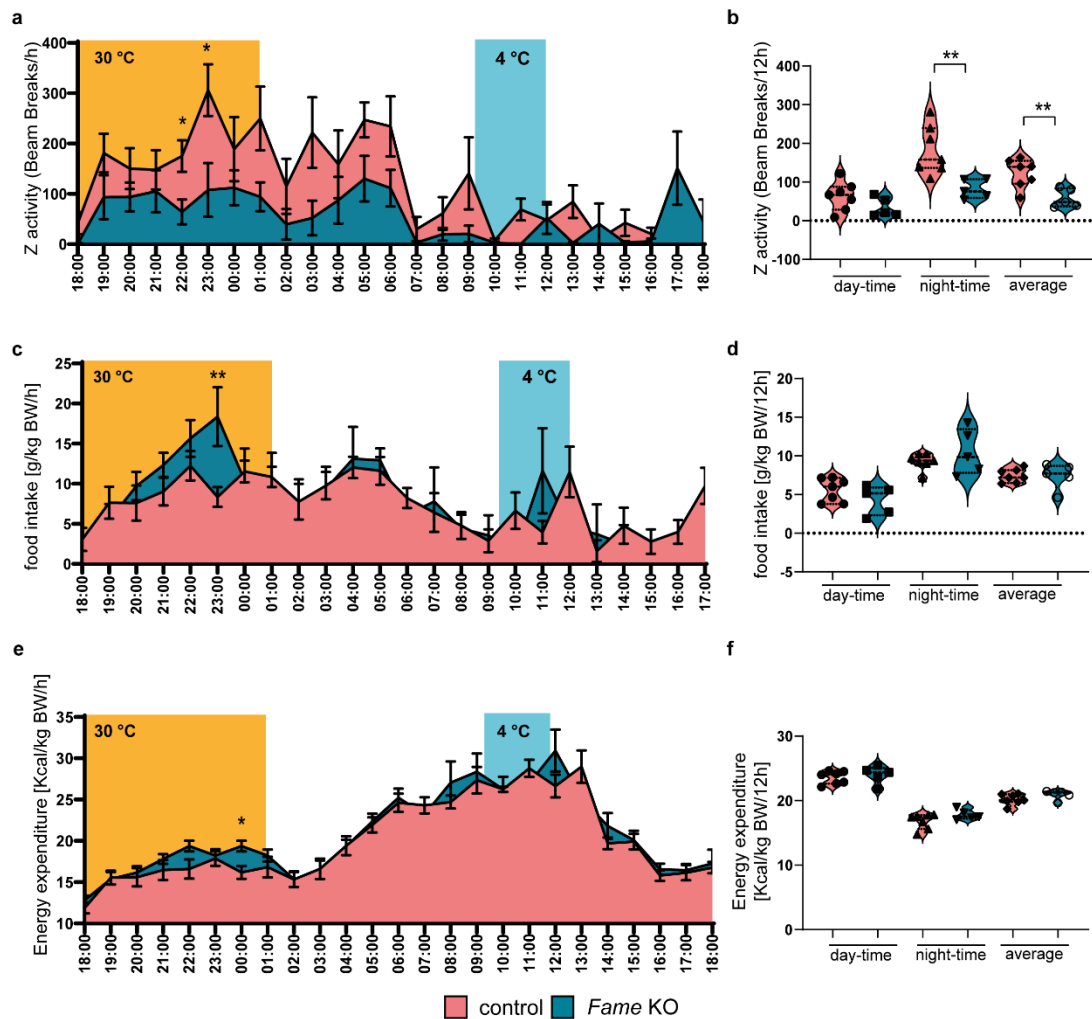
or KO ( $106 \pm 15.63$  n=5), average WT ( $119.2 \pm 15.85$  n=7) or KO ( $61.02 \pm 9.184$  n=5), p-value night-time WT vs KO=0.0272, p-value average WT vs KO=0.0175.



**Supplementary Figure 16: Activity profile and energy expenditure of *Fame* KO mice (FVB/Ant)**

**(a-f)** Metabolic cage experiment with 75-day old male *FVB/Ant* wild type and *Fame* KO mice after an 8-hour fasting period without further access to food **(a)** Time course analysis of the Z-activity of control and *Fame* KO mice. The Z-activity of *Fame* KO mice is significantly lower at the beginning of the night compared to wild type animals. P-value at 20:00 p=0.0130. **(b)** Violin plots of the Z-activity of control and *Fame* KO mice. Average day-time (6:00-18:00), night-time (18:00-6:00) and average (06:00-06:00) for each animal group is shown. Mean  $\pm$  SEM and n for each group: day-time WT ( $148.7 \pm 36.04$  n=4) or KO ( $103.7 \pm 80.43$  n=4), night-time WT ( $671.8 \pm 56.79$  n=4) or KO ( $410.5 \pm 215.1$  n=4), average WT ( $410.2 \pm 14.84$  n=4) or KO ( $257.1 \pm 147.7$  n=4) **(c)** Time course analysis of the Fine activity of control and *Fame* KO mice. *Fame* KO animals are less active at the beginning of the night. p-value at 20:00 p=0.0286 (Mann-Whitney test), p-value at 21:00 p=0.0634 **(d)** Violin plots of fine activity. Mean  $\pm$  SEM and n: day-time WT ( $110.1 \pm 27.9$  n=4) or KO ( $75.34 \pm 23.27$  n=4), night-time WT ( $386.1 \pm 35.05$  n=4) or KO ( $259 \pm 55.67$  n=4) p-value WT vs KO=0.1016, average WT ( $248.1 \pm 22.4$  n=4) or KO ( $167.2 \pm 39.39$  n=4). **(e)** Time course analysis of the energy expenditure of control and *Fame* KO mice normalized to bodyweight. The energy expenditure of *Fame* KO animals is significantly lower than that of wild types at the beginning of the night. p-value at 20:00 p=0.001, p-value at 21:00 p=0.0211 **(f)** Violin plots of energy expenditure. Mean  $\pm$  SEM and n: day-time WT ( $15.74 \pm 0.2364$  n=4) or KO ( $15.15 \pm 0.3387$  n=4), night-time WT ( $17.83 \pm 0.313$  n=4) or KO ( $16.47 \pm 0.3216$  n=4) p-value WT vs KO=0.0228, average WT ( $16.78 \pm 0.1846$  n=4) or KO ( $15.81 \pm 0.2752$  n=4) p-value WT vs KO=0.0261. **(a, c, e)** Descriptive statistics can be accessed in Supplementary Data 13. Source data are provided as a Source Data file.

Analysis of different metabolic parameters after warm-cold challenge at 4 °C (*C57Bl/6NCrI*)

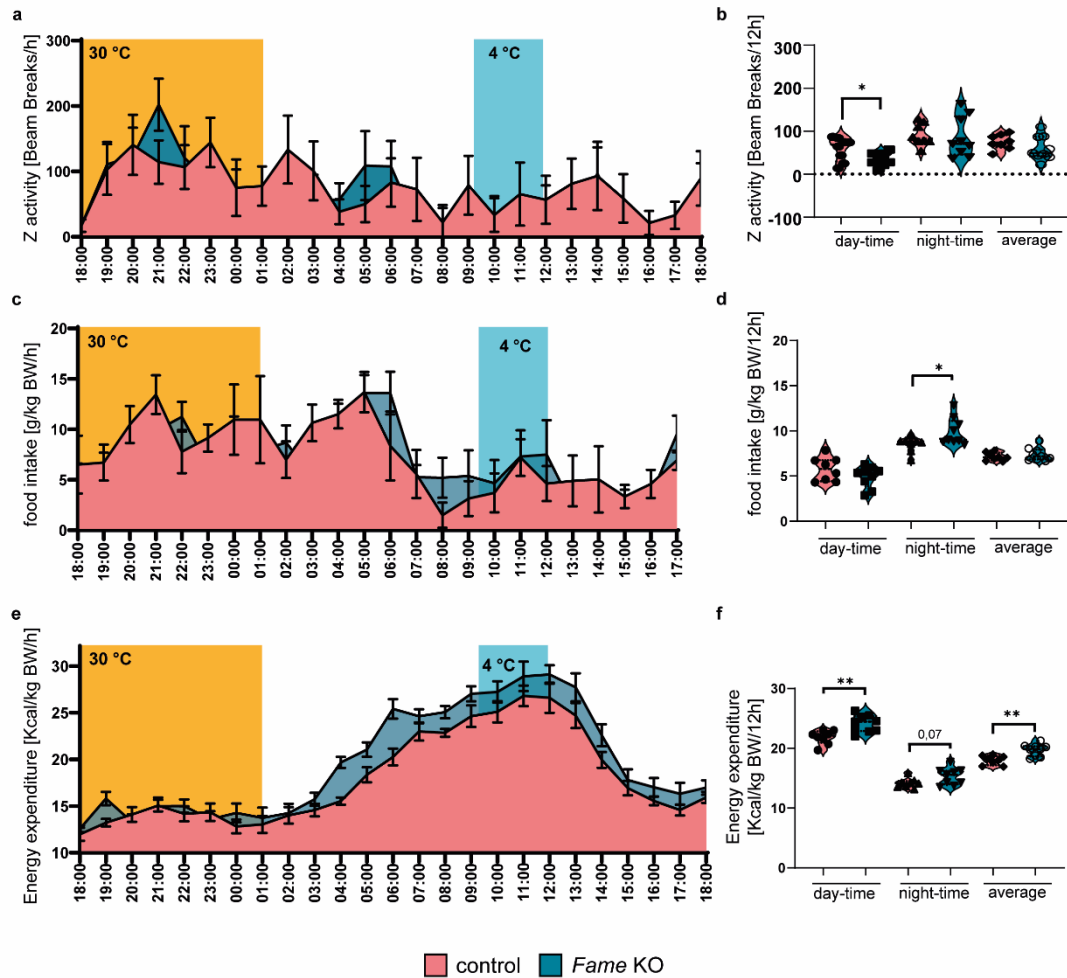
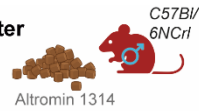


**Supplementary Figure 17: Metabolic parameters after warm-cold challenge in female *Fame* KO mice (*C57Bl/6NCrI*)**

**(a-f)** Metabolic cage experiment with 10-week-old female *C57Bl/6NCrI* wild type and *Fame* KO mice challenged with changing ambient temperature (30°C from 18:00 to 01:00 (grey) and 4°C from 09:30 to 12:00 (blue)) **(a)** Time course analysis of the Z-activity of control and *Fame* KO mice. p-value at 22:00=0.0274, p-value at 23:00=0.0259. **(b)** Violin plots of Z-activity. Mean ± SEM and n: day-time WT (63.33 ± 14.14 n=7) or KO (34.42 ± 11.05 n=5), night-time WT (182 ± 23.77 n=7) or KO (81.73 ± 24.72 n=5) p-value WT vs KO=0.0074, average WT (122.7 ± 14.05 n=7) or KO (58.08 ± 10.92 n=5) p-value WT vs KO=0.0070. **(c)** Time course analysis of the food intake of control and *Fame* KO mice normalized to bodyweight. p-value at 23:00=0.0025. **(d)** Violin plots food intake normalized to bodyweight. Mean ± SEM and n: day-time WT (5.60 ± 0.5746 n=7) or KO (4.325 ± 0.8427 n=5), night-time WT (9.287 ± 0.3998 n=7) or KO (10.47 ± 1.305 n=5), average WT (7.443 ± 0.3287 n=7) or KO (7.398 ± 0.7528 n=5). **(e)** Time course analysis of the energy expenditure of control and *Fame* KO mice normalized to bodyweight. p-value at 00:00=0,0147 **(f)** Violin plots of energy expenditure normalized to bodyweight. Mean ± SEM and n: day-time WT (23.57 ± 0.3762 n=7) or KO (24.01 ± 0.6191 n=5), night-time WT (16.81 ± 0.4491 n=7) or KO (17.79 ± 0.3398 n=5), average WT (20.19 ±

0.3147 n=7) or KO ( $20.90 \pm 0.3225$  n=5). (**a**, **c**, **e**) Descriptive statistics can be accessed in Supplementary Data 13. Source data are provided as a Source Data file.

Analysis of different metabolic parameters after warm-cold challenge at 4 °C (C57Bl/6NCr)



**Supplementary Figure 18: Metabolic parameters after warm-cold challenge in male *Fame* KO mice (C57Bl/6NCr)**

(a-f) Metabolic cage experiment with 10-week-old male *C57Bl/6NCr* wild type and *Fame* KO mice challenged with changing ambient temperature (30 °C from 18:00 to 01:00 (grey) and 4 °C from 09:30 to 12:00 (blue)) (a) Time course analysis of the Z-activity of control and *Fame* KO mice with indicated temperature changes. (b) Violin plots of Z-activity. *Fame* KO animals have decreased Z-activity compared to wild types during the day-time cold challenge. Mean  $\pm$  SEM and n: day-time WT ( $58.23 \pm 9.744$  n=8) or KO ( $35.12 \pm 5.252$  n=9) p-value WT vs KO=0.0478, night-time WT ( $91.71 \pm 9.165$  n=8) or KO ( $85.94 \pm 15.61$  n=9), average WT ( $74.97 \pm 6.048$  n=8) or KO ( $60.53 \pm 9.436$  n=9). (c) Time course analysis of the food intake of control and *Fame* KO mice normalized to bodyweight. (d) Violin plots of food intake normalized to bodyweight. *Fame* KO animals have a significantly higher food intake during the night than wild types. Mean  $\pm$  SEM and n: day-time WT ( $5.776 \pm 0.4664$  n=8) or KO ( $4.911 \pm 0.390$  n=9), night-time WT ( $8.514 \pm 0.3021$  n=8) or KO ( $9.901 \pm 0.5013$  n=9) p-value WT vs KO=0.0366, average WT ( $7.145 \pm 0.1548$  n=8) or KO ( $7.406 \pm 0.2430$  n=9). (e) Time course analysis of the energy expenditure of control and *Fame* KO mice normalized to bodyweight. p-value at

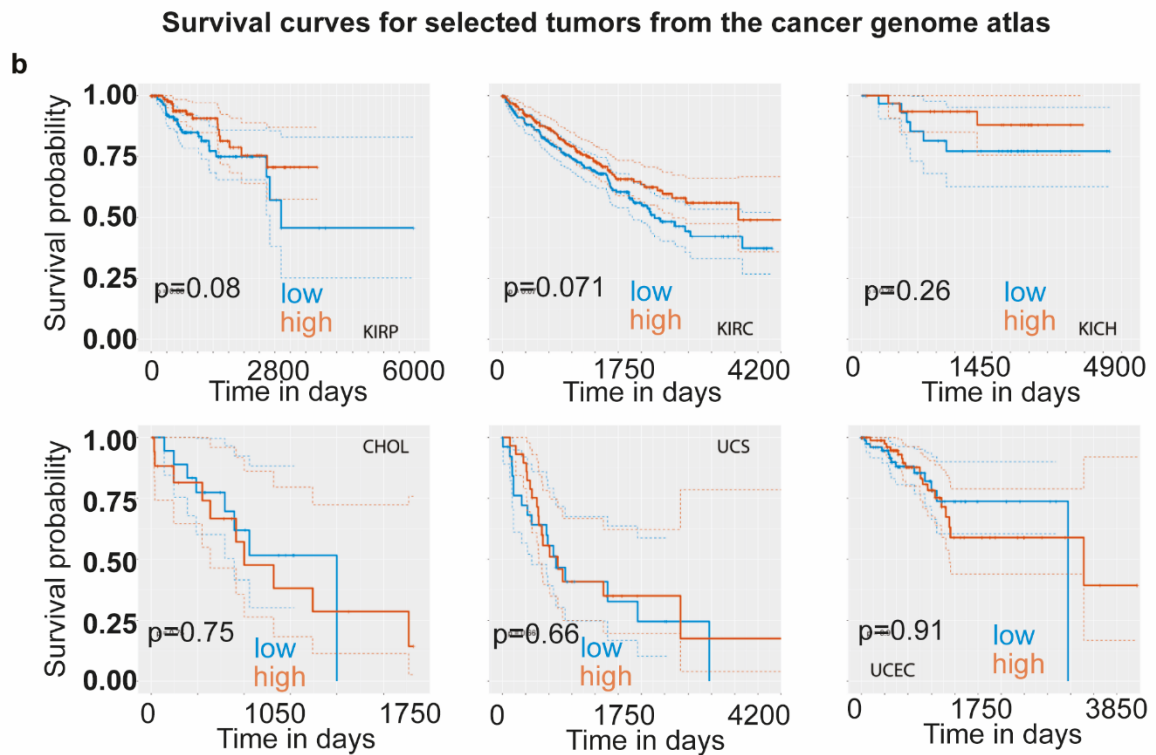
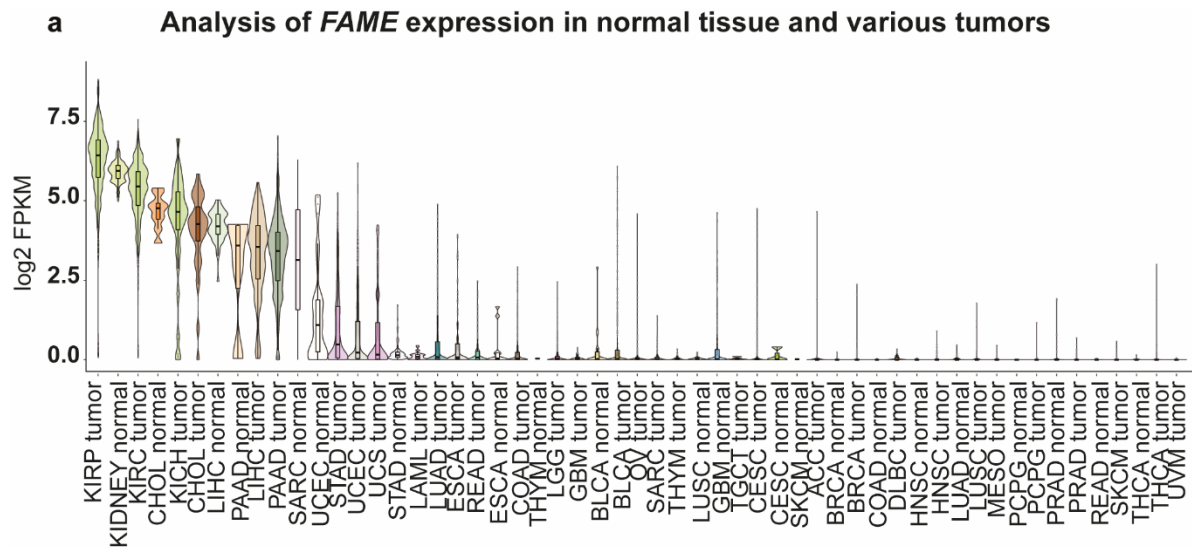
04:00=0.0001, p-value at 05:00=0.0298, p-value at 06:00=0.0037 (Mann-Whitney test) **(f)** Violin plots of energy expenditure normalized to bodyweight. The energy expenditure of *Fame* KO animals was significantly higher than that of controls once the ambient temperature was changed. Mean  $\pm$  SEM and n: day-time WT ( $21.82 \pm 0.4023$  n=8) or KO ( $24.12 \pm 0.4749$  n=9) p-value WT vs KO=0.0024, night-time WT ( $14.18 \pm 0.2891$  n=8) or KO ( $15.28 \pm 0.4705$  n=9) p-value WT vs KO=0.0722, average WT ( $18.00 \pm 0.2673$  n=8) or KO ( $19.70 \pm 0.3323$  n=9) p-value WT vs KO=0.0014. **(a, c, e)** Descriptive statistics can be accessed in Supplementary Data 13. Source data are provided as a Source Data file.

### Genome-Wide Association Study of *FAME*

Phenotype tested in Study	Phenotype ontology annotation	Total p-values in Study	Study	Reference
Age-related macular degeneration	Macular Degeneration	427,832	GWAS of age-related macular degeneration (HGVST4)	(Klein et al., 2005)
Body mass index (HGVP1111)	Body Mass Index	2,471,541	GWAS of body mass index (HGVST640)	(Hindorff et al., 2009; Speliotes et al., 2010)
Diabetic nephropathy in type I diabetes (HGVP1531)	Diabetic Nephropathies	706,749	Genetics of kidneys in diabetes (GoKinD) (HGVST890)	(Pezzolesi et al., 2010)
Fasting glucose-related: homeostatic model assessment of beta-cell function (HGVP827)	Insulin-Secreting Cells	2,456,942	GWAS of glycemic traits (HGVST463)	(Dupuis et al., 2010; Hindorff et al., 2009)
Fasting insulin-related: fasting insulin (HGVP822)	Insulin	2,461,093	GWAS of glycemic traits (HGVST463)	(Dupuis et al., 2010; Hindorff et al., 2009)
Fasting insulin-related: homeostatic model assessment of insulin resistance (HGVP826)	Insulin Resistance	2,458,062	GWAS of glycemic traits (HGVST463)	(Dupuis et al., 2010; Hindorff et al., 2009)
Type II diabetes (HGVP5)	Diabetes Mellitus, Type 2	772,55	GWAS of type II diabetes mellitus (HGVST3)	(Diabetes Genetics Initiative of Broad Institute of et al., 2007)

### Supplementary Figure 19: Genome-wide association study of *FAME*

Genome-Wide Association Studies of *FAME* using gwascentral.org



**c**

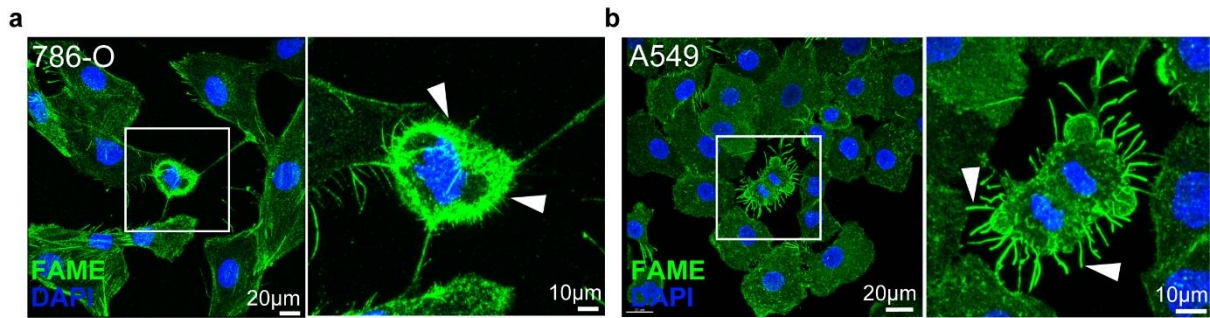
average ct value			
HEK293T	<i>FAME</i>	<i>GAPDH</i>	$\Delta Ct$
WT 1	36,70	20,68	1,51E-05
WT 2	37,40	22,05	2,38E-05
WT 3	37,31	20,30	7,59E-06
WT 4	37,48	20,27	6,62E-06
WT 5	37,22	20,69	1,06E-05

**Supplementary Figure 20: *FAME* expression and survival probability in tumors**

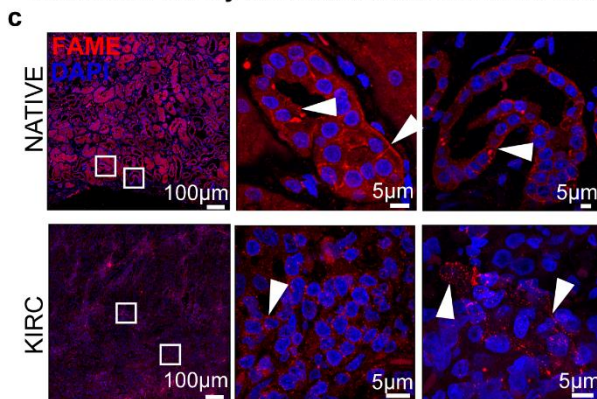
**(a)** Analysis of *FAME* expression in various tumors and healthy tissue using RNAseq data from The Cancer Genome Atlas (TCGA) Program **(b)** Survival curves for selected tumors from

TCGA with detectable *FAME* expression. Samples are binned into high (orange) and low (blue) *FAME* expression. KIRP = Kidney renal papillary cell carcinoma, KIRC = Clear cell renal cell carcinoma, KICH = Kidney Chromophobe, CHOL = Cholangiocarcinoma, UCS = Uterine carcinosarcoma, UCEC = Uterine Corpus Endometrial Carcinoma. **(c)** Table highlighting insignificant background levels of *FAME* expression in HEK293T cells measured by qPCR. Averaged values of technical triplicates per analysed HEK293T clone are shown.

endogenous expression of FAME in 786-O and A549 cancer cell lines

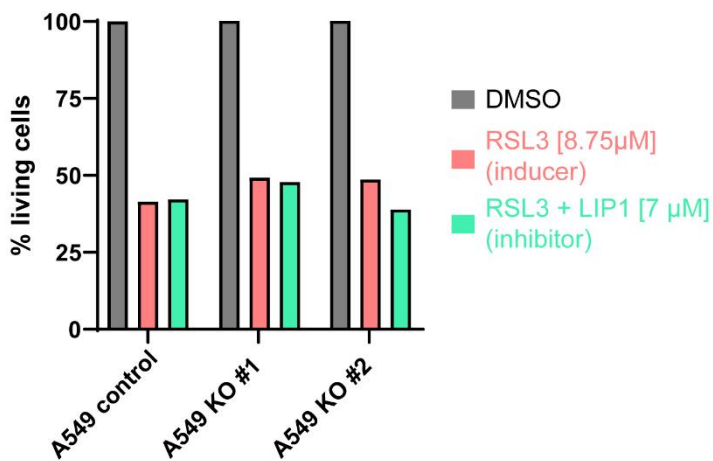


Immunostaining of FAME in native and kidney renal clear cell carcinoma tissue



NOTE:  
This antibody has not been confirmed to detect the human variant of this protein. The results have to be considered with caution

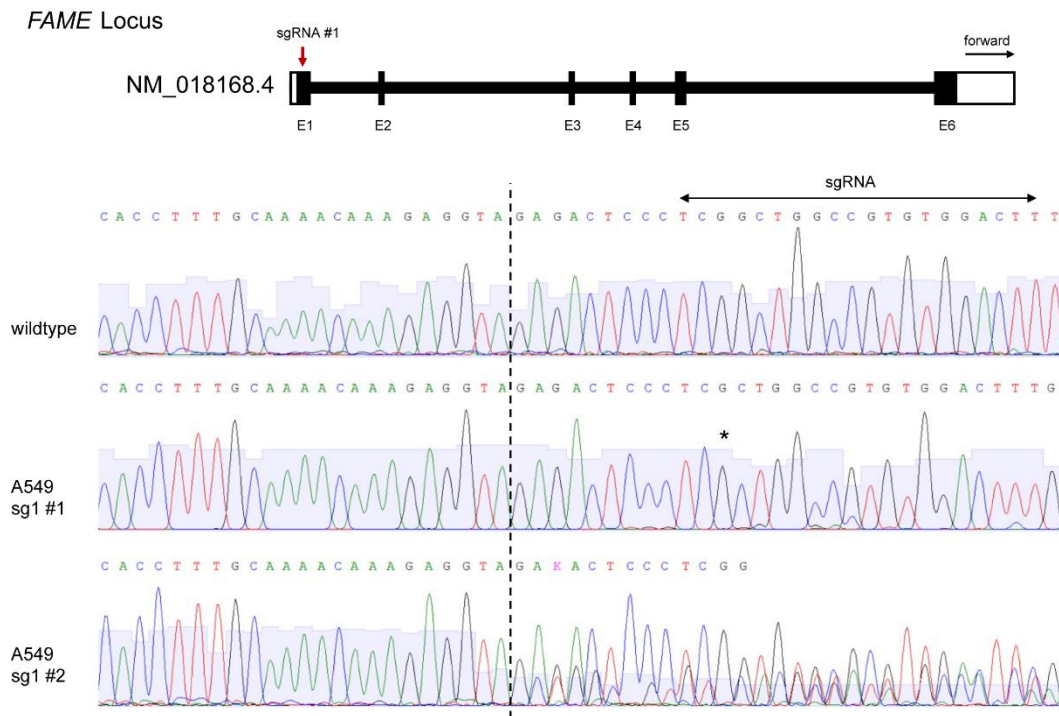
Ferroptosis induction in A549 cells



Supplementary Figure 21: Endogenous FAME in cancer tissues and ferroptosis susceptibility

(a) Immunofluorescence staining of endogenous FAME in the human kidney carcinoma cell line 786-O. A mitotic cell is magnified (white box) with arrows pointing towards high FAME levels near the plasma membrane. (b) The human lung adenocarcinoma cell line A549 is stained as in (a). (c) FAME stainings of kidney renal clear cell carcinoma (KIRC) and healthy control tissue are shown. The white arrows highlight membranous expression (upper panel) as well as vesicular expression (lower panel). (a-c) Representative images from 3

independent stainings are shown. **(d)** Representative analysis of the ferroptosis susceptibility of *FAME* KO cells. Two A549 *FAME* KO and a WT control clone were treated with the ferroptosis inducer RSL3 [8,75  $\mu$ M]. No difference was observed amongst the clones. Of note, the addition of the ferroptosis inhibitor Liproxstatin-1 (LIP1) did not rescue RSL3-induced cell death. Source data are provided as a Source Data file.

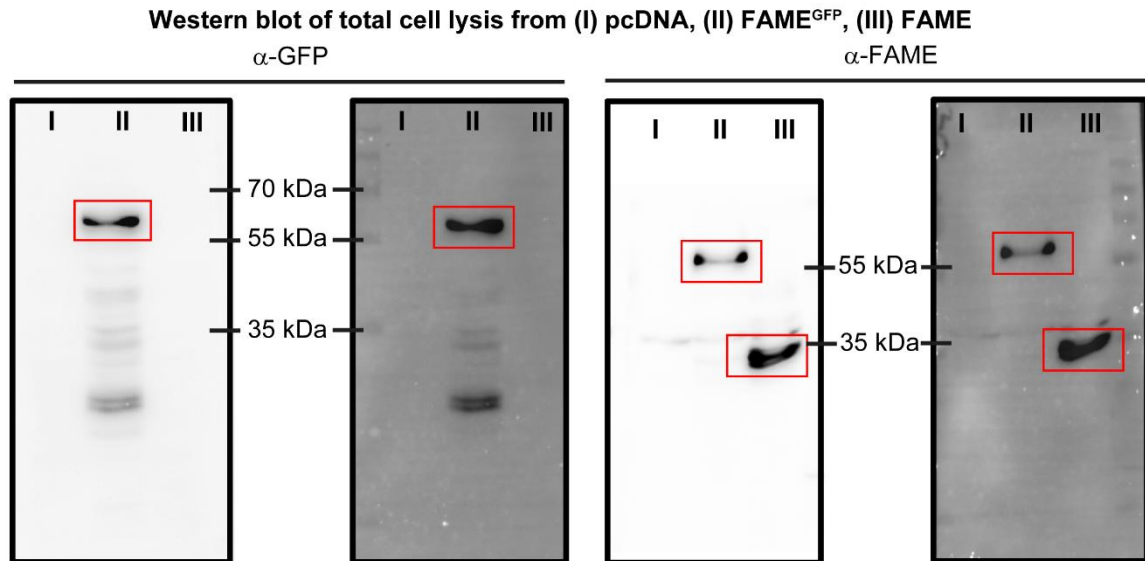


**Supplementary Figure 22: FAME KO validation by genomic DNA sequencing of A549 cells**

FAME KO validation in human A549 cells by genomic DNA sequencing. The FAME locus on chromosome 14 with exons (E) is schematically depicted (top). The target position of the single-guide RNA is shown (red arrow). The used NCBI Reference Sequence is indicated. Sanger sequencing chromatograms of the indicated genomic regions are shown. The 20-nucleotide stretch corresponding to the sgRNA is marked with a black arrow. Editing by Cas9 took place in the expected region, resulting in a homozygous single nucleotide insertion (asterisk) in A549 KO clone #1 and heterozygous editing in clone #2. The dotted line indicates the start of changed positions in the sequence alignments.



spectrometry (MS) are visualized in a human cell map of various organelles and cell compartments. **(d)** Heatmap visualizing Pearson correlations between replicates of the IP-MS show a high degree of consistency amongst the control and FAME overexpression conditions. **(e)** Heatmap of the log<sub>2</sub> Centred Intensity shows strong upregulation of proteins in the Fame overexpression condition.



**Supplementary Figure 24: Western blot-based antibody validation of overexpressed FAME**

Overexpression and subsequent western blot analysis of an empty pcDNA3.1 vector (I), pcDNA3.1-FAME-EGFP fusion protein (II) and pcDNA3.1-FAME (III) plasmids in HEK293T cells. Lane II shows a band corresponding to the fusion protein (predicted molecular mass of Fame 34.69 kDa and EGFP 27kDa). Lane III shows a specific band at the expected height for overexpressed FAME only detectable with the anti-FAME antibody. Data from a single experiment is shown.

### Supplementary References

- Genomes Project, C., A. Auton, L. D. Brooks, R. M. Durbin, E. P. Garrison, H. M. Kang, J. O. Korb, J. L. Marchini, S. McCarthy, G. A. McVean and G. R. Abecasis (2015). "A global reference for human genetic variation." *Nature* **526**(7571): 68-74.
- Machiela, M. J. and S. J. Chanock (2015). "LDlink: a web-based application for exploring population-specific haplotype structure and linking correlated alleles of possible functional variants." *Bioinformatics* **31**(21): 3555-3557.
- Robinson, J. T., H. Thorvaldsdottir, W. Winckler, M. Guttman, E. S. Lander, G. Getz and J. P. Mesirov (2011). "Integrative genomics viewer." *Nat Biotechnol* **29**(1): 24-26.
- Soldatov, R., M. Kaucka, M. E. Kastriiti, J. Petersen, T. Chontorotzea, L. Englmaier, N. Akkuratova, Y. Yang, M. Haring, V. Dyachuk, C. Bock, M. Farlik, M. L. Piacentino, F. Boismoreau, M. M. Hilscher, C. Yokota, X. Qian, M. Nilsson, M. E. Bronner, L. Croci, W. Y. Hsiao, D. A. Guertin, J. F. Brunet, G. G. Consalez, P. Ernfors, K. Fried, P. V. Kharchenko and I. Adameyko (2019). "Spatiotemporal structure of cell fate decisions in murine neural crest." *Science* **364**(6444).

## Reporting Summary

Nature Portfolio wishes to improve the reproducibility of the work that we publish. This form provides structure for consistency and transparency in reporting. For further information on Nature Portfolio policies, see our [Editorial Policies](#) and the [Editorial Policy Checklist](#).

### Statistics

For all statistical analyses, confirm that the following items are present in the figure legend, table legend, main text, or Methods section.

n/a Confirmed

- |                                     |                                     |  |
|-------------------------------------|-------------------------------------|--|
| <input type="checkbox"/>            | <input checked="" type="checkbox"/> | The exact sample size ( $n$ ) for each experimental group/condition, given as a discrete number and unit of measurement  |
| <input type="checkbox"/>            | <input checked="" type="checkbox"/> | A statement on whether measurements were taken from distinct samples or whether the same sample was measured repeatedly  |
| <input type="checkbox"/>            | <input checked="" type="checkbox"/> | The statistical test(s) used AND whether they are one- or two-sided<br><i>Only common tests should be described solely by name; describe more complex techniques in the Methods section.</i>   |
| <input checked="" type="checkbox"/> | <input type="checkbox"/>            | A description of all covariates tested   |
| <input type="checkbox"/>            | <input checked="" type="checkbox"/> | A description of any assumptions or corrections, such as tests of normality and adjustment for multiple comparisons  |
| <input type="checkbox"/>            | <input checked="" type="checkbox"/> | A full description of the statistical parameters including central tendency (e.g. means) or other basic estimates (e.g. regression coefficient) AND variation (e.g. standard deviation) or associated estimates of uncertainty (e.g. confidence intervals) |
| <input type="checkbox"/>            | <input checked="" type="checkbox"/> | For null hypothesis testing, the test statistic (e.g. $F$ , $t$ , $r$ ) with confidence intervals, effect sizes, degrees of freedom and $P$ value noted<br><i>Give <math>P</math> values as exact values whenever suitable.</i>                            |
| <input checked="" type="checkbox"/> | <input type="checkbox"/>            | For Bayesian analysis, information on the choice of priors and Markov chain Monte Carlo settings   |
| <input checked="" type="checkbox"/> | <input type="checkbox"/>            | For hierarchical and complex designs, identification of the appropriate level for tests and full reporting of outcomes   |
| <input checked="" type="checkbox"/> | <input type="checkbox"/>            | Estimates of effect sizes (e.g. Cohen's $d$ , Pearson's $r$ ), indicating how they were calculated   |

*Our web collection on [statistics for biologists](#) contains articles on many of the points above.*

### Software and code

Policy information about [availability of computer code](#)

Data collection

- Incucyte experiments were performed using Essen Bioscience/Sartorius - Software Incucyte 2021C
- For IP data evaluation, the MaxQuant software (2.0.1.0) with inbuild Andromeda search engine was used
- A PhenoMaster (TSE Systems) system was used for the indirect calorimetry. The software used in the PhenoMaster PC was TSE PhenoMaster v.7.1.2.
- Raw single cell sequencing files were processed, mapped, and counted to the Cell Ranger mm10-2020-A genome and its corresponding annotation by Cell Ranger version 4.0.0. The output count matrices for each sample were further processed with the Seurat package pipeline (v.3.2.2.9001)
- Microscopy to capture fluorescence after immunohistochemistry staining using antibodies was performed using a Zeiss LSM880 Airyscan or LEICA THUNDER System with 10, 20, 40 and 63x objectives.
- Quantitative expression analysis was performed using the QuantStudio 5 Real-Time PCR Instrument
- Micro-computed tomography  
The micro-CT scanning of the pups was performed using the laboratory system GE phoenix v|tome|x L 240 (GE Sensing & Inspection Technologies GmbH, Germany), equipped with a 180 kV/15W maximum power nanofocus X-ray tube and high contrast flat panel detector DXR250 with 2048x2048 pixel, 200x200  $\mu\text{m}$  pixel size.

- Library preparation was performed using a 10x controller (10x Genomics) with the Single Cell 3' v3 chemistry. Sequencing was performed using a HiSeq 3000 (Illumina)

-LC-MS/MS analyses of peptide mixture were done using Ultimate 3000 RSLCnano system connected to Orbitrap Elite hybrid spectrometer (Thermo Fisher Scientific).

- For 3D visualization, the segmentation was done by an operator using a combination of software Avizo 2022.2 (ThermoFisher Scientific) and VG Studio MAX 3.4 (Volume Graphics GmbH, Germany).

## Data analysis

Statistical data analysis:  
Statistical analysis was done using GraphPad Prism 9 software.

The quantitative data are provided in the Source Data file.

All custom-made scripts used in the analysis are available at: [https://github.com/ipoverennaya/RIK\\_paper](https://github.com/ipoverennaya/RIK_paper)

For manuscripts utilizing custom algorithms or software that are central to the research but not yet described in published literature, software must be made available to editors and reviewers. We strongly encourage code deposition in a community repository (e.g. GitHub). See the Nature Portfolio [guidelines for submitting code & software](#) for further information.

## Data

Policy information about [availability of data](#)

All manuscripts must include a [data availability statement](#). This statement should provide the following information, where applicable:

- Accession codes, unique identifiers, or web links for publicly available datasets
- A description of any restrictions on data availability
- For clinical datasets or third party data, please ensure that the statement adheres to our [policy](#)

Two knockout mice strains were generated for this manuscript. These will be available upon reasonable request and also be deposited to the Jackson Laboratory. All other relevant data supporting the key findings of this study are available within the article and its Supplementary Information files or from the corresponding author upon reasonable request. The quantitative data generated in this study are provided in the Source Data file. Source data are provided with this paper. The RAW mass spectrometry can be accessed through PRIDE with the identifier PXD039259. RAW Single cell sequencing files can be downloaded from GEO with the accession number GSE206860 [<https://www.ncbi.nlm.nih.gov/geo/query/acc.cgi?acc=GSE206860>]. RAW Yeast-Two-Hybrid data can be accessed through [<https://datadryad.org/stash/share/ojrXiYXvS3yzg5S2wdrXHoggtgeQBdaSgPvhRBdU8Yw>].

## Human research participants

Policy information about [studies involving human research participants and Sex and Gender in Research](#).

Reporting on sex and gender

n/a

Population characteristics

n/a

Recruitment

n/a

Ethics oversight

n/a

Note that full information on the approval of the study protocol must also be provided in the manuscript.

## Field-specific reporting

Please select the one below that is the best fit for your research. If you are not sure, read the appropriate sections before making your selection.

- Life sciences     Behavioural & social sciences     Ecological, evolutionary & environmental sciences

For a reference copy of the document with all sections, see [nature.com/documents/nr-reporting-summary-flat.pdf](https://www.nature.com/documents/nr-reporting-summary-flat.pdf)

## Life sciences study design

All studies must disclose on these points even when the disclosure is negative.

Sample size

In our study, we did not perform a formal sample size calculation. Instead, we followed accepted practices in the mouse facilities where the research was conducted to determine the sample size. We initially conducted preliminary experiments to estimate the number of animals needed to achieve adequate statistical power for our tests. Furthermore, the number of animals involved in this research were chosen to reduce unnecessary animal use and to reach statistical significance with two-sided student's t-test. For the mass spectrometry experiments, we analyzed six independent replicates to ensure the reliability and reproducibility of our findings. For immunofluorescence, single cell sequencing, and transmission electron microscopy, we used three independent samples each. These sample sizes were selected based on the

same approach of balancing statistical power and accepted practices in the research community to yield robust effects.

Data exclusions	To check whether DE genes between wildtype and knockout are not sex-specific, we compared them with the list of the corresponding DE genes between female and male proximal tubule (PT) samples from (Ransick et al., 2019). The genes whose adjusted p-values are less than 0.01 were excluded from the comparative analysis  For plotted graphs we did not exclude any data.
Replication	In vitro experiments were repeated a minimum of three times. All attempts were successful. Parameters related to mice were tested once in several animals (minimum of four). All attempts were successful.
Randomization	Laboratory animals were allocated to the experimental and control groups based on their genotype and sex. The same accounted for the tissues harvested from these mice. In vitro experiments were allocated based on their treatment (control vs. inhibitor) or transfection condition.
Blinding	Blinding was not applicable to the study because the allocation of laboratory animals to experimental and control groups was based on their genotype and sex, and the tissues harvested from these animals were also allocated accordingly. Additionally, the in vitro experiments were allocated based on treatment (control vs. inhibitor) or transfection condition.

## Reporting for specific materials, systems and methods

We require information from authors about some types of materials, experimental systems and methods used in many studies. Here, indicate whether each material, system or method listed is relevant to your study. If you are not sure if a list item applies to your research, read the appropriate section before selecting a response.

### Materials & experimental systems

n/a	Involved in the study
<input type="checkbox"/>	<input checked="" type="checkbox"/> Antibodies
<input type="checkbox"/>	<input checked="" type="checkbox"/> Eukaryotic cell lines
<input checked="" type="checkbox"/>	<input type="checkbox"/> Palaeontology and archaeology
<input type="checkbox"/>	<input checked="" type="checkbox"/> Animals and other organisms
<input checked="" type="checkbox"/>	<input type="checkbox"/> Clinical data
<input checked="" type="checkbox"/>	<input type="checkbox"/> Dual use research of concern

### Methods

n/a	Involved in the study
<input checked="" type="checkbox"/>	<input type="checkbox"/> ChIP-seq
<input checked="" type="checkbox"/>	<input type="checkbox"/> Flow cytometry
<input checked="" type="checkbox"/>	<input type="checkbox"/> MRI-based neuroimaging

## Antibodies

Antibodies used	<p>Mouse monoclonal anti-1700011H14Rik/FAME (B-1) antibody (Santa Cruz, sc-398907, 1:50)          Fluorescein-labeled Lotus Tetragonolobus Lectin (Vector Laboratories, FL13212, 1:200)          Mouse monoclonal VANGL1 (E-3) antibody (Santa Cruz, sc-166844, 1:200)          Chicken polyclonal anti-GFP antibody (Abcam, ab13970, 1:250)          Normal Mouse IgG (1<math>\mu</math>g) (12-371, Merck)          Alexa Fluor 555, Donkey anti-Mouse IgG secondary antibody (Invitrogen, A-31570, 1:1000)          Alexa Fluor 647, Donkey anti-Chicken IgY secondary antibody (Invitrogen, A-78952, 1:1000)</p>
Validation	<p>1700011H14RIK: Overexpression of GFP-tagged 1700011H14RIK in HEK293 cells and subsequent staining using Alexa 568 Antibody. In addition we stained KO and WT kidneys and found a specific signal in WT membranal structures in kidney cells versus no specific signal in the KO condition (For Details see Supplementary Figure 21)</p> <p>Lotus tetragonolobus lectin: Lotus tetragonolobus lectin (LTL) encompasses a family of closely related glycoproteins with similar specificities toward <math>\alpha</math>-linked L-fucose-containing oligosaccharides. Although many of the binding properties of Lotus lectin are similar to those of Ulex europaeus lectin I (UEL I), the binding affinities and some specificities for oligosaccharides are significantly different between these fucose-specific lectins. This fluorescein-labeled LTL features a ratio of fluorophores to lectin protein that provides optimal staining (excitation 495 nm, emission 515 nm). Supplied as a solution essentially free of unconjugated fluorophores, it is preserved with sodium azide. The recommended inhibiting/eluting sugar is 50-100 mM L-fucose.  <a href="https://doi.org/10.1016/j.celrep.2022.110473">https://doi.org/10.1016/j.celrep.2022.110473</a></p> <p>Anti-VANGL1: Vangl1 Antibody is a mouse monoclonal IgG1 <math>\kappa</math> Vangl1 antibody provided at 200 <math>\mu</math>g/ml specific for an epitope mapping between amino acids 281-298 within a cytoplasmic domain of Vangl1 of human origin. Vangl1 Antibody is recommended for detection of Vangl1 of mouse, rat and human origin by WB, IP, IF and ELISA; also reactive with additional species, including and equine, canine, bovine and porcine  <a href="https://doi.org/10.1371/journal.pgen.1007840">https://doi.org/10.1371/journal.pgen.1007840</a></p> <p>anti-GFP: Chicken polyclonal antibody to GFP with over 2500 references: <a href="https://www.abcam.com/products/primary-antibodies/gfp-antibody-ab13970.html?productWallTab=ShowAll">https://www.abcam.com/products/primary-antibodies/gfp-antibody-ab13970.html?productWallTab=ShowAll</a></p>

Normal Mouse IgG: Routinely evaluated by IP/WB as a negative non-specific IgG control.

Alexa Fluor secondary antibodies (Invitrogen): Products have been extensively tested within our own facilities in applications such as cell imaging, flow cytometry and/or fluorescent western blotting. Robust QC procedures guarantee high performance for each individual product. <https://www.abcam.com/secondary-antibodies/validated-alexa-fluor-secondaries-for-guaranteed-performance>

## Eukaryotic cell lines

Policy information about [cell lines and Sex and Gender in Research](#)

Cell line source(s)	HEK293T ( <a href="https://www.atcc.org/products/crl-3216">https://www.atcc.org/products/crl-3216</a> ) - newly purchased from ATCC A549 ( <a href="https://www.atcc.org/products/ccl-185">https://www.atcc.org/products/ccl-185</a> ) - validated
Authentication	A549 cells were authenticated by Mycosynth, Austria. Profiling of the human cell lines was done using highly polymorphic short tandem repeat loci (STRs). STR loci were amplified using the PowerPlex® 16 HS System (Promega). Fragment analysis was done on an ABI3730xl (Life Technologies) and the resulting data were analyzed with GeneMarker HID software (Softgenetics). "The analyzed data of the submitted sample match 100 % to the DNA profile of the cell line A549 (ATCC® CRM-CCL-185™) and 100 % over all 15 autosomal STRs to Microsynth's reference DNA profile of A549 (Mic_150733)."
Mycoplasma contamination	All cell lines were tested negative for mycoplasma
Commonly misidentified lines (See <a href="#">ICLAC</a> register)	HEK293T and A549

## Animals and other research organisms

Policy information about [studies involving animals; ARRIVE guidelines](#) recommended for reporting animal research, and [Sex and Gender in Research](#)

Laboratory animals	FVB/Ant (0 and 75 days) and C57BL/6NCrI (75 days)
Wild animals	No wild animals were used in this study.
Reporting on sex	In our manuscript we used both males and females. These were identified by the animal caretakers. In our manuscript we report some sex specific parameters suggesting that FAME might have a sex-specific role.
Field-collected samples	No field collected samples were used in this study.
Ethics oversight	All animal work was approved and permitted by the Local Ethical Committee on Animal Experiments and conducted according to the Guidelines for Animal Experimentation recommendations (ARRIVE guidelines). In particular, mouse work related to C57Bl/6NCrI was approved and permitted by the Institute of Molecular Genetics of the Czech Academy of Sciences (licence: 45/2017 AVCR). Mouse work related to FVB/Ant by the BMBWF-V/3b (Animal experimentation and genetic engineering, Austria) (licence: BMWFW-66.009/0018-WF/V/3b/2017).

Note that full information on the approval of the study protocol must also be provided in the manuscript.

## Curriculum vitae

### Lukas Englmaier, MSc

CeMM Research Center for Molecular Medicine of the Austrian Academy of Sciences  
AKH BT25.3, 1090 Vienna, Austria  
ORCID 0000-0002-0082-2616

### BIBLIOMETRICS

H-Index: 7 | Citations: 701 (Source: Google Scholar, December 2025)

### EDUCATION

**09/2020 – Present** | **PhD Program UN094** | Molecular Signal Transduction |  
Medical University of Vienna, Austria | CeMM | LBI-RUD

**10/2017 – 09/2020** | **Master of Science (MSc)** | Molecular Microbiology, Microbial Ecology  
and Immunobiology | University of Vienna, Austria | Specialization: Immunology

**09/2014 – 07/2017** | **Bachelor of Science in Engineering** | Medical and Pharmaceutical  
Biotechnology | IMC University of Applied Sciences Krams, Austria

### RESEARCH EXPERIENCE

**06/2019 – 12/2019** | **Master's thesis** | Karolinska Institutet, Stockholm, Sweden |  
Kreslavskiy Group

**02/2019 – 05/2019** | **Researcher** | Masaryk University, Brno, Czechia | RECETOX | Group  
Spáčil

**10/2017 – 02/2019** | **Researcher** | Medical University of Vienna, Austria | Center for Brain  
Research Group Adameyko

**07/2016 – 02/2017** | **Bachelor's thesis** | Medical University of Vienna, Austria | Center for  
Brain Research Group Adameyko

### PUBLICATIONS (\*Contributed equally\*)

1. Zhang S, Owyong TC, Sanislav O, **Englmaier L**, et al. Global analysis of endogenous protein disorder in cells. *Nature Methods* (2025)
2. Zupančič M, Keimpema E, Tretiakov EO, Eder SJ, Lev I, **Englmaier L**, et al. Concerted transcriptional regulation of the morphogenesis of hypothalamic neurons by ONECUT3. *Nature Communications* (2024)
3. Petersen J\*, **Englmaier L\***, et al. A previously uncharacterized Factor Associated with Metabolism and Energy (FAME) regulates lymphoblastoid cell proliferation. *Nature Communications* (2023)
4. Boudier T, Petersen J, Faure L, Abed-Navandi D, Bouchnita A, Englmaier L, et al. Surface flow for colonial integration in reef-building corals. *Current Biology* (2022)
5. Costantini C, Nunzi E, Spolzino A, Merli F, Facchini L... **Englmaier L**, et al. A High-Risk Profile for Invasive Fungal Infections Is... *Infection and Immunity* (2022)
6. Rizzotto D, **Englmaier L**, Villunger A. At a crossroads to cancer: How p53-induced cell fate decisions secure genome integrity. *Int J Mol Sci* (2021) (Review)
7. Costantini C, Nunzi E, Spolzino A, Palmieri M, Renga G, Zelante T, **Englmaier L**, et al. Pharyngeal microbial signatures... *Infection and Immunity* (2021)
8. Dunst J\*, Glaros V\*, **Englmaier L\***, et al. Recognition of synthetic polyanionic ligands by chimeric antigen receptors. *Journal of Leukocyte Biology* (2020)
9. Soldatov R, Kaucka M, Kastri ME, Petersen J, Chontorotzea T, **Englmaier L**, et al. Spatiotemporal structure of cell fate decisions in murine neural crest. *Science* (2019)

## CONFERENCES

Oct 2025 | **Talk** | EMBO Workshop "The Epitranscriptome" | Heidelberg, Germany

Aug 2025 | **Attendee** | Human RNome Project Workshop | Frankfurt, Germany

Nov 2024 | **Poster** | 29th tRNA Conference | Kanazawa, Japan

Apr 2024 | **Poster** | Microsymposium on RNA Biology | Vienna, Austria

June 2022 | **Poster** | 28th tRNA Conference | Columbus, Ohio, USA

Apr 2022 | **Poster** | Microsymposium on RNA Biology | Vienna, Austria